Design, Synthesis and Characterisation of Novel Materials for Photocatalytic Water Splitting

This thesis is submitted in partial fulfilment of the requirements for the Degree of Doctor of Philosophy (Chemistry)

Emily Glover

UCL

2017

I, Emily Glover, confirm that the work presented in this thesis is my own. Where information has been derived from other sources, I confirm that it has been indicated in the thesis.

This thesis is dedicated to my

mother and my sister

Abstract

Rh-doped and Rh/Sb codoped TiO_2 and $SrTiO_3$ powders have been synthesised by solid state reaction of the titanate with the appropriate dopant oxides. The resultant materials have been extensively analysed in order to elucidate their physical, electrical and optical properties in order to determine their characteristics as photocatalyst materials. Powder X-ray diffraction provided information regard phase purity of the samples and indicated that for $SrTiO_3$, direct synthesis of doped materials from the titanate is not possible for total dopant concentration > 1.5 mol. %. A preliminary study indicated that the Sb dopant oxidation state cannot be inferred from photoelectron core line position measured by X-ray photoelectron spectroscopy (XPS) and so X-ray absorption measurements were recorded in both cases. For TiO_2 the presence of Sb (V) was strongly indicated both by the Sb K-edge energy and the EXAFS derived Sb-O bond lengths. In $SrTiO_3$, due to the low concentrations of dopant ion, results were inconclusive. Since the existence of Rh^{4+}/Rh^{3+} in these materials affects the Fermi level position, which is calibrated as 0 eV in XPS, careful handling of XPS data was required. The valence band and O 1s core line spectra were utilised to indicate the position of Fermi level in these materials. Transient absorption spectroscopy was used to probe the charge carrier dynamics of some selected materials and indicated that while the high dopant concentrations in TiO_2 appeared to supress charge carrier formation and increase recombination, low concentrations of dopants in $SrTiO_3$ show no negative effects with respect to pristine $SrTiO_3$ powder.

Acknowledgements

First I would like to thank my supervisor, Dr Robert Palgrave, for his guidance, encouragement and support throughout my PhD studies, and for allowing me to be independent in my research, while still keeping me on track. I was told many times by many people that I was lucky to have you as a supervisor and I would always, and will always, agree. I am grateful to my second supervisor, Professor Claire Carmalt, who has always been helpful to me, despite her being exceptionally busy. Thank you both.

I would like to thank the technical staff at UCL, particularly Dr Steve Firth for his consistently calm and conscientious assistance using SEM. I am also grateful to Professor Gopinathan Sankar for his help with synchrotron X-ray absorption measurements and data processing and to Dr Andreas Kafaizas for similar assistance with transient absorption spectroscopy. I would like to thank Dr Chris Blackman for his guidance with my teaching duties and for many a useful and interesting discussion about all things chemistry. To my group members, in particular Andrew Breeson and Shiny Mathew, thanks for entertaining me over the years. It's been great to have you in my academic family. And thank-you Shiny for all the XRD.

I also wish to thank the people I have shared this experience with, both the PhD students I've studied alongside and the post-docs who have helped me out of a few scrapes. Of course I'm grateful to all of the people from the third floor of the Christopher Ingold Building, but particular thanks go to Dr Helen Kimber, Miss Monika Jurcic, Dr Ana Jorge-Sobrido, Dr Raul Quesada-Cabrera, Dr Carlos Sotelo-Vasquez, Dr Nick Chadwick, Dr William Peveler, Dr Michael Powell, Mr Gwyn Evans, Dr Michael Warwick, Dr Emma Newton, Ms Chiaki Crews (honorary third floor member)- you have all made this a very memorable (in parts) four and a half years.

Outside of university I have to thank my friends, from home, netball and 35 Offord Road. You've all listened to me whinge and picked me up from my numerous downs too many times to count. Thank you.

And finally, to my mother, Denise, and my sister, Naomi, thank you both for making me the person I am today. You have shaped me (so you're to blame), supported me and been the best family a person could ask for. This thesis is for you.

List of Figures

List of Tables

Table of contents

Chapter 1: Introduction

1.1 General introduction and aims

Water splitting is a potential route towards the clean production of hydrogen (H_2), which has many vital uses for energy demand, for example it can be used as a fuel in an internal combustion engine or as an energy carrier in a hydrogen fuel cell[1, 2]. Photocatalysis, which relies on the absorption of light in order to catalyse a reaction, is one such viable route. This phenomenon utilises semiconducting materials to overcome the energy barrier to the water splitting reaction. This thesis presents the results of an investigation into the development and characterisation of materials used for photocatalytic water splitting.

First, some background is given to illustrate the global need for a clean route to hydrogen production. Here the political demands and definitions are given, alongside a description of current hydrogen and alternative hydrogen production methods. A discussion of the requirements for a material to be suitable for photocatalysis follows. Semiconductor band theory and methods of altering the band structure of a semiconductor are described, alongside the general principles of photocatalysis using single materials and combinations of materials (Z-schemes). Finally a summary of the current research landscape is given in a literature review of studies relevant to the work completed in this thesis, regarding titanium dioxide and strontium titanate.

Chapter 2 describes the synthesis methods used to make the photocatalyst materials and the theory behind the techniques used to analyse them. The materials investigated in this thesis are Rh/Sb doped TiO_2 and $SrTiO_3$, which have both been reported in the literature to exhibit photocatalytic activity for H_2 production. The aim of this thesis is to investigate the possible reasons behind this observed activity in order to determine principles that could be applied to other materials and dopant regimes. It should be noted therefore, that the analysis of the materials produced for these investigations focuses heavily on their characterisation, rather than testing their photocatalytic activity which has been proven elsewhere.

Chapter 3 describes a preliminary investigation using Sb oxides undertaken due to issues regarding the analysis of Sb dopant ions in TiO_2 and $SrTiO_3$. There are mixed opinions in the scientific community regarding the presence or absence of chemical shift in Sb XPS between the (III) and (V) ions. Since XPS was used widely in this thesis as a diagnostic tool to determine the presence and environment of dopant ions, it was important to understand how

Sb core-line spectroscopic data should be most appropriately handled. The results presented in this chapter provide the foundation for Sb XPS analysis in subsequent chapters.

Chapter 4 describes an investigation into Rh-doped and Sb codoped TiO_2. In this chapter, the effects of doping are described from a study of varying Rh concentration (1-9 mol. %) and varying Sb/Rh (Rh = 5 mol. %, Sb = 1-9 mol. %) dopant ratio. The characterisation aims to explain possible reasons for previously observed photocatalytic activity and to understand the interesting ways that the dopants in these materials change the electronic structure.

Chapter 5 describes a similar study into Rh and Sb codoped $SrTiO_3$. Here the effects of synthesis method are also investigated; the direct synthesis of $SrTiO_3$ with dopant oxides is attempted, by comparison with the previously reported reaction of $SrCO_3$ and TiO_2 with dopant oxides. An interesting difference between the effects of Sb as a codopant on the electronic structure of $SrTiO_3$ with respect to that of TiO_2 is highlighted and discussed, alongside other similarities and differences between the two systems.

Finally, Chapter 6 concludes this thesis, summarising the findings of all three results chapters in context of each other.

1.2 The need for clean energy

The drive towards a decline in the production of greenhouse gases and a reduction in the rate of global warming is a prevailing topic in governmental discussions across the world. At the 35th G8 summit in 2009, EU and G8 leaders declared the aim to reduce greenhouse gas emissions by 80% (from 1990s levels) by 2050[3]. In order to achieve this it will be necessary to move away from dependence on fossil fuels and towards cleaner forms of energy.

Clean energy was defined by the U.S. Energy Information Administration[4] as:

1. "Electricity generated at a facility placed in service after 1991 using renewable energy, qualified renewable biomass, natural gas, hydropower, nuclear power or qualified waste-to-energy; and

2. Electricity generated at a facility placed in service after enactment that uses qualified combined heat and power (CHP), generates electricity with a carbon-intensity lower than 0.82 metric tons per megawatt-hour (the equivalent of new supercritical coal), or as a result of qualified efficiency improvements or capacity additions at existing nuclear or hydropower facilities.

3. Electricity generated at a facility that captures and stores its carbon dioxide emissions."

Electricity is a clean energy carrier (i.e. zero carbon emission in use), though some of the methods currently used to produce large scale electrical output use fossil fuels, like coal, oil and gas, that contribute immensely to the generation of greenhouse gasses, namely carbon dioxide (CO_2). Data, published by the U.K. Department for Business Energy and Industrial Strategy and shown in Figure 1, illustrates the distribution of sources from which electricity was generated in the UK in 2011 and 2016[5]. Over the five year span shown, use of renewable sources has more than doubled and reliance on coal has diminished to 4% from 29%. However, use of oil (and "other") has remained the same and use of gas has increased by 4%.

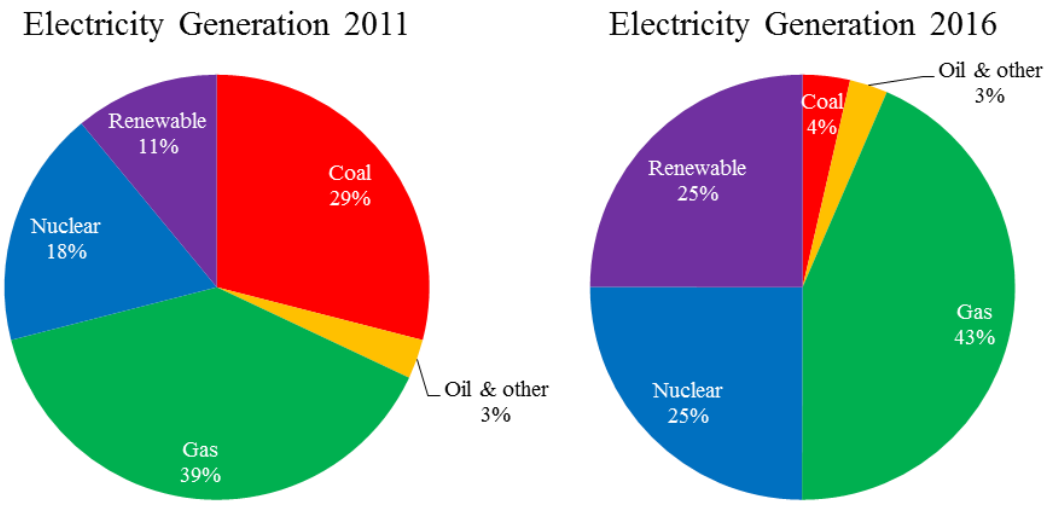

Figure 1: Electricity generation by fuel source from U.K. Department for Business Energy and Industrial Strategy

Electricity is produced by using these fuels to heat water, creating steam to drive a turbine and convert this kinetic energy into electrical energy[6]. In addition to general electricity production, transport is another source of high demand for fuel. The majority of current automotive vehicles rely on the internal combustion engine, which burns carbon based fuel to drive pistons and generate kinetic motion. Projections across the globe agree that these methods are unsustainable with the latest predictions indicating that there could be a maximum of only 90 years of energy production from conventional fossil fuel sources[7].

1.2.1 Hydrogen as a fuel

One viable alternative to fossil fuel combustion is hydrogen gas ($H_{2\,(g)}$) as a fuel source. Hydrogen can be burnt in order to heat water and create steam, used in an adapted internal combustion engine [1, 8] or as an energy carrier in a hydrogen fuel cell [6].

The product of hydrogen combustion in the presence of oxygen is water, as shown by the reaction in Equation 1.

$$2H_2 + O_2 \rightarrow 2H_2O$$

Equation 1

If undertaken in air, as in an internal combustion engine, there are additional products such as nitrogen oxides (NO_x) from reaction with nitrogen in the air and some carbon oxides (CO_x) and hydrocarbons from reaction with lubricating oils found inside the engine [2]; however, research is being undertaken in order to minimise these issues [9, 10].

A fuel cell intakes hydrogen at the anode and oxygen (or air) at the cathode. Hydrogen is catalytically split into an electron and a proton, allowing the electron to create an electrical circuit before re-joining the proton at the cathode with oxygen, generating water [6]. This type of fuel cell is already used in some vehicles [11], and plans to develop the hydrogen economy by introducing hydrogen fuelling stations are well underway in some locations, such as California[12].

1.2.2 Current methods of hydrogen production

Current methods used to produce hydrogen involve the use of natural gas as a precursor. The main component of natural gas is methane (CH_4) alongside smaller concentrations of larger hydrocarbons such as ethane, propane and butane. Trace amounts of nitrogen, carbon dioxide, sulphur and helium can be found in gas sourced from some regions and the general composition of natural gas varies from region to region[13]. Steam-methane reforming is the predominant method for the production of hydrogen in the current energy market[14]. Although the mechanism for the production of H_2 from methane in this manner is complex and widely unknown, research into the rates of formation of the products has been based upon the following reactions[15]:

$$CH_{4\,(g)} + H_2O_{(g)} \rightarrow CO_{(g)} + 3H_{2\,(g)}$$

Equation 2

$$CO_{(g)} + H_2O_{(g)} \rightarrow CO_{2\,(g)} + H_{2\,(g)}$$

Equation 3

Overall,

$$CH_{4\,(g)} + 2H_2O_{\,(g)} \rightarrow CO_{2\,(g)} + 4H_{2\,(g)}$$

Equation 4

It can be easily concluded that CO_2 is a major by-product from the production of H_2 from methane. A major concern regarding steam methane reformation is the reliance on fossil fuels. Whilst hydrogen as a fuel itself only produces water as a by-product, there is inevitably production of carbon oxides when it originates from carbon based sources, which contribute

as greenhouse gases to climate change. Thus the search for a viable clean alternative method of hydrogen production is a vital area of research.

1.2.3 Water Splitting

Water splitting is an endothermic reaction (Equation 5) and can be expressed as its redox components shown in Equation 6 (oxidation) and Equation 7 (reduction).

$$2H_2O \rightarrow 2\,H_2 + \,O_2$$

Equation 5

$$2\,H_2O \;\longrightarrow\; O_2 + 4\,H^+ + \,4\,e^- \quad (1.23\,eV)$$

Equation 6

$$2\,H^+ + 2\,e^- \;\longrightarrow\; H_2 \quad (0.00\,eV)$$

Equation 7

As can be deduced from the above reactions, four electrons are required per two water molecules to successfully split them into two hydrogen molecules and an oxygen molecule, with the overall potential of the reaction measuring -1.23 eV. The energy required to split water can be provided in different forms; an overview of notable methods follows.

1.2.3.1 Thermal Decomposition

Dissociation of water into various combinations of its component parts (H_2, O_2, H_2O_2, H, O etc.) occurs at temperatures above 2000˚C[16]. Since many other industrial processes occur at similarly high temperatures, this has been considered as a potentially viable form of hydrogen production. Two main issues surround this method: separation of the products and the low mole fraction of H_2 that is formed.

One solution is to incorporate filtration membranes in the reactor [17] to collect H_2 as it is formed, however these tend to decompose when in contact with water at high temperatures [18]. Another solution is to rapidly quench the hot reaction mixture; however, since this essentially suspends the process, the low mole fraction of H_2 available limits the efficiency of this method. Only around 4 % of the mixture is H_2 [19], hence the yield is poor.

1.2.3.2 Photobiological Decomposition

The use of biological organisms in order to generate hydrogen was first experimented with in 1942, where research focussed on green algae which could ferment hydrogen under a nitrogen atmosphere [20]. The key component of the green algae is the enzyme hydrogenase which has been determined as important to photosynthetic electron transport in the cells [21]. These systems

use light to convert water into oxygen and hydrogen following a complex biological pathway much the same as photosynthesis in plants.

A limitation of green algae is its low capacity for hydrogen production, which does not show improvement with increasing light intensity. A competitive pathway for the involved electrons exists, whereby they are able to be employed in CO_2 fixation, and furthermore a back reaction between H_2 and O_2 is facilitated in the absence of light [22].

1.2.3.3 Electrochemical Decomposition

Following the findings of Henry Cavendish in 1784 that an electrical spark would cause H_2 and O_2 to combine and form water[23], the reverse reaction was observed and water electrolysis using a battery to evolve H_2 and O_2 first reported the early nineteenth century[24, 25].

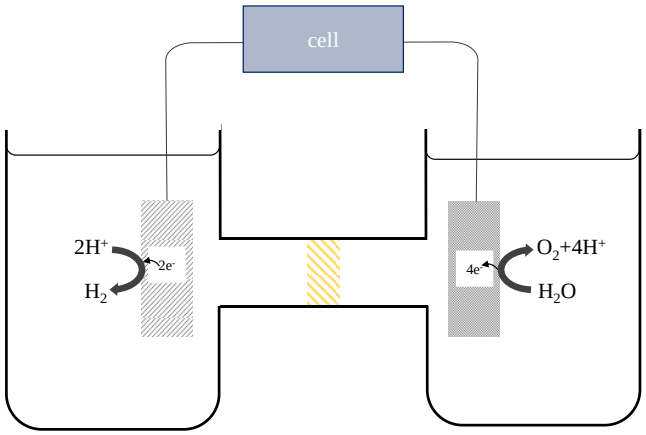

Figure 2: Schematic of photoelectrochemical cell setup showing the water splitting half reactions

A common electrochemical setup is shown in Figure 2, where evolution of H_2 and O_2 is driven by the electrical current provided by a cell. Two electrodes are submersed in electrolytic solution, providing a source of water and electrolytes to carry charge and complete the circuit. The source of electrical energy in this kind of setup is the cell, which can be a conventional battery but could also be a photovoltaic, whereby electrical energy is generated by the absorption of light. When a photovoltaic is used, the system can be termed photoelectrochemical.

1.3 Principles of Photocatalysis

Light induced water splitting was first achieved in 1972 by Fujishima and Honda[26] with their photoelectrochemical cell containing a TiO_2 electrode at which water oxidation occurs and a Pt counter electrode at which H^+ reduction occurs. Light absorbed by the TiO_2 photoelectrode enabled the electrical requirements of the electrochemical cell to be reduced, since the absorbed light energy was facilitating part of the reaction. Following this discovery light

induced water splitting became highly researched in the literature, as can be seen in the citation report in Figure 3, which was generated from a literature search for the phrase "solar water splitting" through the Web of Science search engine on 04/02/2017.

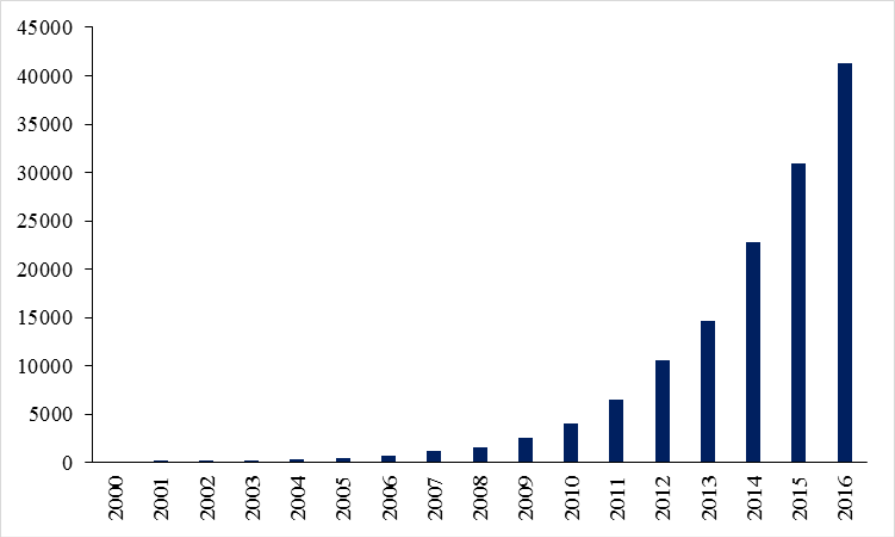

Figure 3: Citation report for articles resulting from a Web of Science search using the term "solar water splitting"

Photocatalytic water splitting differs from that discovered by Fujishima and Honda in that all of the energy requirements for the reaction are satisfied by the absorption of light. This requires photocatalyst materials to fulfil certain electronic requirements, which are outlined in the following sections. The band theory of semiconductors, the materials used for photocatalysis, is described in order to lay foundations for further discussion of the requirements for a material to be a successful photocatalyst.

1.3.1 Basic semiconductor Band Theory

The general electronic structures of a conductor, semiconductor and insulator are shown in Figure 4. In contrast to a simplistic molecular model whereby distinct orbitals are occupied by single or paired electrons, a solid material with an extended crystal structure possesses "bands" of orbitals, contributed to by molecular orbitals of the atoms making up the structure that are very close in energy. These bands are termed the "valence band" (VB), a lower energy band of orbitals containing the valence electrons of the structure and the "conduction band" (CB), a higher energy band of orbitals through which electrons can move more freely, allowing conduction to occur[27]. The energy difference between the valence band maximum (VBM) and the conduction band minimum (CBM) is termed the band gap (E_g) and is of primary importance in both classification of materials and when choosing a semiconductor for photocatalysis.

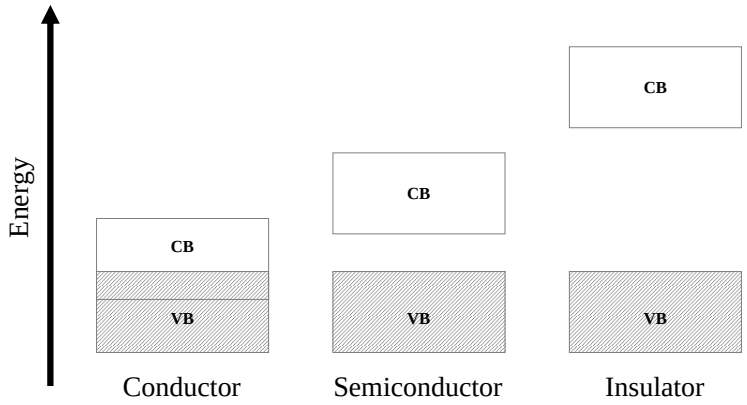

Figure 4: Band structure schematic for conductors, semiconductors and insulators

In a conductor, substantial overlap between the CB and VB means that the CB is partially occupied and thus a proportion of electrons can move freely throughout the solid. In contrast, an insulator has a large band gap meaning that electrons cannot be excited into the CB, which remains empty. Semiconductors can be defined as having a band gap of between 0.5-4 eV[28]. In a semiconductor the size of the band gap is such that electrons can be excited from the VB to the CB upon absorption of energy. The excitation of a negative electron leaves a net loss of charge from the VB which is then described as having a positively charged "hole" (h^+). The electron and hole are termed "charge carriers"; their generation, mobility and lifetimes are of the highest importance in semiconductor catalysis.

Defects in semiconductors

A semiconductor with a perfect crystal structure is termed "intrinsic" where the number of e^- and h^+ are equal. Semiconductors that differ from their pure form are "extrinsic", where either the $e^- > h^+$ (n-type) or $e^- < h^+$ (p-type). Semiconductors can be doped to form n-type or p-type materials by introducing donor or acceptor impurities, respectively. The introduction of donor states just below the CB means that small amounts of thermal energy (i.e. room temperature) can cause an electron to move into the CB, leaving behind an oxidised donor ion. For example, the introduction of Ti^{3+} into a TiO_2 lattice has this effect. The singly occupied Ti^{3+} 3d orbitals lie just below the CB minimum (CBM) in TiO_2, injecting electrons into the CB and resulting in the formation of Ti^{4+}, which is then stable in TiO_2. In p-type doping an acceptor state is introduced close to the VB maximum (VBM) such that electrons from the VB can be thermally excited at room temperature into these acceptor states and thus leave a hole behind.

In practice, most materials are extrinsic semiconductors due to inherent defects that cause them to be n- or p-type. The Fermi level can be considered to be a hypothetical energy level that, at thermodynamic equilibrium, has a 50% probability of being occupied by an electron at any given time [27]. In an intrinsic semiconductor this would lie exactly ion the middle of the

band gap, since there are equal number of electrons and holes. However, in extrinsic semiconductors the position of the Fermi level, $E_{F,}$ is dependent on the nature of the semiconductor. An n-type semiconductor will have an E_F close to the CBM, due to the donor states which are able to inject electrons into the CB and a p-type semiconductor will have an E_F close to the VBM, due to the acceptor states present there.

The band diagrams for p- and n-type semiconductors are shown in Figure 5 below.

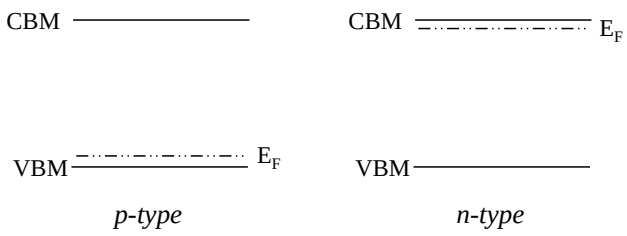

Figure 5: Schematic band diagrams for p-type and n-type semiconductors

Band bending and Fermi level equilibration

Combining two semiconductors via a physical interface (a heterojunction) results in equilibration of the Fermi levels across the junction; the E_F must be the same throughout the material. Equilibration of the Fermi level occurs by "band-bending" at the interface. A p-type semiconductor, placed in contact with an n-type semiconductor forms a p-n junction, which is a simple example of when band bending may occur.

In a heterojunction the alignment of the CBM and VBM of the two materials is important. In order to know the relative positions, these values are measured with respect to the vacuum level, that is, the energy of a free electron (outside of the semiconductor) at rest, with respect to the semiconductor. Thus the alignment of semiconductor band edges is dictated by the electron affinity. When combining materials in a heterojunction, different alignments of VBM and CBM are of course possible. These can be classified into three types: type I (straddling gap), type II (staggered gap) and type III (broken gap), which are illustrated in Figure 6.

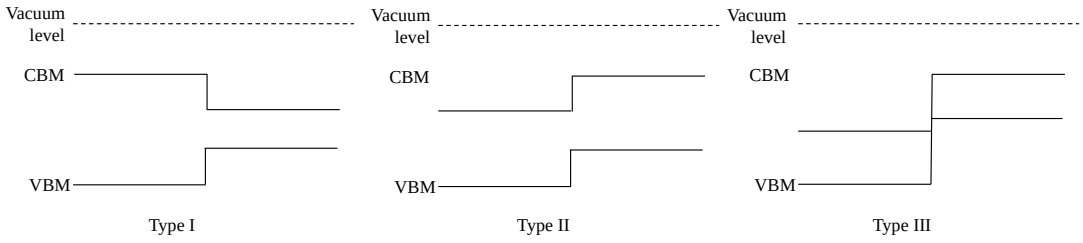

Figure 6: The three types of heterojunction interface type I (straddling gap), type II (staggered gap) and type III (broken gap)

When p-type and n-type materials are combined, electrons move across the junction from n-type to p-type material, combining with positive ions (holes). Thus a layer depleted of charge carriers forms around the junction, called the depletion region denoted between $-x_p$ and x_n on Figure 7[29]. The ionised donors and acceptors in the depletion zone have charge, causing an intrinsic electrical field and thus a drift of charge carriers in the opposite direction. This diffusion of carriers continues until the drift current balances the diffusion current, thereby reaching thermal equilibrium as indicated by a constant Fermi level[29].

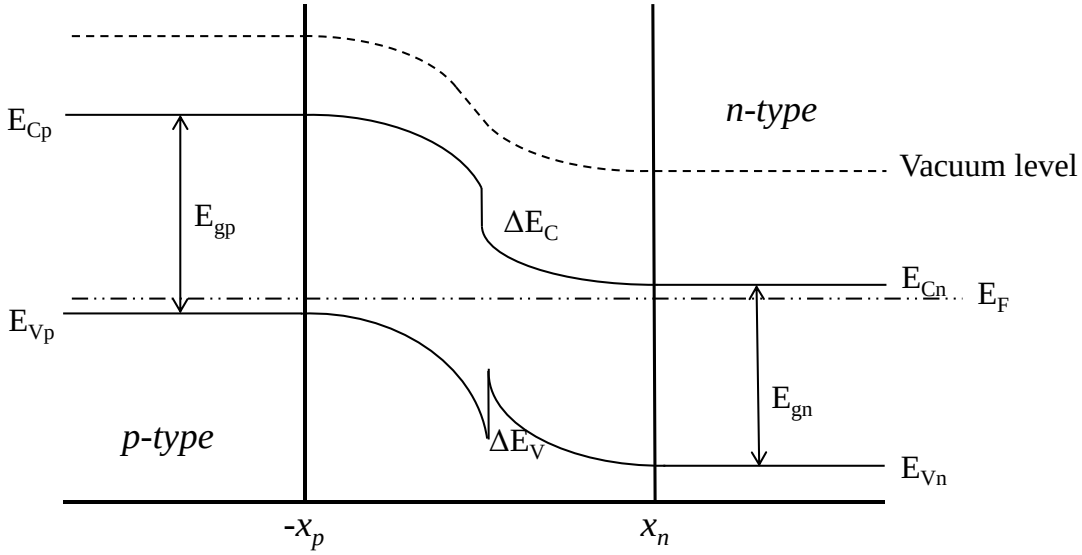

Figure 7: Band-bending diagram for a p-n junction, showing the depletion zone between $-x_p$ and x_n.

Heterojunctions are of importance in photocatalysis due to the intrinsic field they produce and its effect on charge migration, an essential factor in photocatalytic activity. In-depth understanding of the electronic structure of photocatalytic materials, in order to maximise their effectivity is therefore an essential part of photocatalysis research.

1.3.2 Principles of photocatalytic water splitting

Photocatalysis involves the absorption of light to reduce the energy requirement of a reaction. A photon of light, hν, is absorbed by an electron in the VB of a material, resulting in photoexcitation of the electron into the CB and formation of a positively charged hole in the VB. This photoexcitation process is shown schematically in Figure 8. Once generated, the electron and associated hole can go on to catalyse redox reactions for molecules adsorbed to the surface of the semiconductor material [30].

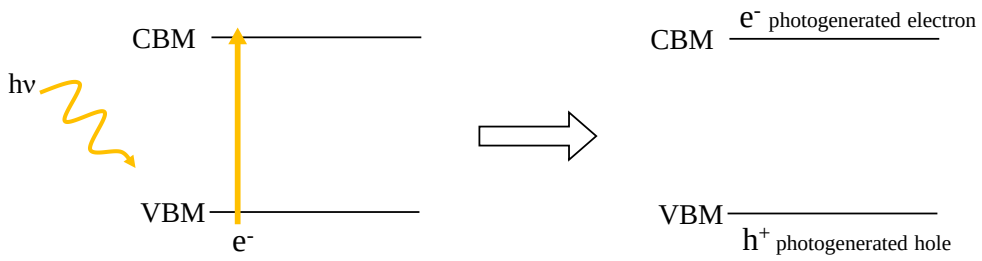

Figure 8: Photoexcitation of an electron and consequential formation of a photogenerated hole in a semiconductor

An excited electron and hole proceed via any of the following pathways:

i. Recombination

ii. Migration to surface where they can:

   a. Recombine

   b. React with adsorbates (which can potentially back-react with the semiconductor)

Charge carrier migration is therefore a very important factor within photocatalysis. Charge carriers must be able to reach the surface of the material in order to have the opportunity to react with any adsorbed molecules. Once at the surface, the e^- and h^+ must have enough potential to partake in the water splitting redox reactions. This translates to the band edge requirement that the CBM must be more negative than the potential for H^+ reduction (0.00 eV vs NHE) and the VBM must lie more positive than the oxidation potential of H_2O to O_2 (+1.23 eV vs NHE). That is, the band edges of the photocatalyst must straddle the redox potentials (see Figure 9)[31]. The band edges of WO_3, shown in Figure 9, only straddle the water oxidation potential and therefore cannot be used for overall water splitting alone but can be combined with another material capable of H^+ reduction. The combination of materials in this way will be discussed in section 1.3.2.1.

In order to achieve excitation of an e^- from VB to CB, the energy of an incident photon must be equal to or greater than the band gap of the semiconductor. Therefore, the size of the band gap is equal to the minimum energy necessary for photoexcitation to occur using that material. This energy requirement is related to light wavelength by the following:

$$E_g = \frac{hc}{\lambda}$$

Equation 8

where E_g = band gap energy, h = Planck's constant, c = speed of light (and thus the constant hc = 1239.8417 eVnm) and λ = wavelength of incident light. Using the known potentials of H^+ reduction and water oxidation, it can be determined that the minimum energy required to split water can be satisfied by light of wavelength ~1008 nm (if E_g = 1.23 eV), which correlates

to the infrared (IR) region of the electromagnetic (EM) spectrum. However, since some activation energy is still required for the reaction to initiate[32], the ideal band gap for a single material to be able to achieve overall water splitting is usually cited as ~1.5 eV, with band edges slightly outside of the redox potentials of water splitting, as shown by the 'ideal position' marker in Figure 9[33].

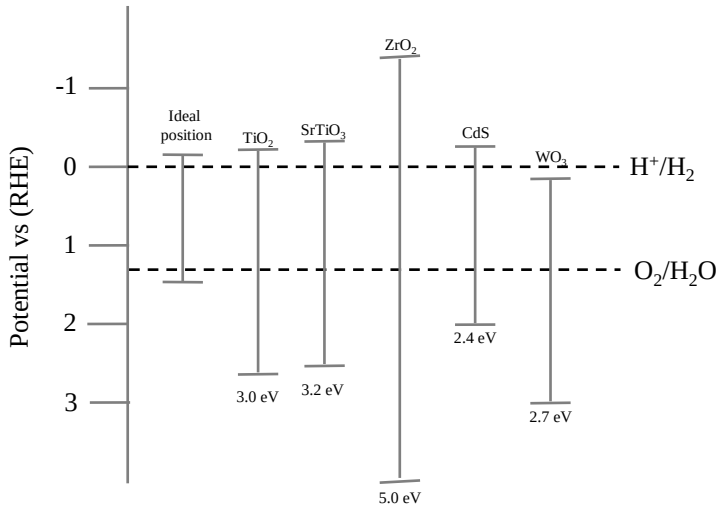

Figure 9: Band edge positions and band gap values for some key semiconductors alongside the ideal position for semiconductor band edges for water splitting

The band gaps of stable semiconductors tend to be wider than this ideal energy; many photocatalysts are only effective under ultraviolet (UV) light which lies at the higher energy end of the electromagnetic spectrum. UV light accounts for only 4-5 % of solar radiation that reaches the earth's surface, whereas visible light accounts for around 40 % of solar photons [34]; hence there is a drive in current photocatalytic research to find stable narrower band gap semiconductors that can utilise visible light (λ = 400-700nm). Such materials could increase the efficiency of the photocatalytic processes since a greater range of wavelengths of incident light would be effective in photogeneration of charge carriers. Many semiconductor conduction band edges lie close to the reduction potential for H^+, though the valence band edges are far from the oxidation potential for H_2O; a common approach to band gap reduction is therefore to alter the valence band in some way to bring the VBM to a less positive potential, whilst maintaining its position as positive with respect to the water oxidation potential.

As mentioned, recombination of electrons and holes in the bulk of the catalyst is an alternative mechanism available to compete with the desirable redox reactions. Whilst a certain proportion of photogenerated electrons and holes are expected to recombine, a high recombination rate (often described as short charge carrier lifetime) negatively affects the efficiency of a photocatalyst. Prevention of recombination involves promoting charge separation, which can be achieved by introducing electron or hole scavengers (other species

that react with e^- or h^+ and can then go on to react with the desired oxidant or reductant) or by improving charge carrier separation to prevent recombination. If the concentration of charge carriers is too high with poor charge separation, recombination is facile; if the concentration of charge carriers is too low, catalysis is slow[35]. Therefore, charge carrier generation alone cannot ensure an effective photocatalyst.

Long term stability of materials must be a consideration when designing photocatalysts. Photocorrosion is an issue most associated with cadmium sulfide (CdS), though other promising semiconductors (for example ZnO[36], $AgNO_3$[37]) can also be prone to it. Using CdS as an example, the catalyst is degraded by photogenerated holes by the following pathway:

$$2h^+_{vb} + CdS \longrightarrow Cd^{2+} + S$$

Equation 9

In the case of CdS it is believed that this mechanism is promoted by traces of cadmium oxide, which can be minimised if the synthesis is carried out in the absence of air[38]. As well as photocorrosion, other catalyst degradation pathways can be problematic, for example Cu_2O possesses an ideal band gap for proton reduction, but is susceptible to oxidation and thus its efficiency diminishes over time.

Stability in water and under light, charge carrier lifetime and band edge alignment are some of the difficulties that must be overcome when designing a photocatalyst system. Synthesis of functioning photocatalysts requires thoughtful design and comprehensive knowledge of the properties of the materials being used.

1.3.2.1 Z-schemes

An alternative to the search for a single material for overall water splitting is the Z-scheme. This involves a combination of two semiconductor photocatalysts, one able to catalyse oxidation of water and the other proton reduction. This two-step photoexcitation mimics the photosynthesis pathway found in plants, in that there are two redox centres at which each process occurs upon the absorption of a photon[39].

In photosynthesis, upon the absorption of a photon of solar light (hv) photosystem II (PS II) oxidises water, receiving the resultant two electrons and promoting them to a higher energy state. Charge transfer occurs between the elevated PS II electrons into the lowest photosystem I (PS I) state. Absorption of a secondary photon occurs and the electrons are elevated to the PS I high energy state, at which they have enough energy to facilitate the production of ATP and NADPH- the energy carriers in green plants[40].

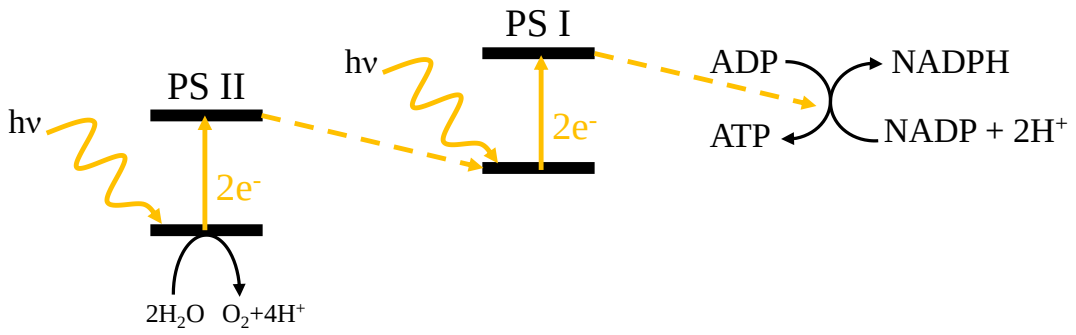

Figure 10: Electron pathway in photosynthesis of green plants using photosystems I and II

The Z-scheme works in much the same manner, the O_2 evolution photocatalyst being equivalent to PSII and the H_2 evolution catalyst being equivalent to PSI. In a Z-scheme the charge transfer process, which in photosynthesis happens across a complex pathway of proteins[41], can be mediated by a redox couple such as IO_3^-/I^-. These redox couples can be generalised as an electron donor (Y) and an electron acceptor (X), as in Figure 11. At the hydrogen evolving catalyst, Y can be oxidised to X ("Y^+"), while H^+ is reduced to H_2, conversely at the oxygen evolving catalyst, X is reduced to Y ("X^-") while H_2O is oxidised to O_2 and H^+.

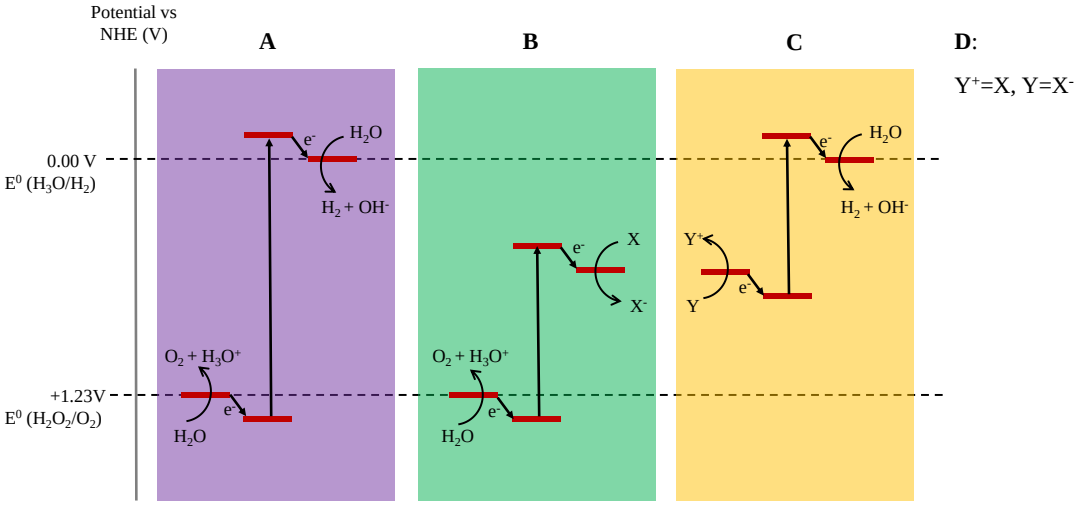

Figure 11: Schematic representation of Z-scheme photocatalysis showing A: single material photocatalysis, B: water oxidation catalyst, C: hydrogen reduction catalyst (where B+C together are mediated by two different ion pairs X/X^- and Y/Y^+) D: where B+C together are mediated by one ion pair

Back reactions of interconversion between A and D can serve to inhibit the forwards water splitting reactions and so it is important to regulate the reactions that will occur by careful design of the z-scheme. The redox mediator must be preferentially reduced on the water oxidation catalyst and preferentially oxidised over the proton reduction catalyst for the system to proceed successfully. Redox potentials of all components must therefore be carefully tuned in order to complement each other.

Z-schemes can be formed by simply combining both the reduction and oxidation catalyst together in solution and using a redox mediator to shuttle electrons between the two, or by forming a direct contact between the two materials[42]. This second option forms a heterojunction, described previously in section 1.3.1. Due to the field created at the junction interface, heterojunction Z-schemes can offer enhanced charge separation, lengthening charge carrier lifetimes and thus improving the efficiency of the photocatalysts. Another advantage of Z-schemes over single material photocatalysts is the wide range of materials that are available to be used. When both the redox potentials of water must be straddled, the band edges of potential photocatalysts must be very specific, however, when only one or other potential needs to be straddled, many more materials, in different combinations can be combined. Additionally, because of the separation of the two parts of the reaction, materials with band gaps < 1.23 eV can be experimented with. A disadvantage of Z-scheme systems is that the quantum efficiency is immediately halved with respect to a single-step photocatalyst, since two photons are required to do the job of one photon in the single-step system. However, due to the low efficiencies experienced by single- material photocatalysts Z-schemes offer an interesting alternative solution.

Initially, research naturally focussed on the combination of two TiO_2 materials (one anatase, one rutile) assisted by Pt co-catalysts as a z-scheme system [43], though visible light active systems are of higher interest since both anatase and rutile are only active in the UV region of the EM spectrum. Strontium titanate is another wide band gap semiconductor that has been observed to exhibit visible light activity when doped and can be used for H_2 evolution[44]. A number of co-catalysts have been tested alongside doped STO; for example rhodium doped $SrTiO_3$ with a ruthenium cocatalyst ($Ru/SrTiO_3$:Rh) found to be an effective system for H_2 production (with WO_3 as the O_2 catalyst throughout comparisons)[45]. In this investigation by Sasaki et al. the difference between photodeposited Ru metal and impregnated RuO_2 was examined due to a large discrepancy between the activities of the two systems. It was found that impregnated RuO_2 is not an effective co-catalyst and that, since metallic Ru is oxidised once deposited, is most likely due to the poor dispersion of RuO_2 throughout the $SrTiO_3$.

For many z-schemes the I^-/IO_3^- redox couple has been used as a mediating pair to shuttle electrons between catalysts. An alternative mediatory couple is Fe^{2+}/Fe^{3+}, which can be included in solution as $FeCl_2$[46]. Some investigations report that the reduction of the mediator can proceed preferentially to water reduction at high concentrations[47]. In order to prevent this and other undesirable side effects of mediators (i.e. shielding the catalysts from incident light) investigation into systems that can split water under visible light using only the catalysts has been undertaken. Sasaki et al. determined that it is possible to split water stoichiometrically

across $Ru/SrTiO_3$:Rh and two different O_2 evolution catalysts ($BiVO_4$, WO_3) as long as the materials were in contact with each other as well as the reaction solution[48].

1.4 Titanium Dioxide

Titanium dioxide (TiO_2) has been investigated heavily for its light harvesting properties. The low cost, low toxicity and stability- both chemically and thermally- make it an ideal material in many applications.

1.4.1 Crystal Structure

Three polymorphs exist: rutile, anatase and brookite. Rutile is the most thermodynamically stable and brookite has not been as actively investigated as the other polymorphs due to its relative thermodynamic instability[49-51]. The Gibbs free energy change between rutile and anatase is small (< 15 $kJmol^{-1}$) and rutile beings to form at 400 – 600 ˚C[52]. All three polymorphs consist of octahedra containing a Ti^{4+} cation coordinated to six O^{2-} anions. Chains of octahedra are connected via edges in rutile, vertices in anatase and both edges and vertices in brookite- shown in Figure 12[53].

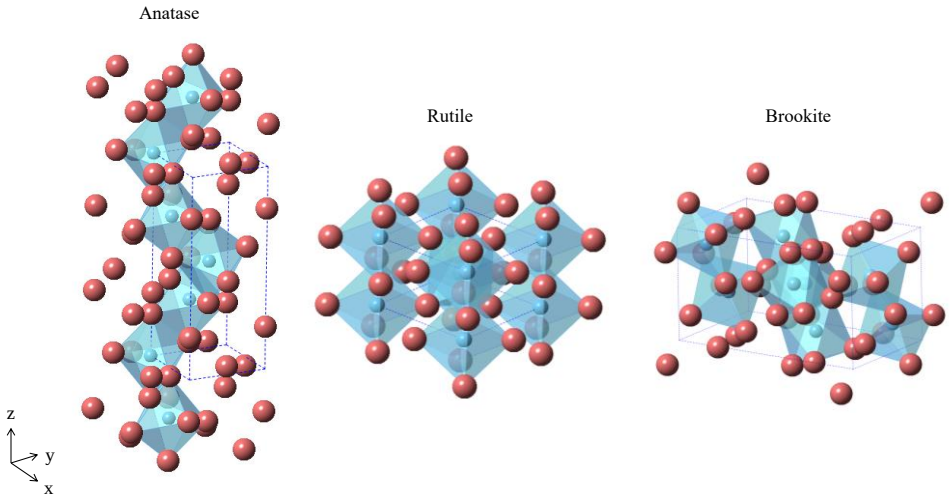

Figure 12: Structures of anatase[54], rutile[55] and brookite[56] TiO_2

TiO_2 is easily reduced, with bulk reduction causing a characteristic colour change in thin films, from transparent to blue[57]. Diffusion of defects from the bulk to the surface can greatly affect the surface structure; the diffusion pathways for different defects vary; O defects generally migrate by vacancy diffusion and Ti defects interstitially. Relaxations of a lattice change the structure of the surface, affecting adsorption and catalysis rates; adsorbates can have the corresponding effect of "re-relaxing" the surface[58].

Anatase and rutile surfaces differ in a number of ways. Their most thermodynamically stable faces are (101) and (110), respectively. Scanning Tunnelling Microscopic (STM) images of the (110) rutile face, revealed alternating rows of titanium and oxygen ions[59]. The following atoms exist at the surface: five-fold coordinated titanium with a dangling bond, in-plane three-fold coordinated oxygen, six-fold coordinated titanium connected to bridging oxygen. The coordinative unsaturation of bridging oxygen atoms makes their removal facile[58]. By comparison, the anatase (101) surface has pm symmetry, which gives rise to preferential orientation of step-edges. Here there are five and six-fold coordinated titanium atoms in the terraces, with four-fold titanium and two-fold oxygen atoms at the step edge[60].

Oxygen vacancies- a common defect in TiO_2- leave an accumulation of electrons in the TiO_2 lattice making it an n-type semiconductor. These vacancies can be created by electron bombardment, followed by interatomic Auger process or by thermal annealing. Resultant defects differ depending on their formation method, the former process tending to give rise to ejection of bridging oxygen, whereas the latter removes two-fold coordinated oxygen atoms[61]. This is an accessible method of tuning the lattice since these vacancies can easily be refilled by thermal treatment under oxygen.

Studies have determined that oxygen defects in the anatase (101) surface are energetically unfavourable in comparison to vacancies in the bulk[62]. This suggests that, since atoms can only leave a material via a surface, oxygen dissociates from the surface and the vacancy subsequently migrates into the lattice. This phenomenon is linked to the stability of the remaining Ti atoms; an oxygen defect leaves one five-fold coordinated and a second, highly unstable, four-fold coordinated Ti^{3+} at the surface, whereas in the bulk all Ti^{3+} are five-fold coordinated and thus stable

1.4.2 Electronic Structure

There is widespread agreement that the electronic structure of bulk TiO_2 and surface TiO_2 is similar[63]. The valence band of TiO_2 is constructed mainly of O 2p orbitals, with a significant amount of Ti-O covalence[63]. Ti 3d orbitals dominate the conduction band though there is some contribution from Ti4s and Ti4p orbitals at higher energy levels.

Crystal-field splitting of the conduction band d-orbitals occurs due to the octahedral coordination around Ti^{4+}. The direct interaction of oxygen ligands with e_g orbitals causes these to exist at a higher energy and form σ-type bonds. At lower energy, due to orbitals pointing between ligands, the t_{2g} levels form π-type bonds with the remaining oxygen atoms.

Clearly the electronic structure is influenced by the positions of individual atoms in the lattice and so variations in crystal structure can affect the band positions.

1.4.3 Modifying TiO_2 to improve its photocatalytic activity

Although there are examples of photocatalytic TiO_2 in commercial applications (for example self-cleaning surfaces[64]) in order to extend their activity to the visible light region, modifications must be made to the electronic structure. One of the most active fields of research with respect to TiO_2 modification has been doping. Both anions and cations can be incorporated into TiO_2, in either a substitutional or interstitial manner. If the size of anion or cation is similar to that of Ti^{4+} or O^{2-}, respectively, then a substitutional mechanism will predominate. Conversely, if the dopant ion is much smaller then they will lie in the interstitial space between the main lattice ions[65]. The addition of different elements into the crystal structure incorporates their accessible electronic states; the VBM position can change to red shift the band gap (i.e. make it smaller narrower and thus able to usefully absorb lower energy light). Alternatively, isolated but accessible intra-band energy levels can be created.

Transition metals have been successfully doped into TiO_2, iron [66], cobalt [67], copper [68] and manganese [69] being some examples. The main function of transition metal doping is to increase the light absorbance into the visible range by inserting donor/acceptor states into the band gap. The dopant d-electrons can inject into the conduction band by absorbing lower energy light than required for the VB → CB transition[70]. However, the transition metal dopant ions can act as electron or hole traps (by the mechanisms shown in equations 10, 11 and 12, for example), which promote recombination and decrease photocatalytic activity[70].

$$Cr^{3+} + h^{+} \rightarrow Cr^{4+}$$

Equation 10

$$Mn^{2+} + e^{-} \rightarrow Mn^{+}$$

Equation 11

$$Mn^{2+} + h^{+} \rightarrow Mn^{3+}$$

Equation 12

Rare earth metals including Yttrium [71], Praseodymium, Lanthanum, Cerium, Neodymium, Europium, Dysprosium, Gadolinium [72] and Holmium [73] have been incorporated into TiO_2 and analysed for their photocatalytic properties. Improved photocatalytic activity is observed and attributed to the 4f orbitals of the rare earth dopants, which are partially occupied[70]. This results in a red shift of the band gap, increasing the visible light activity. Additionally, with the incorporation of lanthanum, for example, a decreased particle size and increase in particle

uniformity is observed[74]. A resultant increase in photocatalytic activity can be ascribed here to increased adsorption due to larger specific surface area.

Of all non-metals that have been investigated as dopants, nitrogen is by far the most prolific in literature, though carbon [75] and sulfur [76] have also received attention. Nitrogen doping, originally investigated by Asahi et al.[77] has the effect of increasing visible light absorption and thus increasing photocatalytic activity by improving quantum efficiency. The original researchers suggested that doping results in mixing of oxygen and nitrogen 2p valence states and that since N2p states lie more positive than O2p the absorption edge is red-shifted. However, following this study there has been much debate in the literature as to the source of this increase in activity. An alternative explanation is that intra-band states are created by the nitrogen dopant ions and that oxygen defects in the lattice (doped or otherwise) give rise to colour centres (also intra band states) that photoactivate TiO_2. [65] Both experimental analysis and computational calculation appear to point toward the latter explanation [78]; defect tailoring could become an important area of future research.

Usually there is an optimum doping concentration, below which the effects of the dopant are minimal and above which degradation of the catalyst or higher rates of recombination can occur[79, 80]. However, as noted by Daghrir et al.[81], variances between synthesis techniques make it difficult to directly compare different TiO_2 dopants.

1.5 Strontium Titanate

1.5.1 Crystal structure

Strontium titanate crystallises in the cubic perovskite structure, ABO_3 (space group *Pm3m*) with Sr^{2+} and Ti^{4+} ions on the A and B site respectively. A central Ti^{4+} ion is coordinated octahedrally to 6 O^{2-} ions (on each face of the unit cell), with Sr^{2+} ions situated at the vertices of the cubic unit cell. Each Sr^{2+} ion is thus 12 coordinated to O^{2-} ions.

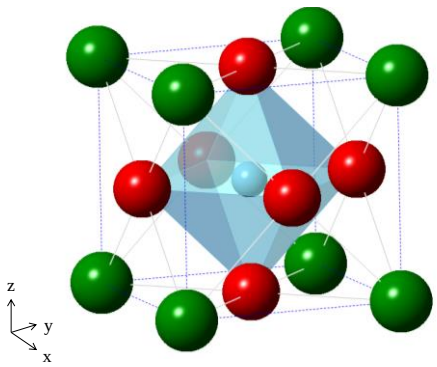

Figure 13: $SrTiO_3$ cubic perovskite crystal structure with a central Ti^{4+} ion (blue) octahedrally coordinated to 6 O^{2-} ions (red) and Sr^{2+} ions (green) situated on the unit cell vertices

At low temperatures or when doped, the structure of $SrTiO_3$ can become distorted due to the size of a dopant ion, non-stoichiometry or the Jahn-Teller effect.

1.5.2 Electronic structure

The valence band of $SrTiO_3$ is made up mainly of O 2p states[82, 83], which overlap considerably with Ti 3d orbitals and therefore there is a high degree of covalence between Ti and O ions in the structure. By contrast Sr^{2+} and O^{2-} exhibit more ionic character[84]. The conduction band is made up mainly of Ti 3d-orbitals[82]; the bulk electronic structure is highly comparable to that of TiO_2.

Eglitis et al. determined that the surface electronic structure of ABO_3 perovskites could differ from that of the bulk. Building on work by Erdman et al.[85], they determined from ab initio calculations of the SrO-terminated (001) surface that O 2p electronic states did not contribute to the VBM, with VBM consisting mainly of central oxygen orbitals in this case, whereas the TiO_2 terminated surface retained its O 2p contribution[83]. This surface termination of $SrTiO_3$ is an important factor in design of photocatalysts based on this structure. Work by Kawasaki et al. has shown that surface preparation to selectively etch the SrO layer can be undertaken and may enhance adsorption of reactants molecules[86].

The predominant intrinsic defects in $SrTiO_3$ are Sr and O vacancies; Ti vacancy formation has a high energy barrier and therefore are seldom found in this material[87]. Dopant ions can alter the electronic structure of $SrTiO_3$ by introducing additional states or by increasing the number of intrinsic defects for the purpose of charge compensation.

1.5.3 Modifying $SrTiO_3$ to improve its photocatalytic activity

Strontium titanate has been less intensely investigated for its photocatalytic properties than TiO_2, despite their similar physical and electronic properties. However, these similarities mean that research into band gap modification has followed a similar path to those used with TiO_2 and doping has been an effective strategy for extending the photocatalytic activity of $SrTiO_3$ into the visible light region.

B-site doping with Cr, Ru, Rh, Mn and Ir has been shown to introduce in-gap states to effectively reduce the energy requirement for photoexcitation. Doping $SrTiO_3$ can make it effective for O_2 evolution or for H_2 evolution and has shown reasonable activities with a number of metals including Cr, Mn, Rh, Ir and Ru[88-92]. Thus $SrTiO_3$ can be used as the basis material for both sides of a Z-scheme. This has been achieved by Hara et al. who doped $SrTiO_3$ with V/Na and Rh to evolve O_2 and H_2 respectively. This system achieved stoichiometric gas evolution (2:1 ratio of H_2:O_2) under visible light using IO_3^-/I^- as a redox mediator[93].

Rh-doping in $SrTiO_3$ has been of particular interest to enhance its activity for use as a H_2 evolution catalyst in a Z-scheme. In a number of studies it has been paired with $BiVO_4$, WO_3, $AgNbO_3$, Bi_2MoO_6 as O_2 evolving catalysts; its combination with $BiVO_4$ has been shown to be particularly effective for overall water splitting, achieving quantum yield of .6 % under 420 nm light. Synthesis method has been shown to be particularly important when making Rh doped $SrTiO_3$ catalysts and the use of excess Sr for hydrothermal synthesis allowed improved apparent yield with respect to stoichiometric reactant amounts.

Lanthanum doping, where La substitutes the A-site, has also been investigated. A study combining La-Cr doped $SrTiO_3$ and La-Cr doped Sr_2TiO_4 also showed visible light activity for H_2 evolution. Codoping Rh:$SrTiO_3$ with La has been determined by density functional theory to passivate localised mid-gap states and supress formation of oxygen vacancies thought to inhibit photoactivity in Rh doped $SrTiO_3$[94].

1.8 Principles of Solid State Synthesis

Solid state synthesis is a widely used technique for the fabrication of solid polycrystalline materials; powders are ground together and heated to high temperatures in order to produce a different phase product, which is a combination of the elements from the starting materials. This is a simple route to making new structures and can also be used to introduce dopant ions into a structure, as completed in this work.

Ions in a solid are normally regarded as thermodynamically trapped on lattice sites and are therefore only able to move when at high temperature. Even at the elevated temperatures utilised for these reactions (> 1000 °C) the reaction is slow and long heating times are necessary to ensure reaction completion. These long reaction times are the major disadvantage of the technique as they make it highly energy intensive and inhibit the reaction from being easily monitored. Thus homogenous products can be difficult to synthesise and it can take much trial and error to produce the desired material.[95]

A schematic representation of what happens in a solid state reaction is shown in Figure 14. Here MgO and Al_2O_3 are reacting to form the new phase $MgAl_2O_4$. The original interface between MgO and Al_2O_3 is the site of reaction, where Mg^{2+} ions are diffusing from left to right and Al^{3+} ions are diffusing from right to left. The product layer begins to grow according to the following reactions:

At the MgO/$MgAl_2O_4$ interface $\quad 2Al^{3+} - 3Mg^{2+} + 4MgO \rightarrow MgAl_2O_4$

At the $MgAl_2O_4$/Al_2O_3 interface $\quad 3Mg^{2+} - 2Al^{3+} + 4Al_2O_3 \rightarrow 3MgAl_2O_4$

These equations illustrate the reason behind the Kirkendall Effect, the observation that a phase boundary will move as a consequence of the difference in rates of diffusion of the ions involved. Since the reaction at the $MgAl_2O_4/Al_2O_3$ interface produces three times as many product units than the reaction at the $MgO/MgAl_2O_4$ interface, the reaction is faster at this interface and thus the product grows faster into the Al_2O_3 layer[96].

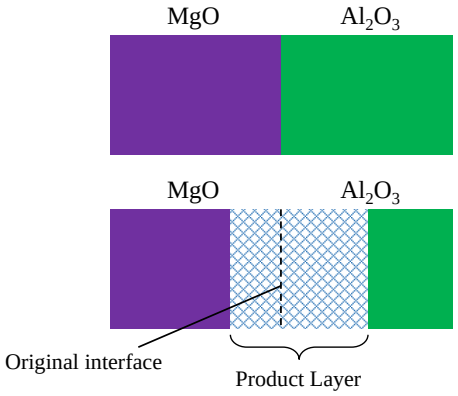

Figure 14: Schematic representation of two materials before solid state reaction (top) and during solid state reaction (bottom) showing a product layer that forms at the interface

Although the Kirkendall Effect will not be pronounced in semiconductor doping, due to the low amount of dopant material with respect to bulk material, it can still be concluded that the contact between the two (or more) materials is of high importance to maximise the likelihood of successful solid state reaction. In practise this translates as ensuring that the starting material particles are small, in order to increase their surface area and that they are well-ground prior to heating. As well as ensuring a good contact between dopant precursor and bulk material, care taken over the grinding step of a solid state reaction will also ensure the homogeneity of dopant distribution throughout the sample. Often, multiple grinding steps are included in syntheses since a homogenous product may not be formed after one calcination. Usually, PXRD is utilised to confirm if any starting materials remain after synthesis, this data is used to inform if any further grinding and heating steps are required to complete the reaction.

In the laboratory, powders can be ground by hand, using a pestle and mortar or by mechanical methods, such as ball milling. Hand grinding is effective for powders that already have small particulate size, whereas ball milling is useful for reducing the particulate size of agglomerated powders. On a small scale, ball-milling can result in the loss of a large proportion of powder and is therefore considered an inappropriate method for preparation of small scale samples. However, the human element to hand-grinding can lead to lack of continuity between samples. It is therefore important when producing multiple, comparable samples by hand grinding, that a methodical approach is taken; the total volume of powder should be kept constant, as well as grinding time.

Chapter 2: Experimental Methodology

This chapter describes the methods used to synthesise various samples made, their preparation for analysis and the techniques used to characterise them. The theoretical background for each analysis technique is also discussed.

2.1 Syntheses

2.1.1 Synthesis of Doped Semiconductor Powders

Rh-doped TiO_2 and $SrTiO_3$ samples were synthesised by solid state reaction (SSR) of the titania/strontium titanate powder (Aldrich 99.99%) with the appropriate molar amount of the Rh_2O_3 (Sigma Aldrich 99.8 %). The reactant powders were ground together using an agate pestle and mortar for 5 continuous minutes and calcined in a ceramic combustion boat for 10 hours at 1100 ˚C. All syntheses were carried out in air, at a ramp rate of 10 ˚C $min^{-1}$and reaction mixtures left to cool passively, overnight. Co-doped samples were produced by grinding 5 mol. % Rh-doped powders with the appropriate molar amount of Sb_2O_3 followed by calcination for 10 hours at 900 ˚C. Table 1 outlines the samples made, dopant oxide used in each instance and calcination temperature. Where codoped samples were made both the single dopant and the codopant oxides are listed, separated by a backslash.

2.1.2 Single Crystal Dopant Diffusion

Single crystals (TiO_2 <110> and $SrTiO_3$ <100>) were doped by solid state diffusion of dopants from the appropriate doped powder. Crystals (10 x 10 x 0.5 mm, purchased from Alineason) were pressed, by hand, between the doped powder, to ensure dopant diffusion into both sides. The crystals were calcined at 1100 °C for 10 hours.

Dopant	Sample	Dopant oxide(s) used	Calcination Temperature (°C)
Rh	TiO_2:Rh[1%]	Rh_2O_3	1100
	TiO_2:Rh[3%]	Rh_2O_3	1100
	TiO_2:Rh[5%]	Rh_2O_3	1100
	TiO_2:Rh[7%]	Rh_2O_3	1100
	TiO_2:Rh[9%]	Rh_2O_3	1100
Rh/Sb	TiO_2:Rh[5%]Sb[1%]	Rh_2O_3/Sb_2O_3	1100
	TiO_2:Rh[5%]Sb[3%]	Rh_2O_3/Sb_2O_3	1100
	TiO_2:Rh[5%]Sb[5%]	Rh_2O_3/Sb_2O_3	1100
	TiO_2:Rh[5%]Sb[7%]	Rh_2O_3/Sb_2O_3	1100
	TiO_2:Rh[5%]Sb[9%]	Rh_2O_3/Sb_2O_3	1100
Rh/Sb	$SrTiO_3$:Rh[5%]Sb[1%]	Rh_2O_3/Sb_2O_3	1100
	$SrTiO_3$:Rh[5%]Sb[3%]	Rh_2O_3/Sb_2O_3	1100
	$SrTiO_3$:Rh[5%]Sb[5%]	Rh_2O_3/Sb_2O_3	1100
	$SrTiO_3$:Rh[5%]Sb[7%]	Rh_2O_3/Sb_2O_3	1100
	$SrTiO_3$:Rh[5%]Sb[9%]	Rh_2O_3/Sb_2O_3	1100
Rh/Sb	$SrTiO_3$:Rh[0.5%]	Rh_2O_3	1100
	$SrTiO_3$:Rh[0.5%]Sb[0.1%]	Rh_2O_3/Sb_2O_3	1100
	$SrTiO_3$:Rh[0.5%]Sb[0.5%]	Rh_2O_3/Sb_2O_3	1100
	$SrTiO_3$:Rh[0.5%]Sb[0.9%]	Rh_2O_3/Sb_2O_3	1100

Table 1: list of samples made, the dopant oxide powders used and the calcination temperature

2.2 Physical Analysis Techniques

2.2.1 Powder X-ray Diffraction (PXRD)

X-ray diffraction is based upon the interaction of X-ray radiation with regions of electron density surrounding the atomic nuclei in a crystal. The periodic arrangement of atoms in a crystalline solid causes the formation of Miller planes, effective layers made up of repeating patterns of atoms and ions that can be "observed" by the X-rays due to the ordered packing that occurs. Since the interatomic and interplanar distances between atoms and layers in a crystal structure are on the order of 0.1 nm, X-rays (0.01-10 nm) are of the appropriate wavelength to interact with the atoms in solid materials. If a Miller plane is present in a crystal structure, X-rays will diffract at a specific angle, θ, with respect to the sample surface. If the path difference between X-rays diffracted by layers of differing depths is an integer multiple of the X-ray wavelength, λ, constructive interference of the diffracted X-rays occurs and the detector receives a signal. Alternatively if the path difference is not an integer multiple of λ, destructive interference will occur and no signal will be detected. This is the basis from which Bragg's law is derived. Bragg's law relates wavelength of an incident X-ray, λ, the interplanar spacing, *d*, and the angle of diffraction, θ. Figure 15 illustrates its derivation, which is outlined below[97].

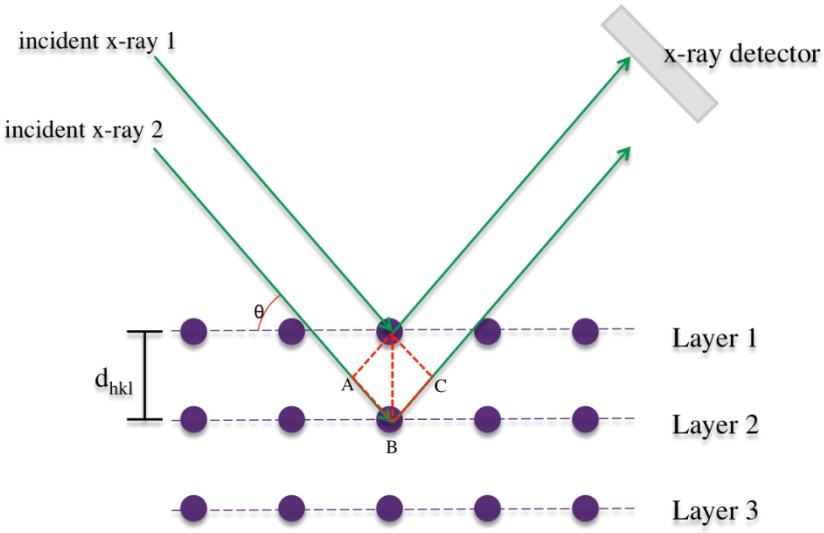

Figure 15: Schematic representation of X-ray diffraction

Simple trigonometry of the triangle ABX tells us that,

$$sin\theta = \frac{AB}{d} \tag{13}$$

therefore,

$$AB = dsin\theta \tag{14}$$

Since,

$$path\ difference = AB + BC \tag{15}$$

where

$$AB = BC \tag{16}$$

then

$$2AB = 2dsin\theta \tag{17}$$

For constructive interference to occur 2AB must be an integer multiple of the incident X-ray wavelength and therefore Bragg's law is stated as,

$$n\lambda = 2dsin\theta \text{From}$$

PXRD is primarily used for phase identification since analysis over a range of angles results in a pattern of peaks of varying relative intensities which can be used to classify a material as

having a certain structure. This is useful for distinction between different structures of the same material i.e. anatase and rutile TiO_2, or for detection of impurities in the product of a reaction.

PXRD data were collected on a Bruker D4 diffractometer using Cu Kα radiation (λ = 1.54 Å) or a Bruker STOE diffractometer in foil mode using Mo Kα radiation (λ = 0.71 Å). On the Bruker D4 patterns were collected between 10 and 70˚ 2θ, at a step size of 0.05˚ and with a sampling time of 2 s $step^{-1}$. On the STOE, patterns were collected between 2 and 40˚ 2θ, at a step size of 0.5 ˚ $step^{-1}$ and a dwell time of 10 s $step^{-1}$. All STOE data were transformed to correlate to angles collected with Cu Kα radiation using Bragg's law:

$$d = \frac{\lambda_{Mo}}{2sin\left(\frac{2\pi}{360}.2\theta_{Mo}\right)}$$

$$sin\theta_{Cu} = \frac{\lambda_{Cu}}{2d}$$

Equation 20

$$\theta_{Cu} = sin^{-1}\left(\frac{\lambda_{Cu}}{2d}.\frac{2\pi}{360}\right)$$

Equation 21

$$2\theta_{Cu} = 2sin^{-1}\left(\frac{\lambda_{Cu}}{2d}.\frac{2\pi}{360}\right)$$

Equation 22

Once collected, the data were compared with Inorganic Crystal Structure Database (ICSD) standard patterns to determine phase purity and to index observed peaks. Using the indexed pattern least squares refinement was performed and the lattice parameters determined.

2.2.2 Ultraviolet-Visible (UV-Vis) Spectroscopy

UV-Vis spectroscopy provides information regarding the interaction of a substance with light of wavelengths 10 nm < λ <2500 nm. For photocatalysts and photoelectrodes, the range of wavelengths of light that a material absorbs is vital information that will greatly impact the effectivity of the catalysis that can occur.

Most UV-Vis spectrometers utilise a deuterium/tungsten dual lamp setup, whereby the tungsten lamp provides light of visible and near-IR wavelengths and the deuterium lamp provides UV-light. The light passes through a scanning monochromator, filtering out all but a very narrow range of wavelengths of light, which then interact with the sample. UV-Vis

spectroscopy can be completed in one of three modes: absorbance, transmittance or reflectance. The sample is placed between the monochromator and a photodiode detector in both absorbance and transmittance modes; the data are reported as either the amount of light at a given wavelength that did not pass through the sample (absorbance), or the percentage of light at a given wavelength that did pass through the sample (transmittance).

When a sample is not transparent to any of the incident light, reflectance spectroscopy can be used. Reflectance of incident light off a powder sample is diffuse, where the light is reflected in multiple directions. Therefore, when recording reflectance spectra an integrating sphere is used to collect and direct the reflected light towards the photodiode detector as shown schematically in Figure 16. All UV-Vis spectra in this work were taken in diffuse reflectance (DR) mode. These data were subsequently transformed into absorbance units using the relation shown below (Equation 23).[98]

$$A = log_{10}\frac{1}{R}$$

Where A = absorbance and R= reflectance In order to determine the position of the band edge and thus the band gap energy for the materials, DR spectra were also converted using the Kubelka-Munk transformation (Equation 24) in order to produce a Tauc plot and extrapolate the band gap energy.[99, 100]

$$f(R) = \frac{(1-R)^2}{2R}$$

24

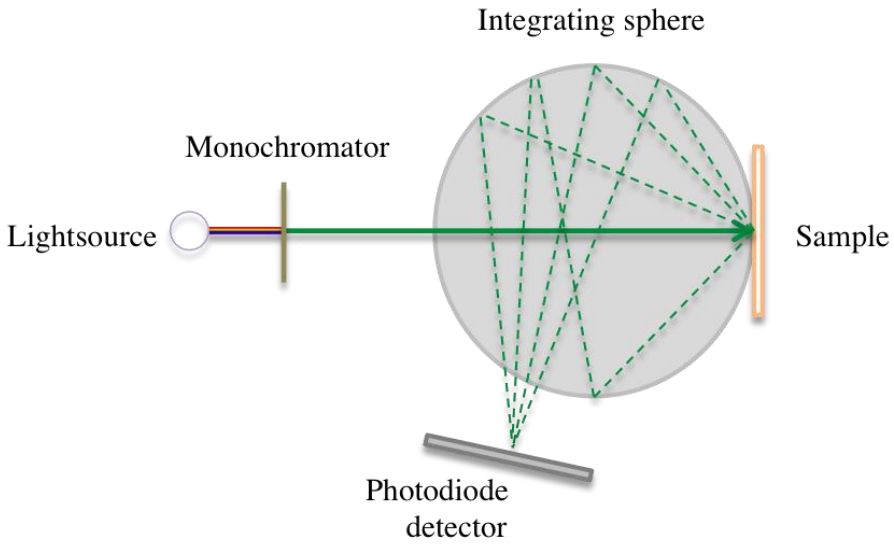

Figure 16: Schematic diagram of diffuse reflectance UV-Vis experiment. Monochromatic incident light is reflected diffusely by the sample and collected by an integrating sphere, which directs the light to the photodiode detector to intensify what would otherwise be a weak signal.

From this, f(R) is plotted against photon energy (eV) and the function of the linear portion of the plot is determined according to the general function $y = mc + c$. Thus the x-intercept can be defined; this is the band gap energy of the material.

2.2.3 X-ray Photoelectron Spectroscopy (XPS)

X-ray photoelectron spectroscopy (XPS) is a technique based upon the photoelectric effect, which states that an electron can be excited and ejected from an atomic orbital upon absorption of a photon of sufficient energy. XPS utilises X-rays to photoexcite electrons from the atoms in a material, in order to measure their kinetic energy, which can be related to their binding energy by Equation 25:

$$K.E. = E - (B.E. + \Phi)$$

Equation 25

Where E = energy of incident photon, K.E. = measured kinetic energy of the photoelectron, B.E. = binding energy of the electron before ionisation and Φ = work function of the instrument, the small amount of energy lost by the photoelectron to the detector. The photons used in XPS possess enough energy to excite core electrons, which are bound in orbitals of specific energies characteristic to each element. Thus the core electron binding energies determined can be used to identify the chemical entities that are present in a given sample. Since XPS relies on the detection of electrons of specific energies, the entire experiment must be completed under Ultra High Vacuum (UHV) conditions in order to ensure that these electrons do not interact with any other matter and are allowed to reach the detector. While

the kinetic energy of the electron is measured, it is usual for an XP spectrum to be plotted on a binding energy scale, though conventionally the binding energy x-axis is reverse-labelled with low energies to the right and high energies to the left.

2.2.3.1 How XPS works (in Fixed Analyser Transmission, or FAT, mode)

Figure 17 shows a schematic representation of the excitation and detection process in an XPS experiment. Points 1-5 labelled on the figure are explained below.[101]

1. An X-ray source (metal anode) is bombarded with electrons, causing the emission of X-rays, which are then monochromated through an optic to ensure that the photons used in the experiment are of quantised energy.
2. Upon irradiation the core electrons in a sample, as long as their binding energy is less than that of the energy of the incident photon, are excited and photoejected from the sample, according to the photoelectric effect.
3. The Hemispherical Analyser (HSA) has a fixed potential applied across it (negative on the outside and positive on the inside) thus only allowing photoejected electrons of a certain energy to pass through it. This energy requirement of the electrons is called the "pass energy".
4. The photoejected electrons are directed to the entrance of the HSA by transfer lenses. These transfer lenses use a voltage to retard the velocity of the electrons such that they are at the pass energy and thus able to pass through the HSA to the detector. The transfer lenses scan through voltages to allow detection of electrons over a range of energies.
5. The detector records the number of electrons of the corresponding energy and a spectrum is produced.

Analysis of semiconducting or insulating samples will result in accumulation of positive charge in the analysis area, due to the ejection of electrons from the sample. Without correction this inevitably leads to an apparent increase in the binding energy of the photoelectrons. This charging can be compensated by use of a low-energy electron flood gun.

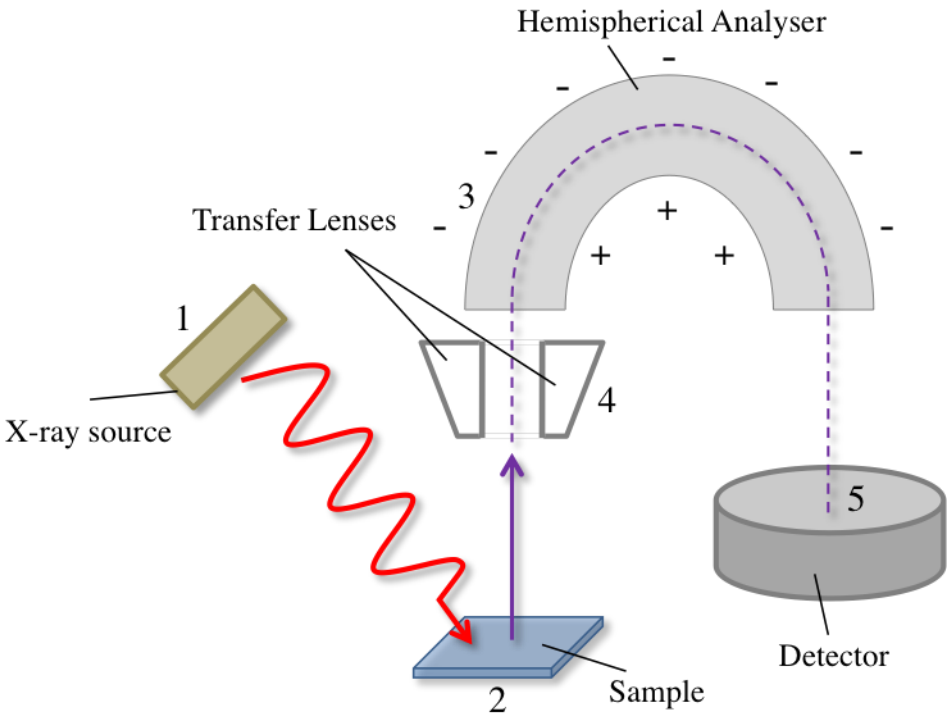

Figure 17: Schematic diagram of XPS setup correlating to 5 steps outlined above. The electron path is represented by a purple line, which is dashed as it becomes attenuated by the transfer lenses and hemispherical analyser.

2.2.3.2 XPS Spectra- Peak shape, quantification and analysis

An XP experiment usually starts with collection of a survey spectrum. This is a wide range, low resolution, spectrum that gives an indication of the elements present. Typically this will be taken over an energy range from around -5 eV binding energy to just below the energy of the X-ray source photon energy. High resolution spectra can be taken over much smaller ranges, detecting only the photoelectrons from specific elemental core levels. From these high resolution core line spectra much information regarding the abundance and environment of the corresponding element can be determined.

Several factors contribute to the intensity of the peak generated for each core level electron. The photoionisation cross section, a measure of how likely an electron from a specific core level of a specific element is to be produced by the incident radiation, combined with the inelastic mean free path (IMFP) of the photoexcited electron and the abundance of the element from which the electron is emitted generates the intensity of the peak. Instrumental factors also play a part in the generation of peak intensity, for example detection probability (the likelihood that the instrument's detector will detect the photoelectron) and angular asymmetry factor (the variations in photoelectron intensities on the unpolarised X-ray and angle). Thus, peak intensities must be normalised in order to determine relative abundances of the elements present. This normalisation is encompassed in the relative sensitivity factor (R.S.F.) for an

element, determined by the instrument software, to allow comparison of data across different instrument geometries.[102]

For core electrons photogenerated from s orbitals a single peak will be observed. However, for those originating from p, d, or f orbitals a doublet peak is observed. This is due to the spin orbit coupling effect on these electrons. According to the j-j coupling rules defining the splitting and intensities of the effect (Equation 26 and Equation 27) the observable peaks and their relative intensities to each other are outlined in Table 2 below.

$$j = l \pm s \tag{26}$$

$$relative\ intensity = 2J + 1 \tag{27}$$

Type of orbital	l value	j value(s)	Relative Intensity
s	0	0	0
p	1	$^1/_2$	1
		$^3/_2$	2
d	2	$^3/_2$	2
		$^5/_2$	3
f	3	$^5/_2$	3
		$^7/_2$	4

Table 2: Orbital types, their associated l and j values and the relative intensities

Spectral resolution is dependent upon three parameters:

(a) The full-width half maximum (FWHM) of the photon source
(b) The line width of the photoelectron emission
(c) The energy resolution of the analyser

Monochromation of the photon source reduces the line width of incident X-rays, usually Al-Kα radiation (as used in all experiments presented in this work) is capable of providing X-rays with FWHM of between 0.2 and 0.3 eV. The emitted photoelectron line widths vary, dependent on sample. This results in a Gaussian-Lorentzian peak shape, due to the irreducible linewidth (Γ) and phonon line broadening, respectively.

The energy resolution of the detector can be fine-tuned by altering the pass energy of the HSA. The detector has a resolution of $^E/_{\delta E}$ and so electrons with a low kinetic energy will result in

high resolution. A low pass energy will therefore result in well-resolved peaks, though this comes at the expense of sensitivity, as fewer photoelectrons will satisfy the low energy requirement. It is important to determine optimum pass energy when analysing different energies; a valence band spectrum, which is often poorly resolved at higher pass energies and not used for quantification purposes, benefits from a lower pass energy whereas core lines used for quantification would benefit from a higher pass energy.[101, 103]

As well as information regarding the amount of an element present in a material, XPS can elucidate the oxidation state(s) and environmental information of the element in question. These initial state effects can be inferred from the position of the peak maximum for a photoelectron signal. The position of the peak maximum is determined by the binding energy of the photoelectron represented, which will be greater or less than that of the ground state atom if it has been oxidised or reduced, respectively. Combining knowledge of the material being analysed- for example which species are likely to be present due to the synthesis conditions- with data produced by XPS can produce a complete picture of the composition of the surface of a material. Sometimes, when multiple oxidation states of an element are present or if the binding energies of core electrons for different elements are very similar, peak fitting must be employed. Typically, a Gaussian-Lorentzian (G-L) function is used in order to account for both the instrumental factors causing peak broadening such as X-ray line shape and thermal broadening (Gaussian) and the natural peak broadening determined by the lifetime of an excited energy level (Lorentzian). Photoelectrons from an s- core level (angular momentum quantum number l=0) can be easily fitted by a G-L function since they produce a singlet, while those arising from p, d or f orbitals, with $l > 0$, produce doublets due to spin-orbit coupling, and must be fitted with multiple G-L functions in the appropriate ratio. XPS analysis software therefore allows the mathematical fitting of collected data with functions that can be constrained to each other via different variables (full-width half-maximum, peak area, peak position etc.) in order to deconvolute the spectrum. Fitting XPS data is often a compromise between the "perfect" mathematical fit and a "sensible" representation of what is known to exist in the sample.[102]

Binding energy values and photoelectron spectra can also be affected by so-called "final state effects". These effects arise from photoelectron-induced rearrangement and polarisation due to perturbation of the electronic structure that results from photoemission of an electron. Koopmans' theorem, which states that "the negative of the eigenvalue of an occupied orbital from a Hartree Fock calculation is equal to the vertical ionisation energy to the ion state formed by removal of an electron rom that orbital, provided the distributions of the remaining electrons do not change[104]", assumes that rearrangement doesn't take place after

photoemission of an electron, however the observance of final state effects in XPS provides evidence that it does.

Rearrangement occurs when a core-hole is created by photoemission. The core-hole is rapidly filled by an electron from a higher energy orbital, the transfer of which can result in fluorescence or emission of a secondary (Auger) electron, depending on the energy levels involved. These excitations and de-excitations can affect the kinetic energy, and thus derived binding energy value, of a photoemitted electron. As well as Auger emission, final state effects include excitation of valence band electrons, termed 'shake-up' processes, removal of valence band electrons, termed 'shake-off' processes and excitation of conduction band electrons or 'plasmon generation'. Whereas Auger peaks are found in different energy regions to the core line with which they are associated, shake-up, shake off and plasmon effects, when intense enough to be measureable, often appear as satellite peaks alongside their core line, since they perturb photoelectrons by a relatively small amount of energy. These satellites can assist in the assignment of oxidation state and local environment of an atom/ion.

Although X-rays are highly penetrating, XPS is a surface sensitive technique, due to the IMFP of the photoelectron. This is the average distance that a photoelectron can travel before it interacts and loses energy to its surroundings. Since IMFP depends not only on the kinetic energy of the photoelectron, but also the structure of the material from which the electron is being excited, the exact sensitivity depth of each experiment is different. An upper detection limit of 10 nm is often quoted, though for some materials the limit will be lower than this. In order to probe below the surface of a material, depth profiling can be completed using an Ar^+ ion beam to etch surface matter. However, the process of etching can alter the oxidation state of the atoms and ions below the surface, making species identification difficult. Usually elemental quantification is the only information that can be reliably inferred from depth profiled XP spectra.

For this work XP data were collected on a Thermo K-alpha instrument utilising a 72 W monochromated Al-Kα X-ray source (with photon energy of 1486.6 eV). A dual beam flood gun was used to compensate for sample charging, instrument specific relative sensitivity factors were used to normalise the data and the binding energy scale was referenced by setting the C 1s peak from adventitious carbon to 284.8 eV. Depth profiles were completed using an Ar^+ ion gun at 3000 kV.

Typically a set of XP spectra were taken using pass energy of 200.00 eV over the range -5.00 to 1350.00 eV for the survey spectrum (x 3 scans at this energy and range). High resolution core line spectra were taken at a pass energy of 50.00 eV and the appropriate number of scans

altered for each element. Valence band spectra were collected over the range -5.00 to 15.00 eV, pass energy 50.00 eV and at least 100 scans recorded to ensure high quality data.

2.2.4 Transient Absorption Spectroscopy (TAS)

Transient Absorption Spectroscopy (TAS) is a pulsed laser spectroscopic technique utilising a pump-probe setup to observe the dynamics of transient changes in absorption after an excitation pulse. The presence (or absence) of photogenerated electrons or hole carriers in a sample cause an increase in the sample's absorbance at particular wavelengths and thus their dynamics can be studied by tracking these changes. It has been shown that mobile carriers in anatase TiO_2 absorb in the visible region (500 - 900 nm) but trapped holes and electrons absorb in the near UV ($\lambda < 500$ nm) and near IR ($\lambda > 800$ nm), respectively.[105]

A typical TAS experiment involves a laser pulse to excite the sample (termed the "pump" pulse), followed by a weaker "probe" pulse after a time delay, τ. This is represented schematically in Figure 18. The absorbance dynamics are tracked and as photoexcited charges recombine, the absorbance decreases. This process is recorded multiple times and the signal averaged in order to achieve a representative spectrum.

By varying the probe pulse spectra over different wavelengths can be collected. Subtraction of the ground state spectrum from the photoexcited spectrum leaves a ΔAbs spectrum, which can be plotted as a function of τ and λ if the time delay is varied. Thus the kinetics of charge carriers in the photoexcited material can be determined.[106]

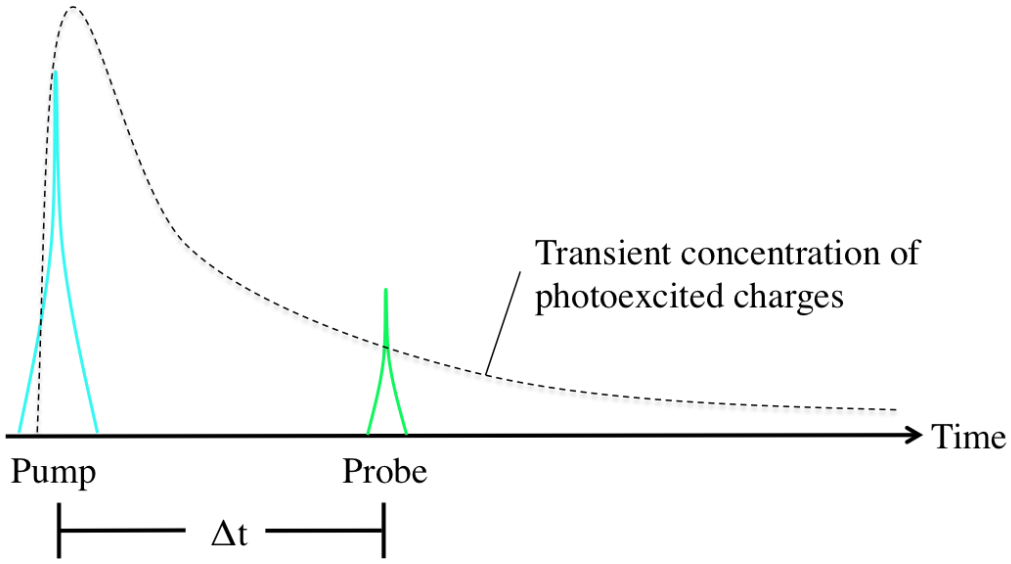

Figure 18: Schematic representation of the TAS experiment. A pump pulse generates charges followed by a probe pulse whose absorption changes dependent on the concentration of photoexcited charges. It is this absorption which is tracked for the remainder of the time after Δt, up to complete recombination (i.e. the ground state absorption prior to excitation)

The TAS experiments completed in this piece of work were taken in collaborations with the Durrant Group at Imperial College London, with the assistance of Dr Andreas Kafizas. They were completed in reflectance mode to allow the analysis of powders, which were pressed between two glass microscope slides and analysed in air at ambient temperature and pressure. A 355 nm excitation pulse (6 nm pulse width, 0.4 $mJ.cm^{-2}.pulse^{-1}$, pulse every 1.1 s) was used.

2.2.5 X-ray Absorption Spectroscopy (XAS)

2.2.5.1 XAS background

X-ray Absorption Spectroscopy (XAS) involves irradiation of a material with X-rays and measurement of the absorption coefficient, μ, as a function of X-ray energy. These two properties are linked by the function outlined in Figure 19 and Equation 28 and *Equation* below, which illustrate a basic schematic of the XAS experiment.

By using synchrotron radiation to vary the incident X-ray energy, a range of absorption coefficients can be determined. However, at a given value the incident X-ray energy will match the energy required to photoexcite an electron from an atomic core level in the material. At this energy, the amount of radiation transmitted, I_t, sharply decreases. This abrupt change in transmittance is called the absorption edge and corresponds to the core electron of a specific element. Absorption edges are named according to the principle quantum number of the excited electron (K-edge for n=1, L-edge for n=2, M-edge for n=3).

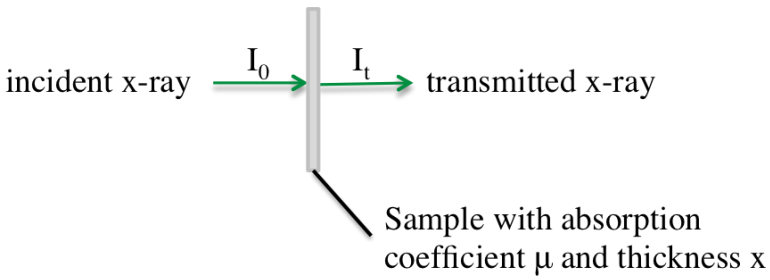

Figure 19: Schematic representation of a simple X-ray absorption experiment

$$I_t = I_0 e^{-\mu x}$$

Equation 28

$$\mu = \frac{-\ln \frac{I_t}{I_0}}{x}$$

The spectrum produced by an XAS experiment can be split into two sections, the near edge and the extended X-ray structures. These are termed X-ray Absorption Near Edge Structure

(XANES) and Extended X-ray Absorption Fine Structure (EXAFS) and are distinguished in Figure 20 below. Each can give information regarding the oxidation state and coordination environment of an atom in the material. Unlike XPS, which is dependent on the IMFP of a photoelectron, XAS is a bulk technique as it relies on the detection of X-rays, which are highly penetrating.

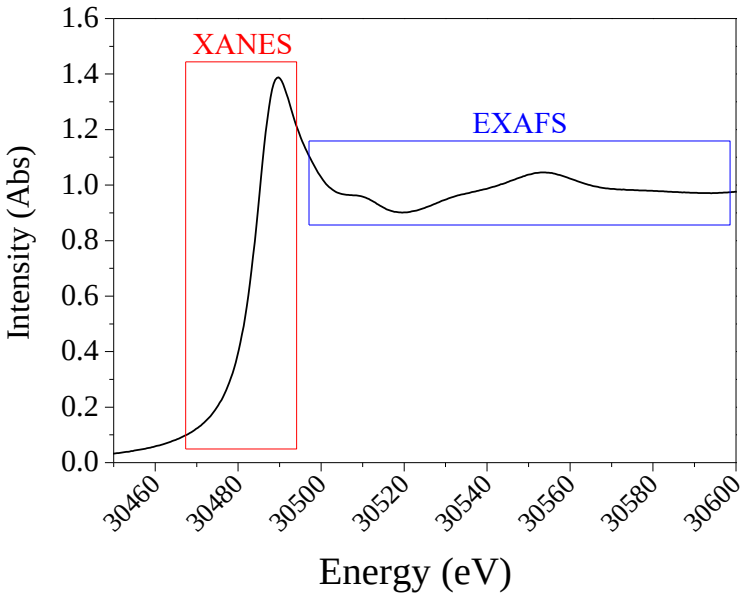

Figure 20: An example X-ray absorption spectrum, outline the XANES and EXAFS sections of the spectrum

2.2.5.2 X-ray Absorption Near Edge Structure (XANES) Analysis

Interpretation of the absorption edge of an XA spectrum involves three segments: the pre-edge section, which occurs before the sharp increase, the absorption edge itself and the XANES section just after the absorption edge. The pre-edge and XANES sections can both provide information regarding geometry around the element being probed, whereas the absorption edge mainly provides information regarding oxidation state. As expected, an increase in oxidation state results in an increase in absorption edge.[107, 108]

Extended X-ray Absorption Fine Structure (EXAFS) Analysis

Extended X-ray Absorption Fine Structure (EXAFS) corresponds to the region of an XAS spectrum approximately 50 eV after the absorption edge and extending out to around 1000 eV.

Once an electron is photoexcited it interacts with the other electrons in the atom from which it originated. These interactions generate waves, which are backscattered by the surrounding atoms and can either constructively or destructively interfere. In the EXAFS region, after the absorption edge, a series of decreasing oscillations are observed corresponding to constructive

(peak maxima) or destructive (peak minima) interference. Hence these oscillations can be related to the distances between atoms.[109, 110]

Sb and Rh k-edge XAS data of TiO_2 samples were taken at beamline (B18), Diamond Light Source, UK. The beamline is equipped with Si (111) double crystal monochromator, ion chambers for measuring incident and transmitted beam intensity and operates at 3 GeV and 300 mA. All measurements were carried out in absorption mode and typically 12 scans were averaged to produce the data. Sb k-edge XAS data of $SrTiO_3$ samples were taken at beamline BM23, European Synchrotron Radiation Facility, France. The beamline is equipped with Si (111) double crystal monochromator, ion chambers for measuring incident and transmitted beam intensity and operates at 3 GeV and 300 mA. All measurements were carried out in absorption mode and typically 2 scans were averaged to produce the data. All spectra from both facilities were processed using Athena software.

2.2.6 Scanning Electron Microscopy (SEM)

Scanning Electron Microscopy (SEM) is an imaging technique allowing much higher resolution at high magnification than optical microscopy. Under ultra-high vacuum (UHV) conditions, a focussed beam of high-energy electrons is fired at the sample and interacts with the sample surface. A variety of signals can be generated from these electron-sample interactions, which can be collected by detectors inside the instrument and used to produce an image of the sample. The detectors have a positive bias to attract electrons, including those from the sample sides, which can greatly reduce the amount of shadowing in images.

Two main detection modes can be employed in SEM utilising two of the different signals generated by the electron-sample interaction. Secondary electrons are those electrons that are knocked out of the atoms in the sample by incident electrons from the electron gun. Detection of these helps to produce an image showing the topography of a sample, since a greater number will be detected from atoms closer to the detector and fewer will be detected from atoms further away from the detector. This results in bright spots indicating projections from the sample surface and dark spots indicating depressions in the sample surface.[111, 112]

Alternatively, backscattered electrons can be detected. These are electrons from the electron gun that interact with the atomic nucleus and are scattered from the sample. They are used to generate an indication of sample density since the likelihood of an electron being backscattered is dependent on the amount of matter (i.e. number of nuclei present to scatter).

Images of samples were taken on a Jeol JSM-6700F. Samples were coated with gold and mounted on carbon tape in order to minimise electrical charging.

2.2.7 Wavelength Dispersive Spectroscopy (WDS)

Elemental characterisation of the sample bulk can be completed using Wavelength Dispersive Spectroscopy (WDS). This technique utilises the X-rays emitted when a valence electron drops down into the hole created by emission of a secondary electron in SEM. Since these transitions are quantised, series of them are characteristic to each element and can thus be used to identify the elements present in a sample. The X-rays produced can penetrate through a sample (unlike photoexcited electrons in XPS) and therefore WDS signals represent an average composition over the entire depth of the sample.

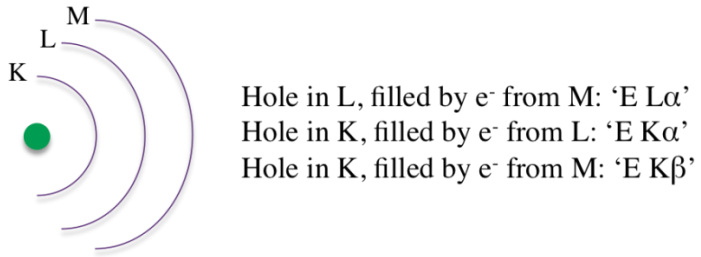

Figure 21: Explanation of X-ray nomenclature and schematic energy level diagram using X-ray notation, which is more commonly used for X-ray techniques, rather than standard spectroscopic notation.

X-rays generated by downward transitions of electrons are characterised by the element from which they are emitted, the energy level the electron comes from and the energy level of the hole it goes to replace. For example in Figure 21 and element 'E' has three orbitals, K (principle quantum number, n=1), L (n=2) and M (n=3). Three possible transitions are described and named in Figure 21, these would provide the characteristic fingerprint of this element and indicate its presence in a sample. [113]

The geometry of the sample stage is aligned to ensure that emitted X-rays hit an analytical diffracting crystal, or bank of analytical crystals. These crystals have specific lattice spacings allowing only certain wavelengths to be successfully diffracted at a specific angle, θ. Although the take-off angle from sample is constant due to the geometry of the machine, the crystal or crystals can be moved in order to vary the wavelengths of radiation successfully diffracted. If a bank of crystals is being used, each will have a different lattice spacing to allow diffraction of a wide-range of wavelengths, thus providing a wide-range of detectable elements.[114]

Since WDS is taken in a SEM, the analysis area is the area being imaged. This allows for a general composition to be determined by low magnification images, but also for high selectivity when working at high magnifications.

Chapter 3: An XPS investigation into the differences between antimony (III) oxide and antimony (V) oxide

3.1 Introduction

Chapter 3 describes an investigation into the differences between orthorhombic antimony (III) oxide (Sb_2O_3) and antimony (V) oxide (Sb_2O_5). Literature surrounding the analysis of Sb oxidation state by XPS shows differing approaches to the analysis of the Sb core lines. The primary Sb core line is the 3d doublet pair, though due to the high degree of overlap between the Sb $3d_{5/2}$ and O 1s peaks, both of which reside around 530 eV, the Sb $3d_{3/2}$ core line is primarily used for analysis. The Sb $3d_{3/2}$ core line has been shown to exhibit a small, variable peak shift and broadening upon oxidation from Sb (III) to Sb (V). This has led to some researchers fitting the Sb 3d core lines with two distinct components, the chemical shift values for which range from 0.5 eV to 2.0 eV between the (III) and (V) states (see Table 3 later). In contrast, other researchers have used a one component model when fitting their Sb XPS positing that the two states are not resolvable and that peak positions are highly variable and not reliably attributed to formal oxidation state.[115-119] These conflicting reports in the literature regarding the observation of a chemical shift in Sb 3d peak binding energy due to oxidation of antimony (III) to antimony (V) have led to debate of whether or not the effects of oxidation can be observed in XP spectra.

When identifying only one species of Sb, most accounts attribute a $3d_{3/2}$ photoelectron binding energy of between 539 and 540 eV to Sb (III) [120-128] and those above 540 eV to Sb (V).[129, 130] Nilsson et al.[130] investigated vanadium doped Sb_2O_5, reporting a slight decrease in Sb $3d_{3/2}$ binding energy when Sb/V > 1; 540.1 eV when Sb/V = 1 to 539.7 eV when Sb/V = 6. For their sample Sb1V1 (equimolar $Sb_xV_yO_4$) they assign the Sb $3d_{3/2}$ peak at 540.1 eV as being "intermediate between those for Sb_2O_4 and Sb_2O_5" and therefore conclude that both Sb (III) and (V) are present in the sample. Wang et al.[131] assign two distinct regions in their Sb $3d_{3/2}$ core line spectrum of an Sb_2O_5 standard compound. In this analysis, they have modelled the Sb $3d_{3/2}$ peak to contain an Sb (III) component at 540.4 eV, the binding energy at which the Sb $3d_{3/2}$ signal was assigned for their standard Sb (III) oxide, and an Sb (V) component, which makes up the majority of the signal (94.8 %) at 540.9 eV. The region at around 530 eV containing both O 1s and Sb $3d_{5/2}$ peaks has been modelled to account for Sb (V) $3d_{5/2}$, Sb (III)

$3d_{5/2}$ and O 1s components for the Sb_2O_5 standard. This model generated binding energy assignments of 532.7 eV and 530.7 eV for Sb $3d_{5/2}$ (V) and (III) respectively, which corresponds a (III)/(V) peak shift of 2.0 eV, whereas the peak shift of the Sb $3d_{3/2}$ (III) and (V) peaks for the same sample is 0.5 eV, which indicates that the peaks have not been modelled correctly. This difference in peak shift could arise from not utilising the Sb $3d_{3/2}$ peak as a way of constraining the Sb $3d_{5/2}$ models by position and therefore binding energies for the Sb 3d $_{5/2}$ and O 1s in this analysis are unreliable. Both the Sb (III) and (V) 3d doublet pairs would be expected to have the same (or very similar) doublet separation; the values extracted here are Sb (V) DS = 8.6 eV and Sb (III) DS = 9.7 eV. In addition, the O 1s contribution has been assigned one broad peak, where it may have been more appropriate to assign an O 1s, with an M-OH peak to the higher binding energy side of it. Both these amendments could alter the values for photoelectron binding energy considerably. This study serves to highlight the importance of complete and correct fitting in Sb oxides, since the only information available is from Sb and O peaks, the primary core lines for which are easily misinterpreted due to their overlap.

A compilation of Sb $3d_{3/2}$ literature data assigned to Sb (III) and Sb (V) cations from XP spectra of the relevant antimony oxides is shown in Table 3. The peak shifts between the reported values for the (III) and (V) cations range from 0.5 eV to 2.0 eV, showing considerable disagreement between researchers as to the nature of these photoelectrons. In all cases the data reported are from mono-valent oxides Sb_2O_3 or Sb_2O_5. The FHWM values are also shown since many studies use this characteristic to infer that the peaks could be made up of multiple environments and therefore indicates that a sample is impure and therefore a mixture of Sb (III) and Sb (V) oxides. Some researchers acknowledge the difficulty in resolving Sb (III) and Sb (V) environments and don't infer the oxidation states that could be present using XPS. Instead they use XPS simply to quantify the Sb in their samples, taking the sum of both environments. [116-119] Birchall et al.[115] compared a large range of Sb containing compounds, not limited to the oxides. From this extensive comparison, they concluded that binding energy values for Sb $3d_{3/2}$ photoelectrons are highly variable but that correlation to formal oxidation state is poor.

A 1972 study by Tricker [132] into the mixed valence compound $Cs_4Sb(III)Sb(V)Cl_{12}$, showed a broad Sb $3d_{3/2}$ peak of FWHM = 3.4 eV, which was modelled as two peaks with a 1:1 ratio and peak shift of 1.5 eV. Another study of Cs_2SbCl_6 by Burroughs et al. reported a Sb 3d spectrum containing two well-separated peaks, with a shift of 1.8 eV between the Sb(III) and Sb(V).[133] By comparison, a study by Izquierdo et al.[134], recorded values for mixed valence compound Sb_2O_4 intermediate between those for the Sb(III) and Sb(V) oxide.

Author (Year)	$3d_{3/2}$ E_b		Peak Shift	FWHM	
	Sb 3d (III) $_{3/2}$	Sb 3d (V) $_{3/2}$		Sb 3d (III) $_{3/2}$	Sb 3d (V) $_{3/2}$
Birchall (1975)[115]	538.6	540.6	2.0	-	
Delobel (1983)[135]	539.8	540.4	0.6	1.8	1.7
Wang (1991)[131]	540.4	540.9	0.5	-	
Benvenutti (1991)[136]	539.5	540.5	1.0	2.0	2.0
Izquierdo (1989)[134]	539.7	540.6	0.9	1.6	1.9
Nilsson (1994)[130]	-	540.3	-	-	
Sundarsan (2001)[137]	537.29	538.11	0.8	-	
Zhang (2006)[138]	539.7	540.7	1.0	-	

Table 3: Binding energy, reported peak shift and FWHM values for Sb 3d $_{3/2}$ peaks from various sources

The FWHM for the Sb $3d_{3/2}$ of this mixed valence Sb oxide was recorded as 1.8 eV and binding energy was 540.3 eV. Comparison of these values with their recorded data for Sb_2O_3 and Sb_2O_5 (reported in Table 3) led them to draw the conclusion that the Sb_2O_4 $3d_{3/2}$ peak was *not* a combination of two peaks representing Sb (III) and Sb (V) components, since a combined peak composed of Sb (III) and Sb (V) with chemical shift 0.9 eV should result in a FWHM much larger than the observed 1.8 eV.

Orchard et al. also observed a difference in Sb $3d_{3/2}$ FWHM dependent on the treatment of their mixed valence Sb_2O_4.[139] Their modelling of the data produced Sb (III) and Sb (V) components with a peak shift of 0.6 eV and FWHM 1.7 and 1.9 eV respectively. Using a point charge model to estimate expected chemical shift, they concluded however that in order to achieve the observed chemical shift of 0.6 eV it was necessary to assume the ionic charges were half their formal value. Thus the conclusion, again, is that the mixed valence oxide Sb 3d peaks cannot be resolved into Sb (III) and Sb (V) components.

Further work in chapters 4 and 5 of this thesis relied heavily on the XPS analysis of oxides containing Sb dopant ions and so it was important to investigate this issue, in order to determine the most appropriate hypothesis regarding Sb oxidation state analysis from XPS. This chapter outlines the analysis of one and two component Sb-component models in order to appropriately analyse further results. As well as analysing as-received Sb_2O_3 and Sb_2O_5, antimony (III) oxide was reacted with hydrogen peroxide (H_2O_2) to partially oxidise its surface creating mixed oxide materials. These materials were then used to test two analytical models

to determine if peak shift is resolvable between Sb (III) and Sb (V) components or if a one-component model, where oxidation state is not determinable, is more appropriate for mixed valence Sb-containing compounds.

Experimental

As-received Sb_2O_3 (0.1 g) was dispersed in 30 wt. % H_2O_2 (15 ml) and stirred in a sealed vessel, for varied lengths of time (5 minutes, 60 minutes, 24 hours and 130 hours) before being filtered by gravity, washed with water (5 x 10 ml) and left to dry in air. The samples, along with as-received Sb_2O_3 and Sb_2O_5 were analysed by PXRD and XPS. PXRD patterns were taken on STOE diffractometer using Molybdenum K-α radiation, recorded between 2 and 40 ˚ 2θ but converted to values for Cu K-α radiation for ease of comparison between chapters in this thesis.

3.1 Results and Discussion

3.1.1 Powder X-ray Diffraction (PXRD)

Powder X-ray diffraction of as-received Sb_2O_3 revealed that it was highly crystalline, as can be seen by the sharp peaks of the pattern shown in Figure 22a. This pattern was indexed in the orthorhombic *Pccn* space group and through least squares refinement of peak positions the lattice parameters and cell volume were determined. The cell volume was found to be within 0.4 % of that of the standard structure.

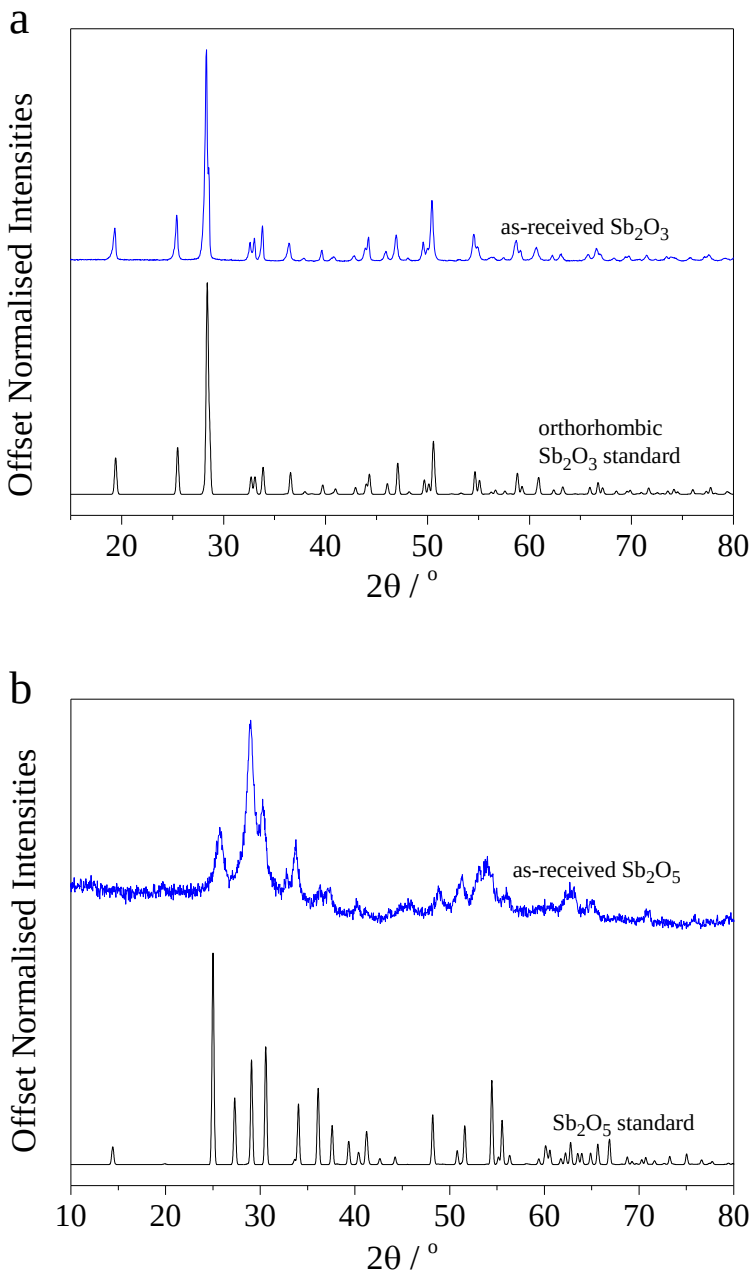

Figure 22a: (top) PXRD pattern of as-received Sb_2O_3 and b (bottom) as-received Sb_2O_5 both by comparison with standard patterns from literature[140, 141]

As- received Sb_2O_5, by contrast, was found to be lacking in crystallinity, as evidenced by the broader peaks and higher signal to noise ratio for the pattern shown in Figure 22b. Inspection of this pattern by comparison with the standard pattern also shown in Figure 22b, shows that there are distinct differences that indicate possible additional phases in the as-received sample. Figure 23a shows that the most intense peak ((11-1) at 25 °) in the Sb_2O_5 standard pattern for example, whilst present in the as-received sample is shifted to 26 ° and is much less intense than the (400) peak found at 27 ° in the as-received pattern. Differences in peak intensity could indicate a different growth orientation between the as-received sample and the sample used as a standard. However, in this case there are further discrepancies between the patterns. Figure 23a shows a different intensity ratio between the (400) and (31-1) peaks between the two

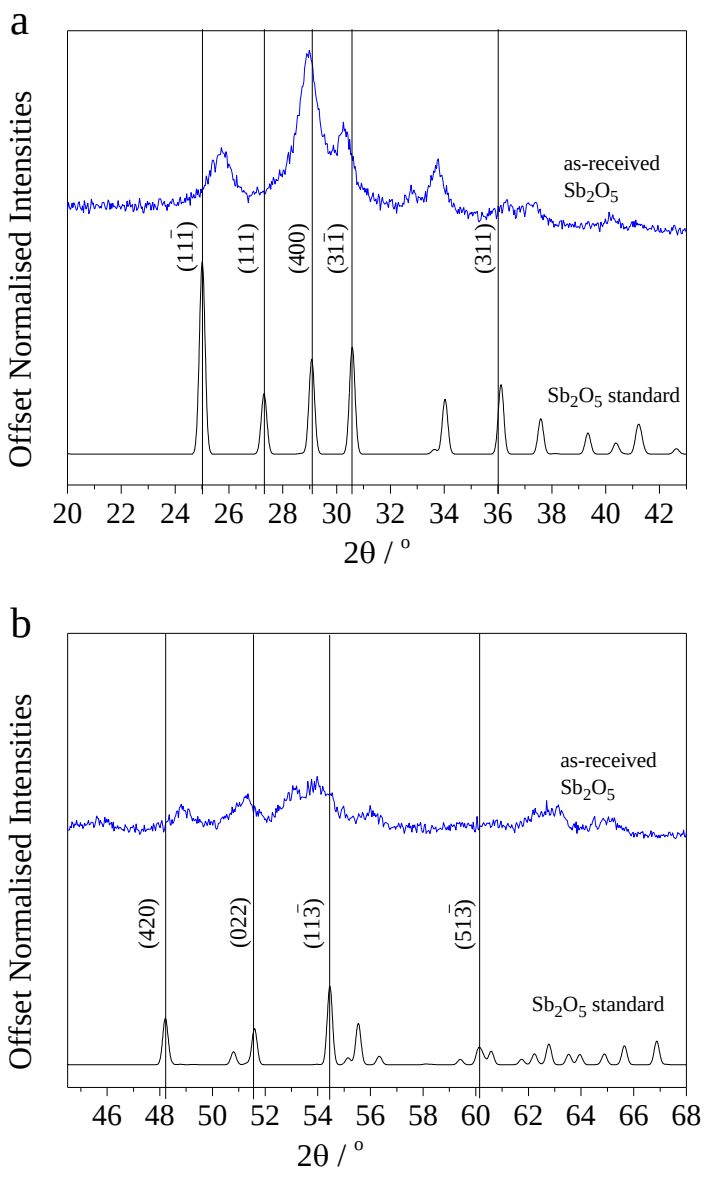

Figure 23a: close up views of a) (top) the 9- 19 ° region and b) (bottom) the 19-29 ° region of as-received Sb_2O_5 PXRD pattern

patterns and the (311) is so diminished in as-received Sb_2O_5 it is questionable if the peak is present, due to the high noise in this region. Figure 23b shows that the (420) and (022) peaks in as-received Sb_2O_5 are shifted in different directions from the standard pattern and therefore it is unlikely that they correlate at all. These discrepancies show that the as-received Sb_2O_5 is of a much poorer quality than the as-received Sb_2O_3.

Given the uncertain quality of commercial Sb_2O_5, it could not be used as a standard for XPS analysis. In order to study samples with mixed Sb (III) and Sb (V) in a well-defined ratio, Sb_2O_3 was oxidised using 30% H_2O_2 solution at room temperature. Powder X-ray diffraction patterns (Figure 24) show that when treated with hydrogen peroxide for varying amounts of time (5 minutes, 1 hour, 4 hours and 24 hours) antimony (III) oxide ostensibly retains its orthorhombic structure as compared with a standard pattern obtained from the ICSD [140]. Minimal peak shift is observed; the most intense (121) peaks found at ~ 13 ° 2θ all lie within ±0.065 ° of the position of the (121) peak in the standard pattern. The patterns were indexed in the *Pccn* space group and through least squares refinement the lattice parameters and cell volumes determined. All lattice parameter and cell volume values for oxidised samples lie within 0.7 % of those calculated for the standard pattern. It can therefore be concluded that there is no detectable crystallographic change to the materials and no indication of the formation of a secondary phase after 24 hours of treatment with hydrogen peroxide.

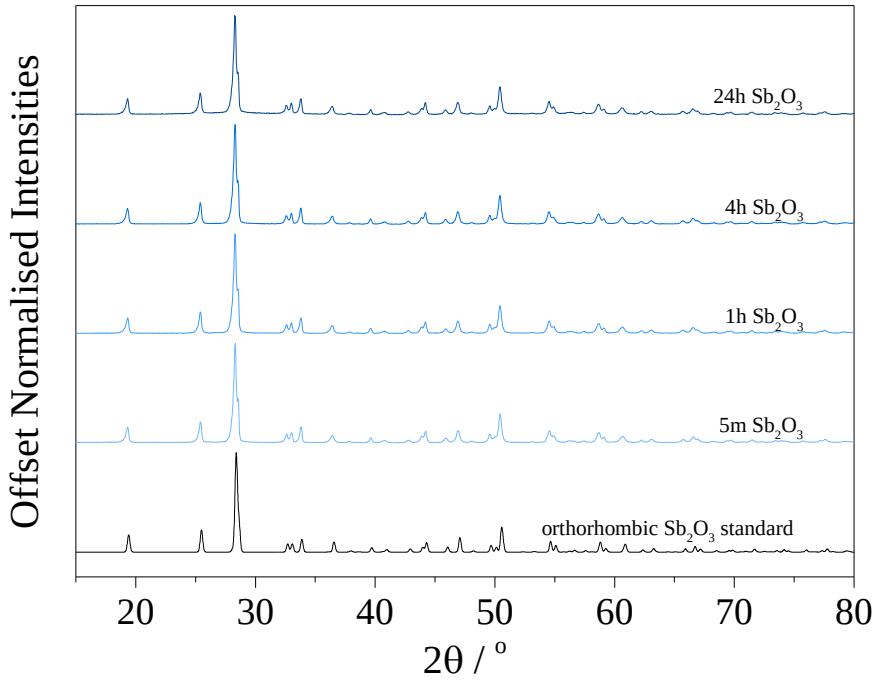

Figure 24: X-ray diffraction patterns of Sb_2O_3 powders treated for varying times in H_2O_2 for oxidation. These data were collected on a STOE diffractometer, in foil mode, using Mo radiation (λ = 0.7107 nm)

The penetrative nature of X-rays results in the detection of a diffraction signal that represents an average of the entire sample. While we can conclude that there has been no substantial oxidation of Sb_2O_3 particles to Sb_2O_5 in these samples, conclusions cannot necessarily be drawn from these PXRD data regarding the extent to which the *surface* of the materials may have been oxidised.

3.1.2 X-ray photoelectron spectroscopy

XPS was utilised in order to determine the extent of oxidation at the surface. This analysis typically has a sampling depth of between 2 and 10 nm and can therefore detect surface characteristics that have not shown up in PXRD. Survey spectra were recorded, detailing all elements present in the sample within the detection limit of the instrument used, as well as high-resolution core line spectra of Sb (3d and 4d) and O (1s). The O 1s and Sb $3d_{5/2}$ core lines (the principal core lines for these elements) directly overlap at a binding energy of around 530 eV such that one signal is indistinguishable from the other. For this analysis, the Sb $3d_{3/2}$ peak, which is well separated from the Sb $3d_{5/2}$ and O 1s peaks as it appears 9.4 eV higher, was used as the main source of information regarding antimony. In order to quantify the amount of oxygen present a constrained model was generated using CASAXPS software; an example spectrum can be seen in Figure 25.

The XP spectrum of the Sb 3d/O 1s core line region showed a peak at 540 eV (Sb $3d_{5/2}$) and at 530 eV (Sb $3d_{5/2}$, O 1s and surface hydroxyls). The peak at 530 eV was fitted with a Sb

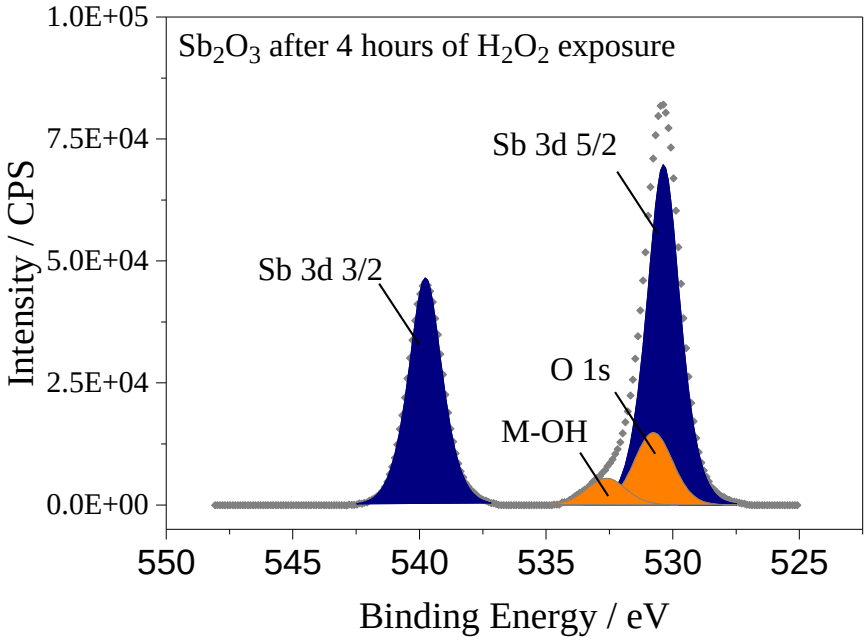

Figure 25: O 1s / Sb 3d core line region of Sb_2O_3 after 4 hours of exposure to H_2O_2. Sb 3d components can be seen modelled in blue, with O 1s and M-OH components modelled in orange.

$3d_{5/2}$ component, which was constrained in position, area and FWHM relative to the Sb $3d_{3/2}$ peak. All Sb peaks were generated with a 40 % Gaussian, 60 % Lorentzian contribution to their line shape since this provided best fit for the Sb $3d_{3/2}$ component. The remainder of the peak at 530 eV was fitted with components representing the lattice oxygen and surface hydroxyls which manifest as a broad shoulder to the high binding energy side of the O 1s. Both O 1s and M-OH models were generated with 70 % Gaussian contribution and 30 % Lorentzian contribution, which has been used previously to fit these components in the absence of Sb. The OH peak was constrained such that its FWHM value did not exceed 2.5 eV and it's position relative to the O 1s peak was + 2 eV (±0.1 eV).

Relative atomic percentages and a Sb/O ratio were determined by integration of the fitted spectra to determine the peak area of each component, followed by normalisation using the appropriate R.S.F., obtained from the instrument used. Sb/O ratio was determined using the combined atomic percentages of Sb $3d_{5/2}$ and Sb $3d_{3/2}$ peaks and the atomic percentages of lattice oxygen and surface hydroxyls. These ratios are plotted in Figure 26. As expected, the Sb/O ratio decreases as the reaction progresses, eventually reaching that of Sb_2O_5, 0.4. The Sb/O ratio calculated for as-received Sb_2O_3 and samples exposed to H_2O_2 for 5 minutes gave higher values than the theoretical Sb/O for Sb_2O_3, 0.667, which is shown as a horizontal bar on the graph. This can be partially attributed to oxygen vacancies at the surface of Sb_2O_3 and has been observed by other researchers.[122, 128] However, the ratio is so high that this explanation alone would indicate an implausibly large number of oxygen vacancies. For example a Sb/O of ~0.77, such as found in as-purchased Sb_2O_3 corresponds to 13 % of its oxygen sites being vacant.

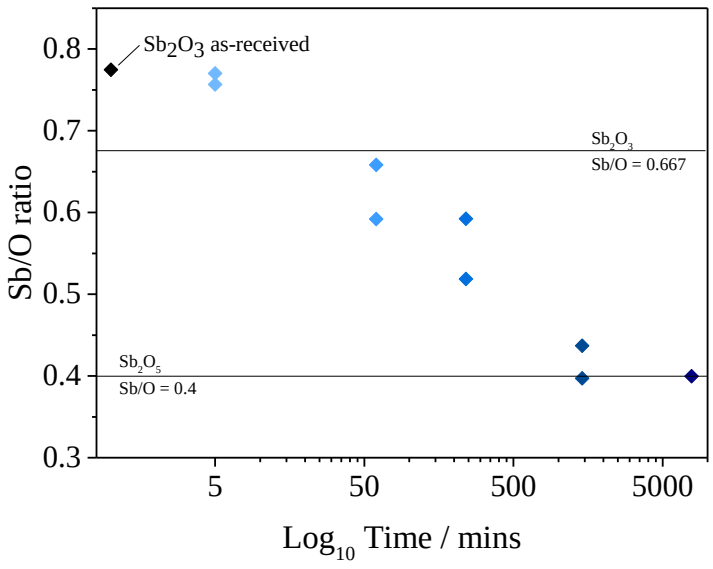

Figure 26: XPS calculated Sb/O ratio of Sb_2O_3 as-purchased powders exposed to hydrogen peroxide for 5 minutes, 1 hour, 4 hours and 24 hours. Reference lines for Sb_2O_3 and Sb_2O_5 Sb/O theoretical ratios have been included for clarity.

A second contributing factor to consider is a possible difference in detection of Sb and O photoelectrons. XPS sampling depth is dependent on the IMFP of the photoelectron, thus it follows that if the IMFP values are different for the elements being analysed then the sample volume and consequent relative concentrations would be different for the elements; other researchers have attributed high Sb/O ratios in their studies of Sb_2O_3 to this.[142] The IMFP of an electron can be determined using Equation 30 [143] below (K.E. = photoelectron kinetic energy and λ_{IMFP} = IMFP in Å) and for a Sb 3d $_{5/2}$ electron is approximately 1.67 Å.

$$\lambda_{IMFP} = \frac{143}{K.E.^2} + 0.054.\sqrt{K.E.}$$

Equation 30

This value can be used to determine the probability of an electron being photoemitted from the material by the relation shown in Equation 31 below:

$$P = e^{-d_{emission.}/\lambda_{IMFP}}$$

Equation 31

Where P = probability of photoemission and $d_{emission.}$ = distance photoelectron must travel to be ejected.

Since Sb $3d_{5/2}$ and O 1s photoelectrons have the same kinetic energy (~956 eV) they must also have the same IMFP (1.67 nm). Therefore, in order to explain the high Sb/O ratio observed in terms of differences in photoelectron detection, it can be concluded that the distance the respective photoelectrons must travel is different.

Sb_2O_3 is effectively Sb-O-Sb layered in the c-direction as shown schematically in Figure 27. Assuming emission along the c-axis, which is perpendicular to these Sb-O-Sb layers, the high Sb/O ratio for Sb_2O_3 and samples with a high proportion of Sb_2O_3 could be accounted for by the termination of the surface by a layer of Sb ions. Fewer photoelectrons would be detected from the O-layers since these photoelectrons would have further to travel and therefore fewer of them would be emitted from the material.

Wyckoff positions of the *Pccn* space group have been used to calculate the probability of photoemission of an electron from each position. The distance an electron would have to travel to be emitted, $d_{emission}$, can be determined by relating its position, W, along the c-axis to the length of the c-axis, c, by Equation 32:

$$d_{emission} = Wc$$

Equation 32

Thus from Equation 31, the probability of electron photoemission from each position can be determined using their known IMFP values. Table 4 lists the calculated c-axis positions for orthorhombic Sb_2O_3, the calculated $d_{emission}$ values and therefore the probability of photoemission for these electrons.

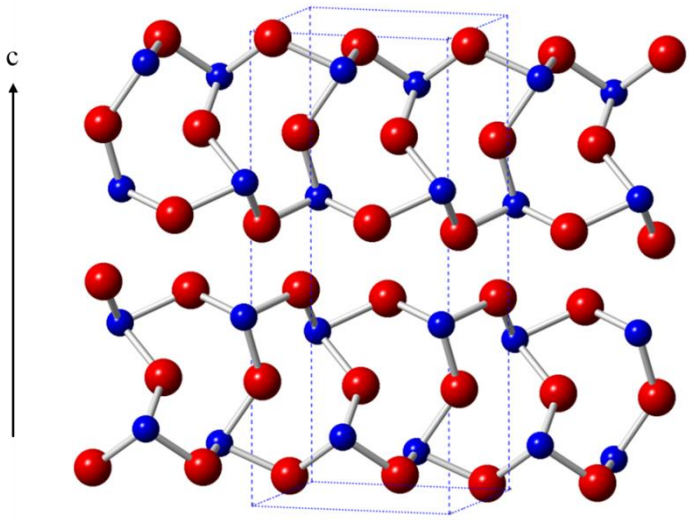

Figure 27: Layered structure of orthorhombic Sb_2O_3, where O atoms are shown in red and Sb atoms shown in blue.

Atom	Position along c-axis, W	Distance e^- travels, $d_{emission}$ (Å)	Probability of photoemission, P
Sb (x2)	0.178	0.96	0.56
	0.678	3.67	0.11
	0.822	4.45	0.07
	0.322	1.74	0.35
O1 (x1)	0.023	0.12	0.12
	0.523	2.83	2.83
	0.977	5.29	5.29
	0.477	2.58	2.58
O2 (x2)	0.855	0.063	0.06
	0.355	0.32	0.32
	0.145	0.63	0.63
	0.645	0.12	0.12

Table 4: Positions of Sb and O atoms in orthorhombic Sb_2O_3 along the c-axis and thus the calculated $d_{emission}$ and probability of photoemission values

Using these calculated probabilities it is possible to determine a theoretical Sb/O, which takes into account the higher likelihood of Sb ion detection if the exposed surfaces are Sb rich. The

quotient of the sum Sb probabilities of photoemission and O probabilities of photoemission using the values calculated in Table 4 yields a Sb/O ratio of 0.81. This is much higher than the theoretical Sb/O ratio if taking into account only the molar amounts of Sb and O ions in Sb_2O_3. However, it is higher than the Sb/O calculated by XPS for as-received Sb_2O_3 and Sb_2O_3 exposed to 30 % H_2O_2 for 5 minutes, which are around 0.77.

Oxygen vacancies are a common defect in metal oxides[144-146] and have been documented as present in Sb_2O_3 in other studies.[147-150] By taking into account a small number of surface oxygen vacancies and accompanying Sb vacancies deeper in the structure (i.e. discounting some contributions from O with small $d_{emission}$ values and some Sb with large $d_{emission}$ values), the theoretical Sb/O calculated from values in Table 4 is 0.76.

This explanation of a combination oxygen vacancies and a structural basis for low O 1s detection is corroborated by Sb 4d Sb/O data. A full summary of results from XPS of these samples can be seen in *Table 5*. Columns 9 and 10 list Sb/O ratios calculated from Sb 3d and Sb 4d core line spectra, respectively. Sb/O values for Sb_2O_3 calculated from Sb 4d spectra are higher than those from Sb 3d spectra. Since Sb 4d photoelectrons have a higher IMFP (2.06 nm) than Sb 3d and O1s (1.67 nm), a higher photoemission probability would be expected for Sb 4d electrons (following the methodology outlined above to calculate P). Both sets of Sb/O values tend to the accurate Sb/O ratio for Sb_2O_5 (0.4) as the reaction progresses. As oxidation occurs and the structure changes from orthorhombic Sb_2O_3 (*Pccn*) to rutile-like Sb_2O_5 (C12/c 1), XPS detects a more accurate surface Sb/O ratio. This serves to further highlight that high Sb/O values for Sb_2O_3 originate from the structural characteristics of the surface. Sb_2O_3 clearly has a higher proportion of Sb terminated ab-planes at the surface.

A larger M-OH contribution was observed for one of the 24h exposed samples, which is reflected in its low Sb/O ratio (0.3972) and could be due to improper drying of the sample. A longer reaction of 5 days (130h) resulted in Sb/O = 0.3995, the ratio expected on Sb_2O_5, which suggests that the oxidation had reached completion at the surface of this sample. This sample was subsequently used in all XPS analysis to represent Sb_2O_5 due to the poor quality of the as-received Sb_2O_5 material. For the purposes of the surface analysis performed on the rest of the data, it was of primary importance that the reference for Sb (V) was representative of an oxidised material and Sb_2O_3 exposed to H_2O_2 for 130 hours was the most appropriate sample from which to base further results. From here on in this sample will be referred to as Sb_2O_5*, as while the bulk of this sample (from XRD) remains Sb_2O_3, the Sb/O ratio within the XPS sampling depth matched that expected of Sb_2O_5.

A summary of the results, including measured peak position of O 1s, Sb 3d and Sb 4d (after charge correction to C1s at 285.0 eV), FWHM of Sb $3d_{3/2}$ and Sb $4d_{3/2}$ and Sb/O ratio, is

shown in Table 5. All O 1s data are those of the oxide anion component determined by modelling of the Sb 3d O 1s core line region.

Sample	Sb Peak positions (eV)				FWHM (eV)		O 1s peak positions (eV)	Sb/O	
	Sb 3d		Sb 4d						
	$^3/_2$	$^5/_2$	$^3/_2$	$^5/_2$	Sb $3d_{3/2}$	Sb $4d_{3/2}$		from Sb 3d	from Sb 4d
Sb_2O_3	539.15	529.75	34.9	33.61	1.353	1.255	530.44	0.6748	0.9062
5m_1	539.34	529.94	35.1	33.81	1.523	1.444	530.68	0.7702	0.9152
1h_1	539.70	530.30	35.49	34.23	1.566	1.619	530.90	0.5919	0.6893
4h_1	539.77	530.47	35.52	34.27	1.610	1.650	531.00	0.5186	0.6080
24h_1	539.87	530.47	35.72	34.47	1.587	1.625	531.15	0.4369	0.4413
5m_2	539.58	530.18	35.31	34.03	1.579	1.518	530.94	0.7569	0.8546
1h_2	539.76	530.36	35.47	34.21	1.609	1.622	531.02	0.6583	0.7447
4h_2	539.78	530.43	35.58	34.33	1.608	1.657	531.04	0.5924	0.6891
24h_2	539.78	530.38	35.67	34.40	1.685	1.715	531.11	0.3972	0.6630
130h	540.2	530.8	35.94	34.68	1.704	1.658	531.57	0.3995	0.4482

Table 5: Peak positions and FWHM for Sb $3d_{3/2}$,Sb $4d_{3/2}$, O 1s and Sb/O ratio for all samples

3.1.2.1 Valence Band Analysis

The Sb/O ratio indicates that Sb_2O_5 character increases as oxidation occurs, however it is difficult to quantify the amount of Sb (III) and Sb (V) due to the non-stoichiometric Sb/O determined for as-received Sb_2O_3. Therefore a novel valence band analysis was utilised to determine this proportion and corroborate the Sb/O findings.

The valence bands of antimony oxides are made up of contributions from the O 2p and Sb 5s; these 5s are all filled and therefore present in the valence band of in antimony (III) oxide but empty in antimony (V) oxide and so the orbitals contribute to the conduction band. Computational studies by Scanlon et al.[151] propose that the valence band edge of Sb_2O_5 is dominated by O 2p since there are no Sb 5s or p electrons. In the model presented below XP VB spectra of Sb_2O_3 and Sb_2O_5* were generated from standard compounds and these fits compiled into the XP VB spectra of compounds of mixed oxidation state in order to determine the proportion of Sb_2O_3 and Sb_2O_5-like character.

The valence band spectra of Sb_2O_3 as-purchased powder and Sb_2O_5* are presented in Figure 28. In each spectrum four modelled components (A-D and E-H) can be seen, which have

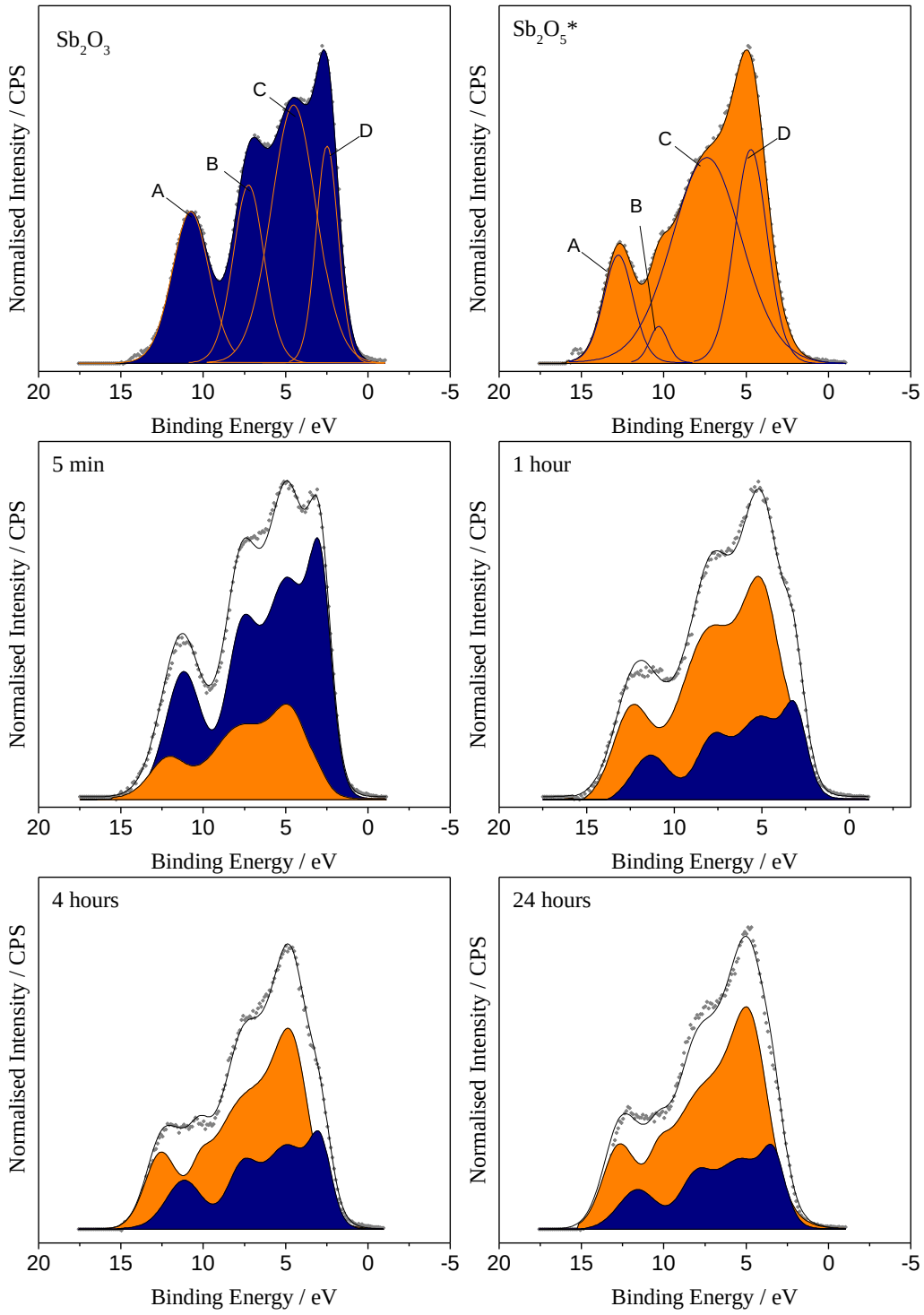

Figure 28: Valence band spectra of bottom: Sb_2O_3 as-purchased powder and Sb_2O_5* used as the 'standard' valence band models. Top and middle: example time resolved valence band spectra modelled with Sb_2O_3 and Sb_2O_5* models.

been generated using a Shirley background and a 70 % Gaussian 30 % Lorentzian peak shape. Both spectra possess a small peak at the higher binding energy side of the valence band, these features (A and E) lie at 10.88 eV (A) in Sb_2O_3 and 12.68 eV (E) in Sb_2O_5*. Feature D in Sb_2O_3 is likely due to population of 5s states in Sb (III). This strong feature lies at 2.6 eV and

masks the rest of the valence band edge. It is not present in the oxidised sample (Sb_2O_5*) - the feature labelled H in this sample is more comparable in position to feature C in the Sb_2O_3 valence band, lying at 4.68 eV (Sb_2O_5*, H) and 4.48 eV (Sb_2O_3, C).

The fitted valence band components for Sb_2O_3 as-purchased and Sb_2O_5* powders were constrained to one another by their position, area and FWHM values, with only the binding energy and area of component A in each spectrum left to vary freely. The shapes of the valence bands were therefore fixed, with only their relative areas and overall positions free to vary.

In order to further track the progress of Sb_2O_3 oxidation, both the Sb_2O_3 and Sb_2O_5* fits were copied into the valence band region of samples at each time resolution and allowed to generate the most appropriate fit ratios. In Figure 28 these fits are shown; Sb_2O_3-like components are shown in blue and Sb_2O_5*-like components are coloured orange. As can be seen, the amount of Sb_2O_3-like character in the valence band, *decreases* with hydrogen peroxide exposure time, whereas the Sb_2O_5-like character of the valence band *increases* with hydrogen peroxide exposure time. That each valence band was successfully modelled as a simple linear combination of the two standard valence band models, with a minimal residual standard deviation (< 5.0) in all cases, is a significant finding. Here only the relative intensities and positions of the Sb_2O_3 and Sb_2O_5* valence band models were variable; the shapes were fixed and when combined (as shown in Figure 28) were able to coherently account for valence bands made up of a combination of the two components. The valence band components were quantified and the increasing amount of Sb_2O_5*-like contribution to the valence band can be seen in Figure 29; the values have also been presented in Table 6. The standard Sb_2O_3 as-purchased and Sb_2O_5* powders have been assigned as 0 and 100 % Sb_2O_5* contribution, respectively. After 5 minutes of exposure to hydrogen peroxide, the amount of Sb_2O_5* contribution to the valence band had increased from 0 to 21 % and 39 %. This increased further, to 44 % and 51 % after 1 hour of hydrogen peroxide exposure, to 59 % and 64 % after 4 hours of exposure and finally 74 % and 75 % after 24 hours of exposure.

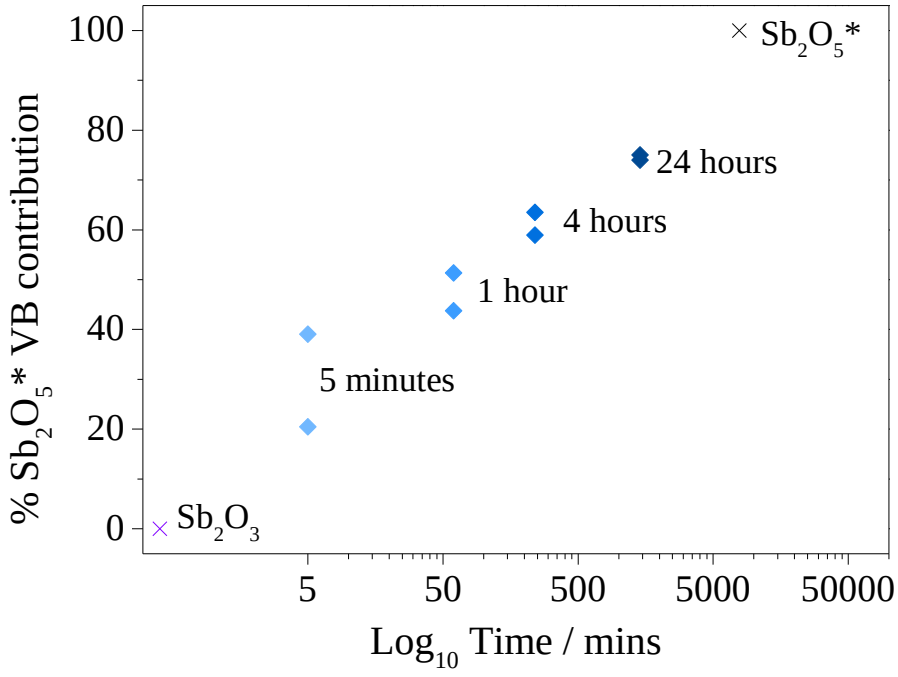

Figure 29: Proportion of Sb_2O_3-like contribution to the valence band as determined by fitting of constrained Sb_2O_3 and 130h H_2O_2 exposed sample valence band components shown in Figure 28.

Sample (Time)	% Sb_2O_3 contribution	% Sb_2O_5* contribution	Sample (Time)	% Sb_2O_3 contribution	% Sb_2O_5* contribution
	Run 1			Run 2	
5m	79.50	20.50	5m	60.96	39.04
1h	48.62	51.38	1h	56.24	43.76
4h	36.49	63.51	4h	41.04	58.96
24h	24.95	75.05	24h	26.01	73.99

Table 6: Percentage contribution of Sb_2O_3 and Sb_2O_5 characterfor oxidised samples as determined by valence band fitting

It is clear that oxidation occurs rapidly in the initial instance; differences in sample handling (for example time taken to filter the sample) at the lower time resolutions have likely affected the amount of oxidation that has occurred. Even small differences between the times the samples were exposed to H_2O_2 have caused large changes in the degree of Sb_2O_5* character in the valence band. This linear relationship on a Log scale indicates a logarithmic relationship between time and oxidation amount.

Since oxidation occurs from the sample surface inward towards the bulk, the proportion of Sb_2O_5 can be thought of as a proportion, d, of the total sampling depth, as shown in Figure 30. From Equation 31, in XPS the probability of an electron being photoemitted is proportional to the $\exp(^{-x}/_{\lambda})$. This function is shown in Figure 31 where a specific depth of Sb_2O_5, d, is labelled.

Figure 30: Schematic diagram of Sb_2O_3 layer at the surface of Sb_2O_3 during the oxidation reaction.

At depth d, the proportion of Sb_2O_5 can be found by integration of Equation 31 between the limits 0 > x > d to find area A. Similarly the proportion of Sb_2O_3 can be evaluated by integration of Equation 31 between the limits d > x > ∞ to find area B. Thus an expression for the change in proportion of Sb_2O_5 as a function of x can be determined.

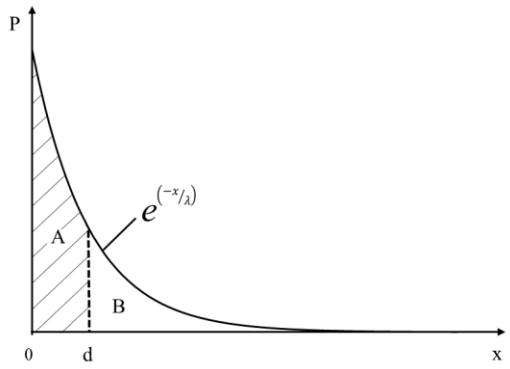

Figure 31: Probability of and electron being photoemitted as a function of depth, x.

Integration between the limits 0 > x > d and d > x > ∞ to find areas A and B in Figure 31 follow in Equation 33 Equation 34.

$$A = \int_0^d e^{\left(-x/\lambda\right)} dx = -\lambda e^{-d/\lambda} - (-\lambda)$$

Equation 33

$$B = \int_d^\infty e^{\left(-x/\lambda\right)} dx = 0 - \left(-\lambda\, e^{\left(-d/\lambda\right)}\right)$$

Equation 34

To determine area A as a proportion of the total area (A+B) these expressions can be combined in the following way:

$$\frac{A}{A+B} = \frac{-\lambda e^{\left(-d/\lambda\right)} + \lambda}{-\lambda e^{\left(-d/\lambda\right)} + \lambda + \lambda e^{\left(-d/\lambda\right)}}$$

Equation 35

$$= \frac{-\lambda e^{\left(-d/\lambda\right)} + \lambda}{\lambda}$$

Equation 36

$$= e^{\left(-d/\lambda\right)} + 1$$

Equation 37

$$= 1 - e^{\left(-d/\lambda\right)}$$

Equation 38

Thus, by knowing the proportion of Sb_2O_5-character from VB analysis and assuming oxidation occurs at the same rate over all exposed faces, the depth of oxidation can be calculated. These results are shown below in Table 7 and plotted in Figure 32, to which a logarithmic trend line can be fitted and a rate equation extrapolated.

Sample (Time)	d (nm)	% Sb_2O_5* contribution	Sample (Time)	d (nm)	% Sb_2O_5* contribution
	Run 1			Run 2	
5m	0.38	20.50	5m	0.83	39.04
1h	1.20	51.38	1h	0.96	43.76
4h	1.68	63.51	4h	1.49	58.96
24h	2.32	75.05	24h	2.25	73.99

Table 7: Oxidation depth per sample as determined by Sb_2O_5-like character from valence band analysis

The rate of oxidation is therefore defined, in this experiment, as:

$$y = 0.3\ ln(x) + 0.024$$

Equation 39

where y is oxidation depth in nm and x is time in minutes.

The results above show that a sample of Sb_2O_5 can be oxidised to Sb_2O_5 at the surface by the action of 30% H_2O_2 solution, that this reaction can be tracked by analysis of the valence band of the mixtures and that a rate for the reaction can be determined from this valence band analysis. This series of samples will now be used to study the behaviour of the Sb core lines and look for evidence of a chemical shift between Sb (III) and Sb (V).

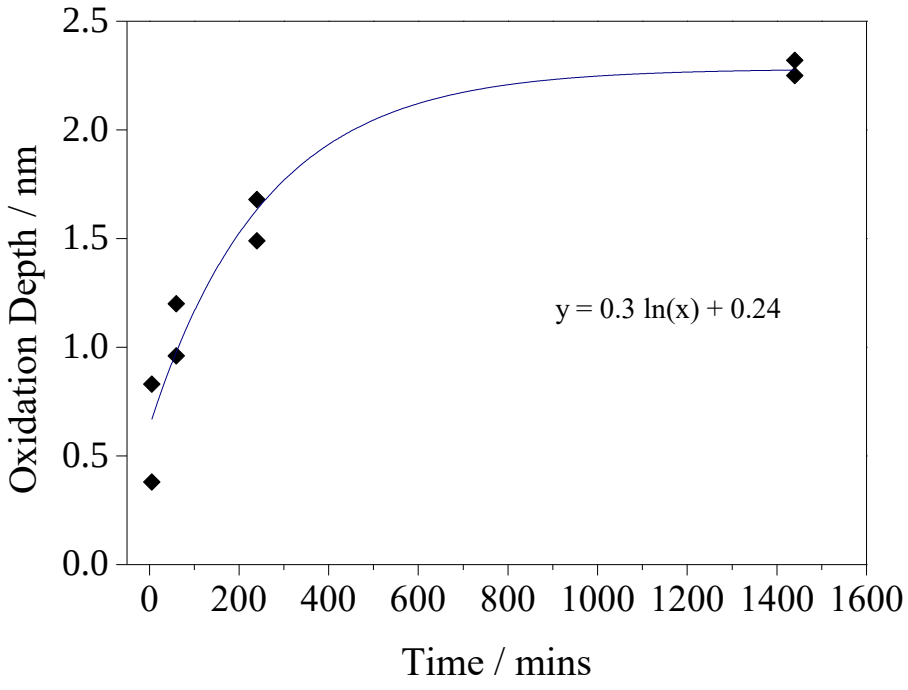

Figure 32: Oxidation depth versus reaction time for Sb_2O_3 to Sb_2O_5 oxidation by H_2O_2. A logarithmic increase is observed and trend line fitted with function as shown on the graph.

3.1.2.2 Quantification of Sb Oxidation State

The oxidation state of an element is usually identified in XPS by the chemical shift of the photoelectron binding energy. When electrons are lost through ionisation, the net nuclear charge felt by the remaining electrons increases. It follows that core electrons of elements in higher oxidation states will have higher binding energies and require more energy to photoexcite them from the element. However, when comparing the same element in materials of different structures, as when Sb_2O_3 is converted to Sb_2O_5, additional factors must be taken into consideration. Firstly, XPS is calibrated with the Fermi level of the material as 0 eV, meaning that all core line binding energy values are in reference to the Fermi level. Therefore, when tracking the progress of a reaction using XPS, differences in the Fermi level energy between compounds render the absolute core line binding energy values incomparable.

A second issue with the comparison of XPS data from Sb_2O_3 and Sb_2O_5 is that the antimony ions in samples being analysed in this investigation can be in vastly different environments. In this study, since Sb_2O_3 is being oxidised the Sb environment is dependent on the degree of oxidation due to the differing structures of the two oxides. Antimony (V) oxide adopts a rutile-like structure, whereas antimony (III) oxide, at low temperatures, is most stable in the orthorhombic crystal structure (both pictured in Figure 33). These differences will mean that

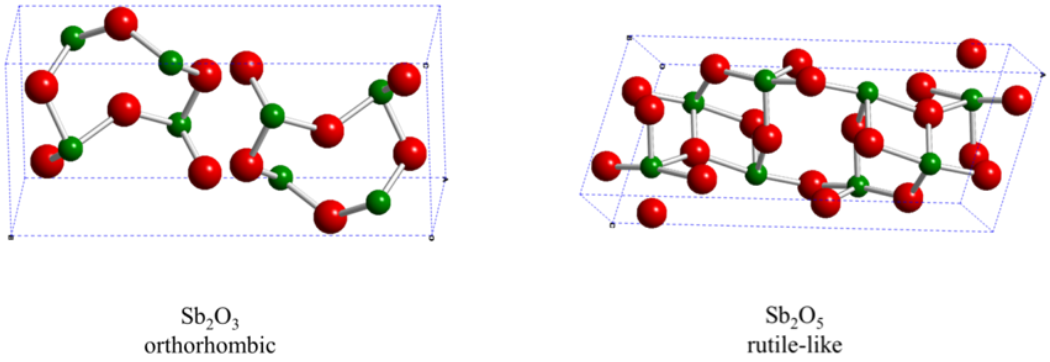

Figure 33: Ball and stick representations of the unit cells of orthorhombic Sb_2O_3 (left) and rutile-like Sb_2O_5 (right). Antimony atoms are green and oxygen atoms are red.

the Madelung constant for each crystal is different. Therefore when the two structures exist close to each other for example in mixed valence compounds like Sb_2O_4 or in oxidised Sb_2O_3, which could be thought of as an Sb_2O_3 core with a Sb_2O_5 shell, there will be an impact on site potentials experienced by ions in the lattice, which may affect the photoelectron energy and thus the XPS peak position. The differences in Sb core line data between samples show a trend of increasing binding energy as oxidation occurs. This can be seen clearly in Figure 34a, where the Sb $3d_{3/2}$ core lines are overlaid, and is more clearly observed in Figure 34b, which is annotated with the absolute binding energy, as determined from fitting.

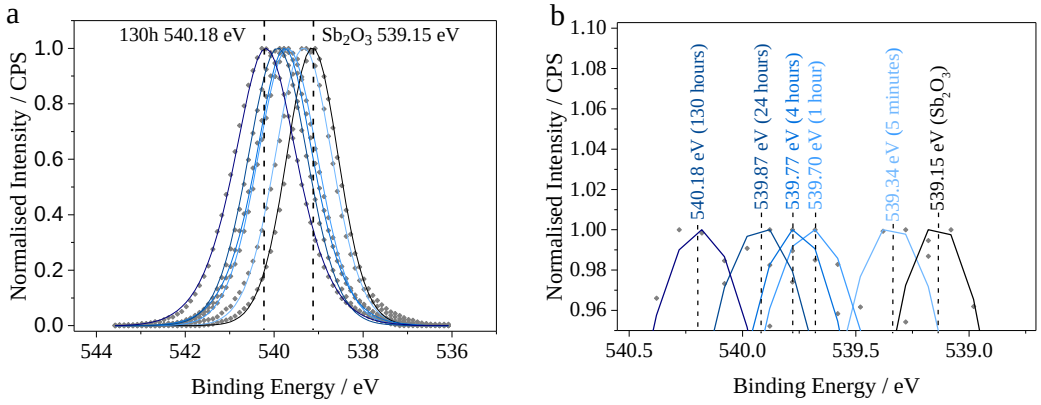

Figure 34: a) Normalised Sb $3d_{3/2}$ core line spectra of Sb_2O_3 (black) and Sb_2O_3 samples exposed to H_2O_2 for 5 minutes, 1 hour, 4 hours and 24 hours (light blue to dark blue and b) the top of the peaks for clarification of position

Though not immediately evident from observation of the core line spectra alone, a broadening of the Sb $3d_{3/2}$ peak was observed in the samples in this investigation, as oxidation progressed. Analysis of Sb 4d spectra revealed similar trends to those found for the 3d photoelectrons. Figure 35a shows the change in Sb 3d and 4d peak positions in plotted against Log_{10} reaction time; orange points (left x-axis) show positions of the 3d peaks whereas blue points (right y-axis) represent the 4d peaks. The trends are almost identical. Overall, both 3d and 4d photoelectrons increase in binding energy by around 1 eV as the reaction progresses and the

samples become more oxidised. The increase in FWHM observed for the 3d photoelectron peaks, is also observed in the 4d photoelectron peaks (Figure 35b). However, the overall trend for Sb 4d FWHM is an increase followed by slight decrease at 130h. This could indicate the presence of a mixture of Sb oxidation states in samples at intermediate time resolutions, which would cause more considerable peak broadening than the presence of a single oxidation state.

The increase in Sb $3d_{3/2}$ peak position is also replicated, almost exactly, for the O 1s photoelectron. As can be seen in Figure 36, the O 1s peak position determined by modelling of the Sb 3d /O 1s core line region increases linearly as the reaction progresses. This has been plotted alongside Sb $3d_{3/2}$ peak position for ease of comparison. The change in O 1s peak position with oxidation is a significant and unexpected result; it would be expected to be approximately constant since the O 1s peak position does not vary largely between metal oxides; here a difference of > 1.0 eV is observed.

In order to determine the origin of Sb 3d peak broadening and to determine if the changes in peak position are solely due to the varying oxidation state of the Sb ions, all Sb 3d and 4d spectra have been be modelled with Sb (III) and Sb (V) components. If there is a genuine, resolvable chemical shift between Sb (III) and (V) photoelectron peaks it would be expected that this chemical shift between modelled components would be constant and also that the resultant O 1s peak position would therefore be approximately constant across all samples.

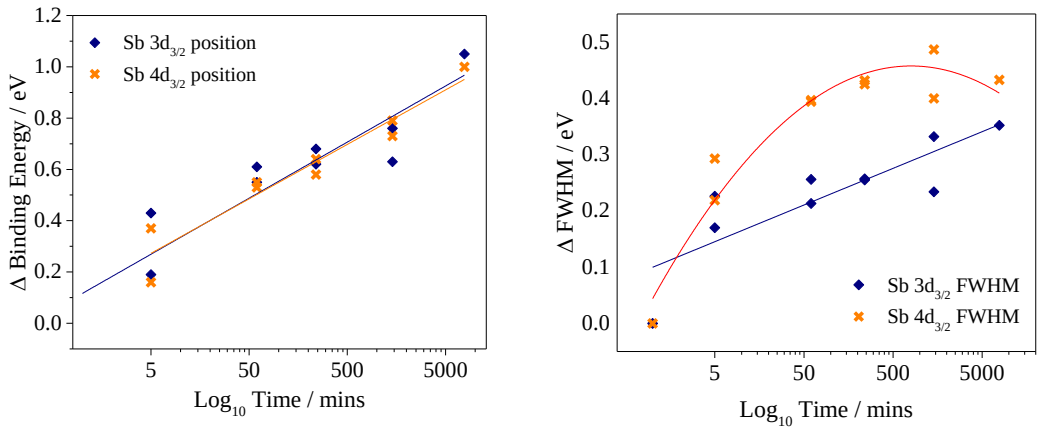

Figure 35: a Peak positions of Sb 3d and 4d photoelectrons as a function of H_2O_2 exposure time and b) FWHM values for Sb 3d (orange, left axis) and Sb 4d (blue, right axis) plotted against Log_{10} time. Peak broadening is experienced by both core lines to the same degree

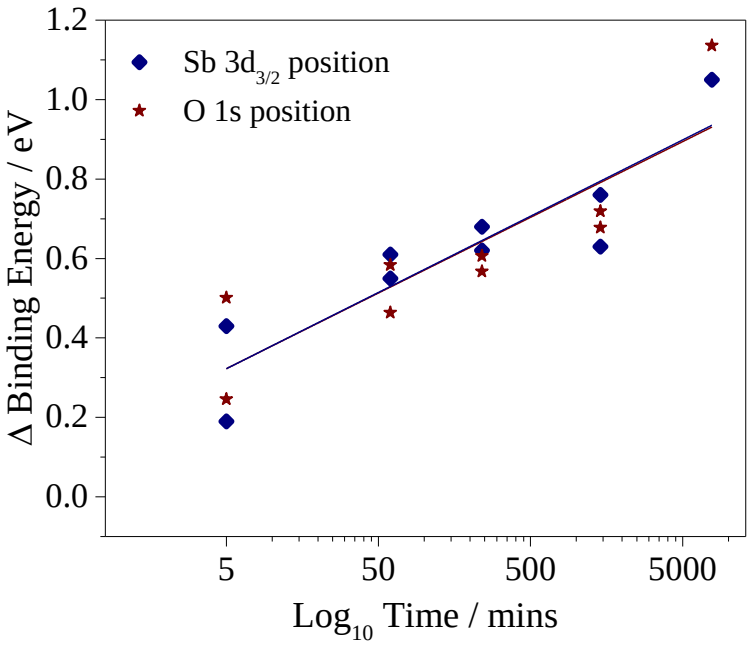

Figure 36: Sb $3d_{3/2}$ and O 1s peak position determined from modelling of the Sb 3d and O 1s core line region, plotted against reaction time.

In light of the results presented above, which show an increase in binding energy of Sb $3d_{3/2}$ peaks, an increase in FWHM, and change in binding energy of the O 1s core line as oxidation progresses, two models for Sb peaks were proposed. The aim of testing these models was to determine if either provided a reasonable answer to the question of whether Sb $3d_{3/2}$ or Sb 4d peaks should be treated as resolvable combinations of Sb(III) and Sb(V) contributions or not. These models are outlined below.

Model 1:

- The Sb 3d and Sb 4d peaks are each modelled with components corresponding to Sb(III) and Sb(V)
- The relative intensity of these components is fixed by the Sb(III)/Sb(V) ratio determined from the core lines and VB analysis above (see Table 6)
- The binding energy of the Sb(III) component is constrained to be lower than that of the Sb(V) component
- The FWHM of these components are maintained as equal to each other at 1.255 eV, the FWHM determined for as-purchased Sb_2O_3

Model 2:

As above except:

- The FWHM of each component is set to the value obtained from Sb_2O_3 (1.255 eV) and Sb_2O_5* (1.704)

The hypothesis here is that if either model is appropriate (i.e. if the Sb 3d and 4d peaks are able to be resolved into contributions from Sb (III) and Sb (V)) then the following should be satisfied:

1. Fit should be reasonable, i.e. a low residual STD (measure of goodness of fit from CASAXPS software used)
2. Peak shift between Sb(III) and Sb(V) should be consistent
3. O 1s peak positions generated from fitted Sb 3d/O 1s core line region spectra should be approximately constant

Model 1 is based upon the hypothesis that both Sb (III) and Sb (V) photoelectron spectra should have the same FWHM and that increases in FWHM are observed due to mixed valence. FWHM values from as-purchased Sb_2O_3 were used due to the purity of the materials as determined by XRD and XPS. This hypothesis does not take into account the data obtained for Sb_2O_5* as a representation of Sb (V) and so Model 2, where Sb (V) components have their FWHM set as that for Sb components in Sb_2O_5* was also proposed.

Model 1 (Equal FWHM)

For this analysis it was initially assumed that the FWHM of both the Sb(III) and Sb(V) components were equal and the value used was that measured for the standard Sb_2O_3 powder, 1.25 eV (±0.05 eV). An example modelled spectrum is shown in Figure 37a and Table 8 shows the resultant data for binding energy and FWHM of Sb modelled peaks and the peak shift between Sb(III) and Sb(V)) calculated by the models. The peak shifts derived using this model range from 0.57 to 0.7 eV. In general these models resulted in a reasonable degree of fit; the residual standard deviation (STD) was found to be below 10.0 in all cases. Table 9 outlines the results for the same analysis performed on Sb 4d core line spectra, and example for which is given in Figure 37b. Again, the residual STD was low, below 5 in all cases; the range of peak shift values was from 0.57 eV to 0.73 eV. Neither the Sb 3d nor 4d peak shift values from this analysis appeared to show any trend across the series. This analysis also does not rectify the issue surrounding the observed increase in O 1s photoelectron binding energies since the resultant O 1s peak positions from this analysis vary by >1.2 eV and show no trend.

These results indicate that Model 1 does not satisfy the requirements set out as necessary for the model to be considered successful. Therefore Model 1 is not an appropriate method of Sb peak fitting.

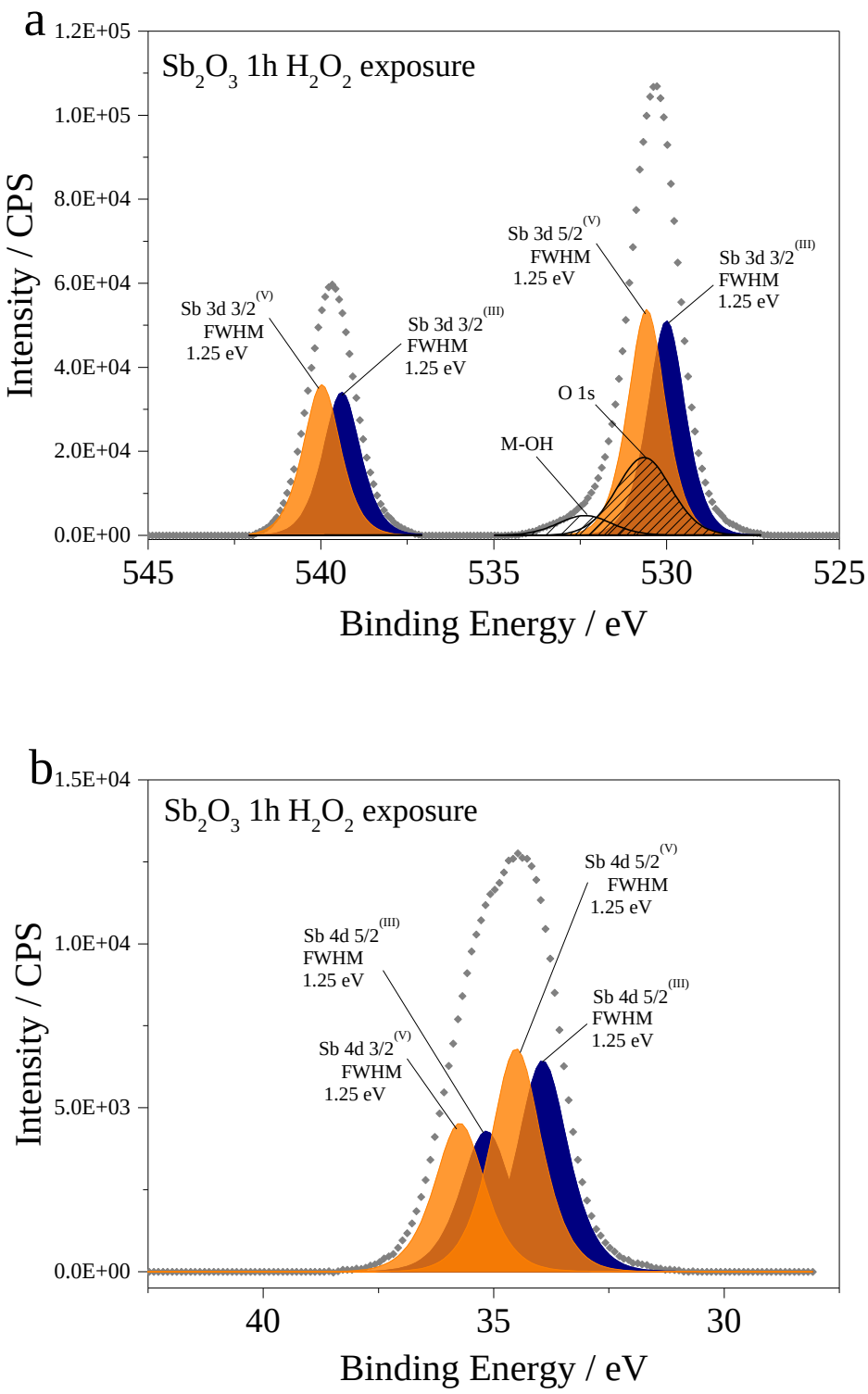

Figure 37: top O 1s / Sb 3d core line region of Sb_2O_3 and bottom Sb 4d core line region. Both spectra show samples after 1 hour of exposure to H_2O_2 modelled with Sb (III) (blue) and Sb (V) (orange) components of equal FWHM. O 1s and M-OH components can be seen in the 3d spectrum with black hatched lines

Sample (Time_repeat)	Peak	Binding Energy (eV)	FWHM (eV)	Sb III/V Peak Shift (eV)	Residual (STD)	O 1s position (eV)
5m_1	$Sb^{(III)}$ $3d_{3/2}$	539.21	1.26	0.69	8.03	530.61
	$Sb^{(V)}$ $3d_{3/2}$	539.9	1.26			
	$Sb^{(III)}$ $3d_{5/2}$	529.81	1.26			
	$Sb^{(V)}$ $3d_{5/2}$	530.5	1.26			
5m_2	$Sb^{(III)}$ $3d_{3/2}$	539.34	1.26	0.64	8.23	530.69
	$Sb^{(V)}$ $3d_{3/2}$	539.98	1.25			
	$Sb^{(III)}$ $3d_{5/2}$	529.94	1.26			
	$Sb^{(V)}$ $3d_{5/2}$	530.58	1.25			
1h_1	$Sb^{(III)}$ $3d_{3/2}$	539.4	1.26	0.57	5.58	530.97
	$Sb^{(V)}$ $3d_{3/2}$	539.97	1.26			
	$Sb^{(III)}$ $3d_{5/2}$	530	1.26			
	$Sb^{(V)}$ $3d_{5/2}$	530.57	1.26			
1h_2	$Sb^{(III)}$ $3d_{3/2}$	539.49	1.26	0.59	9.92	531.36
	$Sb^{(V)}$ $3d_{3/2}$	540.08	1.26			
	$Sb^{(III)}$ $3d_{5/2}$	530.09	1.26			
	$Sb^{(V)}$ $3d_{5/2}$	530.68	1.26			
4h_1	$Sb^{(III)}$ $3d_{3/2}$	539.45	1.26	0.64	6.55	531.08
	$Sb^{(V)}$ $3d_{3/2}$	540.09	1.26			
	$Sb^{(III)}$ $3d_{5/2}$	530.05	1.26			
	$Sb^{(V)}$ $3d_{5/2}$	530.69	1.26			
4h_2	$Sb^{(III)}$ $3d_{3/2}$	539.41	1.26	0.70	7.01	531.84
	$Sb^{(V)}$ $3d_{3/2}$	540.11	1.26			
	$Sb^{(III)}$ $3d_{5/2}$	530.01	1.26			
	$Sb^{(V)}$ $3d_{5/2}$	530.71	1.26			
24h_1	$Sb^{(III)}$ $3d_{3/2}$	539.39	1.25	0.67	8.70	531.16
	$Sb^{(V)}$ $3d_{3/2}$	540.06	1.26			
	$Sb^{(III)}$ $3d_{5/2}$	529.99	1.25			
	$Sb^{(V)}$ $3d_{5/2}$	530.66	1.26			
24h_2	$Sb^{(III)}$ $3d_{3/2}$	539.19	1.26	0.72	7.23	531.58
	$Sb^{(V)}$ $3d_{3/2}$	539.91	1.26			
	$Sb^{(III)}$ $3d_{5/2}$	529.79	1.26			
	$Sb^{(V)}$ $3d_{5/2}$	530.51	1.26			

Table 8: Peak position, FWHM, Sb III/V peak shift, residual standard deviation and resultant O 1s position for Sb3d XPS spectra using model 1

Sample (Time_repeat)	Peak	Binding Energy (eV)	FWHM (eV)	Sb III/V Peak Shift (eV)	Residual (STD)
5m_1	$Sb^{(III)}$ $4d_{3/2}$	34.93	1.22	0.68	3.83
	$Sb^{(V)}$ $4d_{3/2}$	35.61	1.22		
	$Sb^{(III)}$ $4d_{5/2}$	33.71	1.22		
	$Sb^{(V)}$ $4d_{5/2}$	34.38	1.22		
5m_2	$Sb^{(III)}$ $4d_{3/2}$	35.05	1.28	0.57	4.09
	$Sb^{(V)}$ $4d_{3/2}$	35.62	1.28		
	$Sb^{(III)}$ $4d_{5/2}$	33.83	1.28		
	$Sb^{(V)}$ $4d_{5/2}$	34.40	1.28		
1h_1	$Sb^{(III)}$ $4d_{3/2}$	35.15	1.28	0.58	3.15
	$Sb^{(V)}$ $4d_{3/2}$	35.74	1.28		
	$Sb^{(III)}$ $4d_{5/2}$	33.94	1.28		
	$Sb^{(V)}$ $4d_{5/2}$	34.51	1.28		
1h_2	$Sb^{(III)}$ $4d_{3/2}$	35.17	1.28	0.61	4.28
	$Sb^{(V)}$ $4d_{3/2}$	35.78	1.28		
	$Sb^{(III)}$ $4d_{5/2}$	33.95	1.28		
	$Sb^{(V)}$ $4d_{5/2}$	34.56	1.28		
4h_1	$Sb^{(III)}$ $4d_{3/2}$	35.07	1.28	0.66	3.89
	$Sb^{(V)}$ $4d_{3/2}$	35.73	1.28		
	$Sb^{(III)}$ $4d_{5/2}$	33.85	1.28		
	$Sb^{(V)}$ $4d_{5/2}$	34.51	1.28		
4h_2	$Sb^{(III)}$ $4d_{3/2}$	35.17	1.28	0.66	3.83
	$Sb^{(V)}$ $4d_{3/2}$	35.83	1.28		
	$Sb^{(III)}$ $4d_{5/2}$	33.94	1.28		
	$Sb^{(V)}$ $4d_{5/2}$	34.6	1.28		
24h_1	$Sb^{(III)}$ $4d_{3/2}$	35.16	1.28	0.7	2.74
	$Sb^{(V)}$ $4d_{3/2}$	35.86	1.28		
	$Sb^{(III)}$ $4d_{5/2}$	33.93	1.28		
	$Sb^{(V)}$ $4d_{5/2}$	34.64	1.28		
24h_2	$Sb^{(III)}$ $4d_{3/2}$	35.23	1.28	0.73	5.29
	$Sb^{(V)}$ $4d_{3/2}$	35.96	1.28		
	$Sb^{(III)}$ $4d_{5/2}$	33.98	1.28		
	$Sb^{(V)}$ $4d_{5/2}$	34.69	1.28		

Table 9: Peak position, FWHM, Sb III/V peak shift and residual standard deviation for Sb4d XPS spectra using model 1

Model 2 (Unequal FWHM)

This alternative analysis was also completed whereby the FWHM of Sb peaks were constrained to within ±0.05 eV of their standard values, i.e. that of the Sb_2O_3 standard powder for Sb (III) and Sb_2O_5* for Sb (V). From table 2 the FWHM values can be seen as 1.25 eV and 1.70 eV for Sb_2O_3 and Sb_2O_5* respectively. Using these values for FWHM produced models of reasonable fit (an example spectrum can be seen in figure 13a) with STD varying from as low as 2.84 for sample 24h_2 and increasing to 14.75 for sample 5m_1, though residual STDs were consistently higher than those using equal FWHM values. Peak shift values between Sb (III) and Sb (V) can be seen in column 5 of Table 10; they vary from 0.17 eV to 0.62 eV and there is evidently no trend between level of oxidation and peak shift using this model. The results from this analysis also do not satisfy the requirement of producing a consistent O 1s binding energy value for the fitted Sb 3d/O 1s core line region, since the fitted O 1s peak positions from this analysis vary by 0.5 eV.

Table 11 outlines the results for the same analysis performed on Sb 4d core line spectra, an example for which can be seen in in Figure 38b. The residual STD was consistently low, again below 5 in all cases; the range of peak shift values was from 0.43 eV to 0.65 eV though with no evident trend over this series.

These results indicate that Model 2 does not satisfy the requirements set out as necessary for the model to be considered successful. Therefore Model 2 is not an appropriate method of Sb peak fitting.

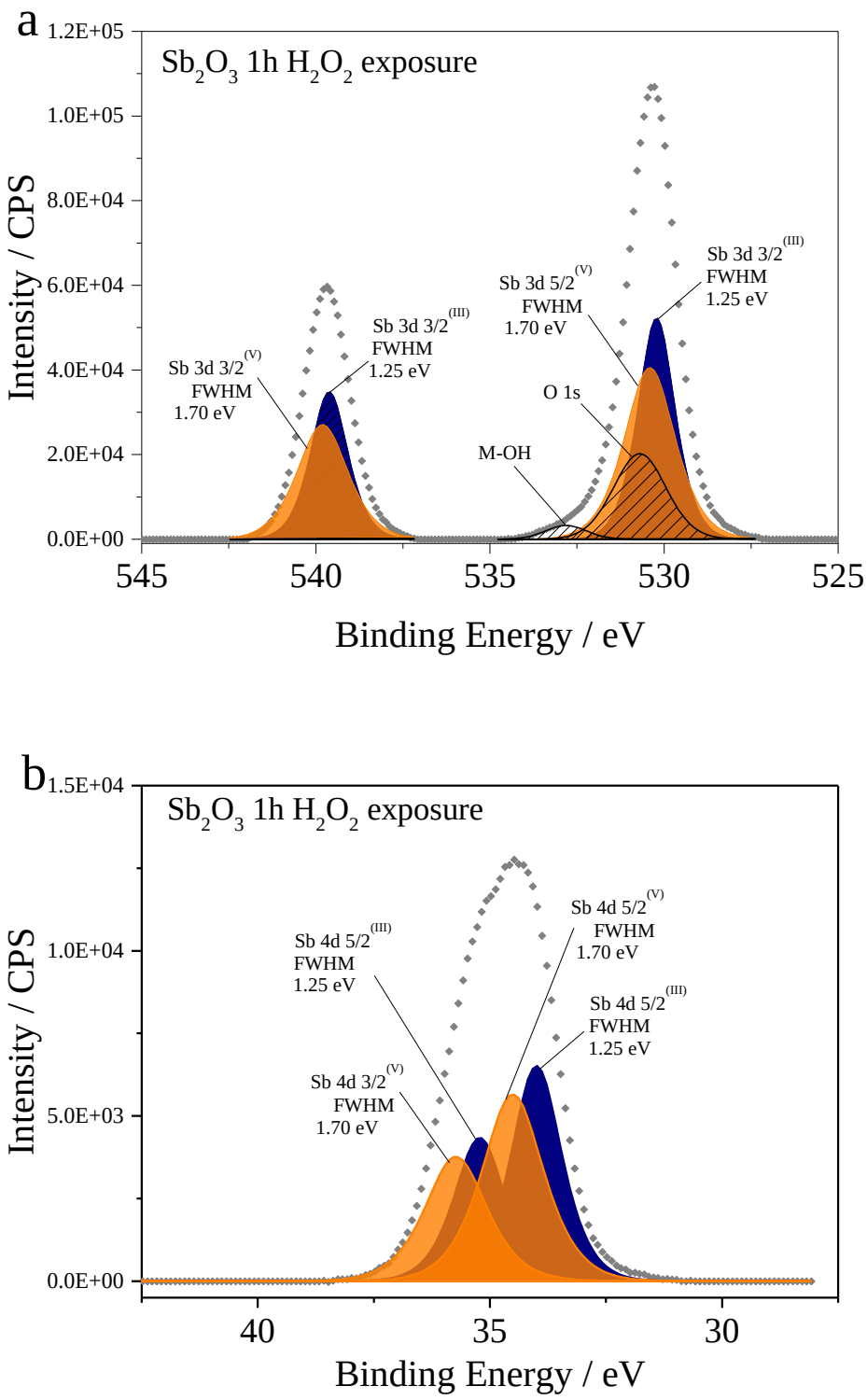

Figure 38: a) top O 1s / Sb 3d core line region of Sb_2O_3 and b) bottom Sb 4d core line region. Both spectra show samples after 1 hour of exposure to H_2O_2 modelled with Sb (III) (blue) and Sb (V) (orange) components of differing FWHM. O 1s and M-OH components can be seen in the 3d spectrum with black hatched lines.

Sample (Time_repeat)	Peak	Binding Energy (eV)	FWHM (eV)	Sb III/V Peak Shift (eV)	Residual (STD)	O 1s position (eV)
5m_1	$Sb^{(III)}$ $3d_{3/2}$	539.24	1.26	0.62	14.75	530.72
	$Sb^{(V)}$ $3d_{3/2}$	539.86	1.71			
	$Sb^{(III)}$ $3d_{5/2}$	529.84	1.26			
	$Sb^{(V)}$ $3d_{5/2}$	530.46	1.71			
5m_2	$Sb^{(III)}$ $3d_{3/2}$	539.46	1.26	0.41	13.15	530.88
	$Sb^{(V)}$ $3d_{3/2}$	539.87	1.71			
	$Sb^{(III)}$ $3d_{5/2}$	530.06	1.26			
	$Sb^{(V)}$ $3d_{5/2}$	530.47	1.71			
1h_1	$Sb^{(III)}$ $3d_{3/2}$	539.61	1.26	0.20	9.60	531.05
	$Sb^{(V)}$ $3d_{3/2}$	539.81	1.71			
	$Sb^{(III)}$ $3d_{5/2}$	530.21	1.26			
	$Sb^{(V)}$ $3d_{5/2}$	530.41	1.71			
1h_2	$Sb^{(III)}$ $3d_{3/2}$	539.61	1.26	0.50	10.85	531.09
	$Sb^{(V)}$ $3d_{3/2}$	540.11	1.71			
	$Sb^{(III)}$ $3d_{5/2}$	530.21	1.26			
	$Sb^{(V)}$ $3d_{5/2}$	530.71	1.71			
4h_1	$Sb^{(III)}$ $3d_{3/2}$	539.68	1.26	0.17	8.95	530.71
	$Sb^{(V)}$ $3d_{3/2}$	539.85	1.70			
	$Sb^{(III)}$ $3d_{5/2}$	530.28	1.26			
	$Sb^{(V)}$ $3d_{5/2}$	530.45	1.70			
4h_2	$Sb^{(III)}$ $3d_{3/2}$	539.72	1.26	0.17	9.86	531.06
	$Sb^{(V)}$ $3d_{3/2}$	539.95	1.71			
	$Sb^{(III)}$ $3d_{5/2}$	530.32	1.26			
	$Sb^{(V)}$ $3d_{5/2}$	530.55	1.71			
24h_1	$Sb^{(III)}$ $3d_{3/2}$	539.92	1.25	0.23	10.11	530.93
	$Sb^{(V)}$ $3d_{3/2}$	539.92	1.70			
	$Sb^{(III)}$ $3d_{5/2}$	530.52	1.25			
	$Sb^{(V)}$ $3d_{5/2}$	530.52	1.70			
24h_2	$Sb^{(III)}$ $3d_{3/2}$	539.55	1.23	0.35	2.84	531.23
	$Sb^{(V)}$ $3d_{3/2}$	539.9	1.70			
	$Sb^{(III)}$ $3d_{5/2}$	530.15	1.23			
	$Sb^{(V)}$ $3d_{5/2}$	530.50	1.70			

Table 10: Peak position, FWHM, Sb III/V peak shift, residual standard deviation and resultant O 1s position for Sb3d XPS spectra using model 2

Sample (Time_repeat)	Peak	Binding Energy (eV)	FWHM (eV)	Sb III/V Peak Shift (eV)	Residual (STD)
5m_1	$Sb^{(III)}$ $4d_{3/2}$	34.95	1.25	0.65	4.44
	$Sb^{(V)}$ $4d_{3/2}$	35.60	1.56		
	$Sb^{(III)}$ $4d_{5/2}$	33.72	1.25		
	$Sb^{(V)}$ $4d_{5/2}$	34.38	1.56		
5m_2	$Sb^{(III)}$ $4d_{3/2}$	35.05	1.23	0.53	3.46
	$Sb^{(V)}$ $4d_{3/2}$	35.62	1.56		
	$Sb^{(III)}$ $4d_{5/2}$	33.83	1.23		
	$Sb^{(V)}$ $4d_{5/2}$	34.40	1.56		
1h_1	$Sb^{(III)}$ $4d_{3/2}$	35.15	1.28	0.51	3.21
	$Sb^{(V)}$ $4d_{3/2}$	35.74	1.56		
	$Sb^{(III)}$ $4d_{5/2}$	33.94	1.28		
	$Sb^{(V)}$ $4d_{5/2}$	34.51	1.56		
1h_2	$Sb^{(III)}$ $4d_{3/2}$	35.17	1.28	0.56	3.50
	$Sb^{(V)}$ $4d_{3/2}$	35.78	1.56		
	$Sb^{(III)}$ $4d_{5/2}$	33.95	1.28		
	$Sb^{(V)}$ $4d_{5/2}$	34.56	1.56		
4h_1	$Sb^{(III)}$ $4d_{3/2}$	35.07	1.28	0.52	2.53
	$Sb^{(V)}$ $4d_{3/2}$	35.73	1.56		
	$Sb^{(III)}$ $4d_{5/2}$	33.85	1.28		
	$Sb^{(V)}$ $4d_{5/2}$	34.51	1.56		
4h_2	$Sb^{(III)}$ $4d_{3/2}$	35.17	1.28	0.52	3.28
	$Sb^{(V)}$ $4d_{3/2}$	35.83	1.56		
	$Sb^{(III)}$ $4d_{5/2}$	33.94	1.28		
	$Sb^{(V)}$ $4d_{5/2}$	34.6	1.56		
24h_1	$Sb^{(III)}$ $4d_{3/2}$	35.16	1.28	0.43	4.14
	$Sb^{(V)}$ $4d_{3/2}$	35.86	1.56		
	$Sb^{(III)}$ $4d_{5/2}$	33.93	1.28		
	$Sb^{(V)}$ $4d_{5/2}$	34.64	1.56		
24h_2	$Sb^{(III)}$ $4d_{3/2}$	35.37	1.21	0.58	1.61
	$Sb^{(V)}$ $4d_{3/2}$	35.95	1.55		
	$Sb^{(III)}$ $4d_{5/2}$	34.11	1.21		
	$Sb^{(V)}$ $4d_{5/2}$	34.69	1.55		

Table 11: Peak position, FWHM, Sb III/V peak shift and residual standard deviation for Sb4d XPS spectra using model 2

3.3 Conclusions

This investigation focussed on the differences between Sb_2O_5 and Sb_2O_3 and the use of XPS as a characterisation tool for Sb valence in oxide compounds. Since PXRD of the as-purchased powders revealed poor crystallinity and phase impurity in Sb_2O_5, a study of the oxidation of Sb_2O_3 by H_2O_2 was used to produce a sample oxidised to an Sb/O ratio of 0.4 (the theoretical Sb/O ratio for Sb_2O_5). XPS quantification of the elements present in Sb_2O_3 samples exposed to H_2O_2 for 5 minutes, 1 hour, 4 hours and 24 hours revealed an approximately logarithmic decrease in Sb/O ratio of the surface of the powders. Since XRD, a bulk analysis technique, of all samples showed single phase orthorhombic Sb_2O_3 it can be concluded that the oxidation observed through XPS is surface localised.

Reports in the literature raise the question of whether Sb XPS core line peak position and FWHM can be used as reliable indicators of the oxidation state of the ions. Some researchers postulate that the Sb $3d_{3/2}$ core line peak, which is not obstructed by the O 1s as its $^5/_2$ spin orbit pair is, increases in binding energy with Sb oxidation state and that peak broadening occurs in the spectra of mixed valence compounds, which could indicate the presence of two unresolved peaks. Contrary arguments that the observed increase in FWHM does not correlate with the proposed III-V chemical shift leave the XPS interpretation of Sb unclear. The data presented in this chapter show an increase in both Sb $3d_{3/2}$ photoelectron binding energy and peak FWHM. Furthermore, modelling of the 525 - 548 eV region (Sb 3d and O 1s core line XP spectra) revealed an increase in binding energy of the O 1s photoelectron as oxidation progressed.

The analyses performed on XPS data in this investigation relied upon the accurate determination of the proportion of Sb(III) and Sb(V) in each sample, in order to generate 'models' to account for Sb(III) and Sb(V) components under the Sb 3d and 4d core lines. It has been shown that the degree of oxidation can be modelled via valence band analysis using standard compounds. This analysis showed a trend of increasing % Sb_2O_5-like character with increasing time exposed to H_2O_2, which reflected the trend observed for Sb/O ratio; that as the oxidation progressed, Sb/O decreased and therefore the percentage of Sb_2O_5* contribution to the valence band increased. While all care was taken to ensure that the OH contribution to the O-environment peak was minimal, further systematic drying of the samples could be performed in corroborative experiments. In order to ensure that the oxidation reaction is not augmented by the drying process this could be completed at temperature (~ 80 ˚C), in an inert atmosphere (N_2, Ar).

Both Sb 3d and 4d core lines were fitted to account for Sb (III) and Sb (V) environments, in the proportions determined from the valence band analysis described above. Two fits were generated for each sample, one where the FWHM values were constrained to be the same as each other (those of the as-purchased Sb_2O_3) and one where the FWHM values were constrained to be $Sb(III)_{FWHM}$ = FWHM of core lines from Sb_2O_3 ("equal FWHM") and $Sb(V)_{FWHM}$ = FWHM of core lines from Sb_2O_5* ("unequal FWHM"). It would be expected that a genuine III-V chemical shift would be approximately constant across the samples, if either of these interpretations were correct. However, all analyses produced III-V peak shifts that differed by >0.15 eV. Additionally, it would be expected that O 1s position would remain constant if these interpretations were correct. However, both models (equal FWHM and unequal FWHM) result in an increase in O 1s photoelectron binding energy as oxidation progresses.

The combination of inconsistent Sb III-V peak shift and the increase in O 1s photoelectron binding energy for both equal and unequal FWHM models leads to the conclusion that neither analysis is a correct interpretation of these data. Thus the conclusion must be that a one-component model for Sb ions is most appropriate and that there is no resolvable III-V chemical shift between Sb (III) and Sb (V) ions in mixed valence oxide compounds; it is likely that the chemical shift is too small to accurately observe. Well-defined separation has been recorded for mixed valence compounds of different composition, for example the Cs_2SbCl_6 studies reported in the introduction to this chapter, where the Sb ions differ in oxidation state but are crystallographically identical. By comparison in Sb_2O_x samples Sb ions of different oxidation state are not crystallographically identical. These differences indicate that the identity of nearest neighbours and coordination environment has a discernible influence on the polarisability of the Sb ions and therefore the binding energy of Sb (III) and Sb (V) core electrons.

The observed increases in Sb FWHM and Sb 3d, 4d and O 1s photoelectron binding energy must still be accounted for. Changes in FWHM can be caused by a number of factors such as X-ray line width, charging, core-hole lifetime, or by differences in the background used for modelling.[101, 102] For the analyses described in this chapter X-ray line width, charging and differences in background can be discounted as causes of peak broadening due to the use of monochromatic X-rays, a flood gun for charge compensation and consistent use of a Shirley background for fitting, respectively. Thus a likely cause of the changes in FWHM between samples could be differences in the core-hole lifetimes generated by photoexcitation. Core hole lifetime, τ, is related to FWHM by Equation 40 below.

$$FWHM \propto \frac{h}{\tau} \qquad (h = Planck's\ constant)$$

Equation 40

Thus when core-hole lifetime decreases, the peak is broadens. It is possible that core holes generated in Sb_2O_5 have a shorter lifetime and therefore result in the broader peaks observed throughout the study and in other literature. Mixed valence compounds would appear to have intermediate FWHM due to a small number of Sb (V) ions with a shorter core hole lifetime causing some broadening of these peaks.

Changes in the O 1s binding energy are consistent across all interpretations of the data. Since it is known that metal oxide O 1s binding energies fall within a narrow range[152-154], the differences in these samples are only the relative compositions of Sb_2O_3 and Sb_2O_5. It is possible that the Fermi level of the two materials lie at different energies and therefore the Fermi level of the mixture is changing in energy as oxidation progresses. Since E_f in XPS is calibrated as 0 eV this explanation would account for the apparent change in O 1s photoelectron binding energy. This would also account for the identical change in Sb photoelectron binding energy, which was also observed.

It can be concluded that changes to the peak position and FWHM in Sb XP spectra cannot be attributed to changes in oxidation state and that the spectra should be fitted with just one component to account for both the (III) and (V) ions. Further investigation could be undertaken into the exact reasons behind the apparent changes in peak position, which could be caused by a change in Fermi level as oxidation occurs. In light of the results from this chapter, further Sb analyses in this thesis were completed using a one-component model for all Sb contributions.

Chapter 4: Investigation of the effects of Sb codoping on the electronic structure of Rh:TiO_2

4.1 Introduction

Despite decades of intensive research, there is currently no single-phase material, which is capable of efficient overall water splitting using only pure water and sunlight. Doping, as explored in Chapter 1, has been a widely researched method of altering the properties of materials that have shown initial photocatalytic promise but whose applications under light of wavelengths >400 nm (i.e. non-UV) are limited. Noble metal doping in titanate semiconductor materials has been an area of interest for a number of years, with much research indicating that these materials produce a visible light response, but may not be ideally electronically aligned for efficient overall water splitting.

An alternative to single material catalysts is to combine materials, forming a heterojunction in order that photoexcited electrons and holes can be separated by migrating across the junction according to the relative energies of the valence and conduction bands of the materials. A notable type of heterojunction currently receiving much attention is the Z-scheme (outlined comprehensively in Chapter 1), a mechanism that mimics biological photosynthesis and is based on two photosystems. This approach also allows for a wider variety of materials to be utilised, since the band gaps of the individual materials do not need to straddle the redox potentials of the reaction to be catalysed. Instead, one material with band edges aligned to catalyse oxidation and another to catalyse reduction can be utilised. Hence, materials with narrower band gaps than the redox potential of the reaction can be considered and visible light activity can be easier to achieve. When selecting materials to combine to form a water splitting Z-scheme it is necessary to consider how the band edges of the two materials align with each other and the redox potentials of water. This can be achieved by comparing the band edges relative to the Fermi level (E_F) for each material. To date, materials that naturally exhibit band edges at appropriate offsets have been used to construct Z-schemes, for example, Ta_3N_5/TaON.

Expanding the functionality of well characterised materials, such as TiO_2, to be used in a Z-scheme has proven an interesting line of research, and many studies focus on the titanates as

a starting point for construction of more complex systems. Simplistic mono-ionic doping regimes are being discarded in favour of more complex doping regimes, which may prove necessary in order to achieve efficient visible light photocatalysis. TiO_2 and other titanates doped with two or more ions together have been studied. The greater complexity afforded by using multiple dopants offers opportunities for fine tuning of electronic, optical and chemical properties that may lead to the desired visible light active catalysts and requires a more detailed understanding of the physical and chemical effects of the dopants on the host material.

In this chapter a better understanding of the effects of a complex doping regime on the properties of TiO_2 is sought. Rh/Sb codoped TiO_2 and related titanates, such as $Y_2Ti_2O_7$, $SrTiO_3$ and $BaTiO_3$, have been recently developed as effective photocatalysts, both as single phase materials and as part of a Z-scheme. A summary of the findings of various studies can be found in Table 12. Domen et al. produced a Z-scheme combining Ta_3N_5 and Rh doped $SrTiO_3$, achieving visible light water splitting, with H_2 evolution at rates of up to 48 μmol $h^{-1}g^{-1}$, when loaded with an Ir co-catalyst. Rosseinsky and co-workers have achieved >7 μmol $h^{-1}g^{-1}$ O_2 evolution using visible light over a Rh-doped $Y_2Ti_2O_7$ catalyst. Kudo and co-workers reported visible light photoactivity of Rh and Sb codoped TiO_2 (where Sb/Rh ratios of 0, 0.5, 1, 2 and 3 were investigated) and showed that, with Sb/Rh ≥ 2, O_2 evolution exceeds 16 μmol h^{-1}. Their Sb/Rh doped $SrTiO_3$ system has also achieved sacrificial O_2 and H_2 evolution under visible light.

Author	Materials Used	Co-catalyst	Gas evolution	
Domen[155]	$LaRh:SrTiO_3$	Ru	H_2	48 μmol $h^{-1}g^{-1}$
	Ta_3N_5	Ir/CoO_x	O_2	24 μmol h^{-1} g^{-1}
Kudo[156]	$Rh:SrTiO_3$	Pt	H_2	52 μmol h^{-1} g^{-1}
	$RhSb:SrTiO_3$	IrO_x	O_2	42 μmol h^{-1} g^{-1}
Rosseinsky[157]	$Rh:Y_2Ti_2O_7$	none	O_2	7.2 μmol h^{-1} g^{-1}
Asai[158]	$Rh:SrTiO_3$	Pt	H_2	3.4 μmol h^{-1} g^{-1}
	$RhSb:SrTiO_3$	IrO_x	O_2	1.5 μmol h^{-1} g^{-1}
Nishiro[159]	$RhSb:TiO_2$	none	H_2	16.9 μmol h^{-1} g^{-1}
	$RhSb:TiO_2$	none	O_2	6 μmol h^{-1} g^{-1}

Table 12: Gas evolution data for doped titanate photocatalysts

Doping TiO_2 with Rh ions introduces 4d t_{2g} states into the band gap, as has been shown in studies by Kitano and Oropeza.[160, 161] The oxidation state of the Rh dopant naturally influences the occupancy of the Rh 4d states. It has been found that Rh^{4+} is the most stable oxidation state of dopant ions, presumably in order to maintain overall charge neutrality when substitutionally inserted onto the Ti^{4+} cation site. A schematic representation of the effect of Rh doping and

Sb/Rh codoping on TiO_2 is shown in Figure 39. Since Rh^{4+} possesses a partially filled 4d t^5_{2g} energy level, the inclusion of this ion causes the Fermi level to be positioned at a lower energy than that of pristine TiO_2 presumably diminishing the photocatalytic activity of TiO_2 for H_2 production. Codoping with Sb (V) increases the number of electrons in the system and allows t^5_{2g} Rh (III) to exist in the system. The resultant material, codoped with Sb (V) and Rh (III) retains the n-type character of pristine TiO_2.[161]

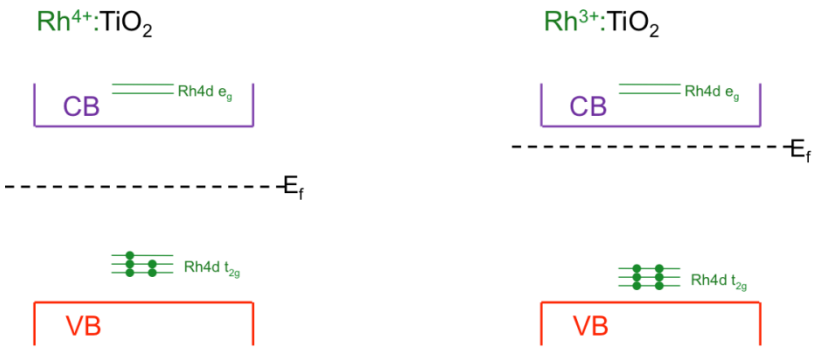

Figure 39: Schematic band diagram showing the change in Fermi level energy between Rh (III) and Rh (IV) doped TiO_2

This chapter describes the extensive characterisation of rhodium and antimony codoped TiO_2 in powder and single crystal forms, the synthesis of which were described in detail in Chapter 2. Doped powders were made via SSR of TiO_2 and the appropriate molar amount of Rh_2O_3 followed by further SSR of TiO_2:Rh[X%] with the appropriate molar amount of Sb_2O_3. The amounts of dopant ion were 1, 3, 5, 7 and 9 molar % for singly doped TiO_2:Rh. In codoped samples the Rh mole % was held at 5 % and the Sb mole % varied from 1-9 % in 2 % increments. The samples were loaded with high amounts of dopant ions in order to exaggerate the electronic properties of these materials, in order that their electronic structure can be fully analysed and understood. All samples were analysed by XRD, XAS, XPS, UV-Vis spectroscopy, SEM, WDS, and TAS.

4.2 Results and Discussion

4.2.1 X-ray Diffraction

4.2.1.1 Phase Identification- TiO_2 starting material and TiO_2 control

PXRD of the TiO_2 rutile starting material used revealed that a small proportion of TiO_2 was present in the anatase phase. However, since the anatase structure is only stable to temperatures of around 600 ˚C [162], this phase impurity was eliminated in the synthesis process. A control sample of TiO_2 rutile fired at 1100 ˚C for 10 hours, with no dopants, was prepared in order to distinguish between the effects of heating and the effects of doping. PXRD patterns of the starting material and control sample are shown in Figure 40; anatase diffraction peaks have been marked with a *.

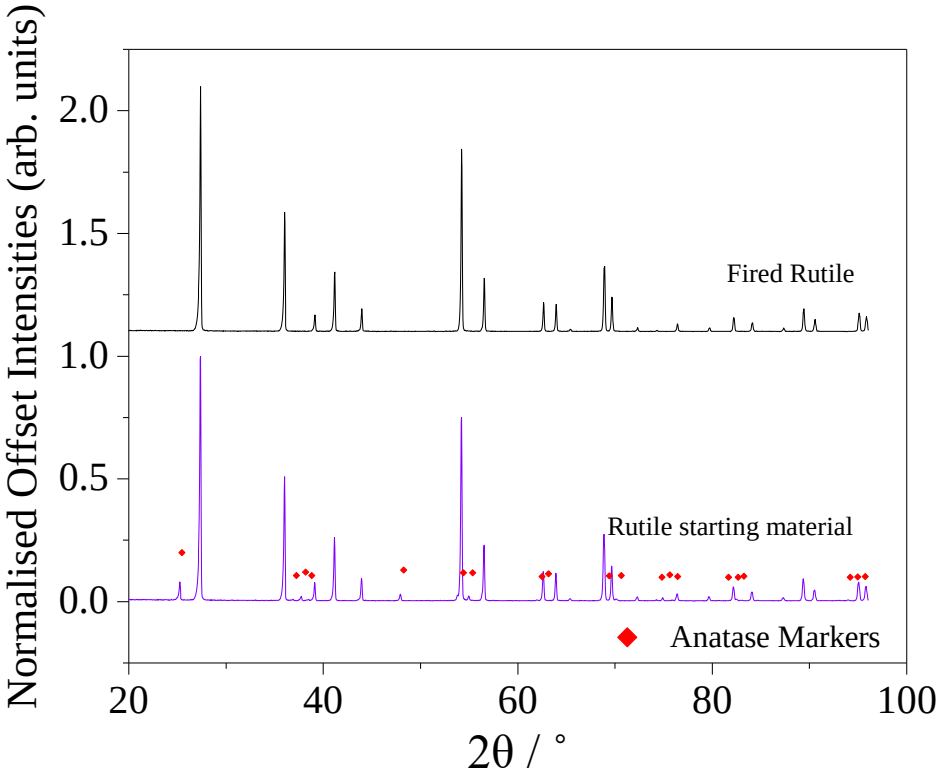

Figure 40: PXRD patterns of as purchased rutile starting material (purple line, bottom pattern) and the same material after 10h calcination at 1100 ˚C (“fired rutile”, black line, top pattern). Bragg angles correlating to the anatase phase are marked in red.

Both patterns were recorded on a Bruker STOE film diffractometer using Mo radiation (λ = 0.709 Å), though the data have been transformed for ease of comparison with other PXRD patterns which were recorded on a Bruker D4 powder diffractometer using Cu radiation (λ = 1.541 Å). Both patterns exhibit asymmetric line shapes, a characteristic which could be caused by crystallite shape effects or instrumental factors.[163] Since the asymmetry appears the be

identical in each, this is likely to be due to instrumental factors and can be disregarded in relation to the current analysis.

The peaks of both patterns align well, with no easily discernible peak shift. In order to quantify any differences, least squares refinement was completed to determine the cell parameters and cell volume. For this, both patterns were indexed in the rutile structure, with the anatase peaks in the pattern of the starting material omitted. The cell volumes of rutile phases were highly comparable, at 62.12 $Å^3$ for the control sample and 62.18 $Å^3$ for the starting material, indicating that heating alone brings about no structural changes. Peak widths are approximately the same between the patterns with a small decrease after heating. Although it is known that diffraction peak width is inversely proportional to crystallite size from the Scherrer equation (shown in Equation 41 below), use of this relation to estimate crystallite size becomes inapplicable when crystallites are greater than nano-scaled. At the micron scale (and above) factors such as dislocation, grain surface boundaries and other microstrain effects override the influence of particle size and peak width.[164]

τ = peak width,
β = crystallite size,
λ = X-ray wavelength,
θ = Bragg angle

$$\tau = \frac{\lambda}{\beta cos\theta}$$

Equation 41

To determine the crystallite size distribution, morphology and other physical characteristics of the doped samples, electron microscopy was employed and these results are discussed in section 4.2.3 of this chapter.

4.2.1.2 Phase Identification- Rh-doped Samples

PXRD patterns of TiO_2:[RhX%] powders (X = 1, 3, 5, 7 and 9) confirmed single phase TiO_2 rutile (tetragonal, $P4_{2/mnm}$) structure, with no discernible peaks indicating any Rh_2O_3, Sb_2O_3 starting material phases or other additional phases after 10 hours of calcination. Figure 41 shows the XRD patterns for these Rh doped samples in comparison to a pattern of the TiO_2 control sample.

It is reasonable to assume that due to the long reaction times and high reaction temperatures undertaken for the synthesis of these samples, a degree of particle agglomeration and growth will occur in the process. Any preferred orientation growth would result in an increase in intensity of peaks indexed to the growth orientation. In all samples the peak intensity ratios remain constant and therefore it can be concluded that growth occurs in a homogenous manner.

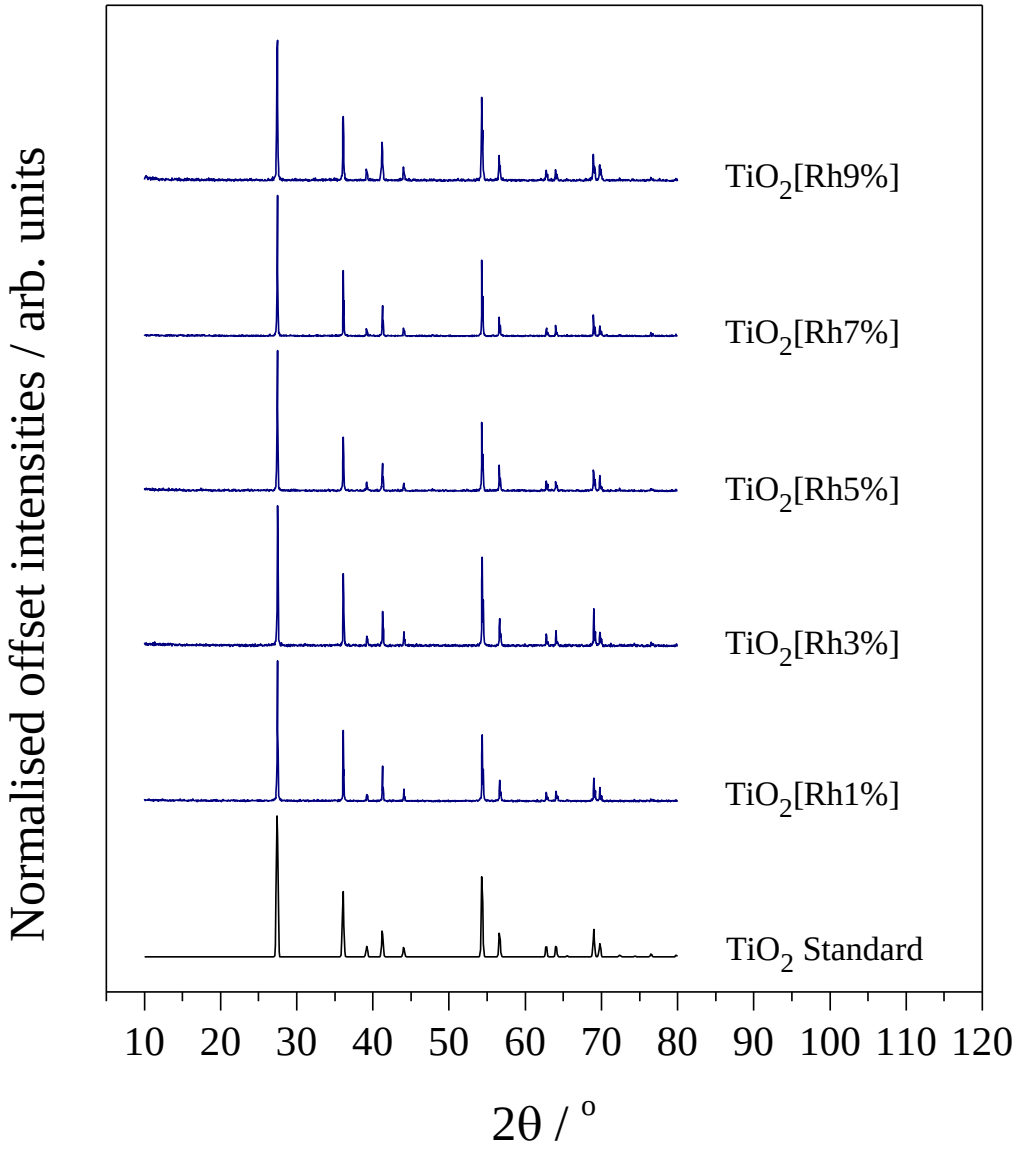

Figure 41: XRD patterns of TiO_2 doped with varying % Rh (1, 3, 5, 7 and 9 %) by comparison with a standard TiO_2 pattern

4.2.1.3 Phase Identification- Sb/Rh Codoped Samples

Figure 42 shows XRD patterns of antimony and rhodium codoped TiO_2 samples TiO_2:[Rh5%][SbY%] powders (Y = 1, 3, 5, 7 and 9) compared with TiO_2 control sample. With the exception of Y = 9, all codoped samples showed no impurity peaks after 10 hours of calcination, and so were assigned as theTiO_2 rutile- tetragonal structure, P 4_2 mnm. Again, the peak intensity ratios appear to be constant, indicating homogenous particle growth.

Figure 43 shows more clearly TiO_2[Rh5%][Sb9%] after one calcination at 1100 ˚C for 10h, where peaks not indexed in the TiO_2 rutile phase are marked with a *. Also shown is the same sample after a second calcination also at 1100 ˚C for a further 10 h (total calcination 20

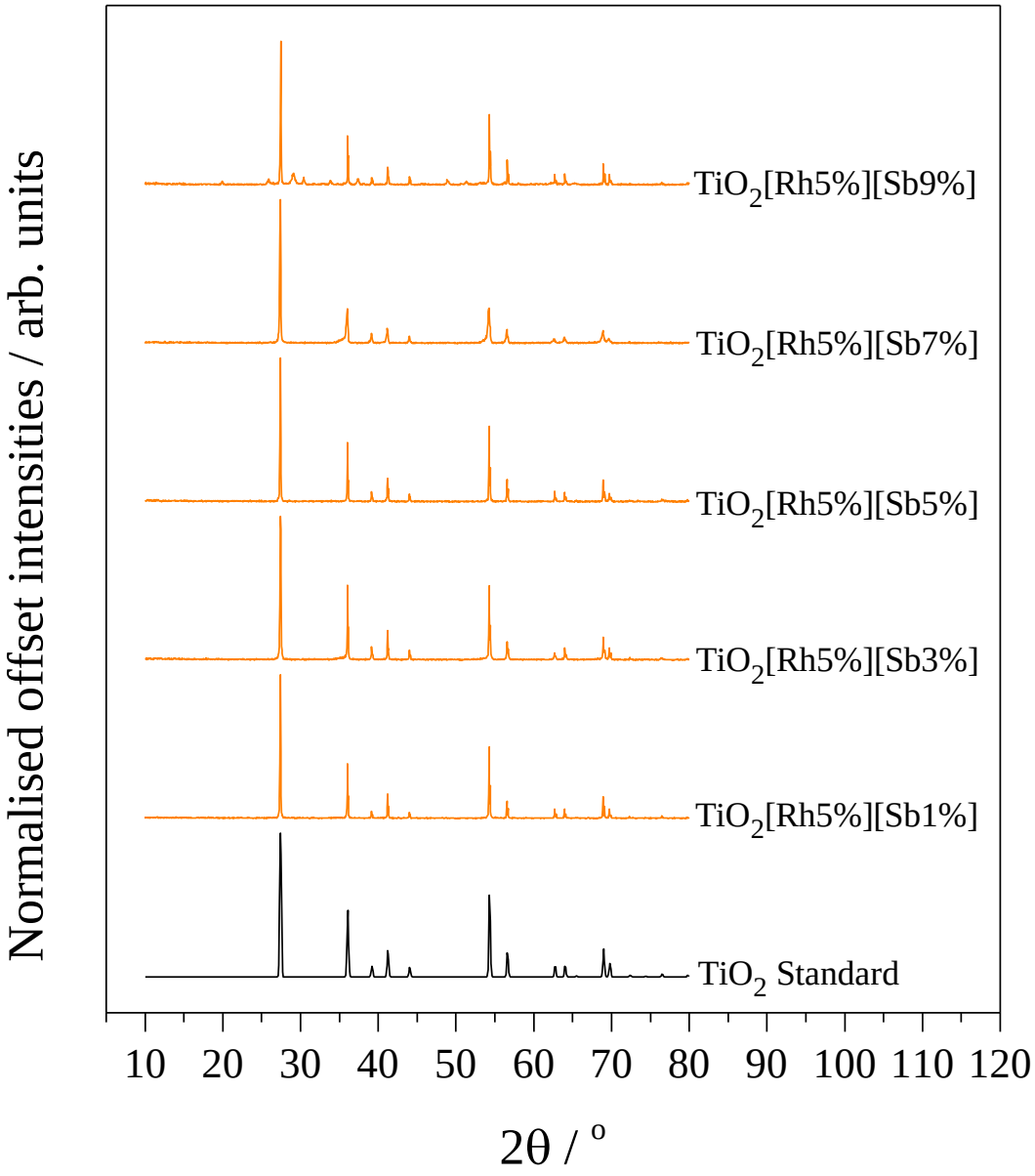

Figure 42: XRD patterns of TiO_2 doped with 5% Rh and varying % Sb (1, 3, 5, 7 and 9 %) by comparison with a standard TiO_2 pattern

h). The additional peaks present after 10 h of calcination had completely disappeared after 20 h; these impurity peaks were compared with PXRD patterns of Rh_2O_3 and other possible Sb-oxide phases. No peaks associated with Rh_2O_3 were found to match the positions of the impurity peaks.

Table 13 lists the angles at which impurity peaks were observed in TiO_2[Rh5%][Sb9%] and the indices of the peaks from Sb-oxide patterns that also appear at these angles. The majority of the peaks can be indexed to the Sb_2O_4 (base-centred monoclinic, C12/c1) structure[4] and in particular the presence of a peak at 26 °, corresponding to the (111) plane, indicates the presence of this phase since this reflection is the only reflection observed in Sb_2O_4 which is

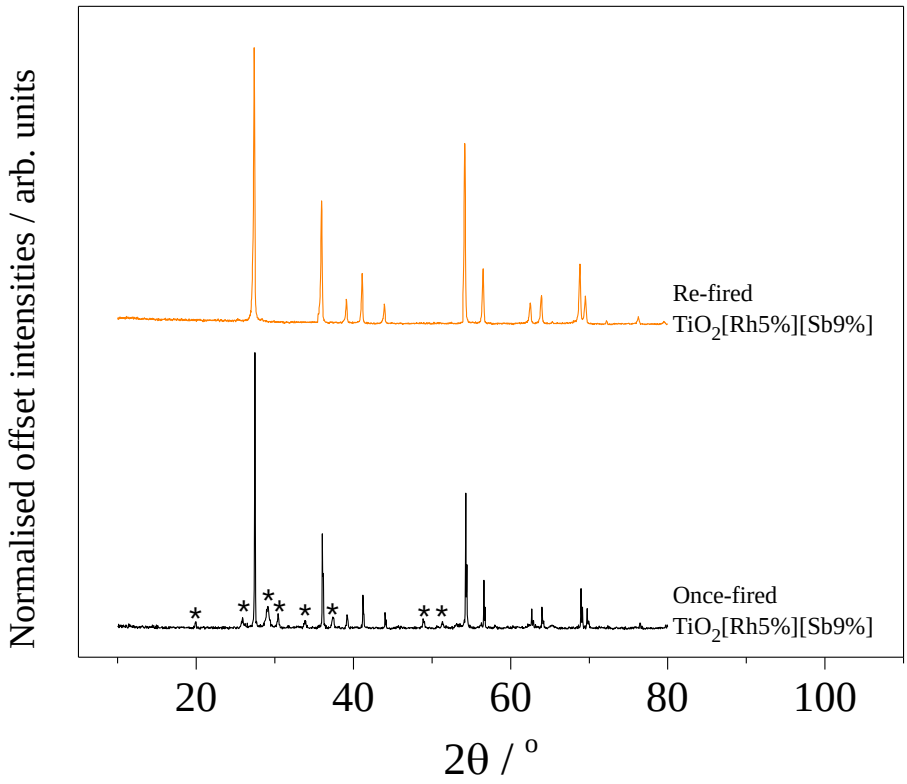

Figure 43: TiO_2[Rh5%][Sb9%] fired once (bottom pattern) and fired twice (top pattern) for 10 hours at 1100 °C each time

not also observed in the pattern of Sb_2O_5. However, due to the similarity in symmetry of monoclinic Sb_2O_4 and monoclinic Sb_2O_5 (both space group C12/c1) and thus the similarity of the PXRD patterns produced [4, 5], the presence of Sb_2O_5 cannot be entirely ruled out. Again, the similar peak ratios indicate no preferential growth orientation in the codoped samples.

Reflection observed 2θ (°)	Possible Sb_xO_y index		
	Sb_2O_5	Sb_2O_4	Sb_2O_3
20	(110)	(011)	
26		(111)	(222)
29	(400)	(112)	
30	(31-1)	(004)	
34	(20-2)	(113)	
37	(020)	(020)	
49	(42-1)	(024)	
51	(22-1)	(221) (205)	

Table 13: Impurity peak angles for sample TiO_2[Rh5%][Sb9%] and possible Sb_2O_x reflections to which they could correlate

4.2.1.4 Lattice Parameters

All PXRD patterns of single phase materials were indexed in the rutile structure from standard pattern 9161 of the Inorganic Crystal Structure Database (ICSD) [3] and least squares refinement completed to determine the lattice parameters (a and c) and the cell volume (V). These results are discussed below.

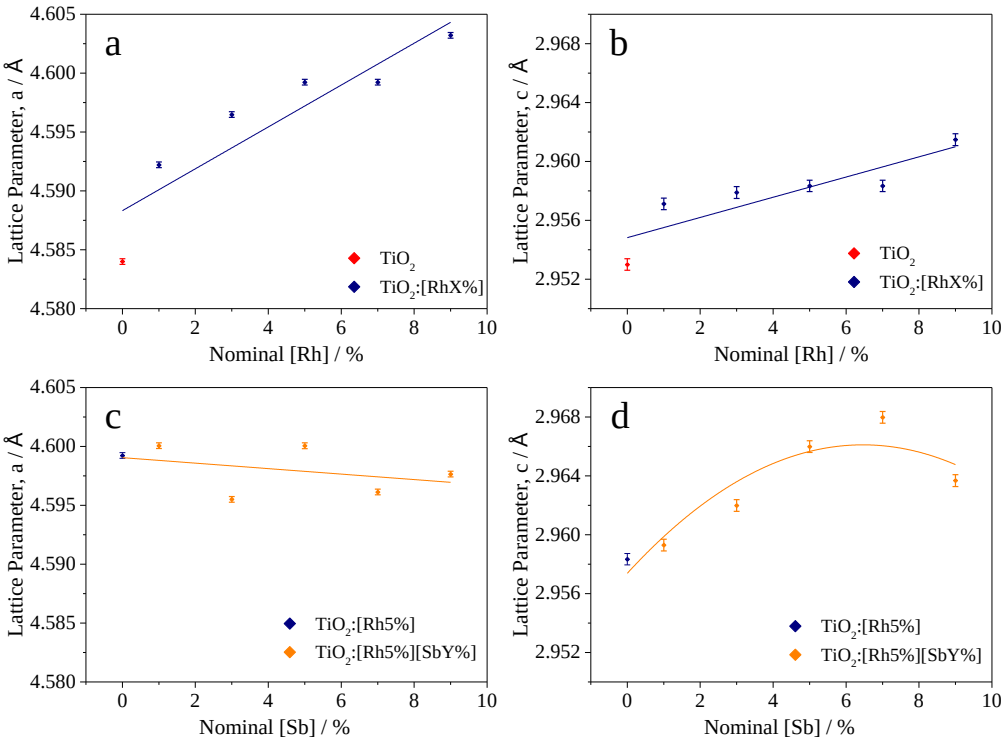

Figure 44: Comparison of lattice parameters for undoped TiO_2 (red) and a) Rh doped TiO_2 lattice parameter a, b) Rh doped TiO_2 lattice parameter c, c) Rh/Sb codoped TiO_2 lattice parameter a and d) Rh/Sb codoped TiO_2 lattice parameter c

Comparison of the lattice parameters of TiO_2:[RhX%] powders (X = 1, 3, 5, 7 and 9) in Figure 44a and b shows an approximately linear increase in both lattice parameter a and c as Rh loading increases. The trend is slightly more pronounced in the a-direction where a maximum ~0.4% increase from standard TiO_2 is observed, than in the c-direction where a maximum ~0.3 % increase is observed.

In codoped samples where TiO_2 is doped with a constant concentration of Rh (5 %) and varied Sb concentration (1, 3, 5, 7, 9 %) the a-parameter (Figure 44c) shows no definitive trend, though a line of best fit indicates a small overall decrease. The c-parameter increases up to 7 % Sb loading, but decreases above this.

As indicated by the small increases in a and c lattice parameters shown above, there is minimal overall increase in cell volume, shown in Figure 45, which implies a substitutional doping

regime of Rh and Sb onto the Ti site. The largest doped cell volume is 62.75 $Å^3$ for TiO_2:[Rh5%][Sb5%] compared with 62.12 $Å^3$ for pristine TiO_2. However, trends can be clearly observed in both series of samples, whereby the cell volume increases linearly for Rh-doped samples and increases to equimolar dopant concentration in Rh/Sb codoped TiO_2, decreasing slightly at higher Sb doping regimes.

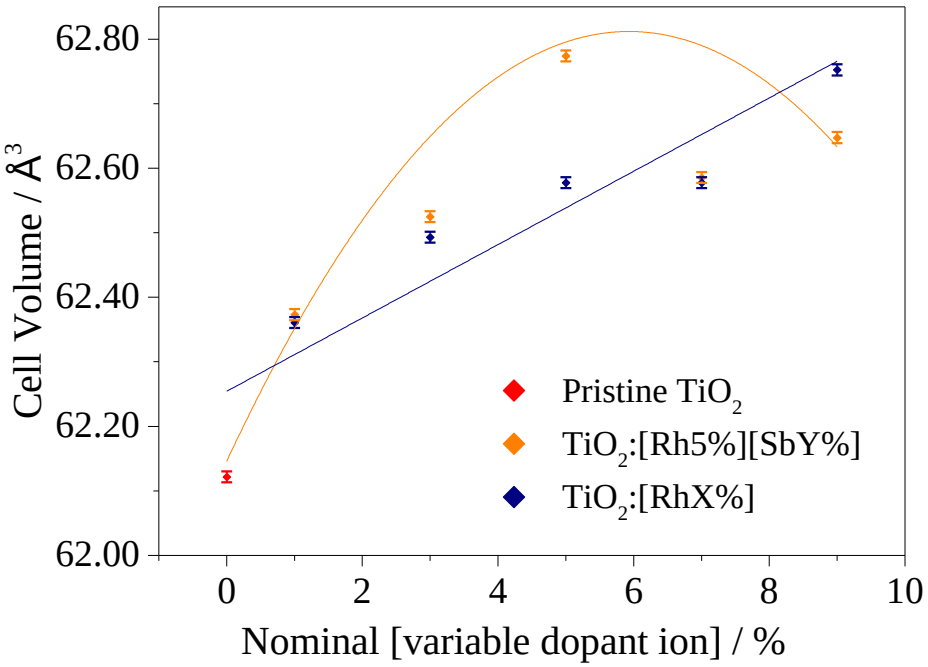

Figure 45: Cell volumes of both Rh and Rh/Sb codoped TiO_2 by comparison with undoped TiO_2

Comparison of the ionic radii of the cations in this system and correlation of these with the observed changes in cell volume allow some explanations to be made regarding the likely oxidation states of the dopant ions. Rh^{4+} and Ti^{4+} have similar ionic radii at 0.600 Å and 0.605 Å, respectively. Since Rh^{3+} has an ionic radius of 0.665 Å, the observed increase in lattice parameter implies that in Rh-doped samples, Rh^{3+} may be present as well as Rh^{4+}. The cell volumes are similar for 3, 5 and 7 % Rh doping, suggesting that Rh is being introduced to the system as Rh^{4+}, which has a radius of similar size to Ti^{4+} that it is substituting. However at 9 % Rh-doping, the cell volume again increases indicating a possible further increase in the amount of Rh^{3+}. An alternative explanation could be that doping is not entirely substitutional. At high Rh doping regimes, a small number of Rh^{4+} ions could reside interstitially, causing a more pronounced increase in lattice parameters.

In codoped samples, both a and c parameters were shown to increase as nominal [Sb] increases up to 5% Sb doping and then decreased above equimolar dopants; this is reflected in the cell volume trend (Figure 45). The addition of Sb^{5+}, which has an ionic radius of 0.600 Å and therefore shouldn't cause lattice expansion, is thought to encourage formation of Rh^{3+} in TiO_2

and so an expansion above that of 5% Rh-doped samples is expected. This is true at [Sb] ≥ 3 %, indicating that the Sb/Rh ratio must be at least 0.6 in order to achieve Rh^{3+} concentration greater than that achieved from Rh doping alone. At high Sb loading (i.e. 9%), a decrease in cell volume is observed. It is likely that the presence of Sb^{5+} in these concentrations is accompanied by oxygen defects in the lattice, which could account for this slight decrease.

It must also be considered that the additional increases in cell volume due to the addition of Sb in the +3 oxidation state, which has an ionic radius of 0.76 Å. As evaluated experimentally in Chapter 3 of this thesis, it is not possible to distinguish between Sb ions in the +3 and +5 oxidation state using XPS and so a selection of Sb/Rh doped samples were examined using X-ray absorption spectroscopy at both Diamond Lightsource and the European Synchrotron Radiation Facility. The results are discussed in section 4.2.2 below.

4.2.2 X-ray Absorption Spectroscopy

Selected samples (TiO_2:[Rh5%], TiO_2[Rh5%][Sb1%], TiO_2[Rh5%][Sb3%], TiO_2[Rh5%][Sb5%]) were analysed using X-ray absorption spectroscopy to determine the oxidation state (XANES) and environment (EXAFS) of the dopant ions. These measurements and the subsequent data analysis were completed with the assistance and supervision of Professor Gopinathan Sankar.

Rh K-edge X-ray absorption near edge structure (XANES) data for Rh_2O_3, Rh-metal, and doped samples TiO_2:Rh[5%], TiO_2:Rh[5%]Sb[1%], TiO_2:Rh[5%]Sb[3%] and TiO_2:Rh[5%]Sb[5%] are shown in Figure 46. The XANES edge jump, from low absorbance to high absorbance, is caused by the absorption of an X-ray exciting a core electron in the element of choice. The edge jump position on the x-axis (energy) can therefore be correlated to the element's oxidation state, since the binding energy of the excited electron will change dependent on its parent ion's oxidation state. By comparing the positions of the Rh K-edges to standard compounds Rh_2O_3 and Rh metal, where Rh has a +3 and neutral charge respectively, information pertaining to the oxidation state of the dopant ions can be inferred. Figure 46b shows an inset of the Rh K-edge clearly indicating that all doped samples resemble Rh (III) more than Rh^0, as would be expected. All Rh K-edge energies are lower than that of Rh_2O_3; it appears that the different Rh environments cause minor differences in the K-edge energy; in Rh_2O_3 the only other ions interacting with Rh are O^{2-} nearest neighbours and Rh^{3+} next-nearest neighbours, whereas in doped TiO_2 there are Ti^{4+}, O^{2-}, Rh^{x+} and Sb^{5+} in the system. It is unlikely, for example, that these results are indicating the presence of highly unstable Rh^+ or Rh^{2+} ions in the doped materials. However,

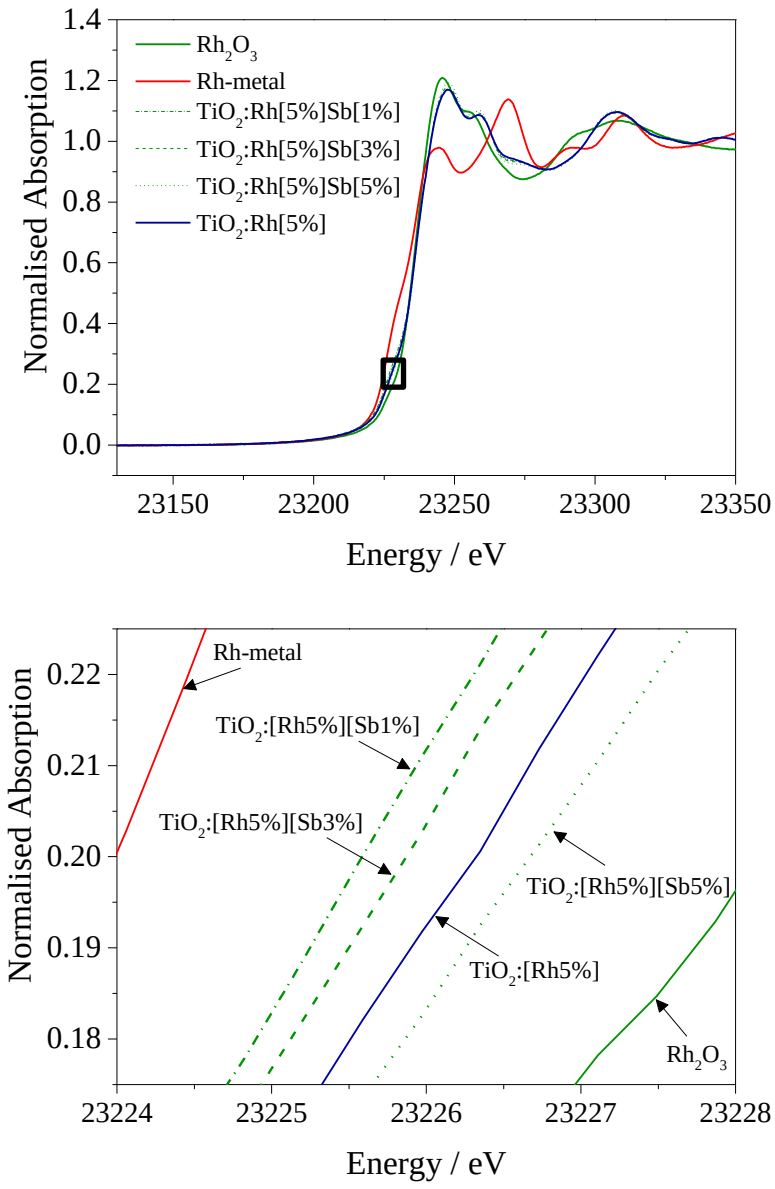

Figure 46: a) Rh X-ray absorption spectrum of Rh_2O_3 and Rh metal compared with TiO_2:[Rh5%], TiO_2:[Rh5%][Sb1%], TiO_2:[Rh5%][Sb3%] and TiO_2:[Rh5%][Sb5%] and b) close up of the Rh k-edge between 23224 and 23228 eV

importantly it can be seen in codoped compounds, which are comparable, that there is variance across the different doping regimes; as Sb doping increases the Rh K-edge increases in energy, indicating that Rh is oxidised by the presence of Sb. The necessity for Sb/Rh to be at least equimolar in order to ensure [Rh^{3+}] greater than that of Rh doping alone is also confirmed since only the TiO_2:[Rh5%][Sb5%] Rh K-edge lies above that of TiO_2:[Rh5%].

The EXAFS Fourier transform of TiO_2:Rh[5%] measured at the Rh K-edge is shown in Figure 47 along with TiO_2 (measured at the Ti edge) and Rh_2O_3 (also measured at the Rh K-

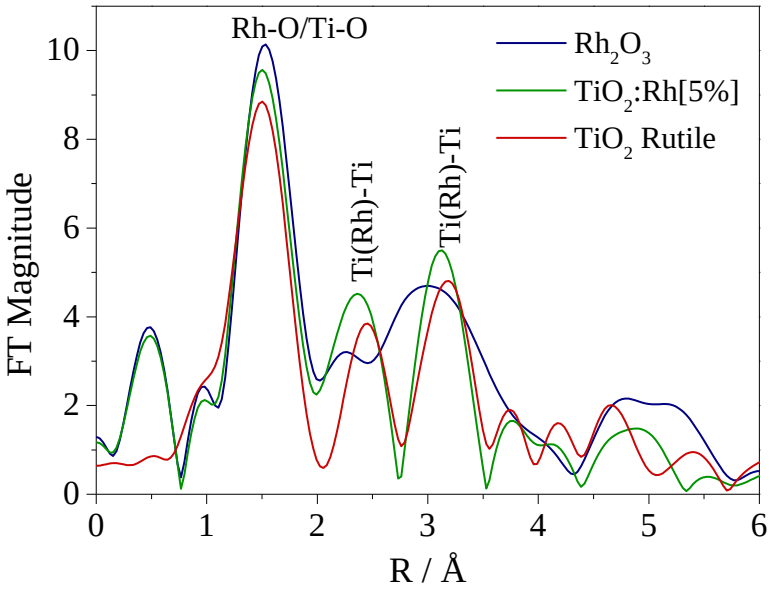

Figure 47: EXAFS Fourier transform of Rh_2O_3, TiO_2:[Rh5%] and TiO2 rutile

edge). From these data the bond distances between nearest neighbours and next-nearest neighbours can be approximated. Peaks have been labelled with the bonds to which they correlate- it should be noted that the data in this figure have not been corrected for phase shift and therefore bond distances appear short (nearest neighbour ~1.5 and next nearest neighbour ~ 2.3-3.5). A more detailed analysis of the Rh K-edge EXAFS data indicates Rh-O distance of ca. 2.0 Å, which is similar to the bond distances in Rh_2O_3. This could indicate substitutional doping of Rh^{3+} onto the Ti^{4+} site, with a longer bond distance due to the higher ionic radius, or the presence of a Rh_2O_3 phase. However, further convincing evidence for Rh^{3+} substitution onto the Ti^{4+} site comes from next nearest neighbour bond distances. Ti-Ti distances in TiO_2 are 2.96, 3.4 and 3.6 Å, whereas in Rh_2O_3 Rh-Rh distance are 2.72, 2.99 and 3.52 Å. Comparing these Fourier transforms, it appears that the Rh-Ti distances are similar to those observed for the TiO_2 structure rather than the Rh_2O_3 structure. Therefore it can be concluded that Rh ions are in fact substituted onto the Ti^{4+} site and that there is no secondary Rh_2O_3 phase.

The Sb K-edge data along with Sb_2O_3 and Sb_2O_5 standard samples are shown in Figure 48, where it can be seen that all doped sample edge jumps align with Sb_2O_5 much more than Sb_2O_3. The edge data indicate that the Sb ions in doped samples are in the +5 oxidation state, rather than the +3 oxidation state. This example is clearer than the Rh data, where a Rh^{4+} standard compound was not available for comparison of the edge positions.

The Sb edge EXAFS Fourier transform data for doped samples TiO2:Rh[5%]Sb[1%], TiO2:Rh [5%]Sb[3%] and TiO2:Rh[5%]Sb[5%], Sb_2O_3, Sb_2O_5 and comparable Ti edge data for TiO_2 are shown in Figure 49. These data demonstrate the lack of a distinct position of Sb

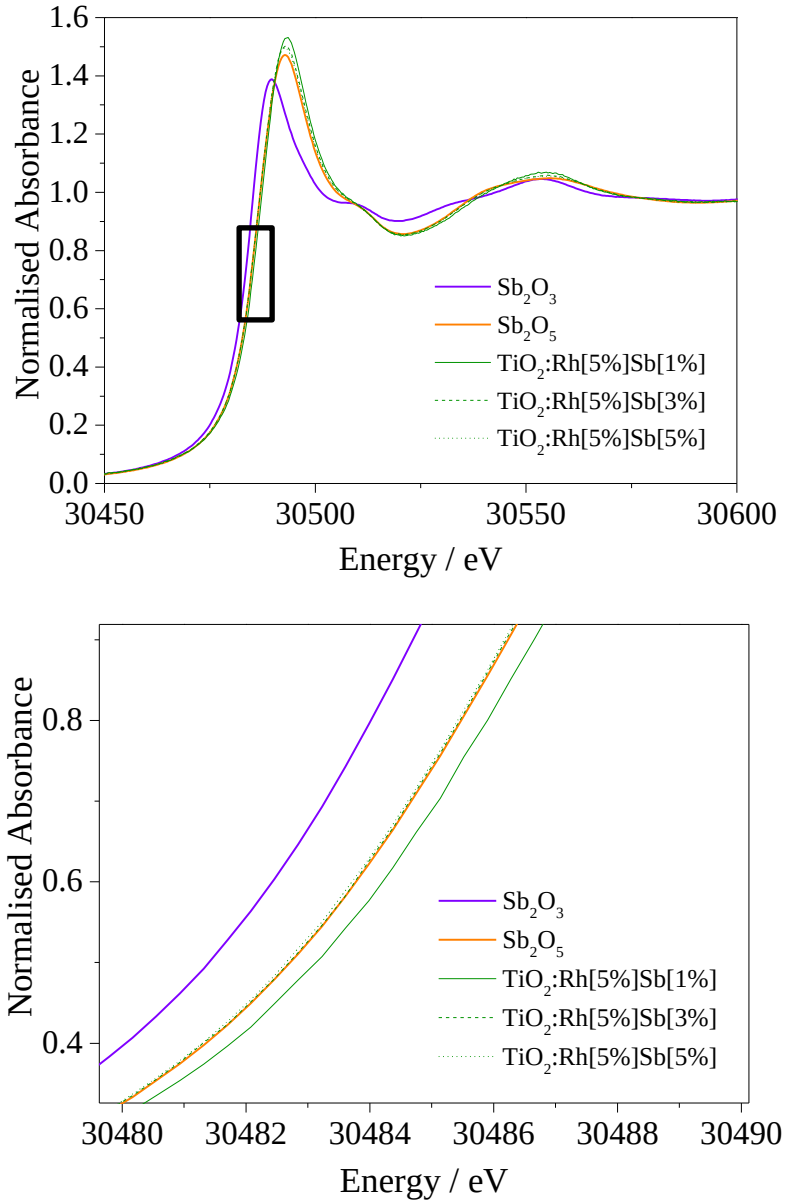

Figure 48: a) Sb X-ray absorption spectrum of Sb_2O_3 and Sb_2O_5 compared with TiO_2:[Rh5%][Sb1%], TiO_2:[Rh5%][Sb3%] and TiO_2:[Rh5%][Sb5%] and b) close up of the Sb k-edge between 30480 and 30490 eV

dopant ions in the doped samples. However, next nearest neighbour distances indicate that as Sb loading increases in doped materials, the Sb environment becomes more Sb_2O_5-like. Since Sb_2O_5 adopts a rutile-like structure, this could serve as an indicator that Sb ions in samples of Sb/Rh ≥ 1 reside on Ti^{4+} sites. This may account for the reduction in cell volume at higher Sb loadings, as Sb ions substitute Ti^{4+} and cause a smaller lattice distortion.

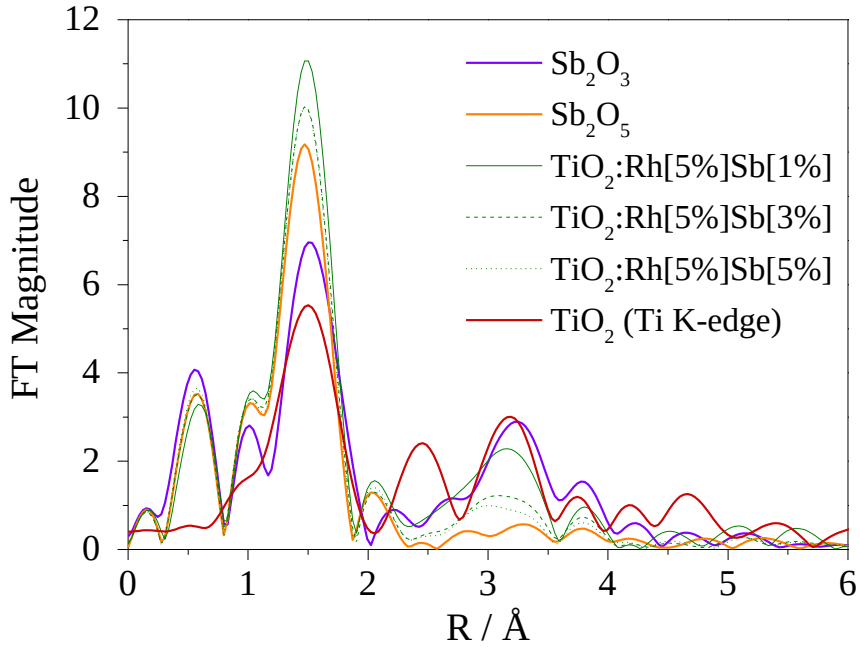

Figure 49: EXAFS Fourier transform of Sb_2O_3, Sb_2O_5, TiO_2:[Rh5%][Sb1%], TiO_2:[Rh5%][Sb3%], TiO_2:[Rh5%][Sb5%] and TiO_2 rutile

4.2.3 Scanning Electron Microscopy

4.2.3.1 Morphology and Particle Size

The long times and high temperatures employed for SSRs lead to a high degree of particle agglomeration and thus a large particulate size and irregular shape. The samples in this work were imaged by Scanning Electron Microscopy (SEM) in order to qualitatively characterise the size and morphology of the particles produced.

All samples produced by SSR resulted in agglomerates in a range of sizes of the order of microns. Most are rounded in shape and in some samples grain boundaries between agglomerates are easily visible. Figure 50a shows the TiO_2 control sample, after calcination at 1100 ˚C for 10 hours with no additional metal oxide powders. The agglomeration between particles here is evident, since the agglomerates are irregular in shape and resemble groups of particles without obvious grain boundaries.

Figure 50b-f show TiO_2 doped with increasing amounts of Rh. In images b, d and f, small amounts of gold are present in the images, from excess sputtering in the preparation of the samples for microscopic analysis. These have been highlighted with red arrows, though in Figure 50b where a high number of these irregularly shaped particles can be seen, not all have been highlighted in order retain image clarity.

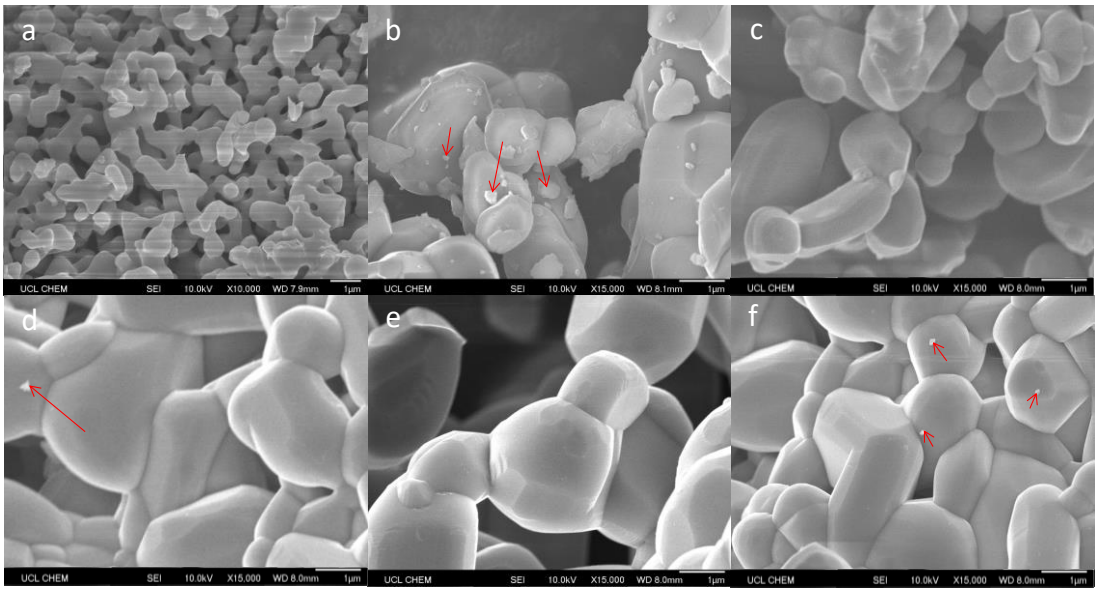

Figure 50: a) TiO_2 Rutile control (heated to 1100 °C for 10h), b) TiO_2[Rh1%], c) TiO_2[Rh3%], d) TiO_2[Rh5%], e) TiO_2[Rh7%], f) TiO_2[Rh9%]

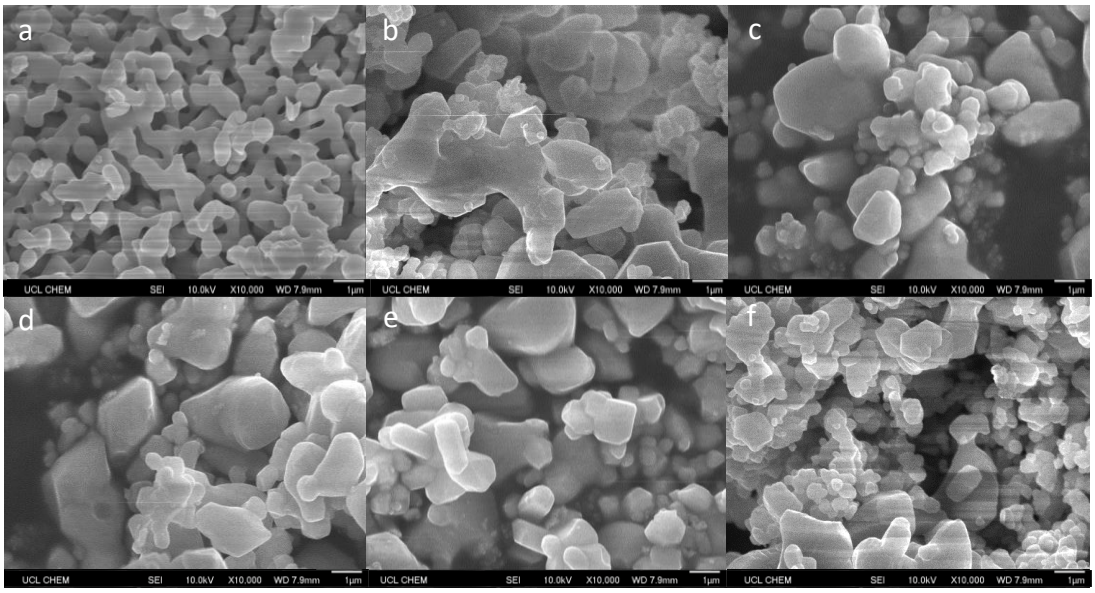

Figure 51:: a) TiO_2 Rutile control (heated to 1100 °C for 10h), b) TiO_2[Rh5%][Sb1%], c) TiO_2[Rh5%][Sb3%], d) TiO_2[Rh5%][Sb5%], e) TiO_2[Rh5%][Sb7%], f) TiO_2[Rh5%][Sb9%]

Comparison of the images shows that the addition of Rh appears to encourage particle agglomeration, since the doped particles are consistently larger than the TiO_2 rutile control, which was calcined at 1100 ˚C for 10 hours. Addition of Sb, as observed in the powders shown in Figure 51 b-f, appears to reduce this effect as these agglomerates, while larger than the control, are not as large as Rh-doped samples.

4.2.4 X-ray Photoelectron Spectroscopy

4.2.4.1 Surface Dopant Composition

High-resolution XP spectra of the Ti 2p, O 1s and Rh 3d core line regions were used to quantify the surface composition of all samples. As explained in Chapter 3, the Sb 3d $^{5}/_{2}$ core line peak is masked completely by the O 1s peak. In order to quantify both Sb and O in codoped samples, the spectra were fitted by constraining a Sb 3d $^{5}/_{2}$ component to the 3d $^{3}/_{2}$ peak, which is found at around 539 eV and is not obscured by any other signals in these samples. A Sb 3d $^{5}/_{2}$ peak was fitted by constraining its area (2:3 ratio with Sb 3d $^{3}/_{2}$), full-width half-maximum (equal to Sb 3d $^{3}/_{2}$) and doublet separation (9.4 eV lower than Sb 3d $^{3}/_{2}$) to that of the Sb 3d $^{3}/_{2}$. The remainder of the peak area at 530 eV was fitted with a component to represent the O 1s oxide anion contribution (FWHM = 1.8 ± 0.1) and another to account for surface hydroxyl groups, which manifest as a shoulder to the high binding energy side of the O 1s. As with previous analysis the OH peak was constrained such that its FWHM value did not exceed 2.5 eV and it's position relative to the O 1s peak was + 2 eV (±0.1 eV). All O 1s binding energy data presented in the following discussion are values determined by this method of fitting. An example fitted high-resolution spectrum showing the O 1s/Sb 3d region and associated fitting is shown in Figure 52.

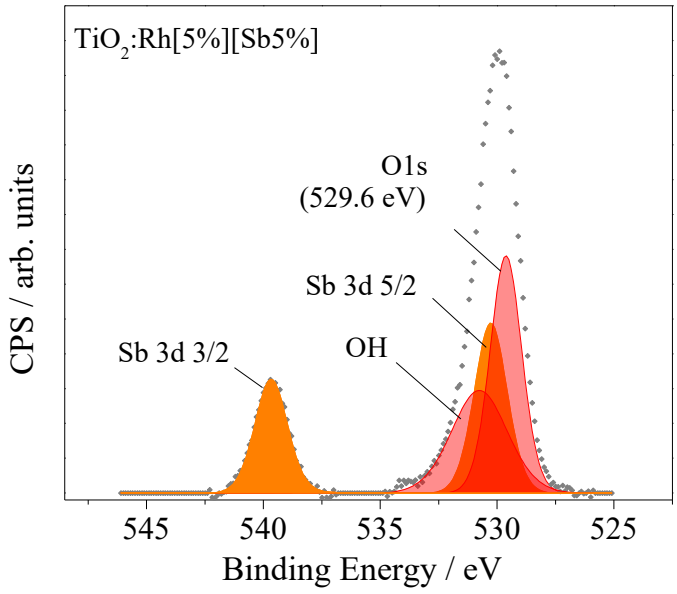

Figure 52: Example of a spectrum of the O 1s/Sb 3d region fitted by constraining an Sb $3d_{5/2}$ component to the Sb $3d_{3/2}$ peak, allowing an O 1s to be generated and its position determined. Sb 3d components can be seen in orange, with O 1s and M-OH components in red

Fitting of all high-resolution spectra, allowed peak areas and thus the relative atomic percentage (R.A. %) of each element to be determined by using the appropriate RSFs for scaling. Cation data are presented in Table 14 below and are represented graphically in Figure 53.

Sample	Ti R.A. %	Rh R.A. %	Sb R.A. %	OH/O^{2-}
TiO_2:[Rh1%]	95.2	4.8	-	0.39
TiO_2:[Rh3%]	95.3	4.7	-	0.42
TiO_2:[Rh5%]	95.1	8.9	-	0.39
TiO_2:[Rh7%]	94.1	5.9	-	0.39
TiO_2:[Rh9%]	91.8	8.2	-	0.37
TiO_2:[Rh5%][Sb1%]	89.7	10.3	0	0.40
TiO_2:[Rh5%][Sb3%]	73.9	17.6	8.5	0.43
TiO_2:[Rh5%][Sb5%]	62.2	19.0	18.8	0.38
TiO_2:[Rh5%][Sb7%]	58.8	19.3	21.9	0.41
TiO_2:[Rh5%][Sb9%]	49.2	21.1	29.7	0.39

Table 14: Relative atomic percentages Ti vs dopant ions in doped TiO_2 samples

TiO_2:[RhX%] samples exhibit XPS-measured concentrations of Rh higher than the nominal doping amount for X = 1, 3, 5 %, though this trend is not true for the higher doping regimes where the measured values are slightly below the nominal amounts. The increase in XPS-measured amount of dopant with respect to nominal amount is more pronounced for both dopant ions in codoped samples.

Accurate elemental analysis is contingent on accurate peak fitting, particularly with regards to the Sb 3d / O 1s region is these spectra since the Sb 3d $^5/_2$ core line peak is masked completely by the O 1s peak. The amount of OH contribution, in these fittings could have a considerable impact on the resultant data derived from the Sb 3d and O 1s peaks. Table 14 also shows the calculated OH/O^{2-} ratio of calculated at. %, which is around 0.4 for all samples. Thus it can be concluded that the XPS calculated data for in this chapter are comparable to each other since any effect of surface hydroxyls on the quantification, is similar across both series.

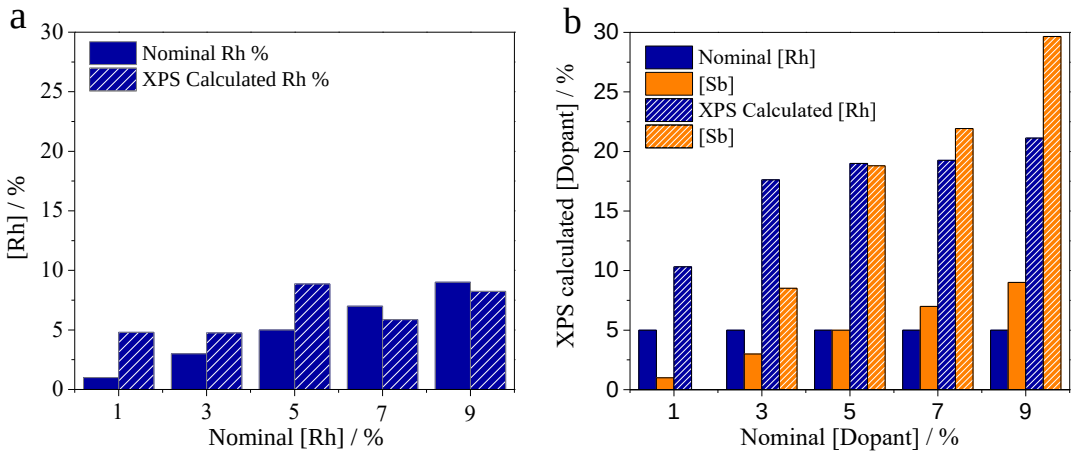

Figure 53: Nominal and XPS calculated amounts of dopant ion for Rh-doped samples (left) and Rh/Sb codoped samples (right). For ease of comparison between the two datasets, the y-axes are equal.

Since XPS is surface sensitive and detection is dependent on the IMFP of the photoelectron, these values should be considered. It is important that the sampling depths are similar for comparison of elemental data. Using equation 1, Chapter 3, the IMFPs for the principle core lines of Ti, O, Rh and Sb excited with Al Kα radiation were determined and can be seen in Table 15 below.

Element	IMFP (Å)
Ti 2p 3/2	1.73
O 1s	1.67
Rh 3d 5/2	1.85
Sb 3d 3/2	1.66

Table 15: IMFP values for Ti $2p_{3/2}$, O 1s, Rh $3d_{3/2}$ and $Sb3d_{3/2}$

As determined in section 4.2.1 from examination of the lattice parameters of these samples, Rh and Sb ions are likely incorporated into the rutile structure in a substitutional doping regime whereby the dopant cations reside on Ti sites in the lattice. The similarity in IMFP of the photoelectrons from the core levels used for quantification is close enough that their normalised areas can be directly compared (i.e. ratios between Ti and Rh or Sb from relative atomic percentages in table 2 are valid) since sampling depths across the range of elements differs by < 0.2 Å, considerably lower than the radius of the ions, which range from 0.600 to 0.665 Å for the cations and 1.4 Å for O^{2-} . Therefore differences in sampling depths are negligible and it can be concluded that the dopant enrichment with respect to Ti ions means that dopants are surface localised.

It is clear that the presence of Sb in codoped samples encourages further surface enrichment of Rh. By comparison with the analogous TiO_2:[Rh5%] sample, which has a calculated surface atomic percentage Rh of 8.86 %, all TiO_2:[Rh5%][SbX%] samples exhibit substantially higher surface Rh atomic percentages, ranging between 10.31 % to 21.12 % for X = 1 and 9 %, respectively. These data are presented in Figure 53b.

Comparison with the average bulk composition of the samples as determined by WDS- shown in Table 16- further supports surface localisation of dopants. Although the concentration increases with increased nominal doping in WDS calculated amounts, these values are much lower than the nominal amounts. All dopant concentrations were calculated to be < 3 % by WDS for any dopant in any sample.

These data suggest that both Rh and Sb are more stable at the surface of TiO_2. To investigate further a depth profiling study using a TiO_2 single crystal was completed. Powder samples present the difficulties of random particle size and orientation, meaning that they cannot provide meaningful compositional information from depth profiling. To overcome these

issues a single crystal diffusion study was completed. In this study a TiO_2(110) polished single crystal was heated under a TiO_2:[Rh5%][Sb5%] powder at 1100 ^oC for 10 hrs to induce diffusion of the dopants into the crystal. XPS depth profiles were recorded after Ar^+ ion sputtering for 10 seconds.

Sample	Rh		Sb	
	Nominal	WDS calculated	Nominal	WDS calculated
TiO_2:[Rh1%]	1	0.21	-	-
TiO_2:[Rh3%]	3	0.24	-	-
TiO_2:[Rh5%]	5	0.68	-	-
TiO_2:[Rh7%]	7	0.95	-	-
TiO_2:[Rh9%]	9	2.66	-	-
TiO_2:[Rh5%][Sb1%]	5	0.97	1	0.38
TiO_2:[Rh5%][Sb3%]	5	0.98	3	0.65
TiO_2:[Rh5%][Sb5%]	5	1.10	5	1.19
TiO_2:[Rh5%][Sb7%]	5	0.99	7	2.11
TiO_2:[Rh5%][Sb9%]	5	1.21	9	2.26

Table 16:Nominal vs WDS calculated dopant concentrations for doped TiO_2 samples

Figure 54 shows a plot of the dopant concentration as a proportion of total cation concentration (i.e. [Ti]+[Rh]+[Sb] = 100%) at intervals through the crystal. Depth profiling data from ion sputtering in XPS must be carefully considered since the process of sputtering can cause changes in the material, which it is possible to misinterpret. It is widely accepted that the process of ion sputtering in vacuum can lead to reduction of ions and therefore data concerning oxidation state cannot be relied upon. It is also important to consider the possibility of preferential sputtering when assessing the validity of depth profiled data pertaining to ion concentration.

Preferential sputtering is the process by which some atoms are removed more easily by an ion etch than others, which could lead to inaccuracies in compositional information. The original viewpoint was that this process is mass-correlated[165], however contradictions to this hypothesis were soon discovered; many alloys exhibit behaviour whereby the heavier atom is preferentially removed.[166-169] After atoms are removed from a surface the remaining structure undergoes a rearrangement in order to minimise the surface free energy; this is called Gibbsian Segregation (GS). If the sputtering rate is slower than the rate of migration of a particular atom, GS can result in their preferential removal. However, GS is most often (and most accurately) correlated to the bond energies of the atoms and ions at the surface of a material.[170-172] Since the Sb-O and Rh-O bond enthalpies are similar (372 $kJmol^{-1}$ and 377 $kJmol^{-1}$, respectively) it is reasonable to assume that they are sputtered at a similar rate and therefore the Sb/Rh ratios presented are accurate.

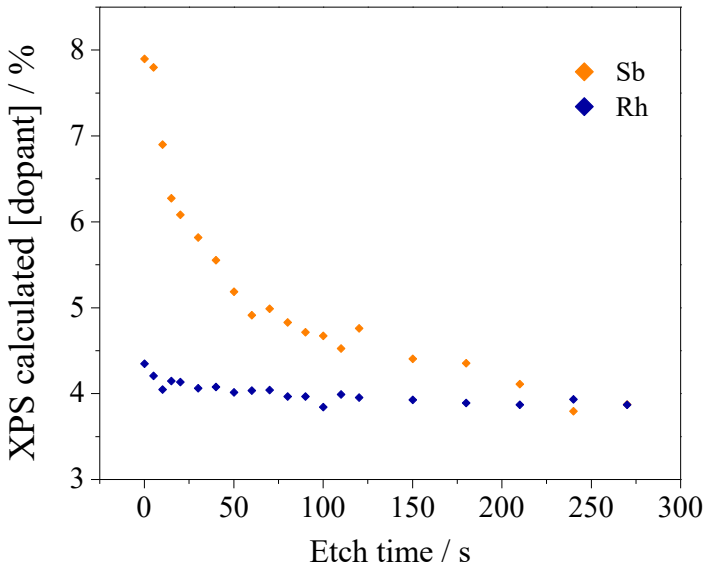

Figure 54: Dopant ion concentration as a function of sputter time into a Rh/Sb doped TiO_2(110) single crystal

Rh ions in the single crystal are considerably less surface enriched than in the powder used to produce the doped crystal, indicating that the ions are able to diffuse more effectively through the ordered structure of a single crystal than through a powder sample of varying orientation. While Sb also has a much lower XPS calculated surface concentration in the single crystal than in the powder sample, the Sb/Rh ratio increased from 1 in the powder to 1.8 in the single crystal. This indicates that Sb ions cannot diffuse as effectively in TiO_2 as Rh ions. Previous studies have indicated that Sb ions tend to surface segregate in metal oxides, for example TiO_2[173, 174] and SnO_2[175, 176], however these studies postulate that this is due to the presence of Sb(III), which sterically favours a surface position due to the presence of a lone pair causing the ions to occupy a position where they are able to adopt a less symmetric coordination. However, since XAS data confirms the absence of Sb (III) dopants in these samples, this indicates that Sb (V) ions must favour surface positions due to thermodynamic stability, rather than steric stability.

The attraction of Rh to Sb dopants at the surface of codoped materials is best explained by a defect clustering model. In order to maintain local charge neutrality Sb^{5+} and Rh^{3+} dopants preferentially reside on neighbouring or closely spaced cation sites. Therefore Sb dopants at surface sites effectively tether Rh ions at the surface, not allowing them to diffuse as penetratingly as when the materials are doped with Rh alone. This is evidence for both electronic interaction between the dopants (*i.e.* reduction of Rh^{4+} to Rh^{3+} through Sb doping) and interdependence of the spatial distribution of dopants within the TiO_2 matrix.

4.2.4.2 Valence Band Spectra and E_f position

Valence band (VB) spectra were recorded in order to probe the electronic structure of these materials. Firstly, the role of Rh as a dopant in TiO_2 is to insert donor levels into the band gap, since the 4d t_{2g} orbitals reside at a higher energy than those of the O 2p, which make up the majority of the TiO_2 VB. It is therefore expected that there should be visible changes in the valence band spectrum of the doped materials by comparison with the pristine materials. Secondly, as outlined in the introduction to this chapter, a major feature of these materials and one of the main points of interest for this research is the potential to tune the Fermi level position by the dopant ratio in the material. Since the Fermi level is calibrated as 0 eV in XPS, changes in the position of the VB could indicate these E_f changes.

To model the VB spectra of all doped samples a VB spectrum for pristine TiO_2 was fitted with two Gaussian-Lorentzian components. The low binding energy component was constrained to the high binding energy component by area, FWHM and position and the fit was used to account for the TiO_2 portion of the VB spectra of doped TiO_2 samples. In each doped sample an additional feature to the low binding energy side of the valence band was required in order to fit the data to the lowest residual STD (i.e. best fit). This feature, centred at a binding energy of ~1.6 eV, is highlighted in blue in the spectra shown in Figure 55. The area of the additional component was found to be proportional to the XPS measured Rh content, and can be assigned to the presence of filled Rh 4d t_{2g} states.

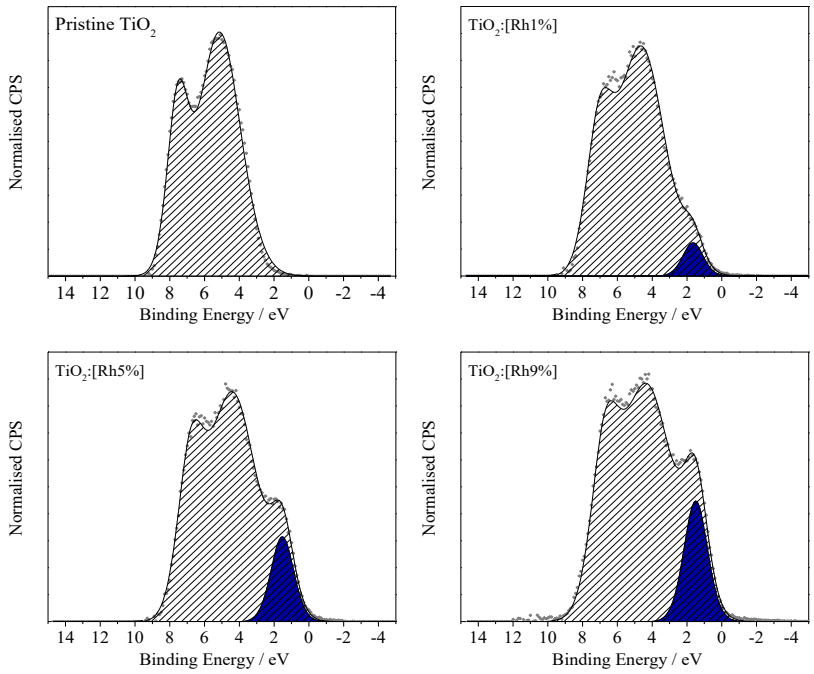

Figure 55: Valence band spectra of pristine TiO_2 and 1, 5 and 9% Rh doped TiO_2. As the nominal amount of Rh increases, the prominence of an in-gap feature due to Rh 4d t_{2g} electrons also increases.

A comparison between TiO_2Rh[5%], TiO_2Rh[5%][Sb1%], TiO_2Rh[5%][Sb5%] and TiO_2Rh[5%][Sb9%] is shown in Figure 56. As indicated by the augmented surface enrichment of Rh in Sb codoped samples, the Rh 4d t_{2g} band gap feature is more prominent in these valence band spectra than in Rh-doped samples and increases with increased Sb doping.

The spectra shown in Figure 55 and Figure 56 were taken from powder samples and represent the average data of 200 scans. Grey markers show the actual data, with the "envelope" line of best fit shown in black. Even with a high total number of scans, the data are noisy; in order to obtain the highest quality spectra to quantify shifts in the VB position, TiO_2 (110) single crystals were doped with Rh only and codoped with Rh and Sb in the manner described previously for depth profiled single crystals. VB spectra from these materials are shown in Figure 57 below, annotated to indicate the changes in VB position with doping and alongside schematic energy level diagrams to explain the perceived shift. In Figure 57a, the pristine TiO_2 valence band is shown. Its Fermi level resides approximately 7.3 eV away from the high binding energy peak of the valence band. This feature of the VB was chosen as the reference point to which the E_f at 0 eV was to be related since it is furthest away from the Rh 4d t_{2g} orbitals, the least affected by their presence and therefore the most ideal indicator of changes in VB position in these series. Figure 57b and c show clearly that Rh doping causes the VB to be positioned at a lower energy, closer to 0 eV (the E_f). TiO_2:[Rh] single crystal high binding

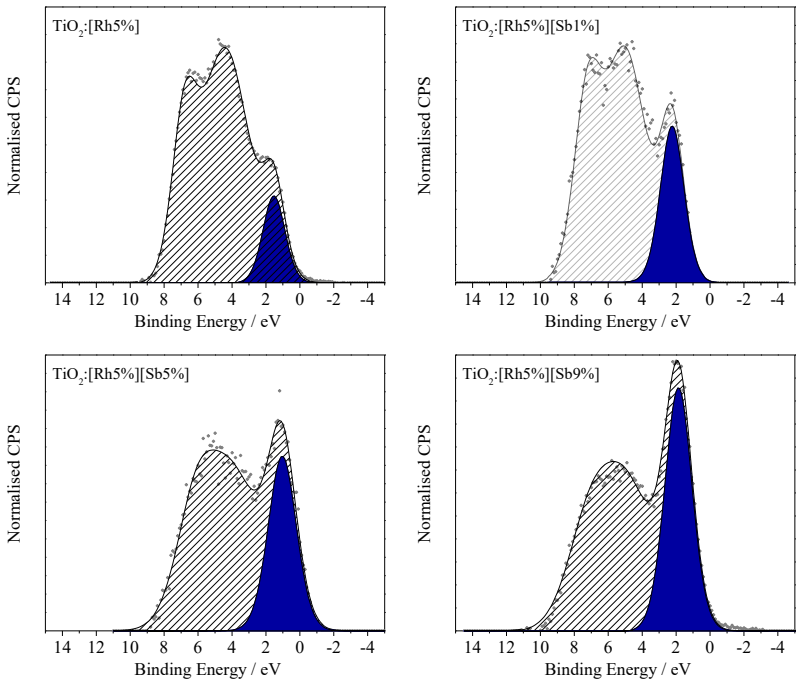

Figure 56: Valence band spectra of pristine TiO_2 and 1, 5 and 9% Rh doped TiO_2. As the nominal amount of Rh increases, the prominence of an in-gap feature due to Rh 4d t2g electrons also increases.

energy peak is positioned at 6.4 eV, whereas the high binding energy peak of the TiO_2:[Rh][Sb] single crystal VB is positioned at 7.1 eV, which is considerably closer to that of pristine TiO_2 at 7.3 eV. The VB in TiO_2 is made up of mainly O 2p orbitals and so, on the assumption that the oxide anion is chemically unchanged by doping, it can be concluded that perceived decrease in VB energy is not due to inherent changes in the VB, caused by structural or electronic changes in the material, but in fact a change in the energy of the Fermi level.

An alternative method to quantify the extent of E_f change which can be applied to materials where a VB spectrum of the high quality that is achieved from a single crystal cannot be obtained, is to use the O 1s core line as a reference point. Since O 1s peaks from oxide anions in metal oxides, of whatever structure and composition, fall within a very narrow range of binding energies it is assumed that the any chemical shift in this core line peak is due to a change in Fermi level energy.[152-154] This premise is explained schematically in Figure 58.

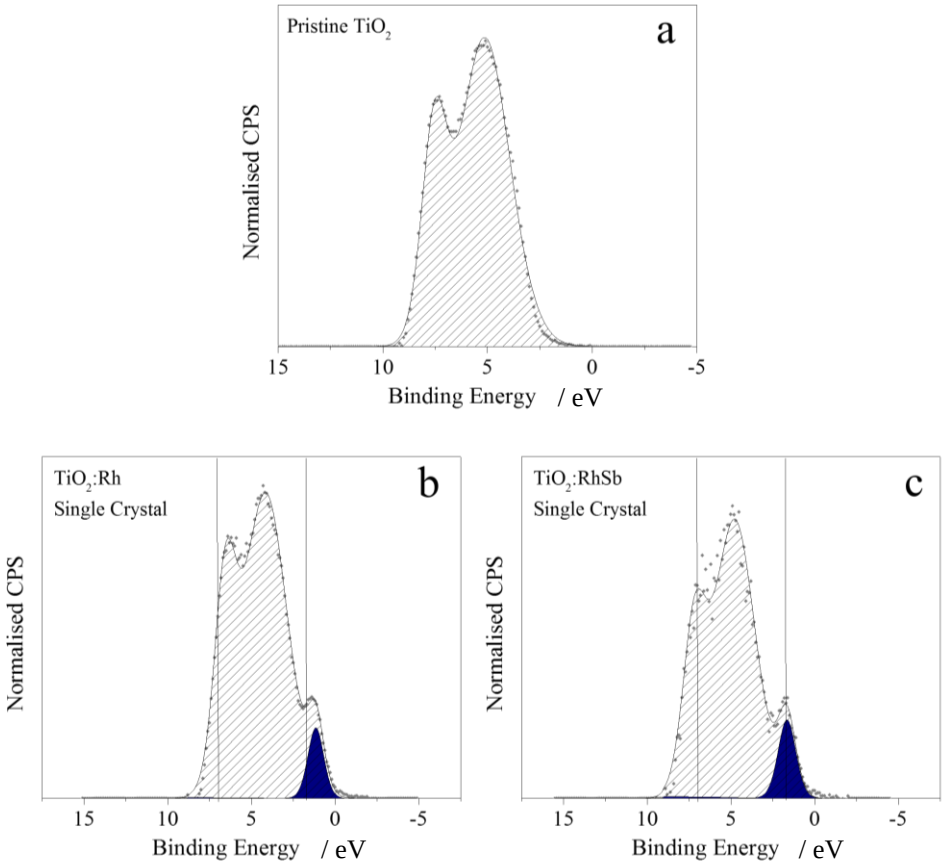

Figure 57: Valence band XP spectra of pristine TiO_2, Rh doped TiO_2 and Sb/Rh codoped TiO_2. Lines on the VB spectra of doped samples indicate the position of the high B.E. VB peak and Rh feature in codoped TiO_2, clearly illustrating the change in position between

Figure 58a presents pristine TiO_2, where the E_f is in its 'usual' position, close to the conduction band in the band gap. The valence band lies lower in energy and the O1s lower in energy still (double grey arrows indicate that the O1s is much deeper than the valence band and that the

y-axis, not pictured, is not to scale). When the E_f is lower in energy than for pristine TiO_2, as shown in Figure 58b, it appears closer to both the VB and the O 1s core line. This manifests in XPS spectra as both the VB and the O1s core line, appearing lower in energy since they are closer to E_f (or 0eV). If E_f is higher in the band gap than it is for pristine TiO_2, the inverse will be true and the O 1s binding energy (and VB position) will appear higher than that of pristine TiO_2 (i.e. further away from E_f at 0 eV).

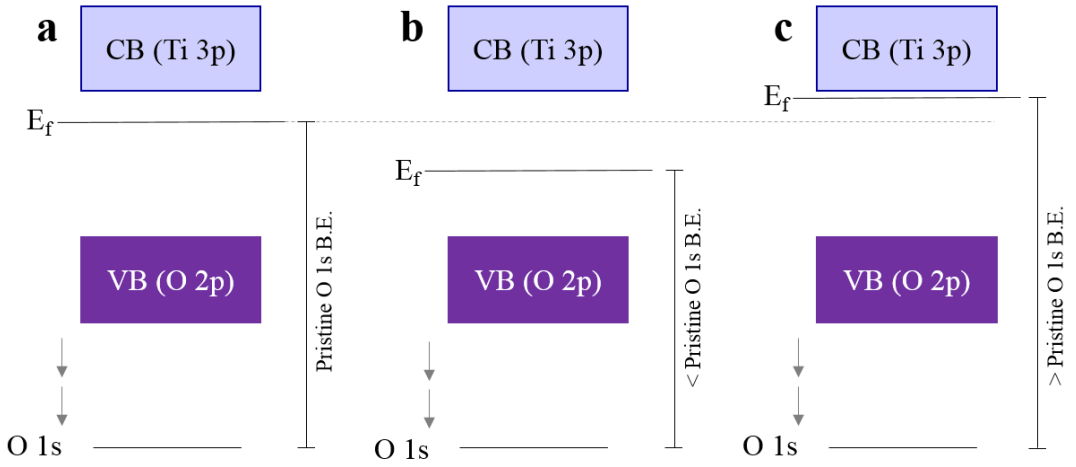

Figure 58: Schematic band gap diagram illustrating actual change in fermi level position with the resultant perceived change in O 1s binding energy annotated

The O 1s core line binding energies of codoped samples are shown in Figure 21, as a function of nominal [Sb%], along with those of pristine TiO_2 and TiO_2[Rh5%] for comparison. Doping with Rh alone causes a considerable 0.4 eV downshift in O 1s binding energy; the O 1s core line in pristine TiO_2 lies at 529.9 eV by comparison with the O 1s core line in TiO_2[Rh5%], which lies at 529.5 eV. This can be translated as a reduction in E_f energy; the Fermi level is deeper in the band gap, and can be assigned to the introduction of incomplete 4d t_{2g} orbitals above the valence band. The vacancy of these orbitals acts as a sink for electrons residing at the Fermi level energy, into which they can drop down. The result is a Fermi level at lower energy than the undoped material.

A clear trend can be seen in Figure 59 correlating O 1s peak position to nominal amount of antimony codopant. The addition of antimony in increasing amounts increases the O 1s core line binding energy, from 529.4 eV in TiO_2[Rh5%][Sb1%] to 530.2 in TiO_2[Rh5%][Sb9%]. This increase in Fermi level energy can be attributed to the filling of the Rh states within the band gap through introduction of Sb^{5+}, an electron dopant and reduction of Rh^{4+} to Rh^{3+}, which has a filled t_{2g}^6 configuration in the low spin state. The total variation seen in the O1s peak across all samples is 0.8 eV. Thus variable levels Sb doping can be used to tune the Fermi Level of these materials within a good proportion of the band gap.

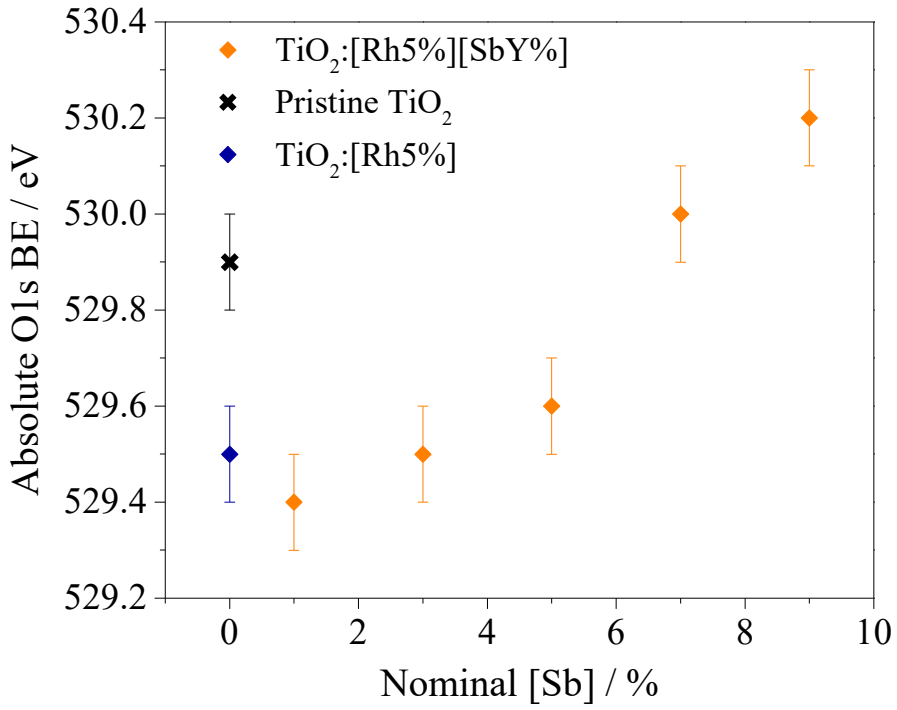

Figure 59: O 1s positions correlated with nominal [Sb%]. O 1s positions of pristine TiO_2 and TiO_2:[Rh5%] included for comparison.

The Rh/Sb ratio can be calculated at each point along the depth profile of the co-doped TiO_2 (110) crystal shown in Figure 54. By matching the dopant ratio as calculated by XPS at each point in the depth profile and correlating these values to a curve drawn through the experimental points in Figure 59, the E_f energy at each depth profile point can be estimated. Assuming that the Fermi level is constant throughout the material and that therefore the CBM and VBM change energy with depth (due to changes in dopant ratio), the CBM and VBM were determined and have been plotted as a function of depth. The result of this analysis can be seen in Figure 60 It is clear that significant band bending, of around 0.5 eV, occurs due to the influence of the dopants spatial arrangement. It should be emphasised that only the effects of the dopants are shown in Figure 60 – there will be other contributions to surface band bending, such as the presence of surface states, as occurs with all semiconductors.

These results indicate for the first time that a photocatalyst system exhibits spontaneous dopant segregation which is expected to cause significant band bending. This may contribute to the high photoactivity reported in this system; as previously stated Kudo and co-workers reported photoactivity of Rh and Sb codoped TiO_2 (where Sb/Rh = 0, 0.5, 1, 2 and 3 were investigated) and showed that, with Sb/Rh $\geq$ 2, O_2 evolution exceeds 10 mmol $h^{-1}g^{-1}$.

This increased understanding of the electronic properties of these materials may serve as a starting point for design of more highly effective photocatalysts. It is important to note that the materials synthesised are model systems; the use of solid state synthesis results in low

surface area powders due to the high temperatures used. This renders the samples unsuitable for photocatalysis, but provides a quick, simple and highly reproducible route to production of the materials, allowing a high throughput of varying doping ratios.

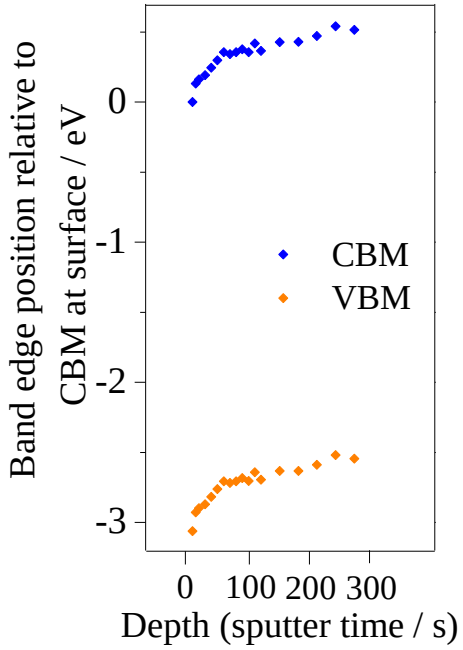

Figure 60: VBM and CBM variation with depth in Sb/Rh codoped TiO_2 (110) single crystal. The CBM at the surface is placed at 0 eV and the band gap is assumed to be 3.06 as in bulk rutile TiO_2.

4.2.4.3 Surface Dopant Oxidation State

As shown with respect to the O 1s core line, the change in Fermi level energy causes chemical shifts in other elemental core lines from XPS spectra of Rh doped TiO_2 materials. This creates a difficulty in the classification of the oxidation state of Rh in these materials. Usually, differences in oxidation state can be determined simply by the binding energy of the element in question; a higher binding energy correlates to a higher oxidation state and many materials have been classified in the literature such that identification of the oxidation state of a dopant is rudimentary. However, the materials studied in this work possess dopant ions of potentially differing oxidation states (Rh^{3+}/Rh^{4+}) accompanied by a change in Fermi level energy, the 0 point in XPS. This results in high resolution Rh spectra where the *absolute* binding energies are irrelevant. Since the extent of change in Fermi level energy was able to be quantified by

use of the O 1s core line position, it is reasonable to use this core line as a reference point to determine the relative oxidation states of other elements, i.e. Rh.

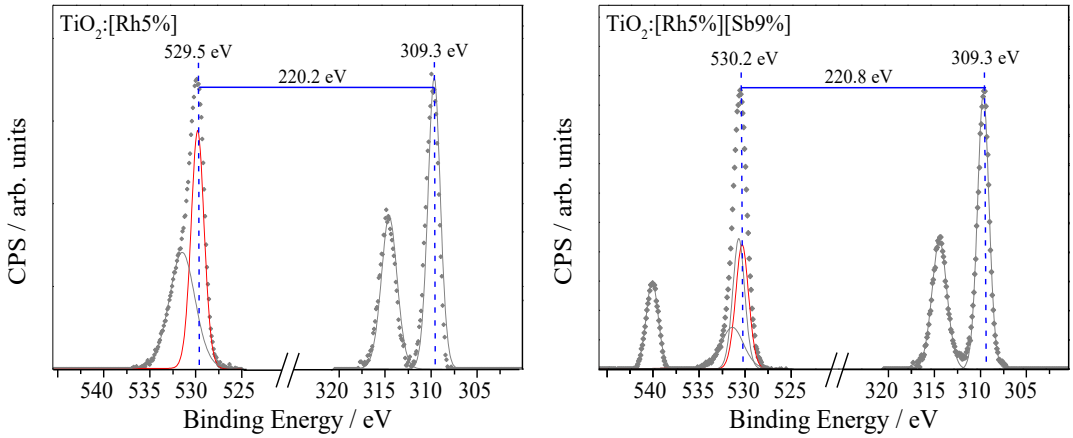

Figure 61: Binding energy separation between O1s and Rh 3d peaks in TiO_2[Rh5%] and TiO_2[Rh5%][Sb9%]. The energy difference between the core lines increases with Sb doping. Assuming a static oxide O1s peak with no chemical shift, the increasing energy difference upon Sb doping can be attributed to a decrease in the binding energy of the Rh 3d core line, corresponding to a less positive oxidation state for Rh.

As shown in Figure 61a and b, the absolute binding energy of Rh 3d $^{5}/_{2}$ electrons in TiO_2[Rh5%] and TiO_2[Rh5%][Sb9%] is 309.3 eV for both samples. Ordinarily, in the absence of Fermi level shifts, this would indicate that Rh in these samples is in the same oxidation state. However, their separations from the O 1s core line are 220.2 eV and 220.8 eV, respectively. Since the Rh 3d core electrons possess a lower binding energy than the O 1s core electrons (309 eV and 530 eV, respectively), a greater core line separation indicates that Rh is in a lower oxidation state.

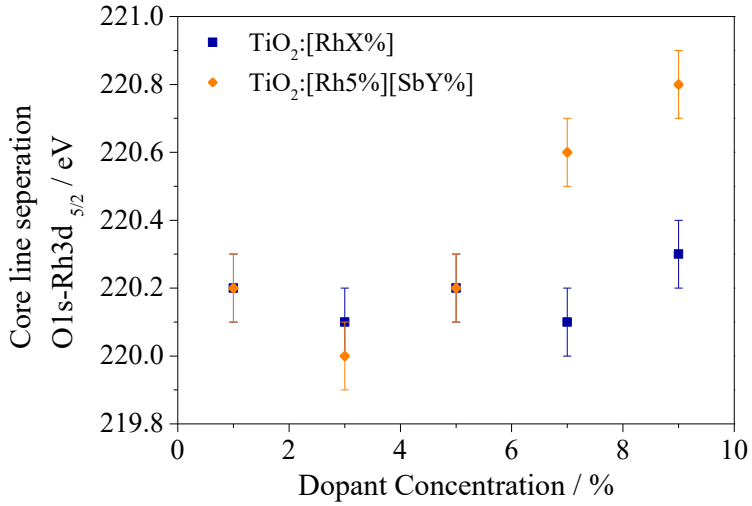

Figure 62: Core line separation values for all doped samples. It can be seen that all Rh doped samples have similar values for their O 1s-Rh 3d core line separation, but that codoped samples exhibit higher core line separation values upon Sb/Rh ≥ 1.4.

The O 1s-Rh 3d $^{5}/_{2}$ core line separation values for all codoped samples are shown in Figure 62. Rh doped samples possess a Rh 3d core line separated from the O 1s core line by between 220.0 eV and 220.3 eV, with no distinct trend. Codoped samples exhibit an increase in O 1s-Rh 3d $^{5}/_{2}$ core-line separation as Sb loading increases indicating that in samples where Sb/Rh ≥ 1.4 a higher proportion of Rh is found in the +3 state.

4.2.5 Ultraviolet-Visible Spectroscopy

The optical properties of the samples were investigated by Ultraviolet-Visible (UV-Vis) spectroscopy. Due to the opaque nature of the samples spectra were obtained in diffuse reflectance mode and the data were transformed into a Tauc plot using the Kubelka-Munk relation, Equation 42 (where R = reflectance), to obtain a spectrum of f(R). Equation 43 shows f(R) to be proportional to absorbance, A. From these Tauc plots the band gap energy was determined by extrapolation of the absorbance edge to the point at which it would intercept the x-axis, where y = 0.

$$f(R) = \frac{(1-R)^2}{2R}$$

Equation 42

$$A = Log_{10}\frac{1}{R}$$

Equation 43

Spectra were collected over a 2000-200 nm range, at a step size of 0.5 nm and a dwell time of 0.36 s. The samples were mounted on to a glass slide using carbon tape, which is black and therefore does not contribute to the spectrum produced. However, variation in the amount of sample analysed due to loading on the tape and position in the spectrometer (which is highly variable sample by sample) leads to variations in spectral intensity that cannot be correctly accounted for. Therefore, all spectra have been normalised for ease of analysis and only relative intensities will be considered.

Normalised Tauc plots of TiO_2, TiO_2:[Sb5%] and TiO_2[Rh5%] are shown in Figure 63. Both TiO_2 and TiO_2:[Sb5%] show absorbance edges at around 3.0 eV, which is characteristic of TiO_2 rutile.[177, 178] Sb doping appears to increase the onset energy of the absorption edge only very slightly; it can be concluded that any considerable lowering of the band gap is entirely caused by the presence of Rh dopant ions.

The Tauc plot of TiO_2:[Rh5%] is different from the those of TiO_2 and TiO_2:[Sb5%] in two ways; the band edge is shifted to lower energy (around 1.8 eV in TiO_2:[Rh5%]) and a broad

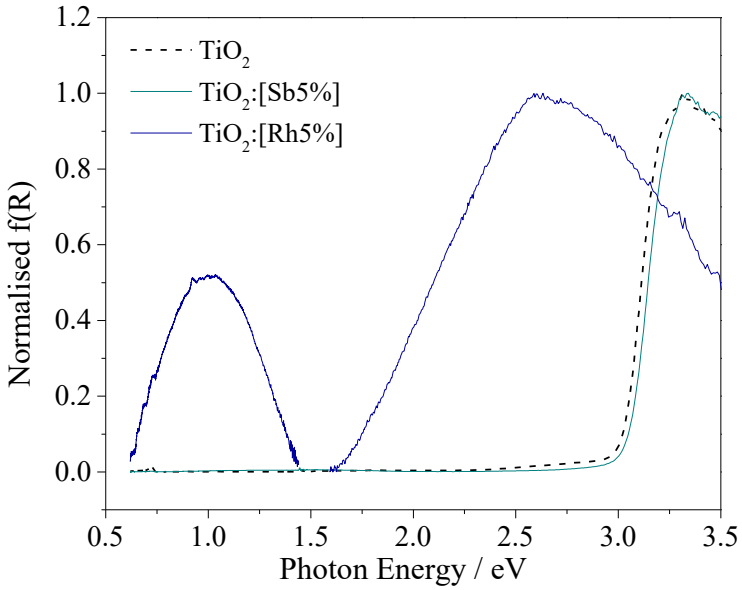

Figure 63: Tauc plot of TiO_2 Rutile control (heated to 1100 °C for 10h) (dotted line), TiO_2:[Sb5%] (dark cyan) and TiO_2:[Rh5%] (blue)

absorption peak exists at around 1.0 eV. The decrease in absorption edge decrease can be attributed to the insertion of donor 4d t_{2g} states in the band gap due to the presence of Rh dopant ions; discussion of the position of this band edge follows later in the context of TiO_2:[Rh5%] by comparison with codoped samples.

The absorption feature at 1.0 eV was not observed in a previous study by Oropeza et al. since their spectra were collected over a shorter range of wavelengths and therefore the low energy transition was not observed.[161] A study using Rh and Sb dopants in $SrTiO_3$ assigned a similar feature at the same energy to a Rh d-d transition[90], which is spin-allowed in Rh^{4+}. Since octahedral Rh^{3+}-O^{2-} is a low spin configuration[179, 180], this transition would not be allowed for Rh^{3+} doped on a Ti^{4+} site in TiO_2 (or $SrTiO_3$) and could be seen as an indication of the presence of Rh^{4+}. Whilst in agreement that this absorption feature indicates the presence of Rh^{4+}, a different explanation is proposed here. Evidence in the literature regarding the electronic structure of Rh ions indicates that the Rh^{4+} d-d transition occurs at around 2.5 eV[181, 182] and while this will vary in oxides, it does not correlate with the absorption observed, indicating that this has been misassigned in other work. Instead, this absorption can be assigned to an O 2p → Rh t_{2g} transition, i.e. a transition from the TiO_2 VB to the partially filled interband gap Rh 4d state. As seen previously in the XPS valence band spectra, filled Rh states appear at around 1.0 eV above the valence band edge. From this analysis, a quantitative picture of the electronic structure of Rh doped TiO_2 can be understood. The TiO_2 valence band orbitals, mainly O 2p, lie 1.0 eV below the Rh 4d t_{2g} donor states in the band gap. Around 2.5 eV above these lie the Rh 4d e_g states, close to the conduction band edge, which lies around 3 eV above the valence band edge.

The introduction of Sb^{5+} into Rh doped TiO_2 should cause the reduction of Rh^{4+} to Rh^{3+}. Careful interpretation of XPS data in section 4.2.4.3 has shown that Rh in codoped samples exists in a lower oxidation state than when Rh is the only dopant in the system. This is further corroborated by the Tauc plots presented in Figure 64, which shows all Sb/Rh samples. It is evident from these plots that the absorption at ~ 1.0 eV diminishes with the addition of Sb^{5+}. As explained above this absorption is due to an O 2p → Rh t_{2g} transition and is therefore indicative of the presence of Rh^{4+} in the sample. All codoped materials with Sb/Rh < 1 possess a strong absorption at ~1.0 eV, which can be seen to decrease when Sb/Rh ≥ 1. Equimolar dopant concentration produces the largest reduction in this absorption, indicating that [Rh^{4+}] is lowest at this ratio.

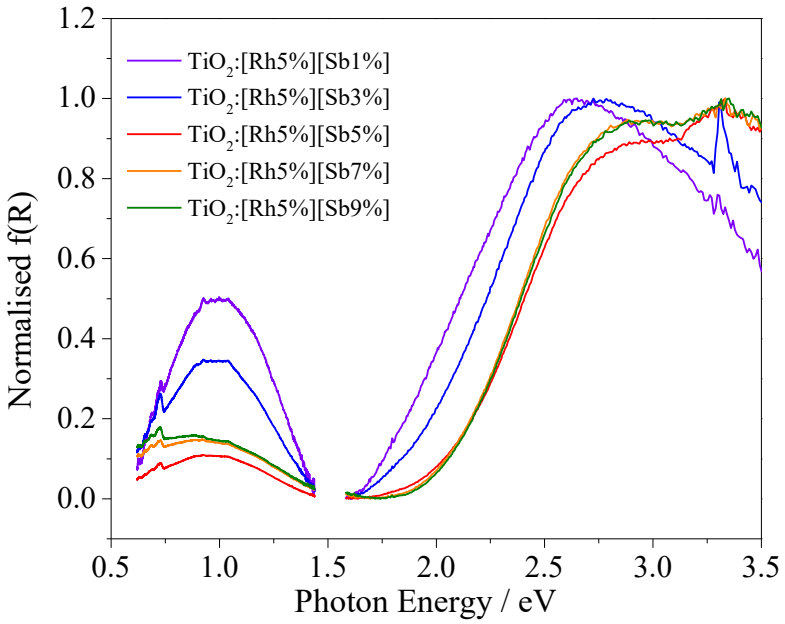

Figure 64: UV-Visible absorbance spectra of TiO_2[Rh5%][Sb1%], TiO_2[Rh5%][Sb3%], TiO_2[Rh5%][Sb5%], TiO_2[Rh5%][Sb7%], TiO_2[Rh5%][Sb9%]

Although codoped samples have a lower band edge than that of pristine TiO_2, they all possess higher band edges than TiO_2:[Rh5%], which is unexpected. Samples that appear to contain a large proportion of Rh^{4+}, indicated by the intensity of the absorption at 1.0 eV (TiO_2:[Rh5%], TiO_2:[Rh5%][Sb1%] and TiO_2:[Rh5%][Sb3%]), all have a lower band edge than expected to be brought about by the insertion of Rh 4d donor states in the band gap. It is likely that the d-d transitions described previously, which are spin-allowed in Rh^{4+} are responsible for this feature resembling a band edge at ~1.8 eV in TiO_2:[Rh5%] and TiO_2:[Rh5%][Sb1%] and TiO_2:[Rh5%][Sb3%]. This, like the O 2p → VB transition at 1.0 eV is attenuated by the addition of Sb, which causes reduction of Rh^{4+} to Rh^{3+}.

Band gap energies were determined for each sample by extrapolation of linear portion of the plot to the x-axis, giving the value of the band edge absorption. An example of pristine TiO_2 is shown in Figure 65, with the linear portion expanded in the inset. Table 17shows the measured band gaps for all samples. Those denoted with a * are the samples of Sb/Rh < 1, which are not believed to be true band gap energies (explained above).

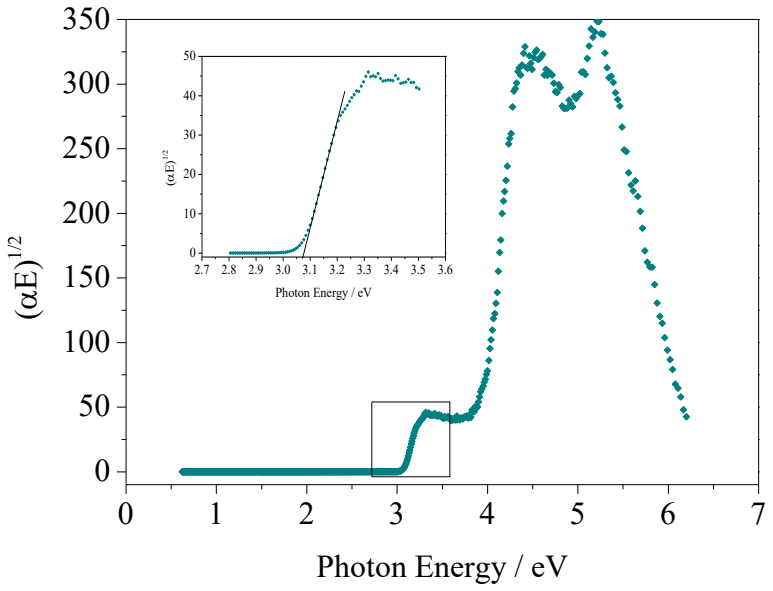

Figure 65: Kubelka-Munk transformed data resultant Tauc Plot, example using TiO_2 fired rutile

All codoped samples with Sb/Rh > 1 exhibit a band gap energy lower than that of undoped TiO_2 rutile and also of TiO_2:Sb[5%]. This is believed to be caused by d-d transitions, explained previously, caused by the presence of small amounts of Rh^{4+}, which has not been completely eliminated since [Sb] < [Rh] and therefore some Rh ions can still reside in the +4 oxidation state. TiO_2:[Rh5%][Sb3%] continues this trend, though less dramatically, as it possesses a band gap ~0.1 eV lower than samples with Sb/Rh > 1. Samples with Sb/Rh > 1 have similar band gaps at 2.25 eV, 2.24 eV and 2.23 eV. From the absorption at 1.0 eV it is known that in these samples a minimal amount of Rh^{4+} exists and therefore this narrowing of the band gap is considered genuine and due to Rh 4d t_{2g} → CB transitions.

Sample	Band Gap Energy
TiO_2:[Sb5%]	3.1
TiO_2:[Rh5%]	1.84*
TiO_2:[Rh5%][Sb1%]	1.89*
TiO_2:[Rh5%][Sb3%]	2.11
TiO_2:[Rh5%][Sb5%]	2.25
TiO_2:[Rh5%][Sb7%]	2.24
TiO_2:[Rh5%][Sb9%]	2.23

Table 17: Band gap energies calculated using Tauc plot extrapolation. *indicates probable d-d transition

A summary of the electronic structure of Rh^{3+} and Rh^{4+} doped TiO_2 as determined from this analysis is explained in Figure 66 below. Rh^{3+} doped TiO_2 samples possess complete Rh 4d t^6_{2g} energy levels within their band gap. The only allowed transitions in this system are VB → CB or Rh 4d t^6_{2g} → CB. These result in a single band edge of around 2.24 eV and can be observed in samples with Sb/Rh ≥ 1. Contrastingly Rh^{4+} doped TiO_2 possess incomplete Rh 4d t^5_{2g} energy levels within its band gap. This configuration can result in additional transitions as well as those described for Rh^{3+}. A transition from VB → Rh 4d t^5_{2g} is caused by absorption of a photon of around 1.0 eV, which can be clearly seen in Tauc plots for samples of Sb/Rh < 1. In addition, a d-d transition, which is spin allowed in Rh^{4+}, can be observed after absorption of photons of around 2.0 eV. This results in an apparent downshift of the band edge of these samples, though this is not a real narrowing of the band gap, since these electrons are confined to the Rh 4d energy levels and cannot be accessed for photocatalysis. Instead they will relax back down to their ground state.

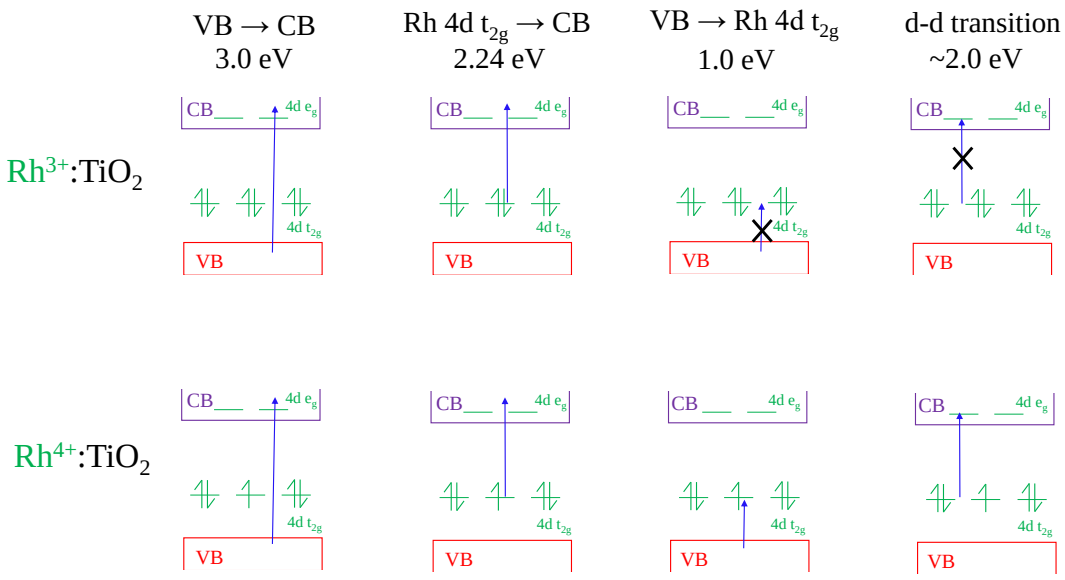

Figure 66: Energy level diagrams illustrating the possible transitions observed in the doped materials, if they are allowed and their approximate energy requirement

4.2.6 Transient Absorption Spectroscopy (TAS)

Charge carrier dynamics of selected powder samples were measured using Diffuse Reflectance Transient Absorption Spectroscopy (DR-TAS) from the microsecond to second time scale at room temperature. A 75 W Xe lamp is used as a probe beam with a monochromator placed before the powder sample, which is compacted between two glass microscope slides. Changes in the light reflected by the sample are measured by a Si PIN photodiode after a UV laser excitation pulse is applied on the sample (355 nm, 6 ns pulse width). The laser intensities used were (~40 μJ cm^{-2} $pulse^{-1}$) with a laser repetition rate of 1

Hz. Each TAS trace is the result of averaging 100 scans. The samples selected for DR-TAS were TiO_2:[Rh5%], TiO_2:[Rh5%][Sb5%], TiO_2:[Rh5%][Sb9%] along with TiO_2:[Sb5%] and TiO_2 rutile (fired at 1100 ˚C for 10 hours) as controls. These measurements were taken at Imperial College London, using the Durrant Group DR-TAS setup and with the assistance of Dr Andreas Kafizas. Transient Absorption Spectroscopy.

4.2.6.1 DR-TAS Spectra

Absorption spectra, shown in Figure 67 and Figure 68, were compiled by taking the average absorption of each sample between 550 and 950 nm in 50 nm increments. The spectral shapes for each sample remained the same across the microsecond timescale, after which the signals were too low to produce a distinctive spectrum.

Previous studies have shown that photoexcited electrons absorb in the near-IR region (λ = 700 nm-1000 nm) and that photogenerated holes absorb in the visible region (λ = 400 nm-700 nm).[183] Multiple studies have made use of solution based TAS, immersing the sample in a solution of a hole or electron scavenger to quench the respective signals and yield a spectrum pertaining to only electron or hole absorption.[184, 185] For example, a study by Kafizas et al. determined from studies using silver nitrate as an electron scavenger and methanol as a hole scavenger, that in rutile TiO_2 electrons absorb at 850 nm and holes at 550 nm.[105] Unfortunately, the large particle size of Rh and Sb/Rh codoped samples discussed in this chapter adversely affected powder dispersion in both MeOH and $AgNO_3$ solutions, preventing solution phase TAS from being carried out with these samples and therefore preventing correlation of deconvolution results with the samples examined here. However, assuming that doping does not dramatically affect the wavelengths at which electrons and holes absorb, some conclusions can be made about the relative proportion of charge carriers in the doped samples.

TiO_2 fired rutile, shown in Figure 67a, produces a spectrum of decreasing absorption as probe pulse wavelength increases, indicating that the majority of mobile charge carriers in this material are holes. It should be noted here that previously reported TiO_2 rutile spectra[105] have produced spectra with stronger absorption in the n-IR region, corresponding to a more even concentration of electrons and holes. Also, nano-sized TiO_2 TAS spectra in the same study produced a higher overall absorption intensity, indicating that the low intensities reported here could be due to particle size effects. For example, the high degree of agglomeration could provide an increased number of grain boundaries, which are known to

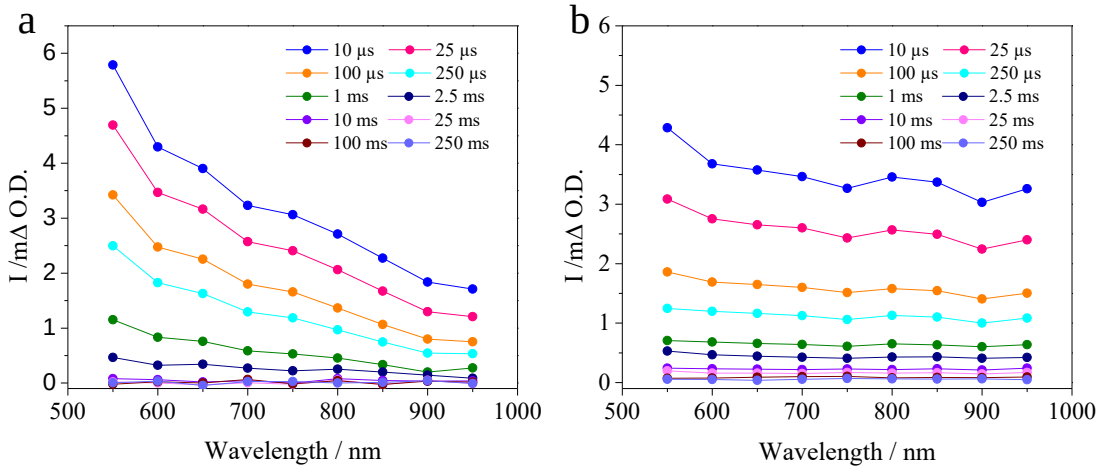

Figure 67: a) TAS spectrum of TiO_2 fired rutile powder and b) TAS spectrum of TiO_2[Sb5%] mobile electrons

act as recombination sites for charges in semiconductors.[186, 187] By comparison, TiO_2:[Sb5%] shown in Figure 67b produces absorption signals of more comparable intensity across the range of probe pulse wavelengths. While the absorption intensity does still decrease with increasing probe pulse wavelength, this decrease is less pronounced in TiO_2:[Sb5%] than in TiO_2 fired rutile. This indicates that the concentration of photogenerated electrons and holes is more equal in TiO_2:[Sb5%] than in TiO_2 fired rutile.

The doped samples produce spectra of similar shapes to each other, but with significantly varying intensities. The TAS spectrum of TiO_2:[Rh5%], shown in Figure 68a, shows a maximum intensity of 0.9 mΔO.D. at 550 nm, at the 10µs timescale. Absorptions sharply decrease as probe pulse wavelength increases, indicating that the majority charge carriers in this material at the microsecond timescale are holes, which as previously stated absorb in TiO_2 rutile at 550 nm. This supports results reported earlier in this chapter, where XPS indicates that the addition of Rh as a dopant alone decreases the energy of the Fermi level, making the material more p-type.

TiO_2:[Rh5%][Sb5%], shown in Figure 68b, produces a spectrum of higher intensities across all wavelengths by comparison to TiO_2:[Rh5%]. The spectral shape is also different to that of TiO_2:[Rh5%]; absorptions at higher wavelengths are more intense, indicating a higher concentration of electrons in this sample than in TiO_2:[Rh5%], though holes are still the majority carrier since the sample is more strongly absorbing at lower wavelengths than at $\lambda \geq$ 700 nm. Again this supports XPS results, which indicate that the Fermi level in codoped samples exists at a higher energy and that the sample is more n-type. TiO_2:[Rh5%][Sb9%] (Figure 68c) produced a spectrum of similar shape to that of TiO_2:[Rh5%][Sb5%], but with lower intensities across all timescales. At the shortest timescale (10 µs after photoexcitation)

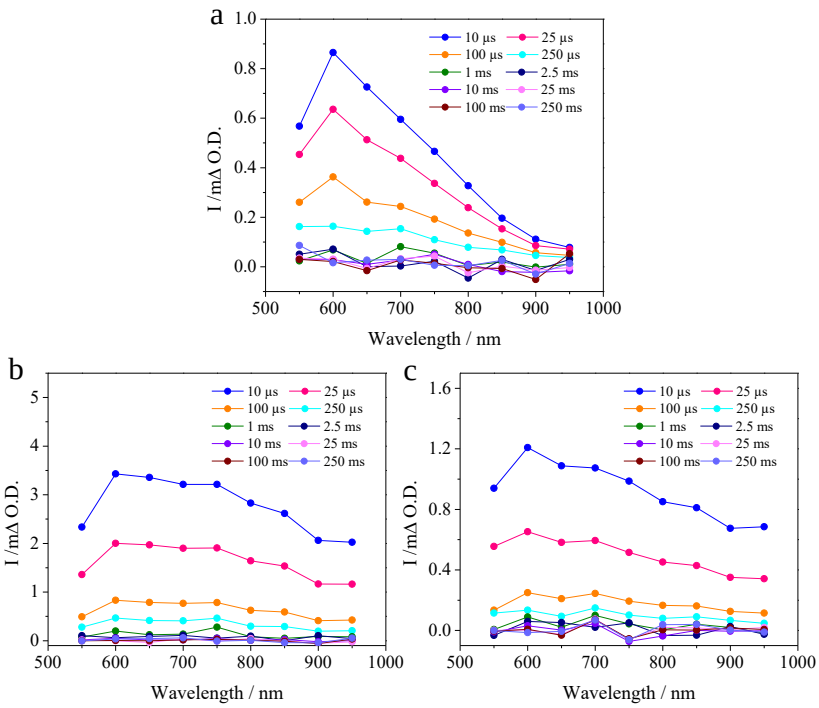

Figure 68: a) DR-TAS spectrum of TiO_2[Rh5%] b) DR-TAS Spectrum of TiO_2[Rh5%][Sb5%] and c) TiO_2[Rh5%][Sb9%]

TiO_2:[Rh5%][Sb9%] absorbed more intensely than TiO_2:[Rh5%] across all timescales, though this diminished at later timescales.

It is important to note the timescale of this analysis; these measurements were made, at the earliest, 10 µs after photoexcitation. Conclusions drawn regarding relative concentrations of photogenerated electrons and holes in different samples do not necessarily indicate that greater or fewer charge carriers are *generated*, but that in samples with less intense signals the electrons and holes possibly recombine on a timescale shorter than that of the resolution of the setup used. This is important information for materials intended for photocatalytic uses, since charge carrier lifetime is an essential property for photocatalytic materials. However, it should be noted that information pertaining to the mobility of these charges is not provided from TAS; some charges could have a long lifetime if they reside in trap states, which do not allow them to recombine, but also do not allow them the mobility required for them to migrate to the surface and facilitate photocatalytic reactions.

4.2.6.2 DR-TAS Kinetics

The decay kinetics of all three doped samples and the two control materials at a probe pulse wavelength of 850 nm are shown in Figure 69. These are indicative of the relative concentration of electrons in these samples at time intervals > 10 µs after a 355 nm laser excitation pulse. TiO_2:[Rh5%] exhibits the lowest concentration of mobile electrons. Since the

laser wavelength used is 355 nm, well into the photoexcitation region for any TiO_2 material, it seems that the majority of photoexcited electrons in this sample have recombined on a much shorter timescale than the other samples. Rh doping in TiO_2 appears to reduce the concentration of long lived mobile electrons. Earlier XPS analysis indicates that Rh doping alone introduces Rh^{4+} with incomplete 4d t^5_{2g} states; the TAS kinetics reported here suggest that these states act as a trap for photogenerated electrons, reducing their lifetime after photoexcitation.

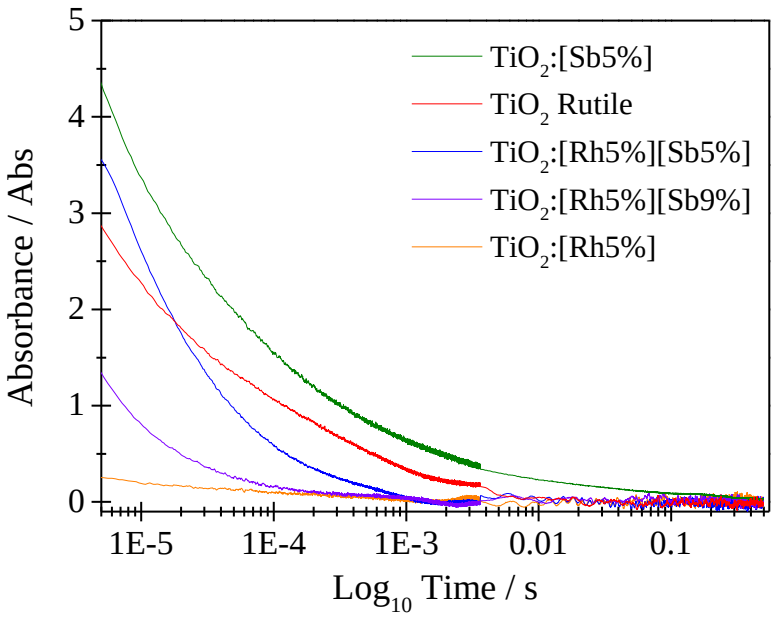

Figure 69: TAS recombination kinetics of TiO_2 fired rutile, TiO_2[Rh5%], TiO_2[Rh5%][Sb5%], TiO_2[Rh5%][Sb9%]

These decay spectra illustrate the effect of the addition of antimony to the system. In equimolar amounts, these dopants positively affect the number of charge carriers generated, as can be seen by the higher initial absorption of this sample, at 5 μs. Again, this result can be correlated with earlier electronic analysis, which indicates that the addition of Sb(V) to the system allows n-type character to be retained (the Fermi level in TiO_2:[Rh5%][Sb5%] is in a much more n-type position than that of TiO_2:[Rh5%]) by reducing Rh^{4+} to Rh^{3+} and filling the Rh 4d t_{2g} donor states. Therefore more electrons are present in the material and the electron trap presented by Rh^{4+} t^5_{2g} states are removed.

By comparison the TiO_2:[Rh5%][Sb9%] spectrum shows that further addition of Sb adversely affects the properties of TiO_2, since it exhibits a much lower initial absorption than both rutile and TiO_2:[Rh5%][Sb5%]. This indicates that additional Sb (V) ions possibly act as electron traps themselves. As shown by XPS depth profiling, Sb (V) ions in these samples reside near the surface- excess Sb (V) ions could act as trap states for electrons, being reduced to Sb (III), which as previously discussed, has been shown to be sterically stable at the TiO_2 surface.

An interesting result in this TAS study was that of the Sb doped control. The results presented indicate that the addition of Sb to TiO_2 alone increases the number of mobile electrons above that of the TiO_2 rutile control, which was fired at 1100 °C for 10 h. As previously stated in this chapter, reports of Sb doped TiO_2 also suggest that that Sb, when doped into TiO_2 alone, is segregated into Sb (III) at the surface and Sb (V) in the bulk with overall charge neutrality maintained.[173, 174] This would appear to eliminate the possibility that Sb is an n-type donor, since there would be no net addition of electrons. Literature studies have reported increased electrical conductivity of Sb doped TiO_2[188], which could indicate that the introduction of Sb 5s states into the conduction band makes electrons more mobile and therefore increases their lifetime once photogenerated.

The electron-hole recombination process can be compared in normalised spectra, shown in Figure 70. Here we can compare the longevity of the charges that have been produced, regardless of their absolute concentration. Fired rutile is shown to be the best performing material in this analysis; its shallow gradient indicates that the charges produced are the longest lived out of the materials tested. Of the doped samples TiO_2:[Rh5%] shows the next slowest decay kinetics, however the minimal number of charges produced makes this result

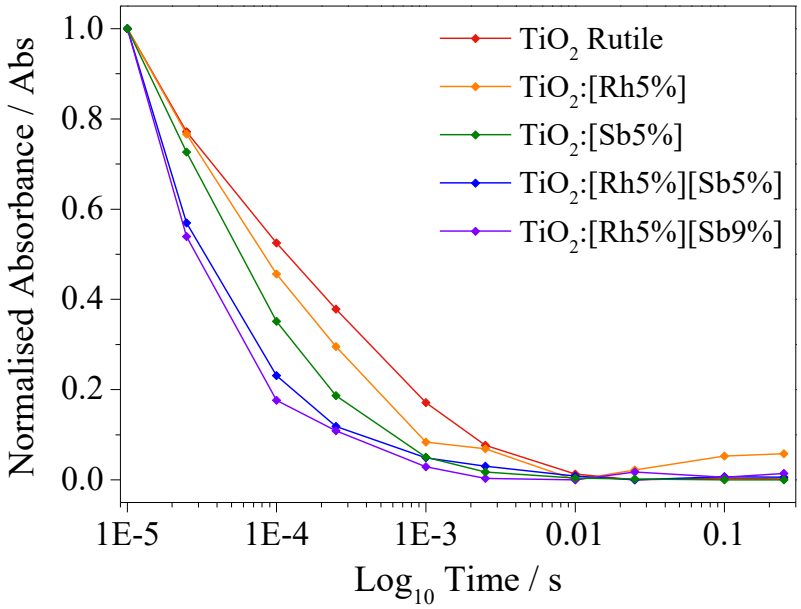

Figure 70: Normalised TAS spectra of TiO_2 fired rutile, TiO_2[Rh5%], TiO_2[Rh5%][Sb5%], TiO_2[Rh5%][Sb9%]

negligible with respect to the others. Interestingly both codoped samples show the fastest decay. This could indicate that the dopants may be providing recombination centres, where electrons and holes are unable to migrate and therefore recombine quickly. The TAS results described here indicate that Rh/Sb codoped samples outperform Rh doped TiO_2 in the absolute photogeneration of long-lived charge carriers. However, both codoped samples showed faster

recombination kinetics by comparison with control samples of fired TiO_2 and TiO_2:[Sb5%], which could indicate that the dopants are acting as trap states. However, previously reported visible light activity for these similar systems still makes them promising materials for photocatalytic processes. The samples presented in this thesis were all fired at 1100 ˚C, meaning that particle agglomeration was extensive. It is possible that increased grain boundaries adversely affected the recombination rates of all samples, however this does not account for the poor performance of codoped TiO_2. All doped samples presented in this thesis contained high concentrations of dopant ions (> 1%), which possibly reduced the charge carrier lifetimes in a way that would be less pronounced with lower dopant loadings; it is possible that an optimum loading could offer visible light activity, without the detrimental recombination kinetics observed in this study.

4.3 Conclusions

This investigation focused on the comprehensive characterisation of Rh and Sb doped titanium dioxide in the context of assessing their suitability for water splitting. Previous results from literature suggest potential superior activity by comparison to other Z-scheme components, from visible light activation offered by the addition of Rh 4d t_{2g} energy levels in the band gap. The addition of Sb has been shown to be instrumental in the activity of these materials.

This investigation determined that solid state synthesis can produce phase pure Rh doped and Sb/Rh codoped materials, though at higher doping regimes multiple grinding and heating stages are necessary to ensure a complete reaction. Scanning electron microscopy indicates that doped samples are highly agglomerated and that particle sizes are of the micron scale, which is to be expected for this type of high temperature synthesis. Lattice parameters determined from PXRD analysis suggest substitutional doping of Rh and Sb ions, since unit cell expansion is observed. The cell volume trend for codoped samples is non-linear, with high Sb loading resulting in a less pronounced expansion than equimolar doped materials; this suggests an increase in the number of oxygen vacancies compensating for additional electrons introduced to the system in the form of Sb (V).

XAS data showed that Rh ions are likely substitutional from nearest neighbour and next nearest neighbour bond distances, which are comparable to Ti-O and Ti-Ti distances in TiO_2. It was also shown that increased Sb loading reduces the oxidation state of Rh ions as the Rh K-edge increases in energy as Sb loading increases. While Sb EXAFS Fourier transform data were more difficult to interpret than the analogous Rh data, there was an indication from the next nearest neighbour distances that as Sb loading increased a more Sb_2O_5-like environment existed around Sb ions. Since Sb_2O_5 adopts a rutile like structure this indicates a substitutional doping regime at higher Sb loadings. This hypothesis is supported by lattice parameter data, which shows a decrease in cell volume at higher loadings. Finally, the Sb XANES edge indicates strongly that all Sb dopant ions are in the +5 oxidation state in the codoped samples.

XPS reveals that dopant ions are localised at the surface. In particular Sb ions are more surface localised than Rh and Sb appears to augment the degree of surface localisation of Rh ions as codoped samples possess higher XPS calculated Rh concentration than their singly doped counterparts. Fermi level energy changes due to dopant concentration were demonstrated by XPS, confirming previous literature reports. This investigation expanded understanding of the effects of this difference by investigating a wider range of dopant ratios than other investigations. By using the O 1s core line as an indicator of the change in Fermi level energy, it was determined that as Sb/Rh ratio increases the Fermi level energy decreases. The inclusion of a single crystal study to probe the change in Sb/Rh ratio as a function of depth in

combination with this data pertaining to the Fermi level position at different Sb/Rh ratios allowed for the position of the CBM and VBM at each point in the depth profile to be estimated. The revealed band bending may also to apply to powders and is likely to strongly affect charge carrier migration. The spatial confinement of dopants to affect (and effect) charge carrier migration is of fundamental importance in the field of silicon electronics. However, despite this the approach has not so far been intentionally taken in designing photocatalysts or photoelectrocatalysts. The results presented in this chapter indicate for the first time that a photocatalyst system exhibits spontaneous dopant segregation which is expected to cause significant band bending. This may explain the high photoactivity reported in this system; as previously stated Niishiro and co- workers[159] reported photoactivity of Rh and Sb codoped TiO_2 (where Sb/Rh = 0, 0.5, 1, 2 and 3 were investigated) and showed that, with Sb/Rh ≥ 2, O_2 evolution exceeds 10 mmol h^{-1}.

Also shown from XPS, was the change in Rh binding energy with addition of Sb. The Fermi level movement renders absolute binding energies meaningless since their relative positions in different samples cannot be compared. Instead the separation between O 1s and Rh 3d core lines was taken and a decrease in relative binding energy (and thus decrease in Rh oxidation state) was observed upon addition of Sb.

Optical data corroborated this decrease in Rh oxidation state with the addition of Sb in two ways. Firstly the strong absorption observed at ~1.0 eV in samples believed to contain high concentrations of Rh (IV), which is caused by VB to Rh 4d t^5_{2g} transitions, diminished on the introduction of Sb to the system. Secondly, the band edge in samples with low Sb content was more blue shifted than samples with Sb/Rh ≤ 1, which lie together at ~2.24 eV. This is thought to be due to the presence of low spin Rh (IV) d-d transitions, which are not allowed in d^6 Rh (III).

TAS of selected samples indicates lower charge carrier concentrations for the doped samples in comparison to undoped rutile. This contradicts literature reports that show similar samples exhibiting good photoactivity. It is possible that the samples generated in this investigation had absolute dopant concentrations high enough that the dopant ions acted as recombination sites and that the electrons and holes generated, recombined on a timescale shorter than the resolution of the DR-TAS setup used. The TAS kinetics for doped samples certainly indicates that higher doping regimes are detrimental to charge carrier mobility and therefore it is clear that an optimum dopant concentration and ratio exist, whereby there is enough Rh and Sb to effect a positive change in the electronic and optical properties of the TiO_2 without detrimentally affecting charge carrier generation and subsequent mobility.

Chapter 5: Investigation of the effects of Rh and Sb doping on the electronic structure of $SrTiO_3$

5.1 Introduction

Strontium titanate is a cubic perovskite semiconductor, which has been investigated for its solar water splitting potential since 1975[189], but with considerably less interest than TiO_2. For example, a Web of Science search conducted (on 3rd January 2017) using the search term "$SrTiO_3$ photocatalysis" revealed 216 results whereas the term "TiO_2 photocatalysis" yielded 17649 results. Interest in $SrTiO_3$ stems from its electronic similarity to TiO_2. Their band gaps are similar at around 3.2 eV[84], the band edges of both materials straddle the redox potentials of water splitting and are made up of similar combinations of orbitals: O 2p with some Ti covalence for the valence band and mainly Ti 3d for the conduction band.[84, 190-193] Strontium titanate has therefore been investigated for its water splitting and other photocatalytic potential regarding, for example, organic pollutant degradation pathways.[194-202]

Like TiO_2, the relatively wide band gap also means that without modification $SrTiO_3$ is only active under UV light and so research has focussed on reducing this energy requirement. Doping is a common method used to alter the electronic structure of a material and work on $SrTiO_3$ has mainly focussed on using different dopant ions to reduce its band gap with the hopes of activating it under visible light and therefore increasing its efficiency. Much of the work on $SrTiO_3$ has been informed by the vast amounts of research done on TiO_2 and therefore the range of dopants that have been tried with $SrTiO_3$ is reflective of this. Nitrogen has been explored as a potential dopant, since the N 2p valence orbitals mix well with O 2p of the $SrTiO_3$ valence band. N-doped $SrTiO_3$ has been prepared by various methods, including PLD of thin films[203, 204], solvothermal[205] and hydrothermal[206] methods to produce nanoparticles. These studies have shown that N-doping can reduce the $SrTiO_3$ band gap and increase the visible light activity of photocatalytic reactions similarly to its effect on TiO_2. A computational study found that co-doping with N/Mo = 2 could theoretically reduce the band gap of the material to 2.07 eV and produce a material with minimal recombination centres (which can arise in doped materials in the form of defects or partially occupied states close to the band edges), whilst also retaining a favourable valence band edge position.[207] Wei et al. determined from first-principles calculations of N-doped $SrTiO_3$ codoped with a variety of non-metals and metals (F, Cl, Br, I, V, Nb, Ta, Sc, Y, La) that the merits of cooping in $SrTiO_3$ include

increase primary dopant solubility, improved charge separation by the advent of an internal field, defect passivation and band gap narrowing. [208]

Scandium doped $SrTiO_3$ single crystals grown by float zone pulling have been reported as having p-type character. A substantial downshift (0.7 eV) in all photoemission core lines and the valence band were observed, indicating a change in the Fermi level position to a more p-type position than in n-type $SrTiO_3$ (Nb-doped).[209] A cathodic (p-type) photocurrent was observed from Ir doping of $SrTiO_3$; Ir, similar to Rh, can exist in the +3 or +4 oxidation state. Films produced by PLD showed that unlike Rh doped TiO_2, as discussed in Chapter 4, Ir doped $SrTiO_3$ shows better photoelectrochemical activity from Ir^{4+} incorporation than Ir^{3+}.[210] Rh^{3+} doped $SrTiO_3$ has been shown to produce cathodic photocurrent, indicating a p-type position of the Fermi level. [211, 212] As a photocatalyst $SrTiO_3$:Rh(1%) has been shown to evolve H_2 from methanol under visible light, with the authors suggesting that an induction period of low activity before an increase, is due to reduction of any Rh^{4+} to Rh^{3+}.[90] The colour of the material has been shown to be indicative of the Rh dopant oxidation state; Rh^{3+} produces yellow materials and Rh^{4+} produces purple materials.[213] Rh:$SrTiO_3$ has been investigated as a H_2 evolving side of a z-scheme, in combination with $BiVO_4$.[45, 48, 214]

This chapter describes a range of samples of Rh and Sb codoped $SrTiO_3$ made by two solid state synthesis routes. The investigation focuses on the oxidation state of Rh in doped samples in order to determine if Sb doping can cause Rh to exist in the preferable +3 oxidation state, in a similar manner to the effects observed for TiO_2 in Chapter 4. Synthesis comparable to that of the doped TiO_2 samples presented in Chapter 3 was attempted, whereby $SrTiO_3$ was directly reacted with the dopant oxide powders. This synthesis method differs from other solid state syntheses reported in the literature, where $SrCO_3$ has been reacted with TiO_2 and the relevant dopant oxide powders. The synthesis presented in this chapter, from which initial structural data are presented, was found to not be viable for high concentrations of dopant, but successful for low concentrations of dopant. Full characterisation of samples with low-doping concentrations (Sb < 1 %, Rh < 1 %) is discussed and the suitability of materials prepared by this method as possible photocatalysts is assessed.

5.2 Results

The results in this chapter are presented in two sections; firstly a study of samples doped with comparable concentrations of dopants to the doped TiO_2 samples presented in Chapter 4 (i.e. Rh 5%, Sb 1-9% at 2% intervals), followed by a study of samples doped with lower concentrations of dopant (Rh 0.5%, Sb 0.1-0.9% at 0.4% intervals).

5.2.1 Doped $SrTiO_3$ from direct reaction of $SrTiO_3$ and dopant oxides: Rh 5%, Sb 1-9%

In this section analysis of $SrTiO_3$ doped through direct synthesis with Rh_2O_3 and Sb_2O_5 is described. These samples were doped with 5% Rh and codoped with 1, 3, 5, 7 and 9% Sb. Throughout the discussion these samples are labelled with this information.

5.2.1.1 Phase Identification

PXRD was used to determine the phase purity of doped $SrTiO_3$ samples. Diffraction patterns were recorded on a Bruker D4 diffractometer using Cu-Kα radiation, λ = 1.541 Å. After one firing at 1100 °C for 10 hours all samples produced PXRD patterns containing impurities. Figure 71 shows PXRD patterns of all samples after *two* firings at 1100 °C for a further 10

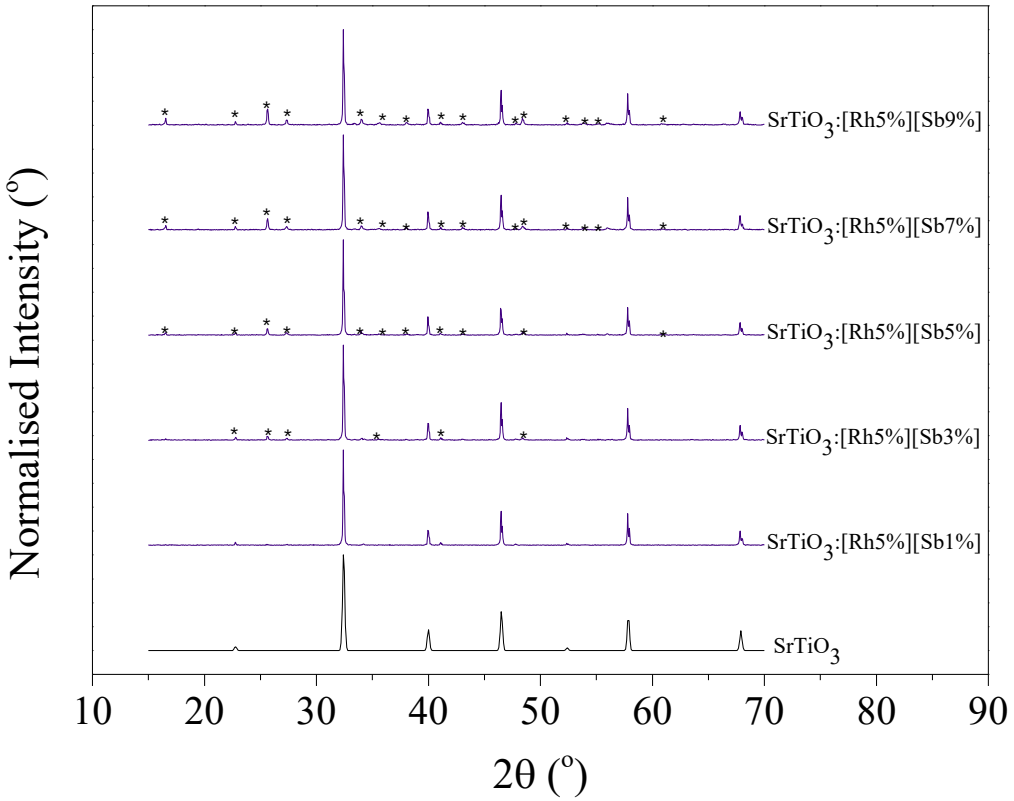

Figure 71: XRD pattern of products from solid state reaction of $SrTiO_3$ with the appropriate molar amount of dopant to yield doped $SrTiO_3$ with 5 % Rh doping and 1-9% Sb doping at 2% intervals. The data shown are for mixtures fired twice at 1100 °C for 10 hours each.

hours; again impurity peaks were present. Further calcination, resulting in a total of 30 hours of high temperature (1100 °C) heating, did not complete the reaction and the patterns shown in Figure 71 are consistent for samples in this series prepared by any length of calcination completed in this study.

The lattice parameter, a, was found to remain the same upon on doping, it was determined as 3.91 Å in undoped $SrTiO_3$ and 3.91 Å ±0.0005 in all doped samples. Since the impurity peaks in these samples are numerous, peaks associated with $SrTiO_3$ were removed from the pattern of $SrTiO_3$:[Rh5%][Sb9%]- this pattern exhibited the most impurity peaks- and this impurity fingerprint has been compared to other patterns in order to identify the impurities. All impurity peaks found in other samples were present in the PXRD pattern of $SrTiO_3$:[Rh5%][Sb9%], and so this collection of peaks can be considered as representative of the impurities of all samples. The impurity fingerprint is shown in Figure 72 by comparison with starting materials Rh_2O_3 and Sb_2O_3 (both cubic and orthorhombic polymorphs) and other possible antimony oxide impurities Sb_2O_4 and Sb_2O_5.

As can be seen in these comparative figures, there is no single pattern that correlates with the impurity fingerprint of $SrTiO_3$:[Rh5%][Sb9%]. The highest intensity peak in the impurity fingerprint appears at 26 ° 2θ; this could correlate to the peak found at 25 ° 2θ in Sb_2O_5, though other prominent peaks in the Sb_2O_5 pattern are absent from the impurity fingerprint, such as the peak at 31 ° 2θ. In addition there are additional peaks in the impurity fingerprint that do not appear in any of the starting material or antimony oxide patterns, such as those found at 17 ° 2θ and 32 ° 2θ. XPS quantification (discussed in section 5.2.1.2 below) indicated that the surface of the materials was Sr-rich and O-poor. However, patterns for different $Sr_xTi_yO_z$ compositions, such as $Sr_3Ti_2O_7$ [215] , Sr_4TiO_{10}[216] and Sr_2TiO_4 [217, 218] (shown in Figure 73) also do not correlate with the impurity fingerprint pattern.

While it is not possible to ascertain the identity of the impurity phases that are present in these samples, it is clear from comparison with a variety of PXRD patterns for other phases that could possibly have been formed, that the Sb_2O_5 pattern exhibits the highest similarity to the impurity fingerprint pattern. However, it is important to note that this would represent a highly distorted Sb_2O_5 lattice, likely distorted by the presence of Sr, Ti and Rh ions in a mixed phase of all elements. The sharp nature of the peaks indicate that this phase or phases

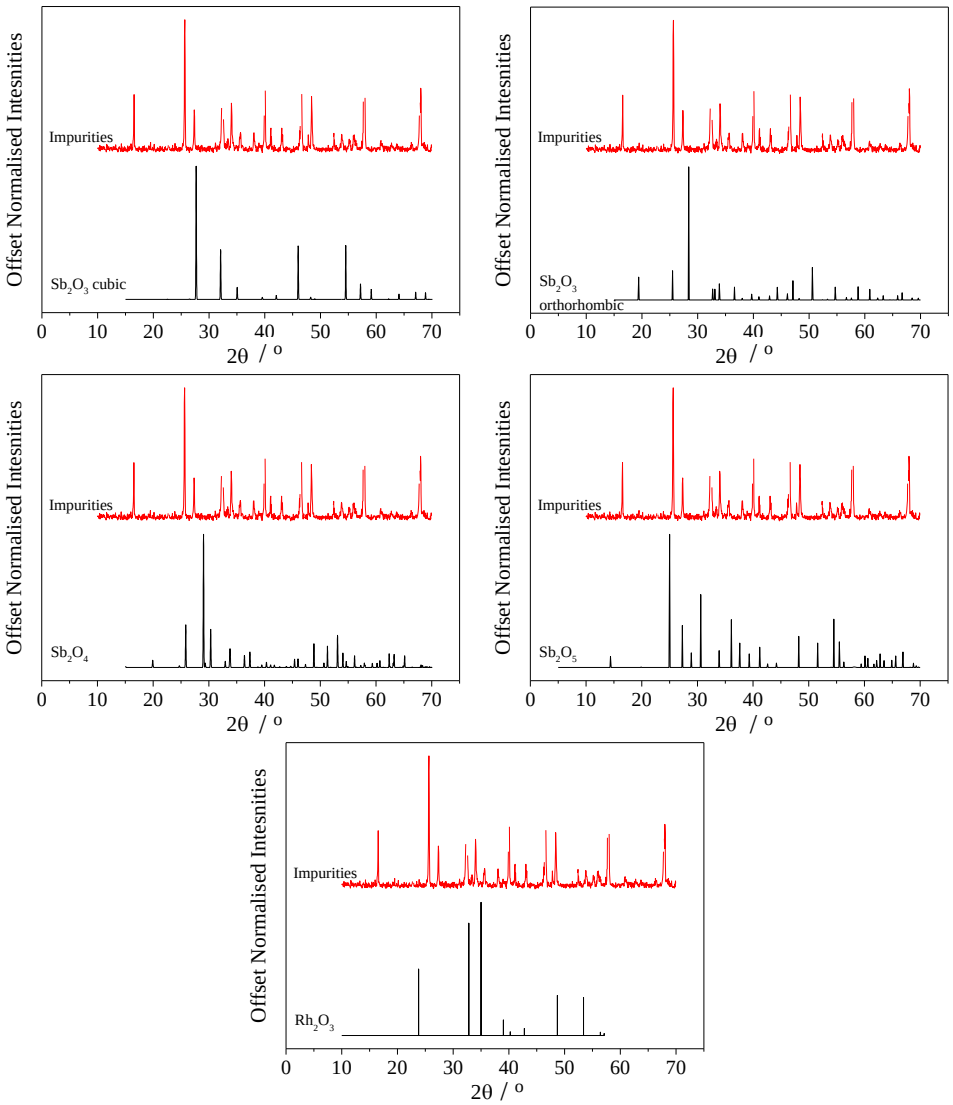

Figure 72: XRD patterns for dopant starting materials Rh_2O_3, both Sb_2O_3 polymorphs and possible other antimony oxide impurities Sb_2O_4 and Sb_2O_5 (all in black) compared with the impurity fingerprint from sample $SrTiO_3$[Rh5%][Sb9%]

are crystalline and therefore ordered; due to the lack of existing data on Sb and Rh mixing into the $SrTiO_3$ lattice, it is difficult to determine the exact nature of the reaction that has occurred. This additional phase was not observed when the same method was used to dope TiO_2; in Chapter 4, only the most highly doped sample TiO_2:[Rh5%][Sb9%] revealed any impurities, which were attributed to unreacted antimony oxide and were eliminated by a second firing of the powder. Thus it is clear that the differences in the $SrTiO_3$ structure, which is cubic perovskite, and the TiO_2 structure (rutile) impact the ability of dopant ions to diffuse into the titanate and replace Ti^{4+} cations.

The cubic perovskite structure of $SrTiO_3$ possesses TiO_6 octahedra that are corner sharing; by comparison TiO_6 octahedra in rutile TiO_2 share edges. This difference could result in dopant ions being more easily able to diffuse and substitute in TiO_2 rutile than in $SrTiO_3$.

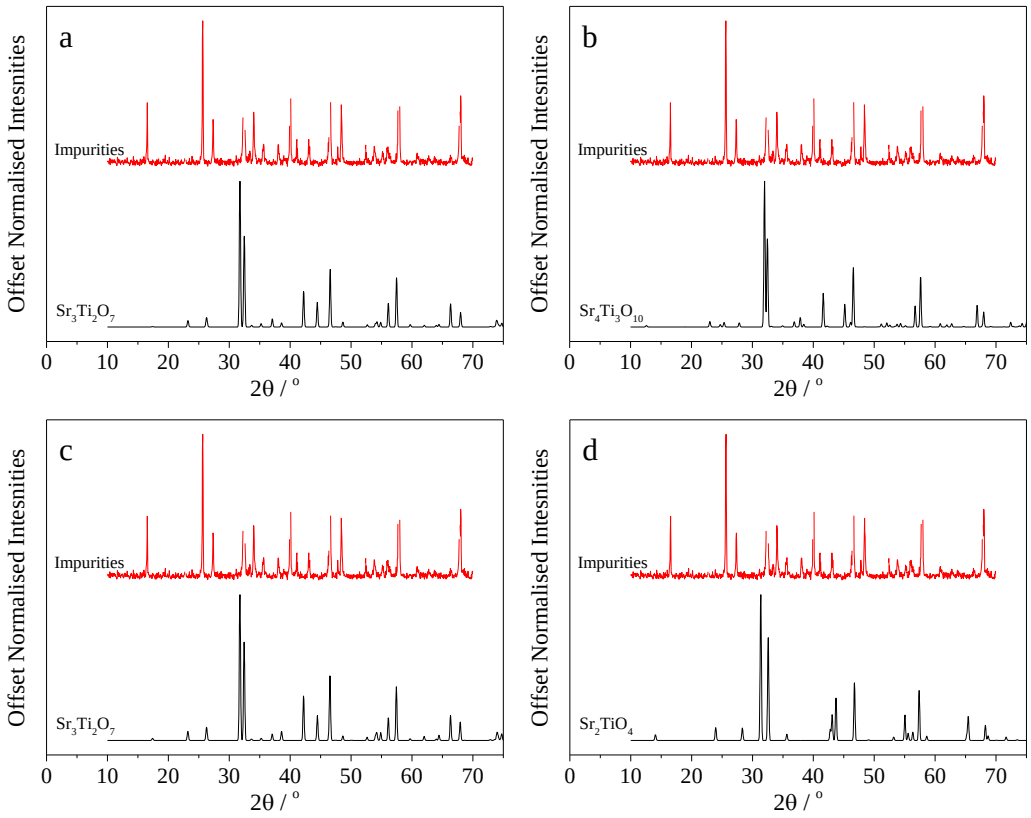

Figure 73: Impurity fingerprint pattern (red, top) by comparison with Sr-rich phases a) $Sr_3Ti_2O_7$ (Ruddlesden-Popper) b) $Sr_4Ti_3O_{10}$ (Ruddlesden-Popper) c) $Sr_3Ti_2O_7$ (Elcombe) and d) Sr_2TiO_4 (Kawamura)

5.2.1.2 XPS Quantification

High-resolution core line spectra were collected for Sr 4d, Ti 2p, O 1s and Rh 3d. As with samples in previous chapters, the Sb 3d region overlaps the O 1s region and so these spectra were collected together and fitted by utilising the Sb $3d_{3/2}$ peak, which lies 9.4 eV higher than the Sb $3d_{5/2}$ / O 1s region. Explanation of this fitting has been described in Chapters 3 and 4 previously and example spectra have been shown. Elemental quantification of the sample surfaces was completed by fitting of core line spectra, determination of peak areas and normalisation with the appropriate relative sensitivity factor ascertained from the instrument used for analysis. The atomic percentages yielded are shown in Table 18 below alongside theoretical ratios for stoichiometric $SrTiO_3$. Comparison of these values with the stoichiometric percentages that are shown in row one of the table highlights the Sr-rich, O-poor composition of the surface of these materials, where the ratio should be Sb/O = 0.33, but is consistently around 0.6 in these samples.

These results confirmed that direct synthesis of $SrTiO_3$ with dopant oxide powders at these concentrations would not yield phase pure, stoichiometric materials, suitable for further characterisation within the scope of this project. Thus, samples with dopant concentrations 10

times lower were prepared, using the same synthesis method. These results are discussed in section 5.2.2.

	Atomic Percentages				
Sample	Sr	O	Ti	Rh	Sb
$SrTiO_3$ theoretical	20	60	20-(x+y)	x	y
$SrTiO_3$[Rh5%][Sb1%]	28.15	50.90	16.63	1.56	2.77
$SrTiO_3$[Rh5%][Sb3%]	25.17	53.38	14.53	2.37	4.55
$SrTiO_3$[Rh5%][Sb5%]	27.80	47.98	16.71	2.03	5.48
$SrTiO_3$[Rh5%][Sb7%]	27.50	48.30	15.44	2.34	6.42
$SrTiO_3$[Rh5%][Sb9%]	28.55	42.70	16.67	3.24	8.85

Table 18: Atomic percentages of all atoms present in doped $SrTiO_3$ samples (total dopant concentration > 1.5 mol. %)

5.2.2 Doped $SrTiO_3$ from direct reaction of $SrTiO_3$ and dopant oxides: Rh 0.5%, Sb 0.1-0.9%

In this section analysis of $SrTiO_3$ doped through direct synthesis with Rh_2O_3 and Sb_2O_5 is described. These samples were doped with 0.5% Rh and codoped with 0.1, 0.5 and 0.9% Sb. For brevity the samples have been coded as follows:

STO 01: $SrTiO_3$:[Rh0.5%]

STO 02: $SrTiO_3$:[Rh0.5%][Sb0.1%]

STO 03: $SrTiO_3$:[Rh0.5%][Sb0.5%]

STO 04: $SrTiO_3$:[Rh0.5%][Sb0.9%]

5.2.2.1 Phase Identification

PXRD was used to determine the phase purity of the doped $SrTiO_3$ and as-purchased $SrTiO_3$ staring material. Diffraction patterns were recorded on a STOE (Mo) STADI P diffractometer. The instrument operates with a Mo X-ray source (Mo tube 50 kV 30 mA,), monochromated (pre-sample Ge (111) monochromator selects Kα1, λ = 0.709 Å) and a Dectris Mython 1k silicon strip detector covering 18° 2θ. Samples were run in transmission mode, with the sample rotated in the X-ray beam. As with other data in this thesis the data have been transformed to represent data collected with Cu Kα radiation (λ = 1.541 Å) for ease of comparison.

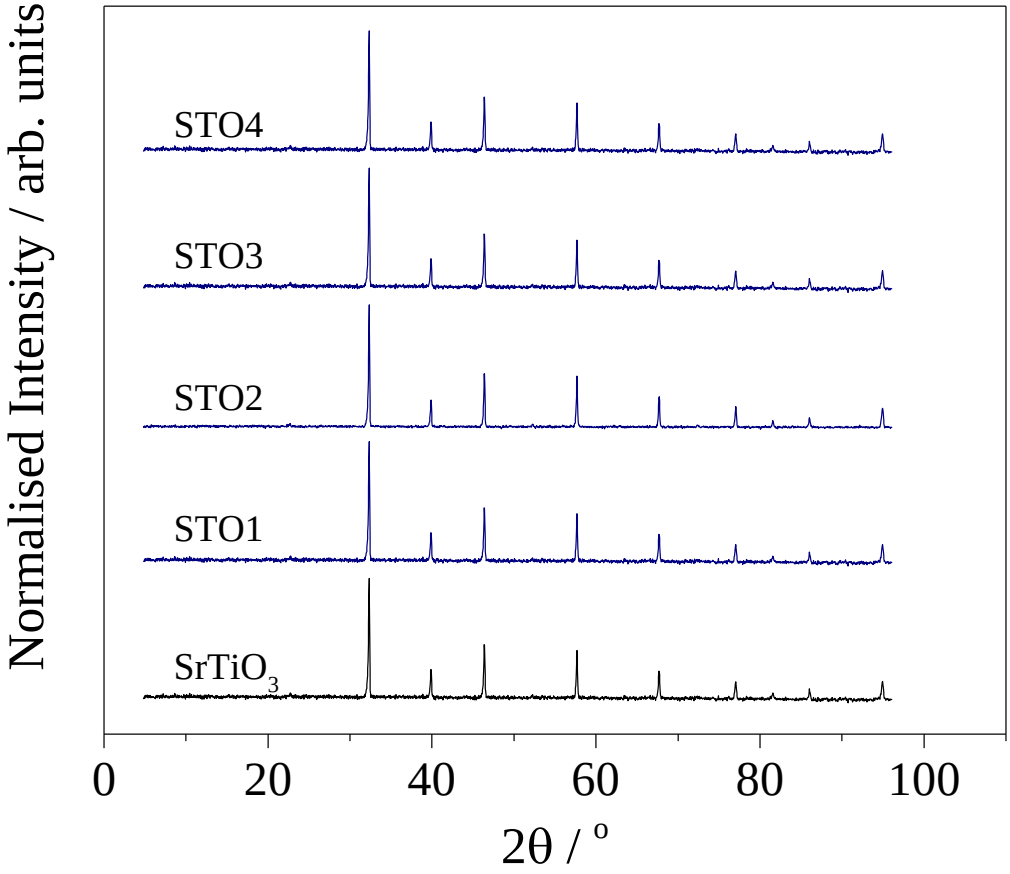

Figure 74: PXRD patterns of SrTiO3 and doped samples STO 01, 02, 03 and 04

As can be seen in Figure 74, PXRD patterns of all doped samples matched well with the starting material, with no additional peaks due to Rh_2O_3 or Sb_2O_3 dopant sources present. Additionally no clear impurity peaks were discernible indicating the absence of Sr-rich phases or anything similar to the impurity fingerprint of samples described in section 5.2.1. However, it is notable that due to the lower signal to noise ratio of the data collected on the STOE diffractometer, small amounts of impurity could be masked. The peaks of all patterns align well, with no easily discernible peak shift indicating at first instance that any doping that has occurred has resulted in minimal changes to the lattice; section 5.2.1.2 explores this in further detail. The intensity ratios of the peaks in all patterns remain the same, indicating that heating did not result in preferential growth at any particular face.

5.2.1.2 Lattice Parameters and Cell Volumes

In order to quantify any differences between the diffraction data, least squares refinement was completed using peak positions to determine the cell parameters and cell volume. Diffraction patterns were indexed in the perovskite structure, *Pm-3m* space group, from a standard pattern.[219] Lattice parameter and cell volume data for doped samples revealed no crystallographic change upon doping.

The lack of lattice expansion could indicate the presence of Rh^{4+} (ionic radius = 0.600 Å) in these samples, which has a similar ionic radius to Ti^{4+} (ionic radius = 0.605 Å) and would therefore not affect the lattice parameter. This is likely the case in STO1, where only Rh is present as a dopant, since the dopant ions are thought (for reasons of size and charge) to substitute onto the titanium site. However, the presence of Sb^{5+} is thought to encourage the formation of Rh^{3+} which has a larger ionic radius (0.665 Å) and therefore in samples STO2, STO3 and STO4 a cell expansion would be expected.

The presence of Sb^{3+} in these samples is unlikely; Sb^{3+} has an ionic radius of 0.76 Å, which would cause a substantial lattice expansion. It is possible that the dopant concentrations in these samples are too small for any lattice expansion to be observed, since XRD is a bulk technique and the data here represent an average value. Thus it is difficult to conclusively draw conclusions regarding the nature of the dopants in these materials from XRD data alone. It could be possible that, as with samples described in section 5.2.1, a secondary phase has been created but that this is masked by the noise in XRD data for these samples, which contain dopants at much lower concentrations.

As well as these explanations, defects associated with the presence of the dopant ions, for example O vacancies, could affect the cell volume. Thus, it's possible that Rh^{3+} is present in codoped samples, but that associated defects allow the lattice to appear to remain the same size. In the absence of a definitive answer, it is difficult to definitively state the nature of dopants in these samples. In order to further investigate the local structure, X-ray absorption measurements were obtained for Sb ions in the structure. This analysis follows in section 5.2.2 below.

5.2.2 X-ray Absorption Spectroscopy of Sb K-edge

Sb K-edge X-ray absorption measurements were taken at the ESRF on BM26.

Sb K-edge data for STO 02, STO 03 and STO 04 are shown in Figure 75 alongside standard compounds, Sb_2O_3 and Sb_2O_5. Spectra have been normalised for ease of comparison; the raw data for doped compounds has much lower signal to noise ratio than that of the standard compounds. These measurements and the subsequent data analysis were completed with the assistance and supervision of Professor Gopinathan Sankar.

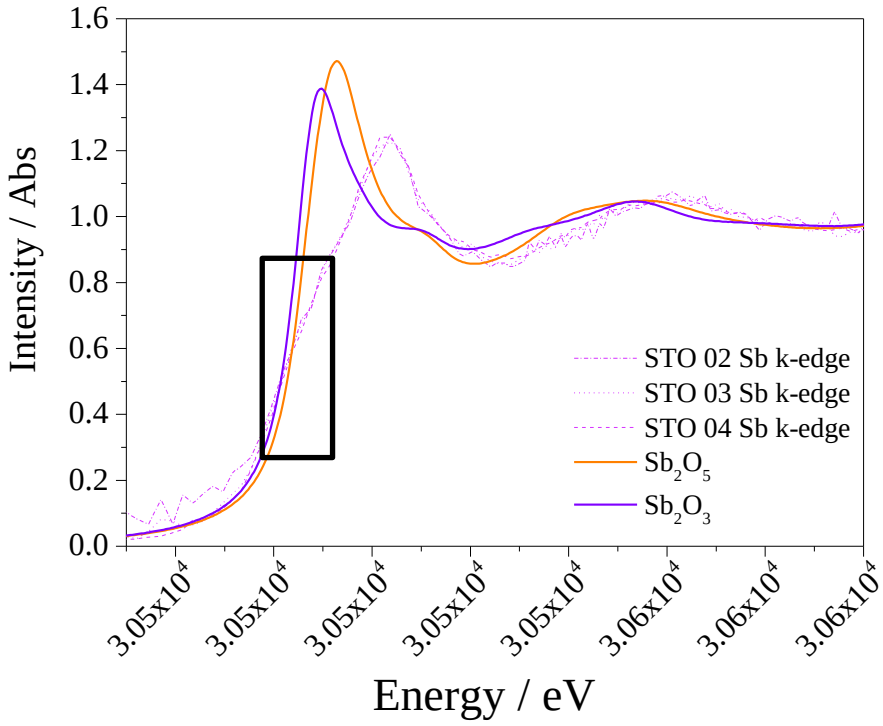

Figure 75: X-ray absorption spectra of STO 02, STO 03 and STO 04 by comparison with Sb_2O_5, Sb_2O_3 standards

It is clear from Figure 75 that the Sb K-edge spectral shapes are very different for Sb ions in doped $SrTiO_3$ samples than for Sb ions in Sb_2O_3 and Sb_2O_5. X-ray absorption is easily influenced by the local structure of the coordination environment surrounding the element analysed. The observed difference between doped sample spectra and Sb-oxide spectra is a strong indication that Sb is incorporated into a structure very different to that of the native (III) and (V) oxides, which are orthorhombic and cubic respectively. Sb^{3+} in Sb_2O_3 is coordinated to O^{2-} in a distorted tetrahedron[140], whereas in Sb_2O_5 it is in octahedral coordination.[220] Thus, these data could indicate that it is possible that Sb in these samples does not reside on the Ti^{4+} site, which is octahedral.

The differences in spectral shape also render the data inconclusive regarding the oxidation state of Sb ions in the doped materials. Figure 76 shows more clearly that the K-edges of STO 02, 03 and 04 do not definitively align with either Sb_2O_3 or Sb_2O_5 and therefore from these data, the antimony dopant oxidation state cannot be determined. Importantly, although no oxidation state information can be determined from these Sb K-edge absorption spectra, all three doped samples align with each other well, indicating that Sb ions are likely in the same oxidation state and have very similar local environment in codoped STO, regardless of Sb/Rh ratio.

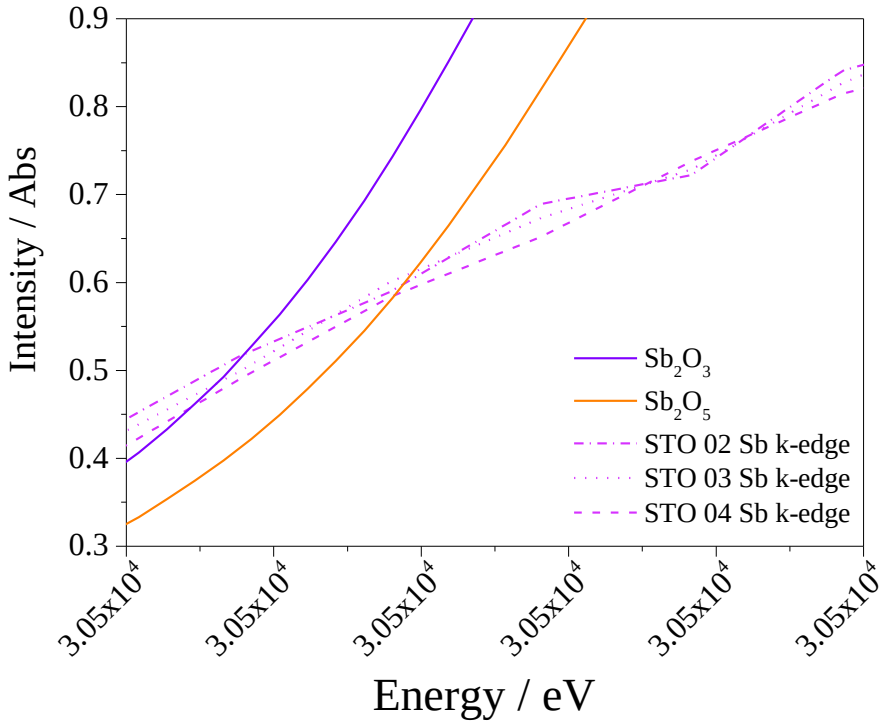

Figure 76: Close up of the Sb K-edge of STO 02, STO 03, STO 04, Sb_2O_5 and Sb_2O_3 between 30500 and 30500 eV

In the absence of perovskite B-site Sb-doped $SrTiO_3$ XAS data in the literature, other B-site doped $SrTiO_3$ data were considered. Studies using Mn, Nb and Cr have all exhibited a pre-edge feature, which is indicative of oxidation state.[221-223] This feature absent in the data collected for doped samples in this thesis, although it is possible that some indicative feature lies below the lower limit of incident radiation used in these measurements. Cr-doped $SrTiO_3$ has been shown to exhibit a difference in K-edge gradient depending on the oxidised or reduced nature of the $SrTiO_3$ host material[221]; a shallower edge was observed for reduced samples with respect to oxidised samples. A similar difference was observed in the Fe K-edge of Fe-doped $SrTiO_3$ which was attributed to the switch between Fe^{3+} (oxidised) and Fe^{2+} (reduced).[224] This could indicate that the broad K-edge observed in the doped samples presented in this thesis is due to reduced Sb, though in the absence of comparative data it is difficult for this to be definitively assigned.

Low concentrations of Sb ions in all three samples also made EXAFS analysis problematic. What follows is analysis of the EXAFS Fourier transform data for STO 04, which contained the highest concentration of Sb (for phase pure samples) at 0.9 mol. %. Since the XA spectra for all three codoped samples appear well-aligned, it is reasonable to tentatively draw conclusions pertaining to all three codoped samples, based upon the analysis of STO 04 alone.

Figure 77 shows the EXAFS Fourier transform and r-fit of the STO 04 Sb K-edge. The data were modelled working from the assumption that Sb in this sample is 6-coordinate, as it should be if it resides on the Ti site. This generated a reasonable fit and corroborates cell volume values, which all increased upon doping and therefore indicated that both Rh and Sb dopants reside on Ti^{4+} sites, rather than the much larger Sr^{2+} sites.

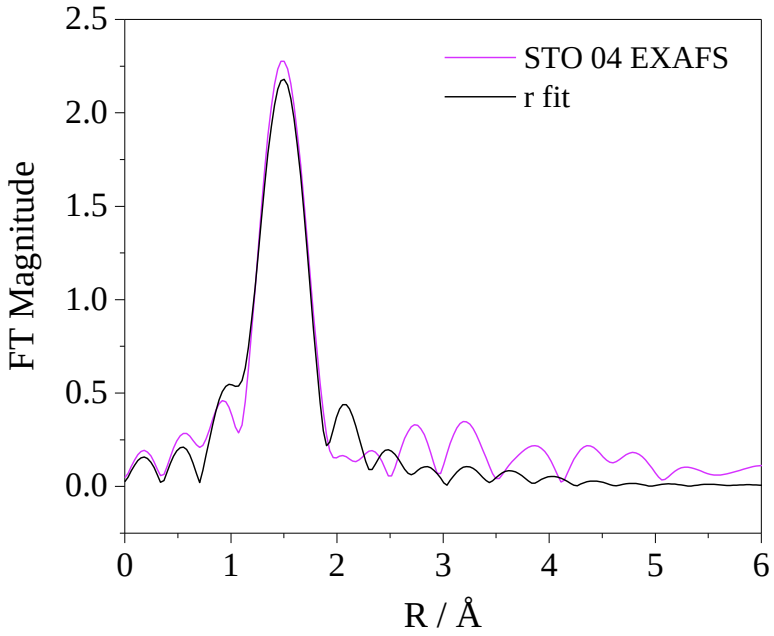

Figure 77: STO 04 EXAFS Fourier transform and r-fit data producing Sb-O bond length 1.95 Å. Note that the data presented have not been corrected for phase shift and therefore x-axis positions correlating to bond length appear short.

The nearest neighbour bond distance was determined from EXAFS to be 1.95 Å. This is indicative of Sb(V)-O bonds[225], rather than Sb (III)-O bonds which are slightly longer at ~1.977 in both orthorhombic and cubic Sb_2O_3.[140, 226] However, since determination of local bond lengths by EXAFS is reliable within an error limit of 0.02 Å[227], this is not conclusive evidence for the presence of Sb(V) in these samples.

XAS data have resulted in contrasting interpretations of the oxidation state of Sb in these samples. The K-edge positions for Sb ions in doped STO samples are not comparable to Sb-oxides, which would usually provide a reasonable indication of the relative oxidation state. Other B-site doped $SrTiO_3$ XAS data however indicates that a broad K-edge shape can be attributed to the reduced form of the dopant cation. Contrastingly, EXAFS modelling indicates that six coordinate Sb-O bond lengths in STO 04 are more comparative to Sb (V)-O than Sb (III)-O. Due to the high degree of similarity between doped sample spectra it is reasonable to expect the same to be true of STO 02 and 03. In conclusion, it is not possible to definitively

assign the oxidation state or describe the environment surrounding Sb ions in these samples without further measurements and investigation.

5.2.3 X-ray Photoelectron Spectroscopy

5.2.3.1 Quantification of dopant ions

High-resolution XP spectra of the Sr 4d, Ti 2p, O 1s and Rh 3d core line regions were used to quantify the surface composition of all samples. Since the O 1s and Sb 3d core lines overlap, the O 1s region was used to also provide information on Sb dopants. All core lines were modelled using Gaussian-Lorentzian fits to determine the relative concentrations of the elements present. All spectra were corrected for charging to adventitious carbon at 284.8 eV.[228] Fitting of the Sb 3d/O 1s region required the same consideration as has been outlined in Chapters 3 and 4 of this thesis, whereby the Sb $3d_{3/2}$ peak was used to quantify Sb contributions and also to provide a way of fitting the Sb $3d_{5/2}$ peak, which is completely masked by O 1s contributions. The Sb $3d_{5/2}$ peak can be modelled from the Sb $3d_{3/2}$ peak by constraining its area (2:3 ratio with Sb $3d_{3/2}$), full-width half-maximum (equal to Sb $3d_{3/2}$) and doublet separation (9.4 eV lower in binding energy than Sb $3d_{3/2}$) to that of the Sb $3d_{3/2}$. Once the Sb $3d_{5/2}$ component was fitted, the remainder of the area under this peak was fitted with an O 1s oxide anion peak at around 530 eV and an OH contribution, which manifests as a broad shoulder to the high binding energy side of the O 1s peak. All O 1s binding energy data presented hereafter are values obtained from this method of fitting and the OH feature was included for all fitting to produce elemental atomic percentages. Example spectra demonstrating this fitting have been shown in both Chapters 3 and 4.

Quantification of the Sb concentration indicated that in all samples containing Sb, these ions were highly localised to the surface. Figure 78 shows the XPS calculated percentage of Sb vs nominal [Sb]. It is clear that STO 02, STO 03 and STO 04 exhibited surface Sb concentrations of at least 3x the nominal amount used. Figure 78 also shows surface enrichment of Rh ions with respect to the nominal amount of Rh used for reaction. In contrast to TiO_2 doped samples discussed in Chapter 4, Sb co-doping in $SrTiO_3$ does not appear to affect Rh surface concentration in a significant way. In all STO doped samples the nominal Rh concentration is held at 0.5 %; when no Sb codopant is present the XPS measured surface concentration of Rh is 0.44 %. As nominal Sb concentration increases across the rage 0.1, 0.5 and 0.9 % the surface concentration of Rh is calculated to be 0.46, 0.41 and 0.43 % respectively. The measured concentration of Rh is lower than the nominal amount used for reaction. This could indicate that some Rh diffusion away from the surface may have occurred. However, error in XPS quantification is approximately ± 0.1%.[229, 230]

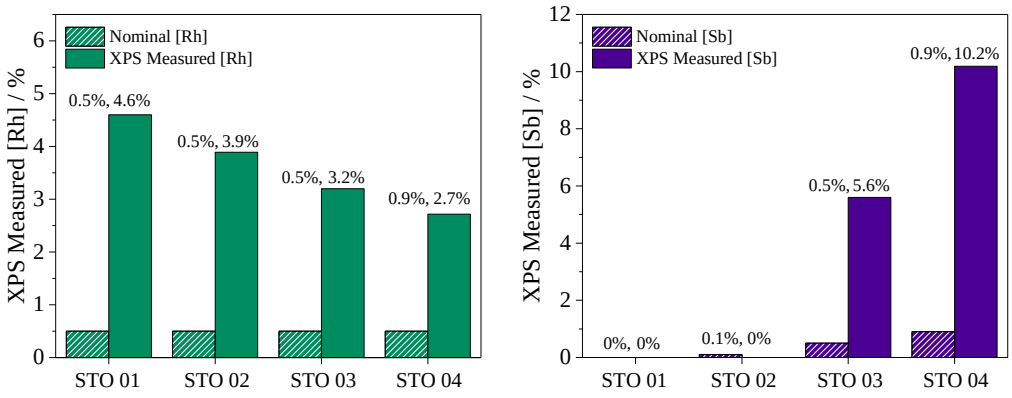

Figure 78: XPS measured Sb concentrations vs nominal Sb concentrations (right) and XPS measured Rh concentrations vs nominal Rh concentrations for STO 01, 02, 03 and 04 (left)

Since XAS measurements were unable to eliminate the presence of Sb^{3+} it is possible that the surface enrichment of Sb is due to the greater steric stability of Sb^{3+} at the surface of doped materials, as shown to be true in TiO_2 and SnO_2.[173, 174, 176] Here the lone pair of Sb^{3+} is more easily accommodated at the surface where there is greater degree of freedom for the formation of compensatory defects in the crystal structure. However, as mentioned in Chapter 4, where Sb^{5+} *was* confirmed in doped TiO_2 by XAS measurements and also exhibited surface enrichment, it is possible that there are thermodynamic reasons for Sb^{5+} to exist at the surface.

Elemental analysis and quantification of the core line spectra revealed pristine $SrTiO_3$ to be slightly O-rich, Ti-poor. The doped samples on the other hand were determined to be Sr-rich, which supports the theory that even a small amount of doping via direct reaction of $SrTiO_3$ and the dopant oxides produces a secondary phase of Sr-rich material. In these samples it is possible that this secondary phase was not detected in PXRD measurements due to the low concentration.

Sample	Sr	O	Ti	Rh	Sb
	20	60	20-(x+y)	x	y
$SrTiO_3$	21.46	63.89	14.64		
STO 01	33.91	46.10	19.55	0.44	-
STO 02	29.28	54.57	18.22	0.46	0.47
STO 03	29.18	51.04	16.54	0.41	2.82
STO 04	29.48	49.87	17.49	0.43	2.74

Table 19: Atomic percentages of all atoms present in doped $SrTiO_3$ samples (total dopant concentration < 1.5 mol. %)

5.2.3.2 Valence band spectra and E_F position

VB spectra were recorded to probe the electronic structure of the doped materials. Comparable to Chapter 4, the role of Rh as a dopant in $SrTiO_3$ is to insert 4d t_{2g} donor levels into the band gap, at a slightly higher energy than the O 2p orbitals, which make up the majority of the $SrTiO_3$ VB. It is expected that by comparison with pristine $SrTiO_3$, a Rh feature should be visible in the spectra of doped samples. Since the doping concentrations in the samples presented in this chapter are much lower than those in samples from Chapter 4, it would be expected that the Rh 4d feature would be much less prominent than VB spectra presented previously. In order to probe the E_F position of these materials the VB edge position will be considered, along with the O 1s binding energy, which can be used as a marker for changes in the E_F position of these materials, since it should remain unchanged across the range of sample if the E_F has not moved.

To model the VB spectra of all doped samples a VB spectrum for pristine $SrTiO_3$ was fitted with three Gaussian-Lorentzian components, as shown in Figure 79. The lowest and highest binding energy components were constrained to the central, largest component by area, FWHM and position. This fit was used to account for the pristine $SrTiO_3$ portion of doped sample VB spectra. Each doped sample required an additional feature to the low binding energy side of the valence band in order to fit the data to the lowest residual STD (i.e. best fit). This feature is highlighted in purple in the spectra shown in Figure 80, which shows comparative VB spectra of STO1, STO2, STO3, and STO4.

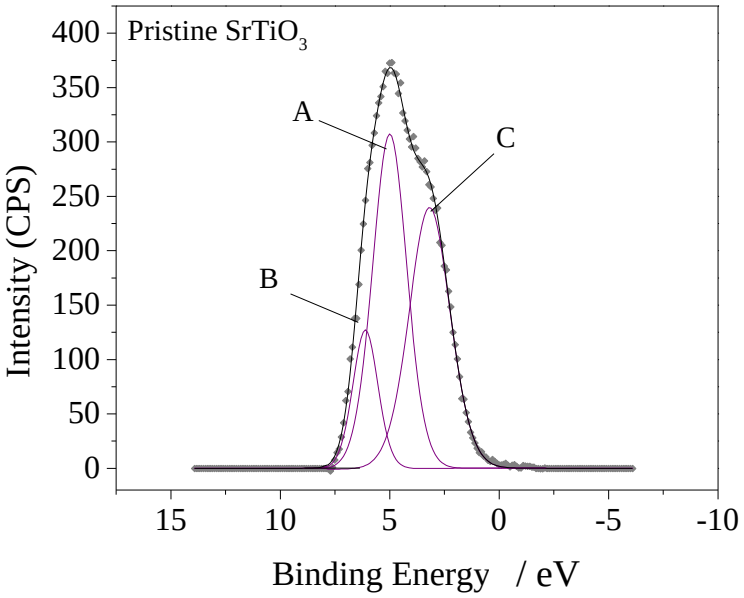

Figure 79: Fitted valence band of pristine $SrTiO_3$

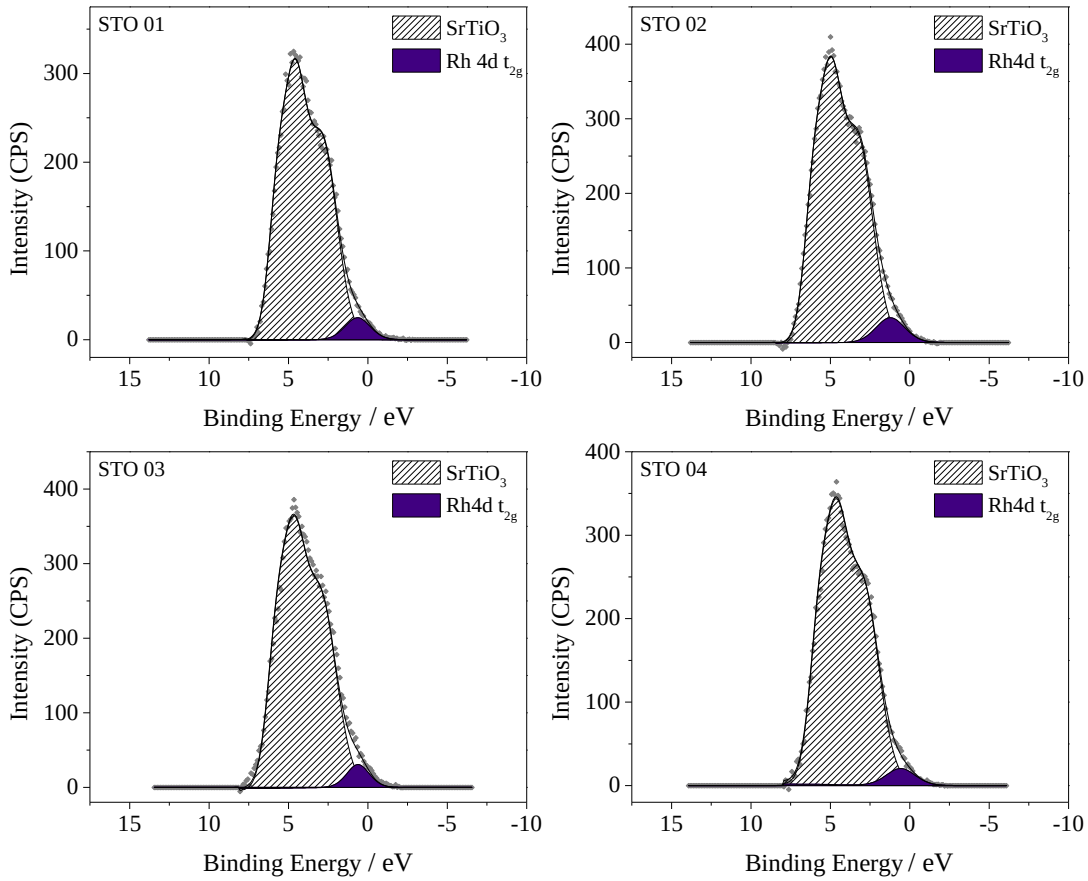

Figure 80: Valence band spectra of STO1, STO2, STO3 and STO4 showing the SrTiO3 portion in hatched lines and the Rh component in purple

As indicated by quantification of Rh in these samples, the Rh 4d t_{2g} band gap feature is of approximately equal size across all samples. The position of component A, to which the rest of the VB fit was constrained, in these spectra is observed to change in position, indicating that E_F changes position. The spectra shown in Figure 80were taken from powder samples and represent the average data of 200 scans. Grey markers show the actual data, with the "envelope" line of best fit shown in black. Even with a high total scans the data are noisy and so, while general conclusions regarding E_F position can be drawn, a more firm idea of the relative change in position has been taken from O 1s binding energy data, which have been plotted in Figure 81.

The changes in O 1s binding energy, which are reflective of the changes in VB position, with respect to those of pristine $SrTiO_3$ do not reflect the trend observed for Rh/Sb codoped TiO_2. It would is expected that Rh^{4+} is present when mono-doped and that this causes a decrease in E_F position, this is certainly observed in $SrTiO_3$ as it was in TiO_2. However, upon codoping with Sb, the E_F position was restored to that of pristine TiO_2 once Sb/Rh > 1.4; this is not the case in $SrTiO_3$. As can be seen from Figure 81, the O 1s positon of STO1 is considerably lower than that of pristine $SrTiO_3$ and while it is raised upon doping with Sb, the dopant ratio

has no effect on O 1s BE. In terms of E_F position, this translates to a lowering of the E_F to a more p-type position upon Rh doping and a raising of the E_F to a slightly less p-type position upon Sb doping. The key difference between doped TiO_2 and $SrTiO_3$ is that addition of increasing amounts of Sb does not raise the E_F position back to that of pristine $SrTiO_3$. Thus, all doped $SrTiO_3$ samples in this study are more p-type in than pristine $SrTiO_3$. The assumptions made in this study are that all dopants reside in the $SrTiO_3$ lattice, that Sb exists as Sb^{5+} and that Rh dopants exist in the +4 state when doped alone, but the +3 state when codoped in at least equimolar amounts. The observation that the amount of Sb does not correlate to incremental changes in the E_F position as [Sb] increases must mean that one or more of these assumptions is incorrect.

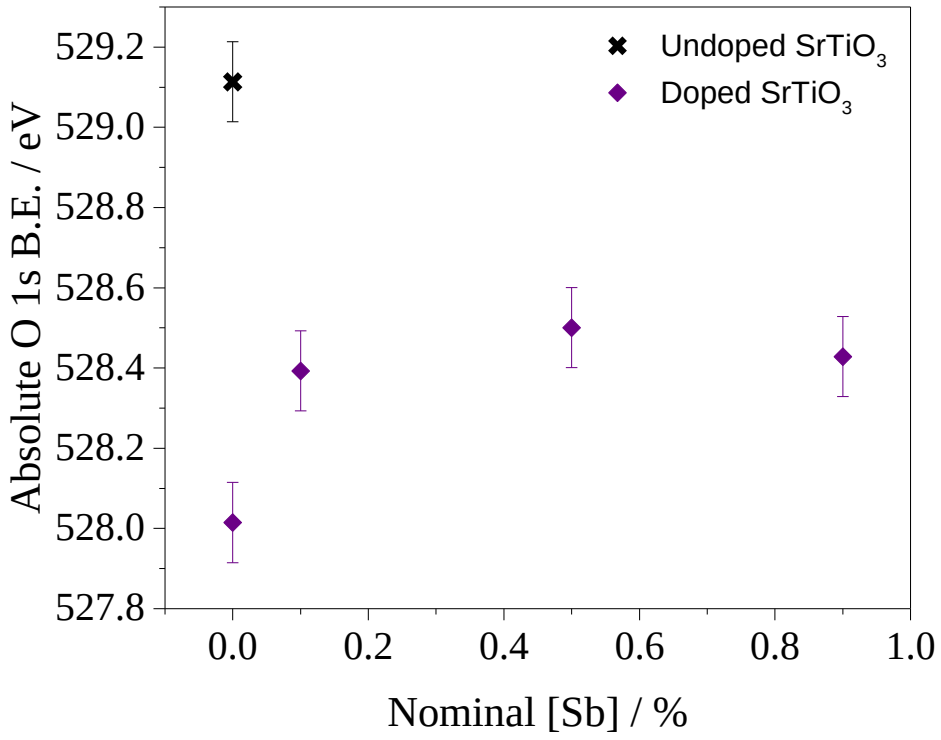

Figure 81: O 1s positions correlated with nominal [Sb%] for all doped $SrTiO_3$ samples including pristine $SrTiO_3$ for comparison.

5.2.3.3 Rh Oxidation State

The relative Rh oxidation state of dopants in these samples was evaluated by taking the core line difference between O 1s and Rh $3d_{5/2}$, as in Chapter 4. The results are presented in table X. It can be clearly observed that the core line differences are all within 0.2 eV of each other and therefore indicate the likelihood that Rh dopant ions are in the same oxidation state across these samples.

Sample	O 1s - Rh 3d $_{5/2}$ Core Line Difference (eV)
STO 01	220.09
STO 02	220.20
STO 03	220.19
STO 04	220.13

Table 20: O 1s - Rh 3d $_{5/2}$ core line difference for doped $SrTiO_3$

5.2.4 Ultraviolet-Visible Spectroscopy

The powders produced from solid state synthesis were pale brown/orange in colour, which indicates the presence of Rh^{3+} as a dopant.[213] The optical properties of these samples were investigated by Ultraviolet-Visible (UV-Vis) spectroscopy in diffuse reflectance mode. Samples were analysed by mounting them to a glass slide with carbon tape and data were collected in DRS mode due to the opaque nature of the samples. Spectra were recorded over a 2000-200 nm range, at a step size of 0.5 nm, a dwell time of 0.36 s and were subsequently transformed into a Tauc plot using the Kubelka-Munk relation, Equation 42 to obtain a spectrum of f(R).

$$f(R) = \frac{(1-R)^2}{2R}$$

Equation 44

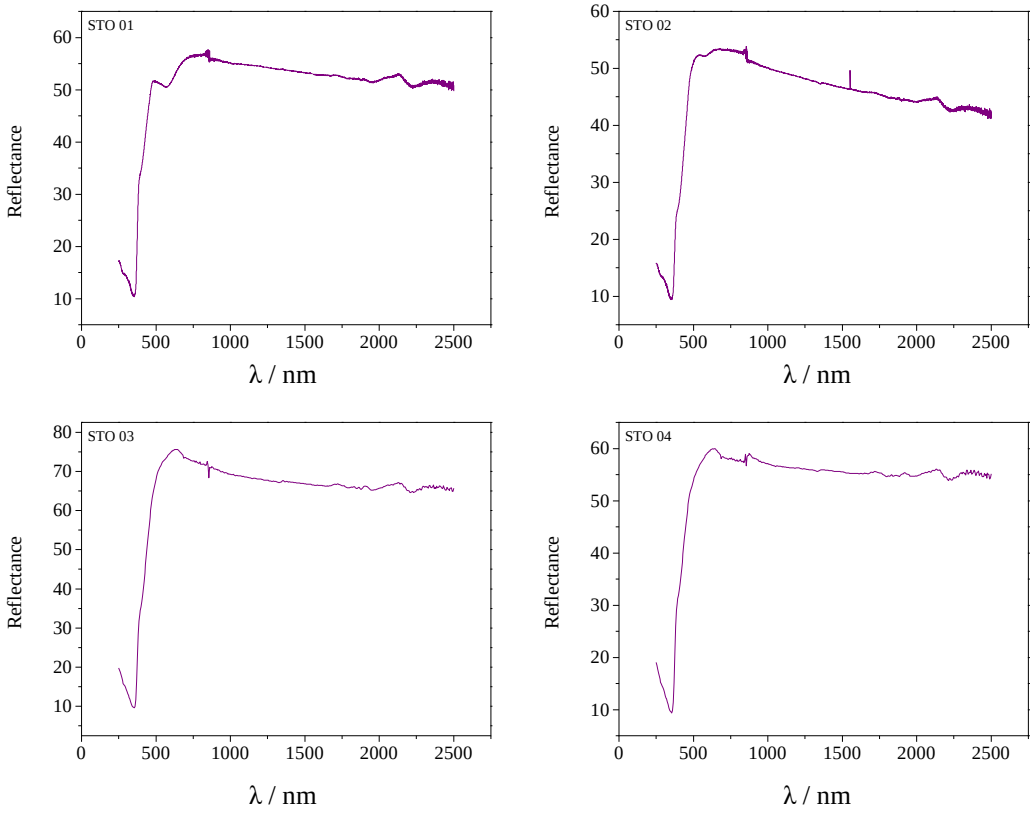

Figure 82: Diffuse Reflectance Spectra of STO1, STO2, STO3 and STO4

Figure 82 compares the DRS spectra of samples STO 01, 02, 03 and 04. All samples exhibit a spectrum characteristic of stoichiometric $SrTiO_3$.[231] Tauc plots for all samples, which allow the identification of optical absorptions and extrapolation of the energies of these absorptions, are shown in Figure 83. These plots for the indirect band gap transition show αE^2 (Equation 42), which is proportional to absorbance, in relation to incident photon energy in eV. The linear portions of these plots correlate to the absorption of photons and extrapolation of $\alpha E^2 = 0$ provides the photon energy responsible for the absorption. This is used as a method for identifying the indirect band gap of a semiconducting material and can be used to identify any additional absorptions due to the presence of dopant ions. Two transitions were identified for all samples; the Tauc plots possess obvious linear portions at around 3.31 eV, as well as weaker, secondary linear portions at around 2.76 eV. These secondary linear portions can be identified in the DRS spectra in Figure 82 as a small shoulder to the main absorption in the region just below 500 nm. Values for transitions observed in doped samples are listed in Table 21, as well as the standard band gap value for $SrTiO_3$ from the literature.[231]

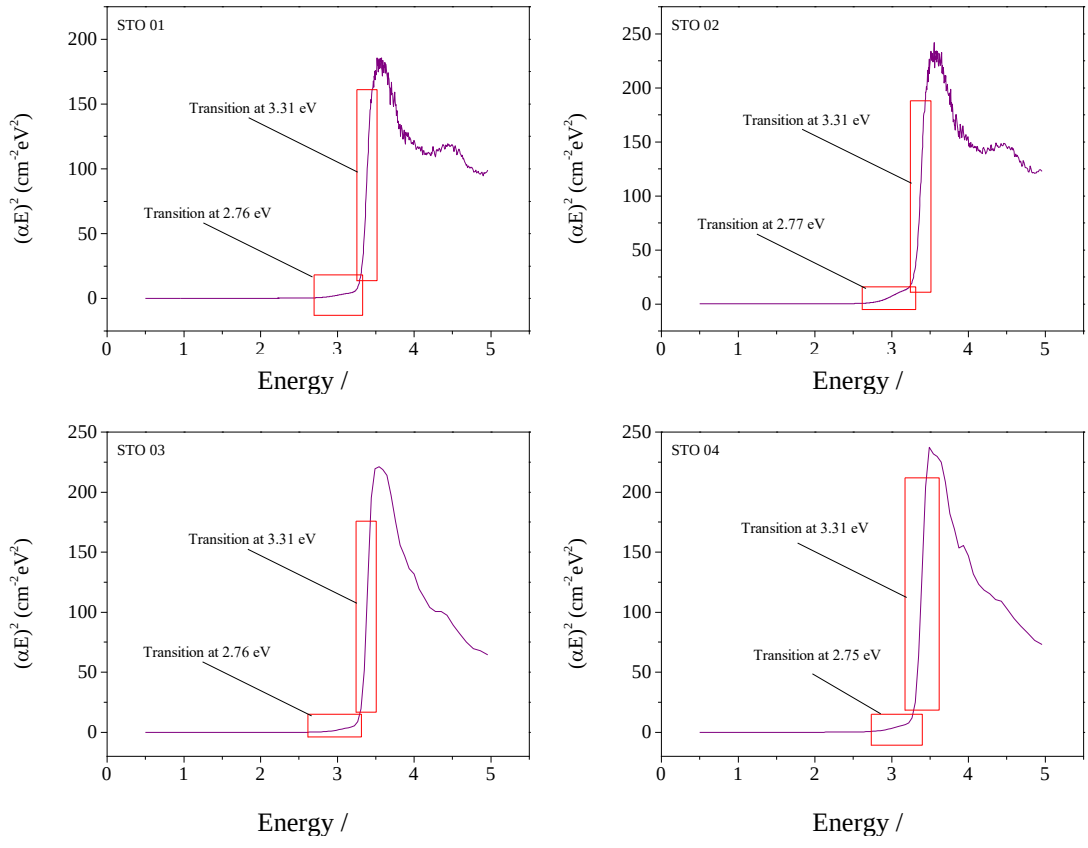

Figure 83: Tauc plots of samples STO1, STO2, STO3 and STO4. Linear sections are highlighted with red boxes and labelled with their effective transitions

Sample	Transition Energies (eV)	
$SrTiO_3$	3.27	-
STO 01	3.31	2.76
STO 02	3.31	2.77
STO 03	3.31	2.76
STO 04	3.31	2.75

Table 21: Extrapolated energies of transitions observed in optical spectra of doped $SrTiO_3$

These spectroscopic results indicate that these samples absorb visible light and therefore may show superior activity to $SrTiO_3$ alone. Importantly, no absorption at 1.0 eV is observed in any of these spectra. As discussed previously, this absorption at 1.0 eV indicates the presence of Rh^{4+} as it can be attributed to a spin allowed VB → Rh $4d_{t2g}$ transition- this interpretation was discussed in Chapter 4 for TiO_2. This feature has been observed in other Rh-doped $SrTiO_3$.[90] Differences in the position of the valence band edges of $SrTiO_3$ and TiO_2 could alter the energy requirement for this feature in a UV-Vis spectrum and Tauc plot. The VBM of $SrTiO_3$ is around 0.14 eV higher than that of TiO_2[94, 232]; a VB → Rh $4d_{t2g}$ transition could therefore be expected at around 0.84 eV. However, this transition is not observed in any of the UV-Vis spectra and Tauc plots of samples in this study, even though XPS data indicated the presence of some Rh^{4+}, which acted as a p-type dopant and caused the E_F to lie below that of pristine $SrTiO_3$.

Large overlap between O 2p and Ti 3d orbitals in the $SrTiO_3$ valence band[84] could contribute to increased d-orbital character in the valence band and therefore the d-d transition from VB to Rh 4d is not allowed, resulting in the dampening of this feature at low concentrations.

Magnification of the region around ~2-2.5 eV (Figure 84) show a similar trend to that found in TiO_2 whereby the spin-allowed Rh^{4+} d-d transition is observed in Rh-doped STO1, but that this feature is diminished in Sb codoped samples STO2, STO3 and STO4.

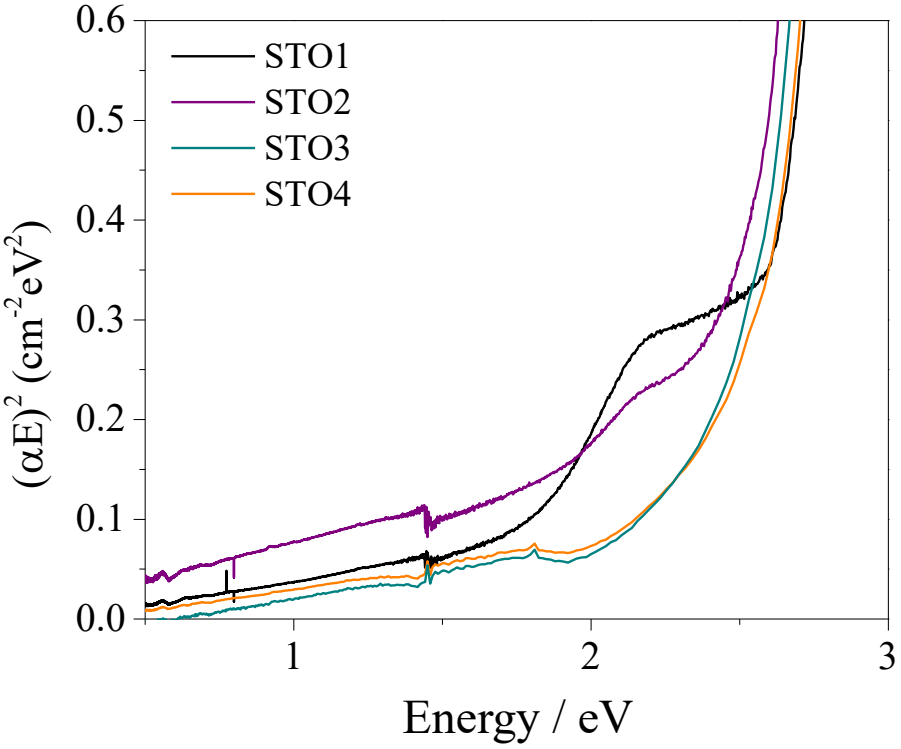

Figure 84: Tauc plot area showing Rh^{4+} d-d transition, which is diminished in STO2, STO3 and STO4 where the presence Sb suppresses formation of Rh^{4+} in favour of Rh^{3+}

5.2.5 Transient Absorption Spectroscopy

Since visible light absorption is observed in all samples, transient absorption measurements were performed to characterise the charge carrier dynamics in these samples. Cr doped Ruddlesden-Popper strontium titanate complexes, $Cr:Sr_2TiO_4$, have been investigated for H_2 production by water splitting[233], as has $LaCr:SrTiO_3/Sr_2TiO_4$ composite[234], indicating that the samples presented in this chapter possessing bulk $SrTiO_3$ with a doped Sr-rich phase at the surface may be promising materials for further photocatalytic investigation. In order to compare

Charge carrier dynamics of all samples and $SrTiO_3$ as-purchased powder were measured using Diffuse Reflectance Transient Absorption Spectroscopy (DR-TAS) from the microsecond to second time scale at room temperature. A 75 W Xe lamp is used as a probe beam with a monochromator placed before the powder sample, which is compacted between two glass microscope slides. Changes in the light reflected by the sample are measured by a Si PIN photodiode after a UV laser excitation pulse is applied on the sample (355 nm, 6 ns pulse width). The laser intensities used were (~40 μJ cm^{-2} $pulse^{-1}$) with a laser repetition rate of 1 Hz. Each TAS trace is the result of averaging 50 scans. These measurements were taken at Imperial College London, using the Durrant Group DR-TAS setup and with the assistance of Dr Andreas Kafizas.

5.2.5.1 DR-TAS Spectra

The DR-TAS spectrum from 500 - 950 nm at 50 nm intervals is shown in Figure 85. The excited material absorbs much more strongly at lower probe wavelengths than at higher wavelengths. In Chapter 4, the deconvolution of TAS spectra for TiO_2 was explained using a study by Kafizas et al.[105] From this study it was determined that in TiO_2 free electrons absorb mainly at higher wavelengths (~850 nm) and that holes absorb at lower wavelengths (~550 nm). Similar results have been reported for other metal oxides; photoholes in α-Fe_2O_3[235] have been shown to absorb at ~580 nm, in $BiVO_4$[236] at ~550 nm and in WO_3[184, 237] at ~450 nm. Consistently, photoelectrons produce red-shifted signals and photoholes produce blue-shifted signals. However, these results do not correlate with the data collected in the present study of $SrTiO_3$.

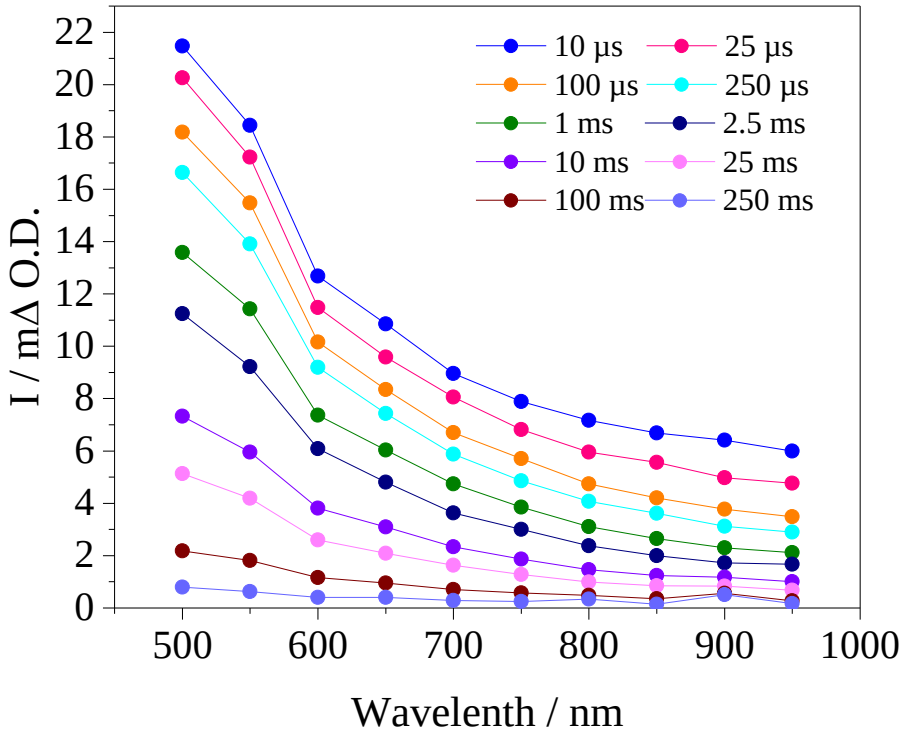

Figure 85: DR-TAS spectrum of $SrTiO_3$ as-purchased powder, from 500 - 950 nm at 50 nm intervals. Spectra are shown from the micro second to second timescale

Figure 85 shows the DR-TAS spectrum of pristine $SrTiO_3$, between 500 nm and 950 nm. This spectrum shows stronger absorption at lower wavelengths, which, according to studies of the other materials mentioned, indicates a higher concentration of photoholes than photoelectrons and thus p-type character. However, $SrTiO_3$ is an n-type material and therefore it appears that photoelectrons and photoholes in $SrTiO_3$ do not absorb in the same regions as in other materials. Unfortunately the large particle size of the powders produced by solid state reaction did not allow for a deconvolution study using electron or hole scavenging solutions to be

completed and therefore it is difficult to draw conclusions from TAS regarding the identities and relative concentrations of the charge carriers in the photoexcited materials.

Spectra of all doped samples, which exhibit a similar shape to that recorded for pristine $SrTiO_3$, are shown in Figure 86. Although the overall the shapes of the spectra appear the same, a comparison of the normalised spectra at 10 µs (Figure 87) illustrates the minor differences between them. STO 01, which is doped with 0.5 % Rh, exhibits a small relative increase in absorption around 600 nm - 800 nm with respect to pristine $SrTiO_3$. STO2 exhibits a similar shape while STO3 and STO4 are almost identical to each other, with a shape intermediate between STO1 and pristine $SrTiO_3$.

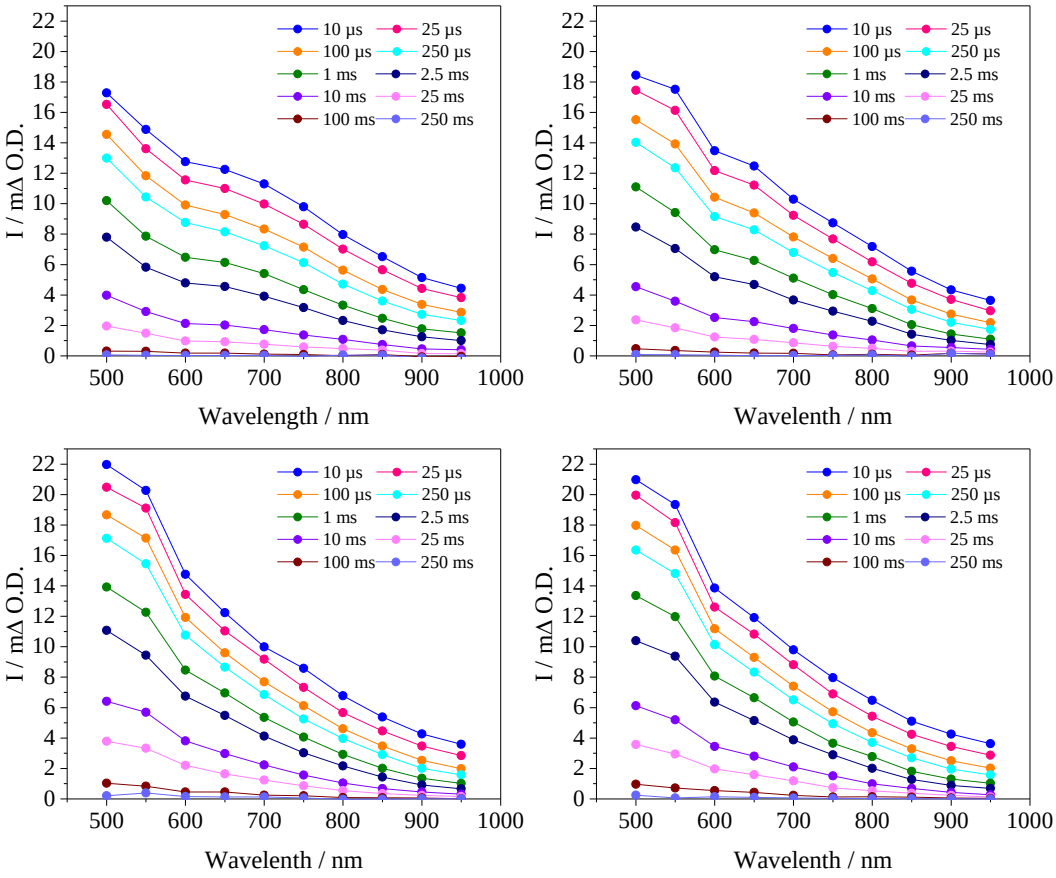

Figure 86: DR-TAS spectra of samples STO 01, 02, 03 and 04 across wavelengths 500 - 950 nm at 50 nm intervals. Spectra are shown from the micro second to second timescale

From VB and O 1s XPS data it has been determined that the E_F of STO1 is positioned lower than blank $SrTiO_3$ and is therefore more p-type. The results presented here indicate that photoholes in $SrTiO_3$ may therefore absorb at around 700 nm, which is where the relative difference between STO1 and pristine $SrTiO_3$ is greatest. This rationale would also account for the relative increase in absorption exhibited by STO2, STO3 and STO4.

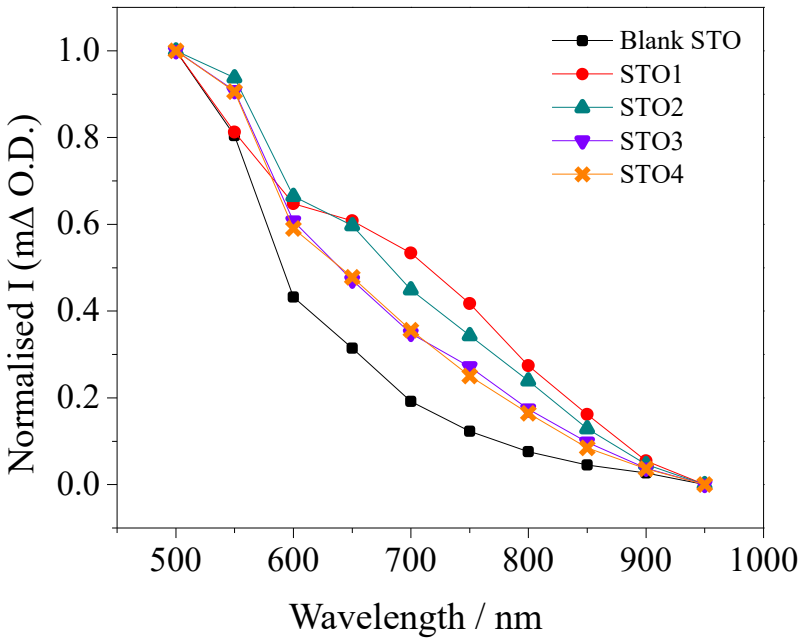

Figure 87: Normalised DR-TAS Spectra of pristine $SrTiO_3$ and all doped samples

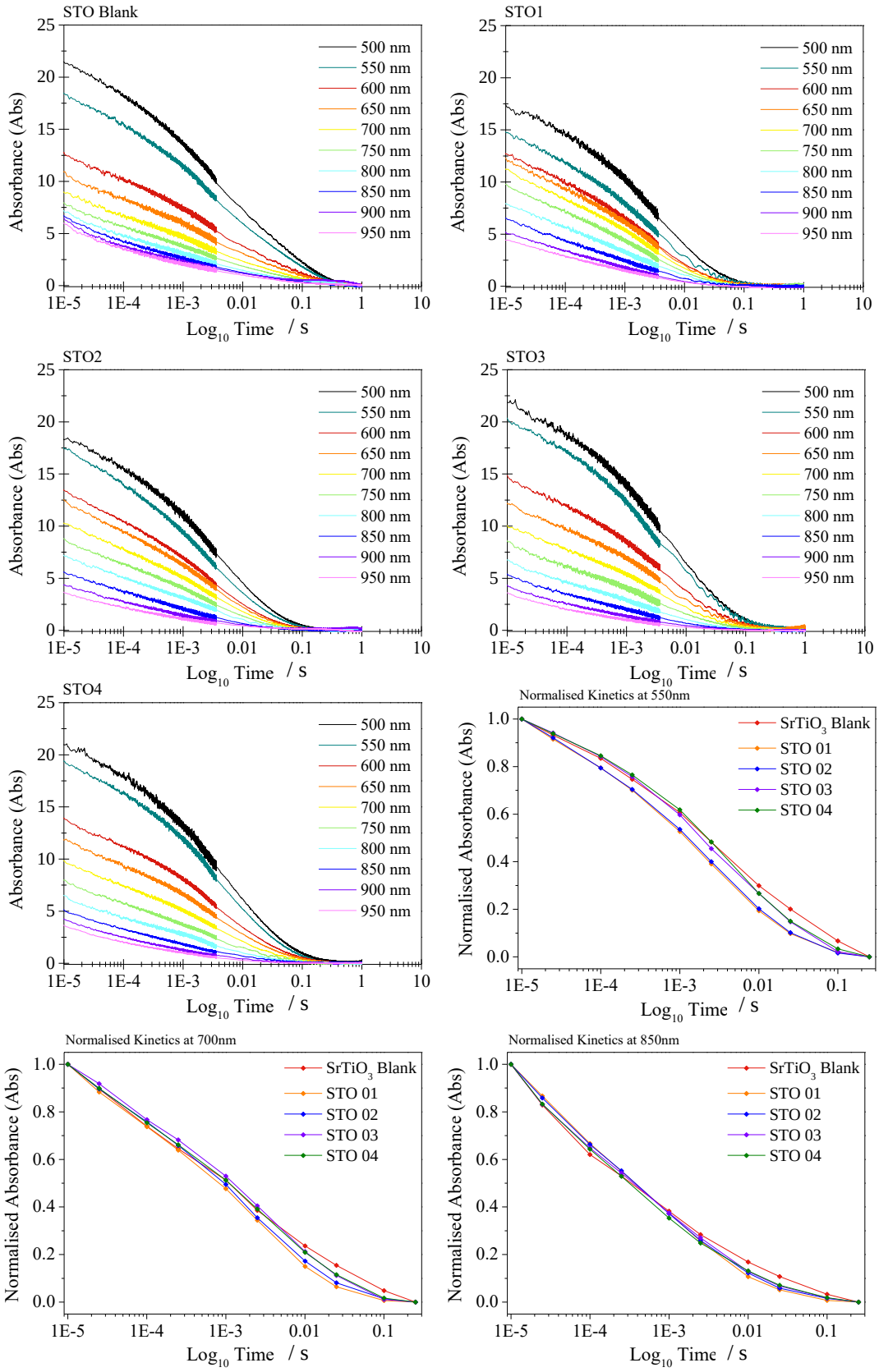

Figure 88: Recombination kinetics for all samples and normalised kinetics for all samples at 550 nm, 700 nm and 850 nm

5.2.5.2 DR-TAS Recombination

Recombination DR-TAS kinetics for all samples and pristine $SrTiO_3$ are shown in Figure 88, alongside normalised recombination kinetics for all samples at 550 nm, 700 nm and 850 nm. As can be easily observed across all of these data, there is minimal difference between the samples and $SrTiO_3$. At 550 nm and 700 nm, samples STO1 and STO2, exhibit slightly faster recombination than STO3, STO4 and $SrTiO_3$, indicating that the suppression of Rh^{4+} is advantageous for elongation of charge carrier lifetime. However, the difference in kinetics in these samples is not nearly as variable as the sample discussed in Chapter 4. This could be explained by the low concentrations of dopants resulting in far fewer recombination centres, or could also be explained by better diffusion of charges in $SrTiO_3$ resulting in greater charge separation and therefore slower recombination. Comparison of the average kinetics of $SrTiO_3$ and TiO_2 kinetics in Figure 89 shows that recombination in $SrTiO_3$ is indeed slower than undoped TiO_2 rutile.

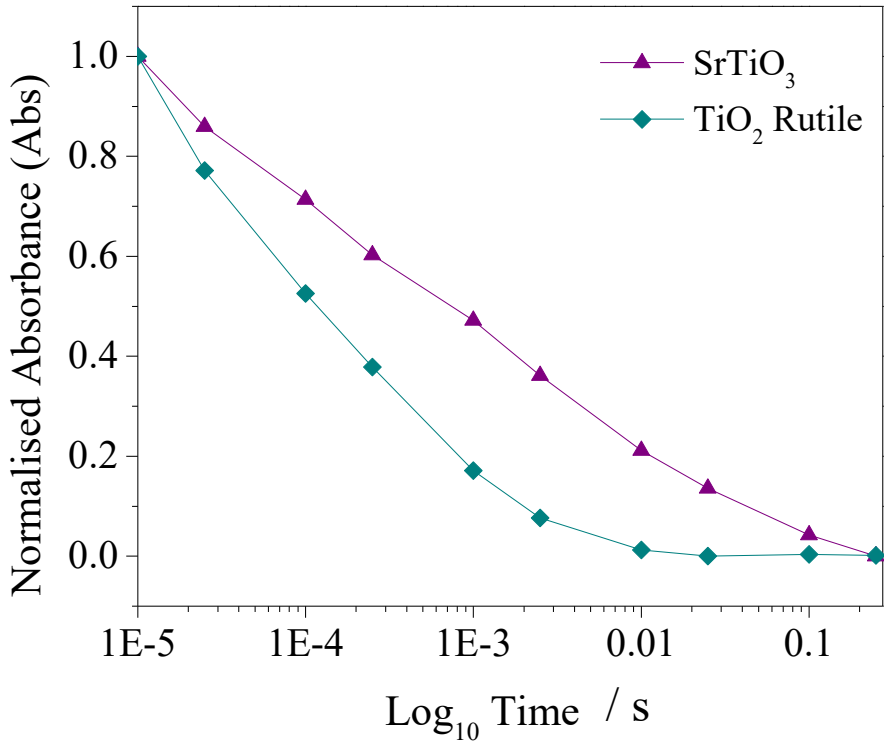

Figure 89: Kinetics for $SrTiO_3$ and TiO_2 at probe wavelengths of 750 nm and nm respectively, which is where their kinetics were observed to be slowest

5.3 Conclusions

This chapter presented work based on the development of doped-$SrTiO_3$ catalyst materials for photocatalytic water splitting. The materials produced were synthesised by direct solid state reaction of $SrTiO_3$ with the dopant oxides, Rh_2O_3 and Sb_2O_5. This method contrasted with previously investigated Rh doped and Sb codoped $SrTiO_3$ studies, which utilised an indirect step synthesis starting from $SrCO_3$, TiO_2 and the required dopant oxide.

PXRD of the resultant samples using 5% Rh and 1-9 % Sb at 2% intervals, revealed that reaction between $SrTiO_3$ and the dopant oxides does not yield phase pure materials after 30 hours (3 x 10) of calcination. Instead a distorted Sb_2O_5 phase and a Sr-rich $SrTiO_3$ phase were produced, which, while not correlating to any specific $Sr_xTi_yO_z$ phase that has been previously recorded, was confirmed by XPS elemental quantification.

A second set of samples were produced with the aim of successfully doping Rh and Sb in lower concentrations using the same direct synthesis method described above. These materials produced PXRD patterns indicating phase pure materials, with cell volumes larger than that of standard $SrTiO_3$ but similar to the pristine powder measured on the same diffractometer, indicating possible instrumental error. Similar cell volumes across the doped series indicated that the amount and identity of the dopants had minimal effect on the cell size. XPS quantification indicated again that the surface of these samples was Sr-rich, although no additional phase was observed in PXRD patterns.

X-ray absorption spectra of the Sb K-edge in samples STO 02, 03 and 04, which were all codoped with Sb in varying amounts (0.1, 0.5 and 0.9 %, respectively), indicated Sb ions in the doped samples were in a different environment to either Sb_2O_3 or Sb_2O_5. Although other B-site doped $SrTiO_3$ dopant K-edge spectra have indicated that a broad K-edge, like those observed for Sb in the doped samples presented, is associated with a lower oxidation state, EXAFS r-fit analysis indicated a Sb (V)-O like bond length. XPS VB data support this theory, since the addition Sb appears to reduce the p-type character of all codoped samples, an effect of Sb^{5+} encouraging formation of Rh^{3+}, rather than the p-type dopant Rh^{4+}. Furthermore, Sb^{3+} itself on the Ti^{4+} site acts as a p-type dopant and therefore would further add to the p-type character of the materials. Since this is not the case, it is likely that Sb exists as Sb^{5+}.

UV-Vis spectra of doped samples appear at first glance to be very similar to pristine $SrTiO_3$, likely due to the low concentration of dopants. A low intensity absorption at around 2.76 eV is associated with narrowing of the band gap as a result of transitions from Rh 4d t_{2g} to the conduction band. In STO1, where Rh is monodoped, a spin allowed d-d transition can be

observed at around 2-2.5 eV. This is diminished with the addition of Sb in all samples and thus supports the conclusion that Rh^{4+} exists in STO1 and that the presence of Sb^{5+} in STO2, STO3, and STO4 supresses its formation and encourages reduction to Rh^{3+}.

TAS was used to probe the charge carrier dynamics in the doped samples by comparison with pristine $SrTiO_3$. It was determined from the TAS spectra, where a slight increase in absorption was observed between 600 and 750 nm for STO1, that photoholes in doped $SrTiO_3$ possibly absorb in this region since this sample has been shown by other analyses to be p-type. Recombination spectra and normalised kinetics illustrated minimal difference between doped samples and $SrTiO_3$, possibly due to the low concentration of dopants in these samples. At 550 nm and 700 nm probe pulse the kinetics of STO3 and STO4 appeared slower than STO1 and STO2, indicating further that the presence of Rh^{4+} is detrimental to the charge carrier dynamics in these samples.

To conclude, the doped $SrTiO_3$ samples in this chapter provided some interesting results in that the addition of Sb over equimolar concentration to Rh did not appear to allow the materials to retain their n-type character as was the case with TiO_2 in similar doping regimes. The formation of p-type $SrTiO_3$ was unexpected due to the nature of the dopants, which have been estimated to be Rh^{4+} in monodoped $SrTiO_3$ and a combination of Rh^{3+} and Sb^{5+} in co-doped $SrTiO_3$. Identification of the dopant oxidation states was troublesome due to the low concentrations used for this study. However, TAS results indicate that these materials have charge carrier dynamics consistent with superior photocatalytic performance to TiO_2 rutile.

Chapter 6: Conclusions and further work

This thesis focussed on the study of TiO_2 and $SrTiO_3$ doped with Rh and Sb for the purposes of improving their photocatalytic activity by narrowing their band gaps. Both TiO_2 and $SrTiO_3$ had been shown in the literature to exhibit visible light activity when doped with Rh and that Sb could be used to charge compensate, reducing the amount of Rh^{4+}, which is detrimental to photocatalysis as it can act as a trap state.

Chapter 3 presented findings from a preliminary study of Sb oxide materials by XPS. There is much disagreement in the literature surrounding the treatment of Sb, particularly regarding chemical shift in XPS due to oxidation state. Some researchers have determined that there *is* a chemical shift between the (III) and (V) ions in XPS, some researchers have found that any chemical shift is unresolvable, and some purport to show that the chemical shift is unresolvable but can be observed through a broadening of the Sb core-line FWHM.

A study of Sb_2O_3 oxidation to Sb_2O_5 by H_2O_2 was undertaken to determine if Sb oxidation state can be accurately determined from chemical shift in XPS and therefore define how Sb XPS would be treated for the remainder of the thesis. This study involved creating mixed Sb_2O_3/Sb_2O_5 powders through oxidation and determining how much Sb_2O_3 and Sb_2O_5 character each mixture had, in order to then model the core line spectra. A novel valence band analysis was utilised where by Sb_2O_3 and Sb_2O_5 valence bands were fitted in the valence band of the mixtures and allowed to change total area and position only, in order to reveal the proportion of each oxide present. This allowed for the proportion of Sb (III) and Sb (V) to be estimated and models for the core line to be generated.

Two models to investigate the possibility of the presence of chemical shift between the Sb(III) and Sb(V) core lines were tested, one with equal FWHM and one with Sb(V) FWHM > Sb(III) FWHM. It was expected that if either model was correct, a consistent chemical shift between the (III) and (V) ions would be observed, however both models produced peak shifts that differed by >0.15 eV. From this analysis it was decided that all Sb core lines in the subsequent investigations would be treated as unresolvable and thus Sb oxidation state was inferred from other analyses in Chapters 4 and 5.

Rh/Sb codoped TiO_2 was investigated as it has shown promise as a H_2 evolution catalyst. Previous literature has illustrated that the Fermi level position is lowered if Rh^{4+} is present as a dopant but that this can be eliminated by the addition of Sb^{5+} as a codopant. This study

expanded this understanding by investigating a wider range of dopant ratios and by utilising the O 1s core line as an indicator of Fermi level position. It was confirmed that as the Sb/Rh ratio increases the Fermi level energy increases, allowing n-type character to be retained. Dopants were found to localise at the surface and a single crystal depth profile study allowed for the positions of the CBM and VBM to be estimated from the surface to the bulk, indicating that band bending at the surface of the material may contribute to the photocatalytic activities observed.

TAS of selected samples indicated lower charge carrier concentrations for the doped samples in comparison to undoped rutile which was surprising, since other literature had presented good photoactivity for similar samples. It was concluded that the dopant concentrations in samples from this study were too high to facilitate good charge migration and that perhaps the high concentration of dopant ions were acting as recombination centres.

Following this investigation further work into various areas of the field could be carried out. Firstly, further single crystal studies could be completed, to corroborate the findings here and to investigate different dopant ratios. Clearly the CBM and VBM can be tuned by dopant ratio. This is something that should be investigated for possible exploitation in the construction of z-schemes due to the possibility of an intrinsic electric field in these materials, a feature that would significantly enhance charge carrier separation.

Powder samples of lower absolute dopant concentrations should be produced in order to determine the extent of this variable on charge carrier generation and migration. Further studies using TAS could provide information to answer this question.

This work focused on rutile due to the high temperature nature of the synthesis method. A future route to take could be the production of anatase analogues of these samples in order to compare the two polymorphs, which are both known to be active photocatalysts. In addition, rutile/anatase mixtures could be created; this particular heterojunction is of high interest in the research community due to the as-yet unexplained high activity of P-25 an 80:20 mixture of anatase and rutile TiO_2.

As well as simple TiO_2 based heterojunctions, the combination of an optimized Sb/Rh codoped TiO_2 material with other materials of well-defined band edges, such as other doped TiO_2 materials or different materials of significance in the photocatalysis community ($BiVO_4$, WO_3, CuO), could produce highly effective Z-schemes. The high degree of electronic characterization undertaken in this investigation assists greatly in the design of these systems. Understanding the changes in Fermi level position, which influences the p- or n-type

characteristics and the possible band bending within a material, can be exploited to produce highly effective photocatalytic systems.

Study into $SrTiO_3$ doped with Sb and Rh by direct solid state reaction of the titanate and dopant powders revealed that reaction does not complete at high concentrations (total dopant concentration > 1.5 mol.%). Samples with lower concentrations of dopant ions (0.5% Rh and 0.1, 0.5, 0.9% Sb) were revealed to be phase pure from XRD, though impurities masked by noise in the baseline cannot be ruled out. The cell volume was not found to change with respect to undoped $SrTiO_3$, making it difficult to conclude if doping had occurred.

XPS indicated the presence of dopant ions but information pertaining to the coordination of dopant ions and thus their position in the lattice cannot be determined by these means. XAS Sb k-edge data was of poor quality due to the low concentration of Sb in the samples, and the spectra did not resemble Sb_2O_3 or Sb_2O_5, making it difficult to determine oxidation state. EXAFS analysis determined Sb-O bond length of 1.95 Å, which is shorter than Sb(III)-O (1.977 Å) and indicates Sb(V), however these values are *just* within error of each other and so this cannot be used as absolute evidence of the presence of Sb(V).

As with TiO_2, the addition of Rh caused a lowering of the Fermi level energy. However, analysis of the valence band spectra and O 1s binding energies indicated that unlike TiO_2 the addition of Sb did not return the Fermi level to a n-type position, instead the Fermi level was positioned between that of Rh doped $SrTiO_3$ and pristine $SrTiO_3$. TAS showed that doping $SrTiO_3$ in the low concentrations used for this study did not alter the charge carrier dynamics vastly with respect to pristine $SrTiO_3$. Therefore the increased activity of these materials from other literature can be attributed to visible light activation allowing for a greater number of charge carriers being generated under the solar spectrum.

The characterisation of these materials, while a comprehensive start has been made, is incomplete. Though XAS and XPS results indicate that a Sr-rich phase exists at the surface, this has not been confirmed by full structural and crystallographic characterisation. Further investigation, for example XAS of the other elements in the samples (Rh, Sr, Ti and O) could provide valuable insight into the structure of these materials and the nature of the dopants. In particular, information regarding the Rh environment and surface XAS of Sr, Ti and O to eliminate the averaging effects of the bulk, could illicit important information. Comparison of the phases formed in higher doped samples discussed in section 5.2.1 could potentially offer an additional point of investigation.

Beyond further structural characterisation, photocatalytic measurements should be taken to compare the response of these samples under visible light with that of $SrTiO_3$ and also other Rh doped $SrTiO_3$ materials that have shown promise in the literature.

Chapter 7: References

1. C. M. White, R. R. Steeper and A. E. Lutz, *International Journal of Hydrogen Energy*, 2006, **31**, 1292-1305.
2. L. M. Das, *International Journal of Hydrogen Energy*, 1991, **16**, 765-775.
3. T. R. A. P. The Energy Research Centre of the Netherlands, The European Climate Foundation, 2010.
4. U. S. S. C. o. E. a. N. Resources, 2012.
5. S. Ashcroft, Annut, A., UK Government Department for Business, Energy and Industrial Strategy, London, 2016.
6. D. W. S. W. Shepherd, *Energy Studies*, Imperial College Press, 2003.
7. M. Höök, A. Sivertsson and K. Aleklett, *Nat Resour Res*, 2010, **19**, 63-81.
8. BMW, BMW Hydrogen, http://www.bmw.co.uk/en/topics/discover-bmw/efficientdynamics/hydrogen.html, Accessed 15-03-2013.
9. J. W. Heffel, *International Journal of Hydrogen Energy*, 2003, **28**, 901-908.
10. J. W. Heffel, *International Journal of Hydrogen Energy*, 2003, **28**, 1285-1292.
11. TFL, Bright first year for London's Fuel Cell buses, http://www.tfl.gov.uk/static/corporate/media/newscentre/archive/4164.html, Accessed 16-03-2013.
12. California Hydrogen Fuel Station Map, http://cafcp.org/stationmap, Accessed 16-03-2013.
13. J. Larminie and A. Dicks, John Wiley & Sons.
14. J. Solsvik, R. A. Sánchez, Z. Chao and H. A. Jakobsen, *Industrial & Engineering Chemistry Research*, 2013, **52**, 4202-4220.
15. J. Xu and G. F. Froment, *AIChE Journal*, 1989, **35**, 88-96.
16. J. Lede, Lapique, F., Villermaux, J., *International Journal of Hydrogen Energy*, 1983, **8**, 5.
17. E. Bilgen, *International Journal of Hydrogen Energy*, 1984, **9**.
18. S. Ihara, *International Journal of Hydrogen Energy*, 1978, **3**.
19. J. W. Warner, Berry, R., S., *International Journal of Hydrogen Energy*, 1985, **11**, 10.
20. H. Gaffron, Rubin, J., *The Journal of General Physiology*, 1942, **26**, 22.
21. L. Florin, A. Tsokoglou and T. Happe, *Journal of Biological Chemistry*, 2001, **276**, 6125-6132.
22. M. Ghirardi, R. Togasaki and M. Seibert, *Appl Biochem Biotechnol*, 1997, **63-65**, 141-151.
23. H. Cavendish, *Philosophical Transactions of the Royal Society of London*, 1784, **74**, 34.
24. G. Pearson, *Philosophical Transactions of the Royal Society of London*, 1797, **87**, 142-158.
25. W. Nicholson, *A Journal of Natural Philosophy, Chemistry and the Arts*, 1800, **4**, 13.
26. K. H. A. Fujishima, *Nature*, 1972, **238**, 1.
27. C. Kittel, *Introduction to Solid State Physics*, Wiley, UK, 2004.
28. A. R. West, ed., *Basic Solid State Chemistry*, John Wiley and Sons Ltd., UK, 2011.
29. S. J., *Band Theory and Electronic Properties of Solids*, Oxford University Press, Oxford/New York, 2001.
30. *Excitons*, Springer-Verlag Berlin Heidelberg, Germany, 1979.
31. C. Acar, I. Dincer and G. F. Naterer, *International Journal of Energy Research*, 2016, **40**, 1449-1473.
32. J. Yang, D. Wang, H. Han and C. Li, *Accounts of Chemical Research*, 2013, **46**, 1900-1909.
33. T. Jafari, E. Moharreri, A. Amin, R. Miao, W. Song and S. Suib, *Molecules*, 2016, **21**, 900.

34. M. Pelaz, Nolan, N. T., Pillai, S. C., Seery, M. K., Falaras, P., Kontos, A. G., Dunlop, P. S. M., Hamilton, J. W. J., Byrne, J. A., O'Shea, K., Entezari, M. H., Dionysiou, D. D., *Applied Catalysis B: Environmental*, 2012, **125**, 19.
35. G. Rothenberger, J. Moser, M. Graetzel, N. Serpone and D. K. Sharma, *Journal of the American Chemical Society*, 1985, **107**, 8054-8059.
36. Y. Cao, Y. Xu, H. Hao and G. Zhang, *Materials Letters*, 2014, **114**, 88-91.
37. C. Feng, G. Li, P. Ren, Y. Wang, X. Huang and D. Li, *Applied Catalysis B: Environmental*, 2014, **158**–**159**, 224-232.
38. H. Kisch, *Angewandte Chemie International Edition*, 2013, **52**, 812-847.
39. K. Maeda, *Acs Catalysis*, 2013, **3**, 1486-1503.
40. H. Li, W. Tu, Y. Zhou and Z. Zou, *Advanced Science*, 2016, **3**, 1500389-n/a.
41. H. J. Yun, H. Lee, N. D. Kim, D. M. Lee, S. Yu and J. Yi, *ACS Nano*, 2011, **5**, 4084-4090.
42. Govindjee, D. Shevela and L. O. Björn, *Photosynthesis Research*, 2017, 1-11.
43. R. Abe, K. Sayama, K. Domen and H. Arakawa, *Chemical Physics Letters*, 2001, **344**, 339-344.
44. K. Sayama, K. Mukasa, R. Abe, Y. Abe and H. Arakawa, *Chemical Communications*, 2001, **0**, 2416-2417.
45. Y. Sasaki, A. Iwase, H. Kato and A. Kudo, *Journal of Catalysis*, 2008, **259**, 133-137.
46. H. Kato, M. Hori, R. Konta, Y. Shimodaira and A. Kudo, *Chemistry Letters*, 2004, **33**, 1348-1349.
47. R. Abe, T. Takata, H. Sugihara and K. Domen, *Chemical Communications*, 2005, **0**, 3829-3831.
48. Y. Sasaki, H. Nemoto, K. Saito and A. Kudo, *The Journal of Physical Chemistry C*, 2009, **113**, 17536-17542.
49. H. Kominami, Y. Ishii, M. Kohno, S. Konishi, Y. Kera and B. Ohtani, *Catal Lett*, 2003, **91**, 41-47.
50. S. Bakardjieva, V. Stengl, L. Szatmary, J. Subrt, J. Lukac, N. Murafa, D. Niznansky, K. Cizek, J. Jirkovsky and N. Petrova, *Journal of Materials Chemistry*, 2006, **16**, 1709-1716.
51. T. A. Kandiel, L. Robben, A. Alkaim and D. Bahnemann, *Photochemical & Photobiological Sciences*, 2013, **12**, 602-609.
52. M. D. Hernandez-Alonso, F. Fresno, S. Suarez and J. M. Coronado, *Energy & Environmental Science*, 2009, **2**, 1231-1257.
53. G. Samsonov, V., *The Oxide Handbook*, IFI/Plenum Press, New York, 1982.
54. M. Horn, Schwerdtfeger, C., Meagher, E., *Zeitschrift für Kristallographie*, 2010, **136**, 9.
55. W. H. Baur and A. A. Khan, *Acta Crystallographica Section B*, 1971, **27**, 2133-2139.
56. E. P. L. Meagher, E.,, *Canadian Minerologist*, 1979, **17**, 9.
57. M. Li, W. Hebenstreit, L. Gross, U. Diebold, M. A. Henderson, D. R. Jennison, P. A. Schultz and M. P. Sears, *Surface Science*, 1999, **437**, 173-190.
58. U. Diebold, *Surface Science Reports*, 2003, **48**, 53-229.
59. S. Fischer, A. W. Munz, K.-D. Schierbaum and W. Göpel, *Surface Science*, 1995, **337**, 17-30.
60. W. Hebenstreit, N. Ruzycki, G. S. Herman, Y. Gao and U. Diebold, *Physical Review B*, 2000, **62**, R16334-R16336.
61. L.-Q. Wang, D. R. Baer, M. H. Engelhard and A. N. Shultz, *Surface Science*, 1995, **344**, 237-250.
62. P. Scheiber, M. Fidler, O. Dulub, M. Schmid, U. Diebold, W. Hou, U. Aschauer and A. Selloni, *Physical Review Letters*, 2012, **109**, 136103.
63. A. T. Paxton and L. Thiên-Nga, *Physical Review B*, 1998, **57**, 1579-1584.
64. C. Brand. L., S., Werner, M., ed. O. NANO, 2011.
65. N. Serpone, D. Lawless, J. Disdier and J.-M. Herrmann, *Langmuir*, 1994, **10**, 643-652.

66. Z. Ambrus, N. Balázs, T. Alapi, G. Wittmann, P. Sipos, A. Dombi and K. Mogyorósi, *Applied Catalysis B: Environmental*, 2008, **81**, 27-37.
67. M. Subramanian, S. Vijayalakshmi, S. Venkataraj and R. Jayavel, *Thin Solid Films*, 2008, **516**, 3776-3782.
68. G. Li, N. M. Dimitrijevic, L. Chen, T. Rajh and K. A. Gray, *The Journal of Physical Chemistry C*, 2008, **112**, 19040-19044.
69. M. M. Mohamed, I. Othman and R. M. Mohamed, *Journal of Photochemistry and Photobiology A: Chemistry*, 2007, **191**, 153-161.
70. C. M. Teh and A. R. Mohamed, *Journal of Alloys and Compounds*, 2011, **509**, 1648-1660.
71. C. M. Fan, P. Xue, G. Y. Ding and Y. P. Sun, *Rare Metal Materials and Engineering*, 2005, **34**, 1094-1097.
72. V. Štengl, S. Bakardjieva and N. Murafa, *Materials Chemistry and Physics*, 2009, **114**, 217-226.
73. J.-w. Shi, J.-t. Zheng and P. Wu, *Journal of Hazardous Materials*, 2009, **161**, 416-422.
74. D. Xu, L. Feng and A. Lei, *Journal of Colloid and Interface Science*, 2009, **329**, 395-403.
75. Q. Xiao and L. Ouyang, *Chemical Engineering Journal*, 2009, **148**, 248-253.
76. T. Ohno, M. Akiyoshi, T. Umebayashi, K. Asai, T. Mitsui and M. Matsumura, *Applied Catalysis A: General*, 2004, **265**, 115-121.
77. R. Asahi, T. Morikawa, T. Ohwaki, K. Aoki and Y. Taga, *Science*, 2001, **293**, 269-271.
78. C. Di Valentin, E. Finazzi, G. Pacchioni, A. Selloni, S. Livraghi, M. C. Paganini and E. Giamello, *Chemical Physics*, 2007, **339**, 44-56.
79. S. Kment, H. Kmentova, P. Kluson, J. Krysa, Z. Hubicka, V. Cirkva, I. Gregora, O. Solcova and L. Jastrabik, *Journal of Colloid and Interface Science*, 2010, **348**, 198-205.
80. C. He, Y. Yu, X. Hu and A. Larbot, *Applied Surface Science*, 2002, **200**, 239-247.
81. R. Daghrir, P. Drogui and D. Robert, *Industrial & Engineering Chemistry Research*, 2013, **52**, 3581-3599.
82. S. Piskunov, E. A. Kotomin, E. Heifets, J. Maier, R. I. Eglitis and G. Borstel, *Surface Science*, 2005, **575**, 75-88.
83. R. I. Eglitis, S. Piskunov, E. Heifets, E. A. Kotomin and G. Borstel, *Ceramics International*, 2004, **30**, 1989-1992.
84. S. Piskunov, E. Heifets, R. I. Eglitis and G. Borstel, *Computational Materials Science*, 2004, **29**, 165-178.
85. N. Erdman, K. R. Poeppelmeier, M. Asta, O. Warschkow, D. E. Ellis and L. D. Marks, *Nature*, 2002, **419**, 55-58.
86. M. Kawasaki, K. Takahashi, T. Maeda, R. Tsuchiya, M. Shinohara, O. Ishiyama, T. Yonezawa, M. Yoshimoto and H. Koinuma, *Science*, 1994, **266**, 1540-1542.
87. M. J. Akhtar, Z.-U.-N. Akhtar, R. A. Jackson and C. R. A. Catlow, *Journal of the American Ceramic Society*, 1995, **78**, 421-428.
88. R. U. E. t Lam, L. G. J. de Haart, A. W. Wiersma, G. Blasse, A. H. A. Tinnemans and A. Mackor, *Materials Research Bulletin*, 1981, **16**, 1593-1600.
89. T. Ishii, H. Kato and A. Kudo, *Journal of Photochemistry and Photobiology A: Chemistry*, 2004, **163**, 181-186.
90. R. Konta, T. Ishii, H. Kato and A. Kudo, *The Journal of Physical Chemistry B*, 2004, **108**, 8992-8995.
91. H. P. Maruska and A. K. Ghosh, *Solar Energy Materials*, 1979, **1**, 237-247.
92. H. Kato and A. Kudo, *The Journal of Physical Chemistry B*, 2002, **106**, 5029-5034.
93. S. Hara, M. Yoshimizu, S. Tanigawa, L. Ni, B. Ohtani and H. Irie, *The Journal of Physical Chemistry C*, 2012, **116**, 17458-17463.
94. B. Modak and S. K. Ghosh, *Physical Chemistry Chemical Physics*, 2015, **17**, 15274-15283.

95. C. N. R. G. Rao, J., *New Directions in Solid State Chemistry*, Cambridge Universtiy Press, New York, 1997.
96. A. R. West, *Solid State Chemistry and its Applications*, Wiley, Chichester, 1984.
97. E. A. V. Ebsworth, Rankin, D. W. H., Cradock, S., in *Structural Methods in Inorganic Chemistry*

Blackwell Scientific Publications, Edinburgh, 1991, pp. 331-377.
98. T. Owen, *Fundamentals of UV-Visible Spectroscopy*, Hewlett-Packard Company, Germany, 1996.
99. J. H. Nobbs, *Review of Progress in Coloration and Related Topics*, 1985, **15**, 66-75.
100. L. Yang and B. Kruse, *J. Opt. Soc. Am. A*, 2004, **21**, 1933-1941.
101. P. van der Heide, in *X-Ray Photoelectron Spectroscopy*, John Wiley & Sons, Inc., 2011, pp. 61-99.
102. P. van der Heide, in *X-Ray Photoelectron Spectroscopy*, John Wiley & Sons, Inc., 2011, pp. 101-140.
103. P. van der Heide, in *X-Ray Photoelectron Spectroscopy*, John Wiley & Sons, Inc., 2011, pp. 27-60.
104. T. A. Koopmans, *Physica*, 1933, **1**, 104.
105. A. Kafizas, X. Wang, S. R. Pendlebury, P. Barnes, M. Ling, C. Sotelo-Vazquez, R. Quesada-Cabrera, C. Li, I. P. Parkin and J. R. Durrant, *The Journal of Physical Chemistry A*, 2016, **120**, 715-723.
106. R. Berera, R. van Grondelle and J. T. M. Kennis, *Photosynthesis Research*, 2009, **101**, 105-118.
107. J. J. Rehr, *Radiation Physics and Chemistry*, 2006, **75**, 1547-1558.
108. J. J. Rehr and A. L. Ankudinov, *Journal of Electron Spectroscopy and Related Phenomena*, 2001, **114–116**, 1115-1121.
109. J. J. Rehr and R. C. Albers, *Reviews of Modern Physics*, 2000, **72**, 621-654.
110. C. A. Ashley and S. Doniach, *Physical Review B*, 1975, **11**, 1279-1288.
111. D. McMullan, *Journal of Microscopy*, 1989, **155**, 373-392.
112. A. D. G. Stewart, *Journal of Microscopy*, 1985, **139**, 121-127.
113. M. Wendt, *Crystal Research and Technology*, 1987, **22**, 788-788.
114. J. Goldstein, Newbury, D. E., Joy, D. C., Lyman, C. E., Echlin, P., Lifshin, E., Sawyer, L., Michael, J. R., in *Scanning Electron Micsroscopy and X-ray Microanalysis*, Kluwer Academic 1/Plenum Publishers,, New York, 2003, pp. 297-353.
115. T. Birchall, J. A. Connor and L. H. Hillier, *Journal of the Chemical Society, Dalton Transactions*, 1975, 2003-2006.
116. R. Bertoncello, A. Glisenti, G. Granozzi and M. M. Musiani, *Journal of Electroanalytical Chemistry*, 1994, **374**, 37-43.
117. E. J. Petit, J. Riga and R. Caudano, *Surface Science*, 1991, **251**, 529-534.
118. Y. Huang, G. Wang and V. C. Corberán, *Surface Science*, 2003, **547**, 55-62.
119. Y. Huang and P. Ruiz, *The Journal of Physical Chemistry B*, 2005, **109**, 22420-22425.
120. K. Lee, B. K. Jeon, G. Park, P. Song and S. P. Choi, *Solid State Communications*, 1991, **79**, 237-240.
121. X. Chen, X. Wang, C. An, J. Liu and Y. Qian, *Materials Research Bulletin*, 2005, **40**, 469-474.
122. L. Song, S. Zhang and Q. Wei, *Crystal Growth & Design*, 2012, **12**, 764-770.
123. Y. L. Ma, Y. Z. Gao, P. J. Zuo, X. Q. Cheng and G. P. Yin, *International Journal of Electrochemical Science*, 2012, **7**, 11001-11010.
124. D.-N. Liu, G.-H. He, L. Zhu, W.-Y. Zhou and Y.-H. Xu, *Applied Surface Science*, 2012, **258**, 8055-8060.
125. G.-H. He, C.-J. Liang, Y.-D. Ou, D.-N. Liu, Y.-P. Fang and Y.-H. Xu, *Materials Research Bulletin*, 2013, **48**, 2244-2249.
126. O. E. Linarez Pérez, M. D. Sánchez and M. López Teijelo, *Journal of Electroanalytical Chemistry*, 2010, **645**, 143-148.
127. G. Fan, Z. Huang, C. Chai and D. Liao, *Materials Letters*, 2011, **65**, 1141-1144.

128. Q. Zhao, X. Zhang, Q. Yang and Y. Xie, *Canadian Journal of Chemistry*, 2005, **83**, 1093-1097.
129. B. Pillep, P. Behrens, U.-A. Schubert, J. Spengler and H. Knözinger, *The Journal of Physical Chemistry B*, 1999, **103**, 9595-9603.
130. R. Nilsson, T. Lindblad and A. Andersson, *Journal of Catalysis*, 1994, **148**, 501-513.
131. J. Wang, D. Feng, W. Wu, M. Zeng and Y. Li, *Polymer Degradation and Stability*, 1991, **31**, 129-140.
132. M. J. Tricker, I. Adams and J. M. Thomas, *Inorganic and Nuclear Chemistry Letters*, 1972, **8**, 633-637.
133. P. Burroughs, A. Hamnett and A. F. Orchard, *Journal of the Chemical Society, Dalton Transactions*, 1974, 565-567.
134. R. Izquierdo, E. Sacher and A. Yelon, *Applied Surface Science*, 1989, **40**, 175-177.
135. R. Delobel, H. Baussart, J.-M. Leroy, J. Grimblot and L. Gengembre, *Journal of the Chemical Society, Faraday Transactions 1: Physical Chemistry in Condensed Phases*, 1983, **79**, 879-891.
136. E. V. Benvenutti, Y. Gushikem, A. Vasquez, S. C. de Castro and G. A. P. Zaldivar, *Journal of the Chemical Society, Chemical Communications*, 1991, 1325-1327.
137. V. Sudarsan and S. K. Kulshreshtha, *Journal of Non-Crystalline Solids*, 2001, **286**, 99-107.
138. H. Zhang, K. Sun, Z. Feng, P. Ying and C. Li, *Applied Catalysis A: General*, 2006, **305**, 110-119.
139. A. F. Orchard and G. Thornton, *Journal of the Chemical Society, Dalton Transactions*, 1977, 1238-1240.
140. C. Svensson, *Acta Crystallographica Section B*, 1974, **30**, 458-461.
141. M. Jansen, *Acta Crystallographica Section B*, 1979, **35**, 539-542.
142. R. Reiche, J. P. Holgado, F. Yubero, J. P. Espinos and A. R. Gonzalez-Elipe, *Surface and Interface Analysis*, 2003, **35**, 256-262.
143. W. S. M. Werner, *Surface and Interface Analysis*, 2001, **31**, 141-176.
144. M. V. Ganduglia-Pirovano, A. Hofmann and J. Sauer, *Surface Science Reports*, 2007, **62**, 219-270.
145. X. Pan, M.-Q. Yang, X. Fu, N. Zhang and Y.-J. Xu, *Nanoscale*, 2013, **5**, 3601-3614.
146. C. J. Kevane, *Physical Review*, 1964, **133**, A1431-A1436.
147. Z. Deng, D. Chen, F. Tang, X. Meng, J. Ren and L. Zhang, *The Journal of Physical Chemistry C*, 2007, **111**, 5325-5330.
148. Z. Deng, F. Tang, D. Chen, X. Meng, L. Cao and B. Zou, *The Journal of Physical Chemistry B*, 2006, **110**, 18225-18230.
149. G. Fan and Z. Huang, in *Micro & Nano Letters*, Institution of Engineering and Technology, 2011, pp. 55-58.
150. G. Fan, Y. Ma, L. Sun, J. Chen and Z. Huang, *Materials and Manufacturing Processes*, 2011, **26**, 1273-1276.
151. J. P. Allen, J. J. Carey, A. Walsh, D. O. Scanlon and G. W. Watson, *The Journal of Physical Chemistry C*, 2013, **117**, 14759-14769.
152. J. E. Castle, *The Journal of Adhesion*, 2008, **84**, 368-388.
153. B. Erdem, R. A. Hunsicker, G. W. Simmons, E. D. Sudol, V. L. Dimonie and M. S. El-Aasser, *Langmuir*, 2001, **17**, 2664-2669.
154. M. C. Biesinger, L. W. M. Lau, A. R. Gerson and R. S. C. Smart, *Applied Surface Science*, 2010, **257**, 887-898.
155. Q. Wang, T. Hisatomi, S. S. K. Ma, Y. Li and K. Domen, *Chemistry of Materials*, 2014, **26**, 4144-4150.
156. R. Niishiro, S. Tanaka and A. Kudo, *Applied Catalysis B-Environmental*, 2014, **150**, 187-196.
157. B. Kiss, C. Didier, T. Johnson, T. D. Manning, M. S. Dyer, A. J. Cowan, J. B. Claridge, J. R. Darwent and M. J. Rosseinsky, *Angewandte Chemie*, 2014, **126**, 14708-14712.

158. R. Asai, H. Nemoto, Q. Jia, K. Saito, A. Iwase and A. Kudo, *Chemical Communications*, 2014, **50**, 2543-2546.
159. R. Niishiro, R. Konta, H. Kato, W.-J. Chun, K. Asakura and A. Kudo, *The Journal of Physical Chemistry C*, 2007, **111**, 17420-17426.
160. S. Kitano, N. Murakami, T. Ohno, Y. Mitani, Y. Nosaka, H. Asakura, K. Teramura, T. Tanaka, H. Tada, K. Hashimoto and H. Kominami, *The Journal of Physical Chemistry C*, 2013, **117**, 11008-11016.
161. F. E. Oropeza and R. G. Egdell, *Chemical Physics Letters*, 2011, **515**, 249-253.
162. D. A. H. Hanaor and C. C. Sorrell, *Journal of Materials Science*, 2011, **46**, 855-874.
163. Z. Jian and W. Hejing, *Chinese Journal of Geochemistry*, 2003, **22**, 38-44.
164. J. I. Langford and A. J. C. Wilson, *Journal of Applied Crystallography*, 1978, **11**, 102-113.
165. R. Kelly, *Surface and Interface Analysis*, 1985, **7**, 1-7.
166. R. Webb, G. Carter and R. Collins, *Radiation Effects and Defects in Solids*, 1978, **39**, 129-139.
167. P. S. Ho, J. E. Lewis and W. K. Chu, *Surface Science*, 1979, **85**, 19-28.
168. P. K. Haff, *Applied Physics Letters*, 1977, **31**, 259-260.
169. N. Andersen and P. Sigmund, *Matematisk-Fysiske Meddelelser Kongelige Danske Videnskabernes Selskab*, 1974, **39**, 1-45.
170. G. Padeletti and G. M. Ingo, *Surface and Interface Analysis*, 2002, **34**, 266-270.
171. M. A. Baker, R. Gilmore, C. Lenardi and W. Gissler, *Applied Surface Science*, 1999, **150**, 255-262.
172. L. E. Rehn and N. Q. Lam, *Journal of Materials Engineering*, 1987, **9**, 205-215.
173. A. Gulino, A. E. Taverner, S. Warren, P. Harris and R. G. Egdell, *Surface Science*, 1994, **315**, 351-361.
174. A. Gulino, G. G. Condorelli, I. Fragalà and R. G. Egdell, *Applied Surface Science*, 1995, **90**, 289-295.
175. P. A. Cox, R. G. Egdell, C. Harding, W. R. Patterson and P. J. Tavener, *Surface Science*, 1982, **123**, 179-203.
176. R. G. Egdell, W. R. Flavell and P. Tavener, *Journal of Solid State Chemistry*, 1984, **51**, 345-354.
177. T. Luttrell, S. Halpegamage, J. Tao, A. Kramer, E. Sutter and M. Batzill, *Scientific Reports*, 2014, **4**, 4043.
178. D. O. Scanlon, C. W. Dunnill, J. Buckeridge, S. A. Shevlin, A. J. Logsdail, S. M. Woodley, C. R. A. Catlow, M. J. Powell, R. G. Palgrave, I. P. Parkin, G. W. Watson, T. W. Keal, P. Sherwood, A. Walsh and A. A. Sokol, *Nat Mater*, 2013, **12**, 798-801.
179. K. Umemoto and R. M. Wentzcovitch, *Physics and Chemistry of Minerals*, 2011, **38**, 387-395.
180. I. Terasaki, S. Shibasaki, S. Yoshida and W. Kobayashi, *Materials*, 2010.
181. S. J. Moon, M. W. Kim, K. W. Kim, Y. S. Lee, J. Y. Kim, J. H. Park, B. J. Kim, S. J. Oh, S. Nakatsuji, Y. Maeno, I. Nagai, S. I. Ikeda, G. Cao and T. W. Noh, *Physical Review B*, 2006, **74**, 113104.
182. G. C. Allen, G. A. M. El-Sharkawy and K. D. Warren, *Inorganic Chemistry*, 1973, **12**, 2231-2237.
183. A. Fujishima, X. Zhang and D. A. Tryk, *Surface Science Reports*, 2008, **63**, 515-582.
184. F. M. Pesci, A. J. Cowan, B. D. Alexander, J. R. Durrant and D. R. Klug, *The Journal of Physical Chemistry Letters*, 2011, **2**, 1900-1903.
185. R. Nakamura and Y. Nakato, *Journal of the American Chemical Society*, 2004, **126**, 1290-1298.
186. D. P. Joshi, *Solid-State Electronics*, 1986, **29**, 19-24.
187. L. Šamaj, *physica status solidi (a)*, 1987, **100**, 157-167.
188. N. Morita, T. Endo, T. Sato and M. Shimada, *Journal of Solid State Chemistry*, 1987, **68**, 106-111.
189. J. G. Mavroides, D. I. Tchernev, J. A. Kafalas and D. F. Kolesar, *Materials Research Bulletin*, 1975, **10**, 1023-1030.

190. H. P. R. Frederikse, in *Electronic Structures in Solids: Lectures presented at the Second Chania Conference, held in Chania, Crete, June 30–July 14, 1968*, ed. E. D. Haidemenakis, Springer US, Boston, MA, 1969, pp. 259-269.
191. B. Reihl, J. G. Bednorz, K. A. Müller, Y. Jugnet, G. Landgren and J. F. Morar, *Physical Review B*, 1984, **30**, 803-806.
192. A. Daga, Sharma, S., Sharma, K. S., *Journal Of Modern Physics*, 2011, **2**, 4.
193. A. H. Kahn and A. J. Leyendecker, *Physical Review*, 1964, **135**, A1321-A1325.
194. D. Hou, X. Hu, W. Ho, P. Hu and Y. Huang, *Journal of Materials Chemistry A*, 2015, **3**, 3935-3943.
195. Y. Bi, M. F. Ehsan, Y. Huang, J. Jin and T. He, *Journal of CO2 Utilization*, 2015, **12**, 43-48.
196. H.-H. Huang, Lin, Y-F., Hu, C-C., *International Science Index, Environmental and Ecological Engineering*, 2016, **3(4)**, 2512-2512.
197. L. Karimi, S. Zohoori and M. E. Yazdanshenas, *Journal of Saudi Chemical Society*, 2014, **18**, 581-588.
198. T. K. Townsend, N. D. Browning and F. E. Osterloh, *ACS Nano*, 2012, **6**, 7420-7426.
199. C. Jiafeng, H. Xianshan, L. Yi, W. Jianguang and J. Yuexia, *Materials Research Express*, 2016, **3**, 115903.
200. F. Cai, Y. Tang, F. Chen, Y. Yan and W. Shi, *RSC Advances*, 2015, **5**, 21290-21296.
201. L. F. da Silva, O. F. Lopes, V. R. de Mendonça, K. T. G. Carvalho, E. Longo, C. Ribeiro and V. R. Mastelaro, *Photochemistry and Photobiology*, 2016, **92**, 371-378.
202. H. Shen, Y. Lu, Y. Wang, Z. Pan, G. Cao, X. Yan and G. Fang, *Journal of Advanced Ceramics*, 2016, **5**, 298-307.
203. I. Marozau, M. Döbeli, T. Lippert, D. Logvinovich, M. Mallepell, A. Shkabko, A. Weidenkaff and A. Wokaun, *Applied Physics A*, 2007, **89**, 933-940.
204. I. Marozau, A. Shkabko, M. Döbeli, T. Lippert, D. Logvinovich, M. Mallepell, C. Schneider, A. Weidenkaff and A. Wokaun, *Materials*, 2009, **2**, 1388.
205. U. Sulaeman, S. Yin and T. Sato, *Journal of Nanomaterials*, 2010, **2010**, 6.
206. G. Xing, L. Zhao, T. Sun, Y. Su and X. Wang, *SpringerPlus*, 2016, **5**, 1132.
207. C. Wang, H. Qiu, T. Inoue and Q. Yao, *International Journal of Hydrogen Energy*, 2014, **39**, 12507-12514.
208. W. Wei, Y. Dai, M. Guo, L. Yu, H. Jin, S. Han and B. Huang, *Physical Chemistry Chemical Physics*, 2010, **12**, 7612-7619.
209. T. Higuchi, T. Tsukamoto, N. Sata, M. Ishigame, Y. Tezuka and S. Shin, *Physical Review B*, 1998, **57**, 6978-6983.
210. S. Kawasaki, R. Takahashi, K. Akagi, J. Yoshinobu, F. Komori, K. Horiba, H. Kumigashira, K. Iwashina, A. Kudo and M. Lippmaa, *The Journal of Physical Chemistry C*, 2014, **118**, 20222-20228.
211. K. Iwashina and A. Kudo, *Journal of the American Chemical Society*, 2011, **133**, 13272-13275.
212. S. Kawasaki, K. Akagi, K. Nakatsuji, S. Yamamoto, I. Matsuda, Y. Harada, J. Yoshinobu, F. Komori, R. Takahashi, M. Lippmaa, C. Sakai, H. Niwa, M. Oshima, K. Iwashina and A. Kudo, *The Journal of Physical Chemistry C*, 2012, **116**, 24445-24448.
213. S. Kawasaki, K. Nakatsuji, J. Yoshinobu, F. Komori, R. Takahashi, M. Lippmaa, K. Mase and A. Kudo, *Applied Physics Letters*, 2012, **101**, 033910.
214. K. Hideki, H. Mikihiro, K. Ryoko, S. Yoshiki and K. Akihiko, *Chemistry Letters*, 2004, **33**, 1348-1349.
215. S. N. Ruddlesden and P. Popper, *Acta Crystallographica*, 1958, **11**, 54-55.
216. M. M. Elcombe, E. H. Kisi, K. D. Hawkins, T. J. White, P. Goodman and S. Matheson, *Acta Crystallographica Section B*, 1991, **47**, 305-314.
217. S. N. Ruddlesden and P. Popper, *Acta Crystallographica*, 1957, **10**, 538-539.
218. K. Kawamura, M. Yashima, K. Fujii, K. Omoto, K. Hibino, S. Yamada, J. R. Hester, M. Avdeev, P. Miao, S. Torii and T. Kamiyama, *Inorganic Chemistry*, 2015, **54**, 3896-3904.

219. Y. A. Abramov, V. G. Tsirelson, V. E. Zavodnik, S. A. Ivanov and Brown I. D., *Acta Crystallographica Section B*, 1995, **51**, 942-951.
220. M. Jansen, *Angewandte Chemie International Edition in English*, 1978, **17**, 137-137.
221. M. Janousch, G. I. Meijer, U. Staub, B. Delley, S. F. Karg and B. P. Andreasson, *Advanced Materials*, 2007, **19**, 2232-2235.
222. I. Levin, V. Krayzman, J. C. Woicik, A. Tkach and P. M. Vilarinho, *Applied Physics Letters*, 2010, **96**, 052904.
223. C. Marini, O. Noked, I. Kantor, B. Joseph, O. Mathon, R. Shuker, B. J. Kennedy, S. Pascarelli and E. Sterer, *Journal of Physics: Condensed Matter*, 2016, **28**, 045401.
224. B. P. Andreasson, in *Physics*, university of Gothenburg, Sweden, 2009.
225. N. E. Brese and M. O'Keeffe, *Acta Crystallographica Section B*, 1991, **47**, 192-197.
226. C. Svensson, *Acta Crystallographica Section B*, 1975, **31**, 2016-2018.
227. C. Hennig, T. Reich, H. Funke, A. Rossberg, M. Rutsch and G. Bernhard, *Journal of Synchrotron Radiation*, 2001, **8**, 695-697.
228. D. J. Miller, M. C. Biesinger and N. S. McIntyre, *Surface and Interface Analysis*, 2002, **33**, 299-305.
229. R. Hesse, T. Chassé, P. Streubel and R. Szargan, *Surface and Interface Analysis*, 2004, **36**, 1373-1383.
230. M. P. Seah, *Surface and Interface Analysis*, 1980, **2**, 222-239.
231. M. S. Wrighton, A. B. Ellis, P. T. Wolczanski, D. L. Morse, H. B. Abrahamson and D. S. Ginley, *Journal of the American Chemical Society*, 1976, **98**, 2774-2779.
232. M. Gärtner, V. Dremov, P. Müller and H. Kisch, *ChemPhysChem*, 2005, **6**, 714-718.
233. Z. G. Yi, H. Iwai and J. H. Ye, *Applied Physics Letters*, 2010, **96**, 114103.
234. Y. Jia, S. Shen, D. Wang, X. Wang, J. Shi, F. Zhang, H. Han and C. Li, *Journal of Materials Chemistry A*, 2013, **1**, 7905-7912.
235. S. R. Pendlebury, M. Barroso, A. J. Cowan, K. Sivula, J. Tang, M. Gratzel, D. Klug and J. R. Durrant, *Chemical Communications*, 2011, **47**, 716-718.
236. Y. Ma, S. R. Pendlebury, A. Reynal, F. Le Formal and J. R. Durrant, *Chemical Science*, 2014, **5**, 2964-2973.
237. V. Cristino, S. Marinello, A. Molinari, S. Caramori, S. Carli, R. Boaretto, R. Argazzi, L. Meda and C. A. Bignozzi, *Journal of Materials Chemistry A*, 2016, **4**, 2995-3006.